A crystal window into the crustal arc magma plumbing system

JING ZHANG

A Crystal Window into the Crustal Arc Magma Plumbing System

Jing Zhang

A thesis submitted for the degree of
Doctor of Philosophy (Ph.D.) at Durham University

Department of Earth Sciences
Durham University
February 2016

Declaration

I declare that the work presented in this thesis, submitted for the degree of Doctor of Philosophy at Durham University, is entirely my own except where clearly stated. To the best of my knowledge, this thesis is distinct from any previously submitted or published at this or any other University.

Jing Zhang

Durham University

February 2016

Acknowledgements

This PhD project is funded by a Durham Doctoral Studentship (Durham University) and the China Scholarship Council (201206170178).

I would like to start with thanking my PhD supervisors who have supported and encouraged me throughout the whole process: Madeleine Humphreys, Jon Davidson and Colin Macpherson. Madeleine, your effort in supervising me throughout my last two years is tremendously helpful. I cannot say how much grateful I am in having you joined my supervision team since January, 2014. Your remarkable patience in leading me through my endless questions knocking on your doors, painful writing skills, and poor lab work experiences is gratefully acknowledged. I have learned so much from you, not only just the knowledge of igneous petrology and volcanology, but also the way of doing scientific research with critical thinking and novel insights. You are a perfect supervisor, and definitely my career role model. It has been a genuine pleasure to work with you in Durham in the last two years. I am sure that your inspirations will continue to influence me in my future academic career. Jon, you gave me the opportunity to come to Durham to take on this PhD project when I was not quite ready for it, and I will be forever grateful that you foresee my potentials in doing academic research. Colin, thank you very much for your continuous support and input to my research in the last three years.

This thesis is hugely benefited from my viva examiners: Yaoling Niu and Kate Saunders. Thank you very much for the insightful and indepth revisions and a wonderful viva experience.

I would also like to thank our postdoc team of the igneous petrology research group: George Cooper, Iain Neil, Vali Memeti, Katy Chamberlin and Morgan Salisbury. Particular thanks to George, who has been giving me valuable advices in doing a PhD, great patience in helping me with my LA-ICP-MS work, sharing data and insights into amphiboles, and most importantly, reading and commenting on all of my thesis chapters. Of course, I will acknowledge that you encourage me to defend my own opinion about amphiboles which even contradicts yours. You are a good friend and absolutely an English gentleman, and I always feel relaxed whenever discuss my work with you.

This PhD project requires extensive lab works. I would like to thank Richard Arculus for providing the lovely Mt. Lamington samples, Ian Chaplin for sample preparation, Chris Ottley for help during ICP-MS and LA-ICP-MS analysis, Leon Bowen and Chris Hayward for help in SEM imaging and EPMA. Particular thanks to Chris Ottley, who rigorously opened the door of geochemical analysis world for me and explained to me about the ICP-MS analysis work step by step from the basic.

This thesis is hugely benefited from continuously constructive discussions with members of Durham Volcanology research group and Durham Geochemistry & Geodynamics group. I would like to thank regular staff attendees of Volc Coffee including Ed Llewellin, Richard Brown, Claire Horwell, as well as current and earlier PhD students including Tom Jones, Jen Truby, Ines Tomašek, Pete Tollan, Alex Burton-Johnson, Claire Nattrass, Iona McIntosh and Hui Huang, etc. Thank you very much for always bringing interesting discussions on various volcanology topics to Volc Coffee, and also thanks for putting up with my terrible coffee-making techniques in the last two years. Members of weekly or semi-monthly GCD seminar including Yaoling Niu, Kevin Burton, Helen Williams, Chris Dale, Pierre Bouilhol, thank you for bring discussions which always broaden my limited knowledge of geochemistry and geodynamics. Particular thanks to Helen Williams and Kevin Burton for being my annual progress reviewers and providing rewarding comments, and Yaoling Niu for genuine help and care about my research progress in the last three years.

I would also like to take this chance to thank people outside of Durham who have once provided exciting discussions on my research with me. Brandon Browne and Majorie Wilson's review of my first publication in Journal of Petrology, Cal Barnes, Adam Kent, Roger Nielsen, Scott Paterson and Keith Putirka's enthusiasm and contribution in amphibole perspectives are gratefully acknowledged.

I must also thank our Department staff for their support in administrative issues: April Furnal, Karen Atkinson, Paula Elliot, Laura Haswell, Janice Oakes and Matthew Hepburn, etc.

It is the friendships offered kindly by my PhD colleagues in the Department that give me strength to enjoy my academic life in Durham, and England. I want to thank the following people in particular: Alex Peace, Jordan Phethean, Alex Baker, Mark Brodie, Racheal Bullock, Kate Horan, Bob Jamieson, Rikan Kareem, Ben Maunder, Loraine Pastoriza, Bansri Raithatha, Stephan Stricker, Iza Walczak, Jinxiu Yang, Yang Li, Zhuoli Zhang, Edward Inglis, Helen Foster, Hongliang Wang, Fienke Nanne, Ian Boothroyd, Suzie Qassim, Clayton Grove, as well as PhD students mentioned earlier.

My genuine friends off the work, Yuexian Hong, Ang Li, Xiaolin Mou, Difu Shi, Dan Li, Jie Tang, Mengwei Sun, Manjun Liu, Xuan Chen, you are the sunshine of my life in the rainy and cloudy English days, and you are the spirit of my life in the memorable cheerfully crazy time (you know what I mean☺).

Lastly but most importantly, my biggest thanks go to my family, mother, father, brother, sister-in-law and my lovely niece Yaqing, you are my incredible source of love and happiness, even though I am thousands of miles away from home.

This thesis is dedicated to my dearest grandparents, who once gave their unselfish love to this man but too unfortunate cannot see him graduated. Their memory will be with me always.

Abstract

A Crystal Window into the Crustal Arc Magma Plumbing System

Jing Zhang

Open magmatic processes, including magma mingling, fractionation and assimilation, are responsible for the diversity of magma and crystal compositions common in subduction zone settings. This thesis focuses on investigating pre-eruptive open-system processes using crystal-specific studies. Particularly, we develop calcic amphibole as a robust recorder of magmatic processes. Amphibole is a common mineral phase in water-bearing arc magmas. Its stability is a complex function of temperature, pressure, oxygen fugacity, and melt and volatile compositions. We have developed a new multiple regression analysis of published trace element partitioning data between calcic amphibole and melt. We are able to retrieve statistically significant relationships for REE, Y, Sr, Pb, Ti, Zr and Nb. We also present new pressure-independent and temperature-independent empirical chemometric equations to predict melt major element chemistry from amphibole crystal compositions. This enables us to reconstruct melt chemistry from in situ analyses of amphibole in magmas and plutonic xenoliths. Linking these inverted melt compositions to the observed crystal textures allows us to make robust interpretations of magmatic processes throughout the magma plumbing system.

We take the 1951 eruption products of Mt. Lamington volcano as a primary case study. Mt. Lamington is a composite volcano sitting on the Papuan Ultramafic Belt (PUB) ophiolite. The 1951 eruption produced andesitic dome lavas with numerous basaltic-andesitic enclaves and a few PUB ultramafic xenoliths. The mineralogy of the enclaves is dominated by amph+plag, similar to the andesitic lava hosts. The textures of the enclaves vary from fine-grained diktytaxitic to coarser-grained plutonic textured. We interpret this variation to result from variable cooling rates in the enclave-forming magma body when it invades the overlying andesite. The diktytaxitic enclaves contain variable proportions of host-derived amph+plag antecrysts and xenocrysts of ol+sp±cpx±amph with disequilibrium textures, indicating interaction with host lava and assimilation of foreign materials, respectively. A previous study argued that the olivine xenocrysts with chromian spinel inclusions are derived from the PUB, and thus that the PUB contaminated the Mt. Lamington magmas. We demonstrate that this is highly unlikely on the basis of morphological and compositional discrepancies between PUB ol+sp and the xenocrysts. The olivines are considered to represent crystal mush fractionated from precursor(s) of andesitic and/or pre-1951 shoshonitic lavas. Their presence in enclaves represents recycling of earlier-fractionated components through magma recharge.

We also revisit and bring new insights on magmatic processes shaping the Ongatiti eruption of Mangakino volcano, amphibole-bearing plutonic nodules exposed in the lavas in Grenada, and the 1991 eruption of Mt. Pinatubo. We demonstrate that reconstructed melt compositions inferred from the rims of amphiboles in pumice clasts of the Ongatiti ignimbrite are in good agreement with the matrix glass compositions. This suggests that equilibrium between the amphibole rims and melts of matrix glass compositions is achieved. The cores of amphiboles from the Ongatiti ignimbrite show large compositional variation as well as disequilibrium textures (e.g. patchy zoning, resorption/dissolution texture), and the predicted melt compositions also display large variations. We interpret that these variations may be due to different degrees of equilibration of the amphiboles derived from crystal mushes with evolved melts over a range of timescales. This interpretation is an alternative to the model provided by an earlier study which instead suggests that source heterogeneity is a major contribution to the crystal chemical diversity in the Ongatiti ignimbrite.

For amphiboles in plutonic nodules in Grenada lavas, we are able to predict the melts compositional variations from amphiboles in clinopyroxenite, hornblendite and hornblende gabbro xenoliths, in consistency with melt inclusions hosted in those cumulates. We interpret that the variations may be a result of in situ melt evolution due to extensive crystallization of the cumulate mineral phases, or equilibration of cumulate fragments with later evolved melts.

Bimodal amphibole populations and hence inferred melt compositions in Mt. Pinatubo indicate magma mingling process, in consistency with conclusions of earlier studies. The inferred

melt trace element compositions from bimodal groups also record co-crystallization of plagioclase, ilmenite, zircon and apatite together with amphiboles to varying extent, and the interpretation can be generally supported by petrography evidences.

Thesis Contents

CHAPTER 1

Introduction

1.1. THESIS RATIONALE

Magmatism provides valuable insights into understanding the structure, dynamics and evolution of the Earth. Of particular research interest in this Ph.D. study is the magmatism occurring in subduction zone settings. One plate sinks underneath the other plate at subduction zone settings, and fluids released from the sinking plate lower the liquidus of the above-lying mantle wedge and result in partial melting. The magma produced during this process, ascended through the crust and finally erupted at the surface, is fundamental to understanding the thermal evolution and chemical differentiation of the Earth. Therefore, it is important to study the subduction-related magmatism through studying volcanic eruption products produced by volcanic activities at subduction zone settings.

Volcanic activities at subduction zone settings can be extremely hazardous, however, they are also commongly associated with mineral deposits with economic significance, e.g. copper porphritic deposits. Distinct from basalt produced at mid-ocean ridges (MORB) and oceanic islands (OIB), volcanic products erupted at subduction zones are generally relatively more evolved and have geochemical features that are comparable to bulk continental crust (Davidson, 1996, Kelemen *et al.*, 1990, McCulloch & Gamble, 1991, Pearce & Peate, 1995). This has prompted extensive discussions on the mechanisms for production of continental crust in the 'subduction factory' since the concept of plate tectonics was introduced to geology (Grove & Kinzler, 1986, Rudnick, 1995, Tatsumi, 2005, Tatsumi & Kogiso, 2003). The volcanic products erupted at subduction zone settings are well known for the diversity and complexity of magma chemistry and crystal texture and compositions, which are commonly attributed to open magmatic processes, including magma mingling, fractionation and assimilation (Davidson, 1996, Grove & Kinzler, 1986, Humphreys *et al.*, 2006).

There is increasing evidence that mid- to deep-crustal fractionation of hydrous mafic magmas is an important process in generating the intermediate to silicic rocks that are typically erupted at the surface (Annen *et al.*, 2006, Melekhova *et al.*, 2015). This process may involve crystallization of pyroxene and/or amphibole and generation of abundant mafic cumulates (Davidson *et al.*, 2007a, Smith, 2014). Assimilation of crustal country rocks during magma migration from depth to the surface is also evidenced petrologically and geochemically (Bezard *et al.*, 2015, Chadwick *et al.*, 2007, Hildreth & Moorbath, 1988, Meade *et al.*, 2014, Nelson & Davidson, 1993). Moreover, recharge of mantle-derived mafic melts into shallow-stalled evolved magmas can introduce further complexity to the chemistry and petrology of the erupted products (Alves *et al.*, 2009, Barclay *et al.*, 2010, Browne *et al.*, 2006, Pallister *et al.*, 1996, Zhang *et al.*, 2015). Importantly, magma recharge followed by magma mingling/mixing processes appears to be a major trigger of explosive eruptions in arc volcanoes (Degruyter *et al.*, 2016, Druitt *et al.*, 2012, Kent *et al.*, 2010, Pallister *et al.*, 1992, Stock *et al.*, 2016). Therefore, it is essential to understand those open-system processes in order to improve our recognition of volcanic activities and ability to forecast volcanic eruptions (Cashman & Sparks, 2013, Saunders *et al.*, 2012a).

Previous explorations of open-system magmatic processes often rely on bulk rock petrology and geochemistry techniques, including analyzing bulk-rock major and trace element chemistry and isotopic compositions, etc. Such studies can robustly reveal inputs from various components in the mantle source (e.g. sediments vs. fluids attached to and/or hosted in the subducted slab; Davidson, 1983, Elliott, 2003, Plank & Langmuir, 1993), and during magma migration in the crust (Hildreth & Moorbath, 1988, Reubi *et al.*, 2011), in contributing to the diversity in the erupted products. More recently, facilitated by the fast development of *in situ* analytical techniques such as electron probe microanalysis, Laser Ablation-ICPMS, microsampling-TIMS analysis and ion probe, etc., increasing

numbers of petrological and geochemical studies switched their focus to using *in situ* chemical and textural variations in crystals, matrix glasses, and melt inclusions to unravel open magmatic processes (Jerram & Davidson, 2007, Putirka, 2008). They are termed as 'crystal-specific studies' or 'subcrystal-specific studies'. They are tremendously advantageous over traditional studies investigated through bulk-rock samples, because crystals often respond sensitively to melt thermal and chemical variations during magmatic processes and leave informative hints in their textures and compositions (Blundy & Cashman, 2008, Ginibre *et al.*, 2007, Streck, 2008). Different directions of crystal-specific and subcrystal-specific studies such as crystal size distributions (Marsh, 1998, van der Zwan *et al.*, 2013), quantification of igneous microstructures and textures (Hersum & Marsh, 2007, Humphreys *et al.*, 2012), *in situ* isotopic fingerprinting (Davidson *et al.*, 2007b, Davidson *et al.*, 2007c, Davidson & Tepley, 1997), chemical profiling and imaging (Ginibre *et al.*, 2002, Saunders *et al.*, 2014), volatile saturation and degassing (Humphreys *et al.*, 2008, Kent, 2008, Métrich & Wallace, 2008, Stock *et al.*, 2016), diffusion chronometry (Costa *et al.*, 2008, Saunders *et al.*, 2012a, Saunders *et al.*, 2012b), etc., have profoundly broadened our knowledge of magmatic processes occurring in the crustal arc magma plumbing systems and timescales over which these processes occur.

This thesis also focuses on investigating pre-eruptive open-system processes using crystal-specific studies, with a particular focus on Mt. Lamington volcano, Papua New Guinea. This is a useful case study because the 1951 eruption of Mt. Lamington took about 3,000 lives tragically without warning, and the nature of this eruption is only discussed by a few studies (Arculus *et al.*, 1983, Taylor, 1958). However, key questions remain about magmatism at this volcanic centre, including the interrelationship between the dome-forming andesitic lavas and less evolved magmatic enclaves hosted therein, the petrogenesis of the andesitic lavas and magmatic enclaves, potential effect of modifying the geochemistry of volcanic products by engulfing ophiolite country rocks in the crust, etc.

In the later parts of the thesis, we concentrate on developing calcic amphibole as a robust recorder of magmatic processes, in order to bring greater insights into the subvolcanic processes operating at Mt. Lamington and at other subduction zone volcanoes (see below) more generally. Amphibole is a common mineral phase in water-bearing arc magmas. Its stability is a complex function of temperature, pressure, oxygen fugacity, and melt and volatile compositions. We have developed a new multiple regression analysis of published trace element partitioning data between calcic amphibole and melt. We are able to retrieve statistically significant relationships for REE, Y, Sr, Pb, Ti, Zr and Nb. We also present new pressure-independent and temperature-independent empirical chemometric equations to predict melt major element chemistry from amphibole crystal compositions. This enables us to reconstruct melt chemistry from *in situ* analyses of amphibole in magmas and plutonic xenoliths. Linking these inverted melt compositions to the observed crystal textures allows us to make robust interpretations of magmatic processes throughout the volcanic system.

We demonstrate the potential of this approach using examples from Mt Lamington, Papua New Guinea; Mangakino volcano, New Zealand; Mt. Pinatubo, Philippines; and Grenada, Lesser Antilles. The reason of choosing Mt. Lamington as a case study is stated earlier. Pumice clasts from the Ongatiti ignimbrite of Mangakino volcano are amphibole-rich, and amphibole crystals display geochemical and textural diversity (Cooper & Wilson, 2014), which serve as a good case study in understanding the formation of complex amphibole textures and crystal chemical varaitions. The 1991 eruption of Mt. Pinatubo is well explored by historical studies, and in this study we use amphibole major and trace element ananlytical data collected by Loewen (2013) to infer melt compositions and thus open-system magmatic processes, and compare our results with historical interpretations, for the purpose of demonstrating the role of volcanic amphibole as a robust magma archivist. We take the Stamper *et al*. (2014)'s geochemical data of plutonic amphiboles from cumulate nodules in Grenada lavas to demonstrate the reliability of applying the melt-calibration method to plutonic amphiboles.

Throughout the thesis, we use terms 'phenocryst', 'antecryst' and 'xenocryst' ('xenolith') to denote different types of crystals. The usage of those three terms is following the definition of Davidson *et al*. (2007b). Phenocryst refers to the crystal that has directly crystallized from the

magma/rock where it is hosted; antecryst refers to the crystal of magmatic origin but not originated from the host melt observed in the solid sample, instead it is inherited from a closely related but different magma body; xenocryst/xenolith refers to material accidentally picked up from wallrock.

1.2. THESIS STRUCTURE

The research conducted during this PhD project is presented in Chapters 2, 3, 4 and 5 in the form of scientific papers. Chapter 2 is published in Journal of Petrology (DOI: 10.1093/petrology/egv071), and Chapters 3-5 are prepared as paper manuscripts to be submitted to American Mineralogist/Contributions to Mineralogy and Petrology, Journal of Petrology, and Lithos, respectively. Throughout the thesis, the term 'we' represents co-authorship denoted after the title of each chapter. The complete body of text and the production of tables and figures are purely my own work, following detailed corrections suggested by coauthors, especially M.C.S. Humphreys.

The topic of Chapter 2 is 'the petrogenesis of Mt. Lamington 1951 andesite and magmatic enclaves'. In this chapter, we introduce the petrology, mineralogy and geochemistry of the 1951 eruption products of Mt. Lamington and focus on exploring the following questions:

- *What is the interrelationship between the 1951 andesite and its magmatic enclaves?*
- *What is the origin of olivine crystals with disequilibrium textures in the 1951 andesite and diktytaxitic enclaves?*
- *What is the petrogenesis of the 1951 andesite and magmatic enclaves?*

A key early finding from Chapter 2 was that variations in some bulk rock trace element ratios might have arisen from assimilation or fractionation of amphibole between andesites and enclaves at Mt. Lamington. This interpretation prompted a deeper interest in understanding the trace element compositions of the Mt. Lamington amphiboles in detail. However, further investigation revealed the huge complexity of amphibole chemistry and partitioning, and eventually resulted in the extensive and detailed regression analysis that forms Chapters 3 and 4.

Thus, the topic of Chapter 3 is 'open-system processes revealed by melt major element inversion from calcic amphiboles'. In this chapter, we use the pressure, temperature, melt chemistry (P-T-X) conditions of published experimental studies in which calcic amphiboles are crystallized to calibrate chemometric equations, the purpose of which is to infer melt major element compositions from amphibole crystal chemistry. The following questions are investigated in this chapter:

- *What are the P-T-X conditions of crystallization of calcic amphiboles according to experimental studies?*
- *Can we improve our ability to infer accurately the major element compositions of melts from which calcic amphiboles are crystallized, using the crystal chemistry and/or the crystallization temperature of calcic amphibole?*
- *What are the implications of using the chemometric equations in reconstructing major element compositions of melts in equilibrium with volcanic and plutonic amphiboles?*

The topic of Chapter 4 is 'new insights into trace element partitioning in calcic amphiboles from multiple regression analysis'. In this chapter, we try to link trace element partition coefficients of calcic amphiboles ($^{Amph/L}D$) with amphibole crystal chemistry using multiple regression analyses. The new approach is tested using published datasets and then applied to different arc settings in order to demonstrate the future potential of the method. The following questions are explored in this chapter:

- *Can we infer $^{Amph/L}D$ from the crystal chemistry and/or crystallization temperatures of calcic amphiboles?*
- *What is the dominant control over trace element concentrations in calcic amphiboles: melt compositions or $^{Amph/L}D$?*
- *What magmatic processes can we infer from the reconstructed melt major and trace element compositions?*

The topic of Chapter 5 is ‘amphibole compositional bimodality reflects arc magma hybridization’. In this chapter, we revisit Mt. Lamington with a specific focus on amphibole crystal chemistry and textures, and attempt to infer greater detail on volcanic processes and bring together different strands of information from earlier parts of the thesis. The following two main questions will be addressed in this chapter:

- *How does amphibole compositional bimodality form in arc magmas and what are the implications?*
- *What can we infer from the sub-crystal scale compositional bimodality revealed in the two types of oscillatory zoned amphibole phenocrysts in Mt. Lamington 1951 andesites?*

Finally, we summarize our answers to the above-listed key questions and also point out directions for future work in Chapter 6.

1.3. REFERENCES

Alves, A., Janasi, V. D., Simonetti, A. & Heaman, L. (2009). Microgranitic Enclaves as Products of Self-mixing Events: a Study of Open-system Processes in the Maua Granite, Sao Paulo, Brazil, Based on in situ Isotopic and Trace Elements in Plagioclase. *Journal of Petrology* **50**, 2221-2247.

Annen, C., Blundy, J. D. & Sparks, R. S. J. (2006). The genesis of intermediate and silicic magmas in deep crustal hot zones. *Journal of Petrology* **47**, 505-539.

Arculus, R. J., Johnson, R. W., Chappell, B. W., Mc Kee, C. O. & Sakai, H. (1983). Ophiolite-contaminated andesites, trachybasalts, and cognate inclusions of Mount Lamington, Papua New Guinea: anhydrite-amphibole-bearing lavas and the 1951 cumulodome. *Journal of Volcanology and Geothermal Research* **18**, 215-247.

Barclay, J., Herd, R. A., Edwards, B. R., Christopher, T., Kiddle, E. J., Plail, M. & Donovan, A. (2010). Caught in the act: Implications for the increasing abundance of mafic enclaves during the recent eruptive episodes of the Soufriere Hills Volcano, Montserrat. *Geophysical Research Letters* **37**.

Bezard, R., Turner, S., Davidson, J. P., Macpherson, C. G. & Lindsay, J. M. (2015). Seeing through the Effects of Crustal Assimilation to Assess the Source Composition beneath the Southern Lesser Antilles Arc. *Journal of Petrology* **56**, 815-844.

Blundy, J. & Cashman, K. (2008). Petrologic Reconstruction of Magmatic System Variables and Processes. *Minerals, Inclusions and Volcanic Processes* **69**, 179-239.

Browne, B. L., Eichelberger, J. C., Patino, L. C., Vogel, T. A., Dehn, J., Uto, K. & Hoshizumi, H. (2006). Generation of porphyritic and equigranular mafic enclaves during magma recharge events at Unzen volcano, Japan. *Journal of Petrology* **47**, 301-328.

Cashman, K. V. & Sparks, R. S. J. (2013). How volcanoes work: A 25 year perspective. *Geological Society of America Bulletin* **125**, 664-690.

Chadwick, J. P., Troll, V. R., Ginibre, C., Morgan, D., Gertisser, R., Waight, T. E. & Davidson, J. P. (2007). Carbonate assimilation at Merapi volcano, Java, Indonesia: Insights from crystal isotope stratigraphy. *Journal of Petrology* **48**, 1793-1812.

Cooper, G. F. & Wilson, C. J. N. (2014). Development, mobilisation and eruption of a large crystal-rich rhyolite: The Ongatiti ignimbrite, New Zealand. *Lithos* **198**, 38-57.

Costa, F., Dohmen, R. & Chakraborty, S. (2008). Time Scales of Magmatic Processes from Modeling the Zoning Patterns of Crystals. *Reviews in Mineralogy and Geochemistry* **69**, 545-594.

Davidson, J., Turner, S., Handley, H., Macpherson, C. & Dosseto, A. (2007a). Amphibole "sponge" in arc crust? *Geology* **35**, 787-790.

Davidson, J. P. (1983). Lesser Antilles Isotopic Evidence of the Role of Subducted Sediment in Island-Arc Magma Genesis. *Nature* **306**, 253-256.

Davidson, J. P. (1996). Deciphering mantle and crustal signatures in subduction zone magmatism. In: Bebout, G. E., Scholl, D. W., Kirby, S. H. & Platt, J. P. (eds.) *Subduction Top to Bottom*. Washington, D. C.: American Geophysical Union, 251-262.

Davidson, J. P., Morgan, D. J. & Charlier, B. L. A. (2007b). Isotopic Microsampling of Magmatic Rocks. *Elements* **3**, 253-259.

Davidson, J. P., Morgan, D. J., Charlier, B. L. A., Harlou, R. & Hora, J. M. (2007c). Microsampling and Isotopic Analysis of Igneous Rocks: Implications for the Study of Magmatic Systems. *Annual Review of Earth and Planetary Sciences* **35**, 273-311.

Davidson, J. P. & Tepley, F. J. (1997). Recharge in volcanic systems: Evidence from isotope profiles of phenocrysts. *Science* **275**, 826-829.

Degruyter, W., Huber, C., Bachmann, O., Cooper, K. M. & Kent, A. J. R. (2016). Magma reservoir response to transient recharge events: The case of Santorini volcano (Greece). *Geology* **44**, 23-26.

Druitt, T. H., Costa, F., Deloule, E., Dungan, M. & Scaillet, B. (2012). Decadal to monthly timescales of magma transfer and reservoir growth at a caldera volcano. *Nature* **482**, 77-U97.

Elliott, T. (2003). Tracers of the slab. *AGU Geophysical Monograph Series* **138**, 23-45.

Ginibre, C., Kronz, A. & Worner, G. (2002). High-resolution quantitative imaging of plagioclase composition using accumulated backscattered electron images: new constraints on oscillatory zoning. *Contributions to Mineralogy and Petrology* **142**, 436-448.

Ginibre, C., Worner, G. & Kronz, A. (2007). Crystal zoning as an archive for magma evolution. *Elements* **3**, 261-266.

Grove, T. L. & Kinzler, R. J. (1986). Petrogenesis of Andesites. *Annual Review of Earth and Planetary Sciences* **14**, 417-454.

Hersum, T. G. & Marsh, B. D. (2007). Igneous textures: On the kinetics behind the words. *Elements* **3**, 247-252.

Hildreth, W. & Moorbath, S. (1988). Crustal Contributions to Arc Magmatism in the Andes of Central Chile. *Contributions to Mineralogy and Petrology* **98**, 455-489.

Humphreys, M. C. S., Blundy, J. D. & Sparks, R. S. J. (2006). Magma Evolution and Open-System Processes at Shiveluch Volcano: Insights from Phenocryst Zoning. *Journal of Petrology* **47**, 2303-2334.

Humphreys, M. C. S., Blundy, J. D. & Sparks, R. S. J. (2008). Shallow-level decompression crystallisation and deep magma supply at Shiveluch Volcano. *Contributions to Mineralogy and Petrology* **155**, 45-61.

Humphreys, M. C. S., Edmonds, M., Plail, M., Barclay, J., Parkes, D. & Christopher, T. (2012). A new method to quantify the real supply of mafic components to a hybrid andesite. *Contributions to Mineralogy and Petrology* **165**, 191-215.

Jerram, D. A. & Davidson, J. P. (2007). Frontiers in textural and microgeochemical analysis. *Elements* **3**, 235-238.

Kelemen, P. B., Johnson, K. T. M., Kinzler, R. J. & Irving, A. J. (1990). High-field-strength element depletions in arc basalts due to mantle-magma interaction. *Nature* **345**, 521-524.

Kent, A. J. R. (2008). Melt Inclusions in Basaltic and Related Volcanic Rocks. *Minerals, Inclusions and Volcanic Processes* **69**, 273-331.

Kent, A. J. R., Darr, C., Koleszar, A. M., Salisbury, M. J. & Cooper, K. M. (2010). Preferential eruption of andesitic magmas through recharge filtering. *Nature Geoscience* **3**, 631-636.

Loewen, M. W. (2013). Volatile mobility of trace metals in volcanic systems. Ph.D. thesis, Oregon State University.

Marsh, B. D. (1998). On the interpretation of crystal size distributions in magmatic systems. *Journal of Petrology* **39**, 553-599.

McCulloch, M. T. & Gamble, J. A. (1991). Geochemical and geodynamical constraints on subduction zone magmatism. *Earth and Planetary Science Letters* **102**, 358-374.

Meade, F. C., Troll, V. R., Ellam, R. M., Freda, C., Font, L., Donaldson, C. H. & Klonowska, I. (2014). Bimodal magmatism produced by progressively inhibited crustal assimilation. *Nature Communications* **5**.

Melekhova, E., Blundy, J., Robertson, R. & Humphreys, M. C. S. (2015). Experimental Evidence for Polybaric Differentiation of Primitive Arc Basalt beneath St. Vincent, Lesser Antilles. *Journal of Petrology* **56**, 161-192.

Métrich, N. & Wallace, P. J. (2008). Volatile Abundances in Basaltic Magmas and Their Degassing Paths Tracked by Melt Inclusions. *Minerals, Inclusions and Volcanic Processes* **69**, 363-402.

Nelson, S. T. & Davidson, J. P. (1993). Interactions between Mantle-Derived Magmas and Mafic Crust, Henry Mountains, Utah. *Journal of Geophysical Research-Solid Earth* **98**, 1837-1852.

Pallister, J., Hoblitt, R., Meeker, G. P., Knight, R. J. & Siems, D. F. (1996). Magma Mixing at Mount Pinatubo: Petrographic and Chemical Evidence from the 1991 Deposits. In: Newhall, C. & Punongbayan, R. S. (eds.) *Fire and Mud: Eruptions and Lahars of Mount Pinatubo, Philippines*. Seattle: University of Washington Press, 687-731.

Pallister, J. S., Hoblitt, R. P. & Reyes, A. G. (1992). A Basalt Trigger for the 1991 Eruptions of Pinatubo Volcano. *Nature* **356**, 426-428.

Pearce, J. A. & Peate, D. W. (1995). Tectonic Implications of the Composition of Volcanic Arc Magmas. *Annual Review of Earth and Planetary Sciences* **23**, 251-285.

Plank, T. & Langmuir, C. H. (1993). Tracing Trace-Elements from Sediment Input to Volcanic Output at Subduction Zones. *Nature* **362**, 739-743.

Putirka, K. D. (2008). Introduction to Minerals, Inclusions and Volcanic Processes. *Minerals, Inclusions and Volcanic Processes* **69**, 1-8.

Reubi, O., Bourdon, B., Dungan, M. A., Koornneef, J. M., Selles, D., Langmuir, C. H. & Aciego, S. (2011). Assimilation of the plutonic roots of the Andean arc controls variations in U-series disequilibria at Volcan Llaima, Chile. *Earth and Planetary Science Letters* **303**, 37-47.

Rudnick, R. L. (1995). Making continental crust. *Nature* **378**, 571-578.

Saunders, K., Blundy, J., Dohmen, R. & Cashman, K. (2012a). Linking Petrology and Seismology at an Active Volcano. *Science* **336**, 1023-1027.

Saunders, K., Buse, B., Kilburn, M. R., Kearns, S. & Blundy, J. (2014). Nanoscale characterisation of crystal zoning. *Chemical Geology* **364**, 20-32.

Saunders, K., Rinnen, S., Blundy, J., Dohmen, R., Klemme, S. & Arlinghaus, H. F. (2012b). TOF-SIMS and electron microprobe investigations of zoned magmatic orthopyroxenes: First results of trace and minor element analysis with implications for diffusion modeling. *American Mineralogist* **97**, 532-542.

Smith, D. J. (2014). Clinopyroxene precursors to amphibole sponge in arc crust. *Nature Communications* **5**.

Stock, M. J., Humphreys, M. C. S., Smith, V. C., Isaia, R. & Pyle, D. M. (2016). Late-stage volatile saturation as a potential trigger for explosive volcanic eruptions. *Nature Geoscience*.

Streck, M. J. (2008). Mineral Textures and Zoning as Evidence for Open System Processes. *Minerals, Inclusions and Volcanic Processes* **69**, 595-622.

Tatsumi, Y. (2005). The subduction factory: How it operates in the evolving Earth. *GSA Today* **15**, 4-10.

Tatsumi, Y. & Kogiso, T. (2003). The subduction factory: its role in the evolution of the Earth's crust and mantle. *Geological Society, London, Special Publications* **219**, 55-80.

Taylor, G. A. (1958). The 1951 eruption of Mount Lamington, Papua. *Bureau of Mineral Resources, Geology and Geophysics* **38**.

van der Zwan, F. M., Chadwick, J. P. & Troll, V. R. (2013). Textural history of recent basaltic-andesites and plutonic inclusions from Merapi volcano. *Contributions to Mineralogy and Petrology* **166**, 43-63.

Zhang, J., Davidson, J. P., Humphreys, M. C. S., Macpherson, C. G. & Neill, I. (2015). Magmatic Enclaves and Andesitic Lavas from Mt. Lamington, Papua New Guinea: Implications for Recycling of Earlier-fractionated Minerals through Magma Recharge. *Journal of Petrology* **56**, 2223-2256.

CHAPTER 2

Magmatic Enclaves and Andesitic Lavas from Mt. Lamington, Papua New Guinea: Implications for Recycling of Earlier-fractionated Minerals through Magma Recharge

J. ZHANG[1]*, J. P. DAVIDSON[1], M. C. S. HUMPHREYS[1], C. G. MACPHERSON[1], I. NEILL[1,2]

[1]DEPARTMENT OF EARTH SCIENCES, UNIVERSITY OF DURHAM, DURHAM, DH1 3LE, UK

[2]SCHOOL OF GEOGRAPHICAL AND EARTH SCIENCES, UNIVERSITY OF GLASGOW, GLASGOW, G12 8QQ, UK

*Corresponding author. E-mail: jing.zhang5@durham.ac.uk

ABSTRACT

Mt. Lamington is a composite, dome-forming volcano in Papua New Guinea, sitting on the Papuan Ultramafic Belt (PUB) ophiolite. The 1951 eruption produced andesitic dome lavas with numerous basaltic-andesitic enclaves and a few PUB ultramafic xenoliths. To understand the nature of the 1951 eruption, and to assess the effect of assimilating ophiolitic crust in modifying the geochemistry of arc magmas, we carried out petrological, mineralogical and geochemical studies on andesitic lavas as well as magmatic enclaves and ultramafic inclusions. The mineralogy of the enclaves is dominated by amphibole and plagioclase, similar to the andesitic lava hosts. The textures of the enclaves vary from fine-grained diktytaxitic to coarser-grained plutonic textured. We interpret this variation to result from variable cooling rates in the enclave-forming magma body when it invades the overlying andesite. The diktytaxitic enclaves contain variable proportions of host-derived amph+plag antecrysts and xenocrysts of ol+sp±cpx±amph with disequilibrium textures, indicating interaction with host lava and assimilation of foreign materials, respectively. A previous study argued that the olivine xenocrysts with chromian spinel inclusions are derived from the PUB, and thus that the PUB contaminated the Mt. Lamington magmas. We demonstrate that this is highly unlikely on the basis of morphological and compositional discrepancies between PUB ol+sp, sampled in nodules, and the xenocrysts. Mass balance indicates that the high whole-rock Ni contents of enclaves and andesitic hosts can be explained by olivine incorporation and do not require any PUB involvement. The olivines are considered to represent crystal mush fractionated from precursor(s) of andesitic and/or pre-1951 shoshonitic lavas. Their presence in enclaves represents recycling of earlier-fractionated components through magma recharge. We argue that this recycling is an important and underestimated process in shaping arc magmas.

KEY WORDS: assimilation; magmatic enclaves; magma recharge; Mt. Lamington; ophiolite contamination; Papuan Ultramafic Belt

This chapter is published in Journal of Petrology, Oxford University Press.

Zhang, J., Davidson, J. P., Humphreys, M. C. S., Macpherson, C. G. & Neill, I. (2015). Magmatic Enclaves and Andesitic Lavas from Mt. Lamington, Papua New Guinea: Implications for Recycling of Earlier-fractionated Minerals through Magma Recharge. *Journal of Petrology* **56**, 2223-2256. DOI: 10.1093/petrology/egv071

2.1. INTRODUCTION

Volcanism on the Papuan Peninsula is of particular interest because it represents arc-like magmatism decoupled from active subduction (Jakeš & Smith, 1970; Johnson *et al.*, 1978; Smith *et al.*, 1979; Smith, 1982; Smith & Compston, 1982; Arculus *et al.*, 1983; Smith & Milsom, 1984; Smith, 2013a). The most recent volcanic activity on the Papuan peninsula was represented by the 1951 eruption of Mt. Lamington, Papua New Guinea (PNG). The eruption initiated on 21st January 1951; this climactic phase, followed by another 8 major explosive episodes which lasted until 5th March, 1951, resulted in the devastation of an area > 100 km^2, as well as around 3000 deaths (Taylor, 1958). Prior to this eruption, Mt. Lamington had never been regarded as a volcano, due to a lack of observations or eruption records. A lava dome was constructed intermittently within the craters during and after the explosive eruptions. In 1956, the dome approximated a truncated cone with an estimated size of ~550 m in height and ~1300 m and ~600 m in width at the base and summit, respectively (Taylor, 1958; Arculus *et al.*, 1983), representing a volume of about 0.4 km^3. The dome sits on older volcanic products of shoshonitic composition (pre-1951 shoshonite, unknown age). It comprises andesitic lavas (1951 andesite) and contains abundant mafic-intermediate magmatic enclaves, as well as ultramafic xenoliths (Taylor, 1958; Arculus *et al.*, 1983). The 1951 andesite and the enclaves are characterized by high Cr and Ni contents, and enrichment in incompatible elements relative to volcanism at the adjacent New Britain arc (Arculus *et al.*, 1983). The high concentrations of Cr and Ni were previously ascribed to assimilation of ultramafic material that is found in PNG and thought to underlie Mt. Lamington (Papuan Ultramafic Belt, PUB; Arculus *et al.*, 1983), but this hypothesis cannot also explain the high incompatible element concentrations; the heat budget required to assimilate such refractory material is also problematic.

In order to investigate further the nature of volcanism on the Papuan Peninsula and to understand potential compositional variations in the magma source region and in the magmatic processes which occurred at crustal levels, we obtained new trace element element and Nd-Sr isotope whole-rock and mineral composition data for the andesites and magmatic enclaves produced during the 1951 eruption of Mt. Lamington. We link these new data with petrographic observations to bring additional insights on the inter-relationships between the 1951 andesite and its magmatic and ultramafic inclusions.

2.2. TECTONIC AND GEOLOGICAL SETTING

Mt. Lamington (8º57'S, 148º09'E) is a Quaternary composite volcano located on the Papuan Peninsula, together with other dormant edifices: Hydrographers Range, Mt. Victory and Mt. Trafalgar. The Papuan Peninsula occurs in a tectonically complex boundary region where the north-northeast moving Australian Plate converges with the westward moving Pacific Plate (Baldwin *et al.*, 2012, Davies, 2012; **Fig. 2.1a**). The Papuan Peninsula lies on the Australian Plate, which is actively subducting beneath the Pacific Plate at the New Britain Arc and the Solomon Arc (Baldwin *et al.*, 2012). To the east of the Papuan Peninsula, seafloor spreading in the Woodlark Sea Basin started ~3.5 Ma ago and has been propagating westward (Taylor *et al.*, 1995; Taylor *et al.*, 1999), probably resulting from slab pull owing to the subduction of the Solomon Sea Plate (Weissel *et al.*, 1982). The Pocklington Trough to the south of the Papuan Peninsula represents a former continental passive margin formed as a result of the Coral Sea Basin opening in the Middle-Late Eocene (Davies & Smith, 1971, Smith & Milsom, 1984). To the north of the Papuan Peninsula, the Trobriand Trough is the trench of a south-dipping subduction zone. The absence of a seismically-defined Benioff Zone (Hall & Spakman, 2002; Wallace *et al.*, 2004), suggests that subduction is presently inactive, although it might have been active in the Miocene (Hill & Raza, 1999). Current magmatism on the Papuan Peninsula is speculated to be a product of delayed partial melting of subduction-modified mantle (Johnson *et al.*, 1978; Arculus *et al.*, 1983), triggered by upwelling asthenospheric mantle as a result of westward propagation of the Woodlark Spreading-Rifting System (Smith, 2013a).

The Papuan Peninsula contains (**Fig. 2.1b**; Davies, 2012; Smith, 2013b): (1) Quaternary composite volcanoes and sedimentary deposits (including Mt. Lamington); (2) the Papuan Ultramafic Belt (PUB; see below); (3) the Owen Stanley Metamorphic Complex, composed of the largely

metasedimentary Kagi Metamorphics and the largely metabasic Emo Metamorphics (see below); (4) the Aure Fold Belt, a westward-facing thrust and fold belt composed of thick Late Oligocene-Pliocene clastic-dominated sediments; and (5) the Milne Terrane, made up of Cretaceous-Eocene MORB-like basalts, interpreted as the northern margin of the uplifted Coral Sea Basin.

The Mt. Lamington and Hydrographers Range volcanic edifices sit on a basement of PUB and Emo Metamorphics (Taylor, 1958; Arculus *et al.*, 1983). The PUB comprises obducted Late Cretaceous oceanic crust (ophiolite) lying above the Owen Stanley Metamorphic Complex; the emplacement of the PUB is thought to have taken place in the Eocene (Davies & Smith, 1971; Davies & Jaques, 1984; Lus *et al.*, 2004). From bottom to top, the PUB comprises three layers: ultramafic rocks (thickness of 4-8 km), gabbro (~4 km) and basalt (4-6 km; Davies & Smith, 1971). The ultramafic section is predominantly harzburgitic tectonite with olivine ($Fo_{91.6-93.6}$), orthopyroxene ($En_{92.1-93.4}$) and chromian spinel (Cr/Cr+Al = 0.9), as well as peridotite containing olivine ($Fo_{89.3}$), diopside, accessory chromian spinel (Cr/Cr+Al = 0.7), poikilitic orthopyroxene (En_{84}), and rare anorthitic plagioclase (An_{81-86}; Davies & Smith, 1971; England & Davies, 1973; Jaques & Chappell, 1980). The gabbro section varies from olivine-rich gabbro at the base to olivine-poor norite-gabbro at the top, with cumulus olivine ($Fo_{80.6}$), plagioclase (An_{81-93}) and poikilitic augite/hypersthene (Davies & Smith, 1971; England & Davies, 1973; Jaques & Chappell, 1980). The basalt section is mainly composed of aphanitic pillow lavas, with rare microphenocrysts of Fe-rich augite ($En_{40-21}Wo_{35-48}Fs_{25-31}$) or labradorite (Davies & Smith, 1971; England & Davies, 1973; Jaques & Chappell, 1980). The geochemistry of the basalts (SiO_2 = 47-50 wt %) is characterized by high Fe (FeO_{tot} = 14-15 wt %) and a MORB-like trace element signature (Davies & Smith, 1971; England & Davies, 1973; Jaques & Chappell, 1980).

The Emo Metamorphics that underlie Mt. Lamington and the PUB are composed of greenschist, amphibolite, and lawsonite/garnet blueschist thrust sheets of tholeiitic protoliths (Worthing & Crawford, 1996). The geochemistry varies from occasional LREE-depleted N-MORB with Zr/Nb > 40, to more dominant LREE-enriched E-MORB with Zr/Nb of 8-16. $^{143}Nd/^{144}Nd$ displays a large variation from 0.512744±13 in garnet-bearing blueschists to 0.513107±18 in amphibolites (Worthing & Crawford, 1996).

2.3. ANALYTICAL METHODS

The samples used in this study are those described by Arculus *et al.* (1983). The major element data (XRF) from Arculus *et al.* (1983) are re-evaluated together with new trace element and isotopic data collected for this study.

For trace element analysis sample powders from the Arculus *et al*. (1983) study were dissolved using a routine HF-HNO_3 digestion procedure (Ottley *et al.*, 2003) and analysed on a Thermo Scientific X Series 2 inductively coupled plasma mass spectrometer (ICP-MS) at the Durham Geochemistry Centre, Durham University. Monitoring of instrumental performance was achieved by sample-standard-blank bracketing using procedural blanks (n=15) and international reference standards W2 (n=8), BHVO-1 (n=4), AGV-1 (n=4), NBS688 (n=4), and BE-N (n=4), with Re-Rh spike solutions. Two Mt. Lamington sample duplicates (a shoshonite, LAM-27D and an andesite, LAM-14) were used as internal standards. Repetitive runs of W2 across two batches of analysis typically gave relative standard deviations (%RSD) of rare earth element (REE) analyses of <3.5%, with transition metal, large ion lithophile (LILE) and high field strength element (HFSE) analyses giving RSDs of <9% (**Table 2.1**). ICP-MS analyses of the Mt. Lamington samples agree very well with the XRF data (Arculus *et al.*, 1983), except that V concentrations are slightly higher and Zr concentrations are lower by 30-80% relative to the XRF data (**Supplementary Data Appendix Fig. 2.1**). For Zr, ICP-MS analyses reproduce reference standards very well, however they failed to reproduce Zr by multiple analysis of an internal rock standard (LAM-27D) within and between batches of measurements, and the XRF data. Therefore, we believe this discrepancy is due to incomplete dissolution of accessory minerals such as zircon during our sample preparation. Considering that zircon is one of the most important host of Hf, the concentrations of Hf should also

be biased by this effect. Thus, the original XRF Zr data from Arculus *et al.* (1983) are used instead and Hf data are not considered. Ta data are not reported since the rock samples were prepared in a tungsten carbide mill.

For whole-rock Sr-Nd isotopes, sample powders were dissolved in Teflon beakers using HF-HNO_3 solution and analysed on a thermal ionization mass spectrometer at the University of California, Los Angeles. Sr and Nd separation followed standard cation exchange techniques (e.g., Richard *et al.*, 1976). Sr isotope ratios were determined using a VG Sector multicollecting mass spectrometer in dynamic mode. Nd isotopic ratios were measured on a VG Sector 54-30 multicollecting mass spectrometer in static mode. Total procedural Sr and Nd blanks are ~350 pg and ~100 pg, respectively. Duplicate analyses of the international reference standard NBS987 gave $^{87}Sr/^{86}Sr = 0.710248 \pm 17$ (n=5) and the La Jolla standard gave an average $^{143}Nd/^{144}Nd$ of 0.511840 ± 11 (n=4; Davidson *et al.*, 1993). The full dataset of bulk-rock geochemistry is given in **Table 2.1**.

For backscattered electron (BSE) imaging and electron probe microanalysis (EPMA), the samples were prepared as standard polished probe sections and carbon-coated to a thickness of 25 nm. BSE images were collected with a Hitachi SU-70 FEG scanning electron microscope at Durham University. EPMA was carried out at Edinburgh University, using a Cameca SX100 electron microprobe equipped with 5 wavelength-dispersive spectrometers. Minerals were analysed using a 15 kV accelerating voltage, with 4-10 nA beam current for major elements and 100 nA for trace elements. A PAP correction procedure was applied to all analyses. Anhydrous minerals (plagioclase, olivine, orthopyroxene, clinopyroxene and oxides) were analysed using a 2-5 µm spot; for hydrous minerals (amphibole and biotite) a 10 µm defocused beam was used. Glasses were analysed using a 15 kV accelerating voltage, 4 nA for major elements, 80 nA for minor elements and a 12 µm defocused beam. Calibration was undertaken using the following standards: wollastonite (Si, Ca), spinel (Al, Mg), fayalite (Fe), jadeite (Na), orthoclase (K), rutile (Ti), celestite (Sr), pure metal (Mn, Cr, Ni), NaCl (Cl) and synthetic $RbMnF_3$ (F). Representative EPMA data with typical 1 σ analytical errors are given in **Tables 2.3-2.9**; the full dataset is included in the Supplementary Data.

2.4. RESULTS

2.4.1. Petrology

2.4.1.1. 1951 andesite

The dome lavas are a vesicular, porphyritic andesite with 56-64% phenocrysts/antecrysts of plagioclase (30-37%), amphibole (18-26%), biotite (1-2%), Fe-Ti oxides (1-3%) and rare clinopyroxene and orthopyroxene (point counting results, **Table 2.2**). Plagioclase phenocrysts/antecrysts are large and euhedral (typically 2.5–3 mm), with abundant inclusions of amphibole, biotite, oxides and apatite, as well as melt inclusions. Three types of plagioclase are distinguished based on the textures: i) oscillatory zoned, ii) patchy-zoned with oscillatory overgrowth rims, and iii) sieve-textured grains with oscillatory cores (**Fig. 2.2a-c**). Amphibole phenocrysts/antecrysts, typically 1.0-1.5 mm, are euhedral and fresh, without any evidence of breakdown. They contain abundant inclusions of plagioclase, Fe-Ti oxides, biotite and vesicle-bearing glass. Pleochroism varies from light green/brownish green in some samples to bright red/deep reddish brown in others. The majority of amphiboles are optically unzoned; some, however, show simple zoning with compositionally contrasting cores and rims (**Fig. 2.2d**). Many titanomagnetite microphenocrysts contain exsolution lamellae of ilmenite (**Fig. 2.2e**). The groundmass of the 1951 andesite is predominantly feldspathic with microlites of plagioclase, amphibole and Fe-Ti oxides. Xenocrystic olivine is present (e.g., **Fig. 2.2f**), typically with reaction coronae of amphibole ± orthopyroxene. Apatite, cristobalite and zircon are accessory phases; apatite is found as inclusions in phenocrysts and cristobalite is mainly found inside vesicles.

2.4.1.2. Magmatic enclaves

Dark-coloured magmatic enclaves range from 12 mm to >50 mm based on hand specimen observations. They have sharp margins and no clear grain size variation within individual enclaves (**Fig. 2.3a-d**). Two major types of enclave are distinguished in hand specimen: those with a *diktytaxitic* texture and those with a *plutonic* texture.

Diktytaxitic textures in volcanic rocks are typified by a highly vesicular glassy groundmass and the presence of abundant elongated crystals (Bacon, 1986). In Mt. Lamington, diktytaxitic-textured enclaves (**Fig. 2.3a**) are characterized by the presence of glass, 3.7-16.3% sub-spherical vesicles or vesicle networks and abundant acicular amphibole crystals, with crystals protruding into the irregular-shaped vesicles. Phenocryst or antecryst phases in these enclaves consist of amphibole (40-47%), plagioclase (21-31%), Fe-Ti oxides (<3%), and biotite (<1%). Amphibole in the diktytaxitic enclaves occurs as: (i) large tabular crystals with compositionally distinct cores and rims (**Fig. 2.4a,b**), (ii) acicular crystals with long axes ranging from a few hundred microns to 2 mm (**Fig. 2.4a,b**), (iii) euhedral crystals growing as part of olivine reaction rims (**Fig. 2.4a,b**), (iv) amphibole xenocrysts rimmed by amphibole (**Fig. 2.4e**) and (v) in plutonic crystal clots with plagioclase and biotite, characterized by coarse, cumulus embayed crystals with minor amounts of glass present along grain boundaries (**Fig. 2.4e,f**). We term the tabular amphiboles *phenocryst-like* because the crystal morphology is similar to amphibole phenocrysts from the 1951 andesite (*antecrysts*). Plagioclase in the diktytaxitic enclaves occurs as square-shaped crystals (<0.5 mm), commonly with a resorbed core surrounded by normally zoned rim. Large plagioclase crystals with patchy and sieve textures are also found (e.g., **Fig. 2.4d**). Spinel-bearing olivine (1.3-4.3%) is present as an abundant relict phase with reaction rims of opx+oxides and amphibole (**Fig. 2.2f, 2.4a-c**).Olivine crystals tend to be euhedral when the reaction rim is thin (**Fig. 2.4b**). Rare clinopyroxenes are present and are characterized by breakdown textures such as amphibole rims and the development of amphibole blebs along their cleavage planes; thus they are identified as xenocrysts (**Fig. 2.4a**).

In contrast, the *plutonic-textured* enclaves (**Fig. 2.3c,d**) have lower vesicularity (4.9-8.0%), higher vesicle-free crystallinity (94.7-97.5%), and a larger grain size. They are composed of amphibole-dominated clusters (long axes up to 3-5 mm) with Fe-Ti oxide inclusions, individual euhedral amphibole crystals (2-4 mm) and granular-poikilitic plagioclase (**Fig. 2.5a,b**). Amphibole is optically unzoned. Plagioclase is mainly normal or oscillatory zoned; some have spongy cores. Olivine is absent from these enclaves. The textural variation from diktytaxitic to plutonic appears to be gradational; this is evidenced by generally increasing crystallinity with decreasing glass and vesicle content (**Fig. 2.3**; 2.**4b,c**; **Table 2**). For convenience, those enclaves with intermediate texture (e.g., 13.8% vesicularity, 84.0% vesicle-free crystallinity, lacking olivine; **Fig. 2.3b**) are grouped with the plutonic-textured enclave suite.

One of the plutonic-textured enclaves (sample LAM-10I, **Fig. 2.3d**) contains anomalously high proportions of amphibole compared with the other enclaves (69.1% compared with 40.3~48.0%, **Table 2.2**). The high amphibole content is consistent with the abundance of amphibole-dominated clusters (**Fig. 2.3d, 2.6b**). This enclave also contains a small region with distinctive coarse-grained texture that we speculate could represent part of a hornblendite nodule in this enclave (**Fig. 2.3d**). Some of the plagioclase from this enclave is poikilitic, filling the gaps between amphibole clusters, whereas others are granular with spongy cores and zoned interstitial overgrowths (**Fig. 2.6a**).

One plutonic-textured enclave contains abundant interstitial anhydrite, which is strongly altered, with a dark-coloured rim. Apatite is present as an accessory phase in all enclaves.

2.4.1.3. Pre-1951 shoshonite

The older lavas from the crater walls of Mt. Lamington are shoshonites (previously documented as *trachybasalt;* Arculus *et al.*, 1983). Compared to the 1951 andesite, the shoshonites are also porphyritic but contain far fewer phenocrysts/antecrysts, and are less vesicular. Phenocryst phases include subhedral olivine and Fe-Ti oxides, euhedral oscillatory-zoned plagioclase and extensively

altered amphibole (**Fig. 2.5c,d**). The strongly resorbed, sieve-textured plagioclase is an antecryst phase (**Fig. 2.5c**). The groundmass consists of microcrystalline (150-200 μm) plagioclase, olivine, Fe-Ti oxides, orthopyroxene and clinopyroxene.

2.4.1.4. PUB xenoliths

A harzburgite and a dunite xenolith (**Fig. 2.5e,f**) hosted in the 1951 andesite have been interpreted as fragments of the PUB (Arculus *et al.*, 1983). An inner rim of orthopyroxene and outer rim of low-Al_2O_3 amphibole and/or phlogopite separate the xenoliths from the host andesite magma. Abundant chromite inclusions and numerous trails of fluid inclusions are present in the olivines which show cumulus embayed textures. The phenomena of kink-banding, wavy extinction and grain size reduction in the olivines are also evident. These are suggested to result from dislocation and granulation of larger primary crystals during solid-state deformation, as in previous studies (e.g., Jaques & Chappell, 1980).

2.4.2. Major and trace elements

Major element data (Arculus *et al.*, 1983) are reported in **Table 2.1** and plotted in **Fig. 2.7**. The 1951 andesite and magmatic enclaves have bulk compositions of medium/high-K andesite (58.7-61.2 wt % SiO_2, 2.1-2.2 wt % K_2O) and medium-K basalt to basaltic andesite (49.0-54.2 wt % SiO_2, 1.1-1.7 wt % K_2O), respectively; the pre-1951crater wall-building lavas are shoshonitic (54.9-55.1 wt % SiO_2, 3.2-3.3 wt % K_2O; Le Maitre, 2002). The 1951 andesite suite has a narrow range of compositional variations, but linear arrays versus SiO_2 are seen for CaO, TiO_2, MgO and Na_2O+K_2O (**Fig. 2.7a, c, d, f**). The enclaves have a broader range of SiO_2 variation and CaO, TiO_2, MgO and FeO_{tot} progressively decrease with increasing SiO_2, whereas Na_2O+K_2O and Al_2O_3 increase. In plots of CaO, Na_2O+K_2O and TiO_2 versus SiO_2, the linear trends shown by the enclaves display a slight offset from the trends within the andesite suite (**Fig. 2.7a, c, f**).

Trace elements are plotted versus Rb in Fig. 8. The LILE (e.g. Ba, Sr) generally increase with Rb in the enclaves and andesite suite (**Fig. 2.8a,b**). Within individual suites of diktytaxitic and plutonic enclaves and the andesite, HFSE (e.g. Zr, Th and Nb) vary unsystematically with Rb (**Fig. 2.8c-e**). The REE (e.g., La, Ce and Dy) do not show clear variation trends with increasing Rb in the diktytaxitic and plutonic enclave suites, whereas in the 1951 andesite they display slightly negative trends (**Fig. 2.8f**). With increasing Rb, concentrations of compatible elements (e.g., Cr, Ni) in the 1951 andesite remain relatively unchanged at low levels; however, they decrease dramatically within the diktytaxitic and plutonic enclave suite (**Fig. 2.8g,h**).

Primitive mantle-normalized incompatible element patterns (**Fig. 2.9a**) show that the Mt. Lamington volcanic products have the typical trace element signature of subduction-related volcanism: depletions of HFSE (e.g. Zr, Nb) and Th and U, together with enrichment of LILE (e.g. Rb, Sr) and LREE relative to middle (MREE) and heavy (HREE) rare earth elements (Tatsumi *et al.*, 1986; McCulloch & Gamble, 1991; Davidson, 1996; Pearce & Peate, 1995). The 1951 andesites are more enriched in LILE and depleted in MREE and HREE than the enclaves. The pre-1951 shoshonite has higher concentrations of the most incompatible trace elements compared to the 1951 andesite, but the two suites are indistinguishable in HREE and Pb. Chondrite-normalized REE patterns (**Fig. 2.9b**) are slightly concave, due to enrichment of LREE and a flat HREE profile. There is a slight negative Eu anomaly amongst all Mt. Lamington volcanic samples. The 1951 andesite REE patterns are slightly steeper than those of the enclaves. Within the enclave group, the plutonic enclaves are more enriched in MREE and HREE relative to the diktytaxitic enclaves. Unlike the light REE enriched pattern of the diktytaxitic enclaves, the REE pattern of the plutonic enclaves is S-shaped, with a peak at Pr.

2.4.3. Sr-Nd isotopes

Bulk rock Sr-Nd isotope data are shown in **Fig. 2.10**. The 1951 andesite and enclaves overlap isotopically. Both have small ranges in $^{87}Sr/^{86}Sr$ (0.7038-0.7040) and $^{143}Nd/^{144}Nd$ (0.51282-0.51290).

The pre-1951 shoshonite is distinctive with lower $^{87}Sr/^{86}Sr$ (0.703683-0.703705). The harzburgite xenolith separated from the andesitic lava host has $^{87}Sr/^{86}Sr$ of 0.704096, higher than the Mt. Lamington volcanic samples, and $^{143}Nd/^{144}Nd$ of 0.512821. However, it is not clear how representative this is of the PUB; because of the very low Sr and Nd concentrations in the harzburgite, the isotopic composition is ultra-sensitive to surface weathering or sample contamination by the host andesite. All samples plot within the field of late Cenozoic volcanic rocks in southeast PNG (**Fig. 2.10a**; Hegner & Smith, 1992).

2.4.4. Mineral and glass chemistry

2.4.4.1. Amphibole

All amphiboles from the Mt. Lamington magmatic rocks are calcic ($[Ca]_{M4}>1.5$ atoms per formula unit (apfu)) with high $[Mg^{2+}/(Mg^{2+}+Fe^{2+})]_{M1-3}$ values of 0.68-0.99. They are classified as magnesiohornblende ($[Na+K]_A<0.5$, $[Si]_T>6.5$), tschermakite ($[Na+K]_A<0.5$, $[Si]_T<6.5$) and magnesiohastingsite ($[Na+K]_A<0.5$, $[Si]_T<6.5$, and $[Al]_{M1-3}<[Fe^{3+}]_{M1-3}$) following the classification of Leake *et al*. (1997) (**Fig. 2.11a**, **Table 2.3**).

Amphibole phenocrysts from the 1951 andesite display a large variation in SiO_2 (40.60-47.70 wt %), FeO_{tot} (8.33-17.22 wt %), MgO (11.81-17.22 wt %), and CaO (11.09-12.23 wt %) versus Al_2O_3 (7.46-13.35 wt %; **Fig. 2.11b-d**; **Table 2.3**). The Al-rich rims of zoned grains, and a small minority of other crystals, are also enriched in MgO and depleted in FeO, MnO and SiO_2.

Amphiboles rimming the PUB dunite xenolith have distinctively low Al_2O_3 (6.37-8.91 wt %), TiO_2 (0.82-1.27 wt %), Na_2O (1.59-1.96 wt %), and higher SiO_2 (47.24-48.46 wt %; **Fig. 2.11f**; **Table 2.3**).

In the diktytaxitic enclaves, phenocryst-like amphiboles have low-Al cores (8.39-10.80 wt % Al_2O_3), which are compositionally similar to amphibole phenocrysts from the 1951 andesite. The phenocryst-like amphiboles also have strongly zoned rims that are Al-rich in the inner rim (10.77-13.09 wt %) and less Al-rich in the outer rim (8.11-12.92 wt %). The Al-rich rims on these phenocryst-like grains are similar to the compositions of framework-forming (acicular) and olivine-rimming amphiboles in the diktytaxitic enclaves (10.59-13.22 wt % Al_2O_3; **Table 2.3**). They are also compositionally similar to the subset of Al-rich compositions observed within the andesite (**Fig. 2.11**).

In the plutonic-textured enclaves, amphiboles in crystal clusters have an Al_2O_3 range of 8.59-12.31 wt % (**Table 2.3**). They are similar in composition to amphibole phenocrysts from the andesite, but with slightly lower FeO_{tot} (12.31-15.58 wt %), and MnO (0.23-0.38 wt %), and slightly higher MgO (12.33-14.97 wt %; **Fig. 2.11c-e**; **Table 2.3**).

In the pre-1951 shoshonite the least-altered amphibole cores display limited compositional variation but are similar to the Al-rich amphiboles found in the diktytaxitic enclaves, albeit with higher TiO_2, Na_2O and K_2O relative to those of the 1951 andesite (**Fig. 2.11**, **Table 2.3**).

2.4.4.2. Plagioclase

In the 1951 andesite, oscillatory zoned plagioclase phenocrysts frequently display a large compositional range (An_{30-60}; Arculus *et al.*, 1983). Patchy-zoned plagioclase is characterized by spongy cores (BSE-bright patch of $An_{41.7}$, dark patch of $An_{37.5}$) overgrown by oscillatory zoned rims ($An_{37.1-47.4}$). Sieve-textured plagioclases have anhedral oscillatory zoned cores (e.g. $An_{47.4}$) separated from a thin, more calcic, normally zoned rim (inner rim of $An_{60.5}$ and outer rim of $An_{39.1}$) by a layer of melt inclusions. Plagioclase microlites have the compositional range $An_{33.3-50.2}$ (**Table 2.4**).

In the diktytaxitic enclaves plagioclase is mainly normally zoned with a compositional range $An_{31.6-55.8}$. One large patchy-textured plagioclase has a BSE-bright patch of $An_{69.5}$, a dark patch of

$An_{28.9}$ and a rim of $An_{42.9}$. In the plutonic-textured enclaves poikilitic plagioclase is either oscillatory ($An_{32.1\text{-}57.5}$) or patchy zoned (**Table 2.4**).

In the pre-1951 shoshonite, euhedral oscillatory-zoned plagioclase phenocrysts have an An range of 35.1-53.6, indistinguishable from those in the 1951 andesite and enclaves (**Table 2.4**).

2.4.4.3. Biotite-phlogopite

In the 1951 andesite biotite occurs as fresh euhedral phenocrysts (0.5-1.0 mm) and as inclusions in plagioclase and amphibole phenocrysts. These have homogeneous compositions (Mg-number 0.43-0.45, MnO 0.18-0.20 wt %, TiO_2 3.89-3.94 wt %, and F 0.26-0.29 wt %). In constrast, the reaction rim phase growing around the PUB harzburgite xenolith is phlogopite with a high Mg-number (0.51-0.65) and F content (0.42-0.69 wt %), and low MnO (0.09-0.12 wt %) and TiO_2 (0.19-2.76 wt %; **Fig. 2.12**, **Table 2.5**).

In the diktytaxitic enclaves biotite is not abundant (<2.4%), whereas in the plutonic-textured enclaves it is found as euhedral crystals in amphibole-dominated clusters, as inclusions in amphibole, or as interstitial grains. Their compositions are homogeneous and indistinguishable from those of biotite phenocrysts in the 1951 andesite (Mg-number 0.44~0.48, MnO 0.14~0.20, F 0.28~0.33; **Fig. 2.12**, **Table 2.5**).

2.4.4.4. Fe-Ti-Cr oxides

In the 1951 andesite, Fe-Ti oxides occur as microphenocrysts and microlites, and plagioclase- and amphibole-hosted mineral inclusions. The compositions of homogeneous (unexsolved) microphenocrysts range from low-Ti magnetite (4.61 wt % TiO_2, 0.16 wt % Cr_2O_3, 86.24 wt % FeO_{tot}) to titanomagnetite (22.72-32.26 wt% TiO_2, 0.04-0.05 wt % Cr_2O_3, 59.57-69.17 wt % FeO_{tot}; **Fig. 2.13a,b**, **Table 2.6**).

In the diktytaxitic enclaves, Fe-Ti-Cr oxides are present as microphenocrysts and mineral inclusions in olivine xenocrysts, as well in the reaction rims around olivine xenocrysts. Microphenocrysts are mainly low-Ti magnetite (4.41-8.81 wt % TiO_2; 76.96-84.38 wt % FeO_{tot}), with Cr_2O_3 contents (1.09-3.72 wt %) slightly higher than those in the 1951 andesite (**Fig. 2.13a,b**, **Table 2.6**). Inclusions in olivine xenocrysts and their reaction rims display a large range of variation in terms of Cr, Ti, Al and Mg-number (**Fig. 2.13c-h**; **Table 2.6**). Two chromian spinel inclusions found in unreacted olivine cores are characterized by high Cr (41.31-47.38 wt % Cr_2O_3), Al (13.87-14.08 wt % Al_2O_3) and low Ti (0.49-0.61 wt % TiO_2), in contrast to the Cr-bearing magnetite that occurs in the reaction rims of olivines (0.14-37.70 wt % Cr_2O_3, 1.50-9.30 wt % Al_2O_3, 0.35-8.69 wt % TiO_2; **Fig. 2.13c, e-f**; **Table 2.6**). In the plutonic-textured enclaves, Fe-Ti-Cr oxides are mainly present in amphibole-dominated clusters. They are Cr-bearing magnetite, with compositions similar to inclusions in olivine reaction rims in the diktytaxitic enclaves. They are distinguishable from magnetite microphenocrysts in the diktytaxitic enclaves by their higher Cr (5.90-12.90 wt %) and lower Ti (1.94-3.93 wt % TiO_2; **Fig. 2.13a**; **Table 2.6**). The chromite inclusions in the PUB xenoliths are strikingly different from the rest of the oxides found in the Mt Lamington magmatic rocks, with low Ti and high Cr (<0.06 wt % TiO_2; 53.96-59.50 wt % Cr_2O_3; **Fig. 2.13a-h, Table 2.6**).

In the pre-1951 shoshonite, one analysis of an oxide microphenocryst gives an ilmenite composition (31.87 wt % TiO_2, 0.08 wt % Cr_2O_3, 59.57 wt % FeO_{tot}; **Table 2.6**).

2.4.4.5. Olivine

Olivine xenocrysts containing Cr-spinel inclusions are present in both the andesite host lava and the diktytaxitic enclaves. Reaction rims have two parts; enstatite-rich orthopyroxene and minor Cr-bearing magnetite form the internal rim whereas the outer rim is dominated by amphibole (**Fig. 2.2f**). In olivines from the 1951 andesite the inner rim of opx+oxides is commonly absent. Despite the reaction rim textures, some of the remnants of olivine preserve euhedral shapes (**Fig. 2.4b**), which are in striking contrast to the rounded, embayed texture of olivines from the PUB ultramafic xenoliths

(e.g., **Fig. 2.5e,f**). Moreover, solid-state deformation textures such as kink-banding and granulation found in olivine from the PUB xenoliths are not observed. Compositions of olivine in the andesite magma are $Fo_{81.3} - Fo_{89.7}$, indistinguishable from those in the diktytaxitic enclaves (**Table 2.7**), suggesting a common source. In some relic olivines, there is a trend of decreasing forsterite content rimward within the crystal ($Fo_{88.2-81.2}$; **Fig. 2.2f**, **Table 2.7**).

These olivine xenocrysts are distinguishable from olivine in the PUB xenoliths, which have higher Fo contents ($Fo_{91.7-92.1}$) and NiO (0.34-0.42 wt %) but lower CaO (<0.02 wt %) and MnO (0.01-0.12 wt %; **Fig. 2.14**, **Table 2.7**). This is consistent with reported compositions for PUB harzburgite olivine ranging from $Fo_{91.6}$ to $Fo_{93.6}$ (England & Davies, 1973; Jaques & Chappell, 1980).

In the pre-1951 shoshonite, a single olivine microphenocryst has a composition of Fo_{85} and a trace element composition indistinguishable from olivine in the 1951 andesite and the diktytaxitic enclaves.

2.4.4.6. Pyroxenes

Pyroxenes are comparatively rare in the 1951 andesite, but both clinopyroxene and orthopyroxene are common as microphenocrysts or microlites in the pre-1951 shoshonite. The clinopyroxene microlites are diopside ($En_{44.5-45.6}$; **Table 2.8**). Pyroxenes in plutonic-textured enclaves are absent, whereas in diktytaxitic enclaves clinopyroxene is a rare xenocryst phase rimmed by amphibole ($En_{45.7-49.3}$; **Fig. 2.4a**), and orthopyroxene composes the inner rims of olivine xenocrysts ($En_{76.6-80.9}$; **Fig. 2.2f**, **Table 2.8**). Clinopyroxene xenocrysts in diktytaxitic enclaves are slightly more magnesian (high En content) and have higher Cr_2O_3 (0.21-0.66 wt %) and lower TiO_2 (0.26-0.49 wt %), Al_2O_3 (1.83-3.64 wt %), MnO (0.11-0.13 wt%) and Na_2O (0.25-0.33 wt %) than the microlites in the pre-1951 shoshonite (**Table 2.8** and **Supplementary Data Appendix Table**). In the PUB harzburgite nodule, orthopyroxenes have a compositional range of En_{95-84}, (Arculus *et al.*, 1983); these are more magnesian than those composing the olivine reaction rims in the diktytaxitic enclaves.

2.4.4.7. Glass

Matrix glasses in the diktytaxitic enclaves are rhyolitic (73.29~77.76 wt % SiO_2), and are indistinguishable from the glasses in the plutonic enclaves (76.96-78.27 wt % SiO_2; **Table 2.9**). The groundmass of the 1951 andesite is full of microlites and thus not analysed.

2.5. DISCUSSION

2.5.1. Origin of olivine xenocrysts with Cr-spinel inclusions

2.5.1.1. Amphibole-dominated clusters represent fully reacted olivines

The olivine crystals in the diktytaxitic enclaves and the 1951 andesite are clearly in disequilibrium with the host melt, as demonstrated by reaction rims of opx+oxides and/or amphibole. This is consistent with observations at Mt. Pinatubo (Matthews *et al.*, 1992; Di Muro *et al.*, 2008), Lascar Volcano (Matthews *et al.*, 1994), Shiveluch Volcano (Dirksen *et al.*, 2006), Unzen Volcano (Browne *et al.*, 2006), and experimental reaction of forsteritic olivine with silicic melt (Coombs & Gardner, 2004). The decreasing Fo content towards the rims (e.g., $Fo_{88.2-81.2}$; **Table 2.7**, **Fig. 2.2f**), is interpreted to be a result of equilibration with the host andesite melt or melt trapped within the enclaves, by diffusion or reaction. This equilibration is also recorded by the spinel inclusions hosted in the olivines. Original chromian spinels away from the olivine reaction rims are characterized by high Mg-number, Fe^{2+}/Fe^{3+} ratio, Cr and Al content, and low Ti (**Fig. 2.13b-h**). The suite of Cr-spinels within or adjacent to reaction rims show a wide range of compositions, with a clear decrease in Cr and Al and corresponding enrichment in Fe^{3+} with decreasing Mg-number (**Fig. 2.13e-g**). In contrast, Fe-Ti oxide microphenocrysts in the diktytaxitic enclaves have much lower Cr-numbers, which are inherited from the melt.

The above distinction is important because it allows us to draw some infererences about the origin of the amphibole clusters in the plutonic-textured enclaves. Oxide inclusions in these clusters have Cr-numbers similar to the Cr-bearing magnetite in the olivine reaction rims from the diktytaxitic enclaves. This implies that their origins have affinity with Cr-spinel inclusions in olivine, and we therefore interpret the amphibole clusters with Fe-Ti oxide inclusions as derived from complete resorption of olivine, as observed at Arenal volcano (Reagan *et al.*, 1987). This is consistent with the gradual increase in olivine reaction rim thickness with decreasing olivine modal abundance in the diktytaxitic enclaves. We suggest that the plutonic-textured enclaves represent the end-member of this process, with olivine completely reacted to form large amphibole clusters.

2.5.1.2. Olivines with Cr-spinel inclusions are not sourced from PUB

Arculus *et al.* (1983) suggested that the olivine crystals present in the Mt. Lamington 1951 andesite and enclaves have an ophiolitic (PUB) origin, supported by the presence of PUB fragments in Mt. Lamington andesite dome lavas. Thus the high Cr, Ni contents of the Lamington magmas were interpreted as a result of ophiolite contamination (Arculus *et al*. 1983). A similar interpretation has been given for the origins of olivine present in diktytaxitic enclaves from Mt. Pinatubo (Di Muro *et al.*, 2008). However in some Mt. Lamington diktytaxitic enclaves the euhedral shapes of olivine crystals are well preserved, despite the presence of reaction rims. This strongly suggests that the olivines have a magmatic origin and could not be sourced from PUB ultramafic rocks or gabbros in which the olivines are coarse grained, with rounded or embayed textures and trails of fluid inclusions (Jaques & Chappell, 1980), features also seen in the PUB nodules examined in this study. Moreover, the compositions of the olivine xenocrysts and their Cr-spinel inclusions are dissimilar to those from the PUB harzburgite and dunite (**Figs. 2.13,14**). We reject the hypothesis that the 1951 olivines originated from the PUB basalt, since according to Jaques & Chappell (1980) the PUB basalt is either aphanitic or rarely loaded with microphenocrysts of augite and plagioclase, which are not observed in the Mt. Lamington magmatic rocks. The distinctive mineral compositions of the 1951 olivines demonstrate that they are also not derived from the pre-1951 shoshonite magmas. Thus we rule out the possibility that the olivine crystals are derived from the PUB and believe they have some other magmatic origin. We will return to this question later.

2.5.2. Constraints on PUB contamination of Mt. Lamington magmas

We have demonstrated that the abundant olivine xenocrysts found in the Mt. Lamington magmas cannot be derived from the PUB. However, the presence of harzburgite and dunite nodules rimmed by phlogopite and amphibole is indisputable evidence of interaction with the PUB during andesite magma ascent towards the surface. This raises the question of how much PUB contamination is feasible and to what extent the bulk-rock compositions might be affected by interaction with the PUB. This involves two factors: (1) incorporation of solid fragments that (presumably) can be picked out and thus, we assume, do not contribute to the bulk-rock composition; (2) partial melting of those solid fragments, which would easily contaminate the host melt, and thus the bulk-rock composition. The efficiency of melting and assimilation is controlled by factors such as the temperature of the magma, the compositional contrast between the magma and the PUB xenoliths (e.g., Mg-number of the melt and PUB olivine), the specific surface area of the PUB xenoliths, the degree of serpentinization of the PUB ultramafic xenoliths and the rigidity of the PUB xenoliths. In general, if PUB xenoliths without significant serpentinization were incorporated into a relatively cool, evolved magma, resorption would not be expected due to their highly refractory nature. If significant contamination did occur, the host melt should be geochemically fingerprinted with typical PUB signatures, such as high Cr and Ni concentrations and low incompatible element concentrations.

Arculus *et al.* (1983) reported that concentrations of Cr and Ni in the Mt. Lamington 1951 andesite are high compared with Bismarck volcanic arc literature data (Johnson, 1982). However, new ICP-MS trace element data from this study show that concentrations of Cr (64-141 ppm, with one exception of 252 ppm) and Ni (25-63 ppm) in the 1951 andesite are high, but do not significantly stand out from the large background dataset of the Bismarck Arc-New Britain Arc compositions,

which includes hundreds of bulk-rock analyses of volcanic rocks (GEOROC, http://georoc.mpch-mainz.gwdg.de; **Fig. 2.15**). Instead, the enclaves have remarkably high Cr (284-1049 ppm) and Ni (57-286 ppm, with one exception of 1271 ppm). To evaluate whether this Cr and Ni could be provided by the Cr spinel-bearing olivine xenocrysts, we carried out a mass balance calculation using the observed NiO content of the olivines from the EPMA data (**Table 2.7**) and the observed modal abundance of olivine (**Table 2.2**). The andesite lavas and magmatic enclaves have average Ni concentrations of c.a. 40 and 150 ppm, respectively. To obtain the olivine- or PUB-free andesite and enclave magma compositions which have bulk Ni concentrations of ca. 20 and 50 ppm (putative values from the background dataset in **Fig. 2.15**), 0.8% and 4.1% of olivine with 2500 ppm Ni (according to EPMA data for Fo_{87-89} olivines) need to be subtracted, respectively. The point counting results show that the 1951 andesites contain up to 1.7% olivine, and the diktytaxitic enclaves contain 1.3-4.3% (vesicle-free; **Table 2.2**). The mass balance calculation results are in good agreement with point counting, which demonstrates that assimilating variable amounts of high Ni olivine is enough to account for the bulk-rock Ni variations. Similarly, high bulk-rock Cr is attributed to the chromian spinel inclusions in those olivine xenocrysts. Thus we do not require extensive PUB assimilation in order to generate the observed bulk-rock compositions, as suggested by Arculus *et al*. (1983). We also note that assimilation of PUB fragments will be restricted by growth of narrow reaction rims of amphibole and, or phlogopite (**Fig. 2.5e,f**), which isolate the PUB components from the melt and prevent further reaction. In summary, we consider the effect of PUB contamination of the Mt. Lamington magmas to be insignificant.

2.5.3. Recycling of earlier-fractionated minerals

We have demonstrated that the Fo-rich olivines and their high Cr, Al spinel inclusions are not sourced from the PUB. Compositions of relict olivine cores, as well as chromian spinel inclusions, imply that they crystallized from a primitive melt (high Mg-number, high Cr and Ni contents). Amphibole crystals with rims of secondary amphibole, some attached to olivine relicts (**Fig. 2.4c**), are also clearly not derived from the enclave-forming magma or host andesite, on the basis of their textures. The same is true of the rare clinopyroxene xenocrysts with disequilibrium textures (**Fig. 2.4a**). These clinopyroxenes are slightly more magnesian and contain higher Cr and Ni, and lower Ti and Na than clinopyroxene microlites from the pre-1951 shoshonite (**Table 2.8**). This suggests that the clinopyroxene xenocrysts cannot be derived from the shoshonite lavas, consistent with our interpretations of the source of the Fo-rich olivines. We therefore suggest that these are all products of early-stage fractional crystallization of a more primitive melt that may be a precursor to the 1951 andesite or pre-1951 shoshonite magmas. We speculate that fractional crystallization may have taken place at high pressure where olivine and Cr-spinel are stable fractionating phases, giving rise to a crystal mush of olivine ± spinel ± amphibole ± clinopyroxene. The enclave-forming magma then remobilized and assimilated some of this crystal mush during ascent, prior to intruding into the 1951 andesite magma reservoir. This interpretation is consistent with recent studies of mafic volcanic rocks from SW Japan (Zellmer *et al*., 2014).

Small nodules of amph+plag+bi found in one of the diktytaxitic enclaves are characterized by the presence of glass along embayed grain boundaries (**Fig. 2.4e,f**). This phenomenon is similar to the textures observed in the plutonic enclaves (**Fig. 2.6b-d**), and is also observed in cumulate nodules entrapped and erupted in lavas from elsewhere. These textures have been interpreted to represent the primary melt-filled porosity in crystallising cumulates (Holness *et al.*, 2007). Therefore, the presence of these nodules in the diktytaxitic enclave seems to indicate recycling of earlier formed plutonic materials including amphibole and biotite.

2.5.4. Formation of the magmatic enclaves

The textures of the magmatic enclaves can yield information on the processes involved in their formation and thus the crystallisation conditions of the intruding mafic magma in the volcanic plumbing system. The diktytaxitic texture indicates rapid magma quenching and fast crystallization,

which is typically produced when hot enclave magma is brought into direct contact with a large volume of relatively cool, more silicic magma and quenched to thermal equilibrium (Eichelberger, 1980; Bacon, 1986). Fast bubble nucleation due to second boiling in response to heat loss produces a low density foam layer, which enables the enclave magma to float upward into the overlying magma body and form inclusions (e.g., Eichelberger, 1980; Ban *et al.*, 2005; Browne *et al.*, 2006; Edmonds *et al.*, 2014).

The diktytaxitic texture is common and also found in magmatic enclaves from many other volcanoes, such as: Soufrière Hills, Montserrat (Murphy *et al.*, 2000; Edmonds *et al.*, 2014; Plail *et al.*, 2014); Narugo (Ban *et al.*, 2005) and Unzen (described as porphyritic; Browne *et al.*, 2006), Japan; Santorini, Greece (Martin *et al.*, 2006); Mt. Pinatubo, Philippines (Di Muro *et al.*, 2008). In most of these examples, plagioclase is the framework-forming phase, whereas in the enclaves from Mt. Lamington, as well as those from Mt. Pinatubo and some from Soufrière Hills, the framework is constructed by acicular amphibole crystals. The preferential crystallization of amphibole relative to plagioclase suggests crystallisation at high pressure and relatively high temperature (e.g., > 250 MPa, > 900 °C), and water-saturated conditions (e.g., Moore & Carmichael, 1998; Krawczynski *et al.*, 2012).

Compared with the diktytaxitic texture, the plutonic texture is consistent with a relatively prolonged cooling history. This is demonstrated by high vesicle-free crystallinity, and crystal clusters dominated by coarse, unzoned tabular amphiboles, which are believed to be derived from complete resorption of olivine crystals (see *Origin of olivine xenocrysts with Cr-spinel inclusions*). We interpret the plutonic-textured enclaves to have formed by slow crystallisation in the mushy margins of the enclave magma body. Floatation cannot be triggered due to an insufficient bubble nucleation-driven density drop and increased viscosity (Bacon, 1986). Alternatively, the plutonic enclaves may be generated by forcible disruption of the crystal mush by a recharging magma (Sparks *et al.*, 1977; Pallister *et al.*, 1992; Nakamura, 1995).

The above interpretation is similar to the model proposed by Browne *et al.* (2006) to explain the juxtaposition of enclaves with textural variability in host magmas. According to this model the diktytaxitic enclaves can be produced as hybrid buoyant blobs at the mutual interface when hot enclave-forming magma intrudes below the host magma. Meanwhile, the rest of the intruding magma below the mutual interface experiences a relatively longer history of gradual crystallization at a slower rate of undercooling, resulting in a heavily crystalline margin. Subsequent recharge events may disrupt the margin and inject the fragments into the overlying magma, generating plutonic enclaves (**Fig. 2.16**).

2.5.5. Crystal transfer of 1951 andesite components to magmatic enclaves

We earlier described the large, simple zoned, tabular amphiboles from the diktytaxitic enclaves as *phenocryst-like* because they have a crystal morphology similar to the amphibole phenocrysts in the 1951 andesite. Moreover, the compositions of their cores are in agreement with the unzoned amphibole phenocrysts from the 1951 andesite host, and the rim compositions are consistent with the acicular and olivine-rimming amphibole crystals in the the diktytaxitic enclaves. This indicates that the rims of the phenocryst-like amphiboles, as well as the olivine-rimming amphiboles, must crystallize together with the acicular framework amphiboles during enclave magma quenching against the andesite. Therefore, the cores of the phenocryst-like amphiboles must be already present in the enclave magma prior to or during quenching. Given the close compositional similarity of these cores with the amphibole phenocrysts from the andesite, we propose that these phenocryst-like amphibole crystals are transferred from the andesite or andesite-related crystal mush to the enclave magma, during ascent, quenching and interaction of the enclave-forming magma with the andesite host. We infer that a similar process explains the presence of sieve-textured and patchy-zoned plagioclase in the enclaves, with crystal sizes equivalent to phenocrysts in the andesite host and much bigger than the microphenocrysts in the enclaves.

Crystal transfer from the andesite or andesite-related crystal mush to the enclave-forming magma must occur before the boundary between the two rheologically different magmas is rigid enough to become a barrier prohibiting crystal transfer from the andesite host during quenching (Ubide *et al.*, 2014). Assimilation of crystals could occur from a partially mobile crystal mush, or alternatively in the contact zone (foam layer) where the diktytaxitic enclaves are generated (**Fig. 2.16a**). This mechanical constraint is consistent with the plutonic-textured enclaves being relatively free from andesite components, as these are presumed to form in a more rigid part of the mush that does not significantly interact with the superjacent andesite (**Fig. 2.16c**).

We also observe evidence for return crystal transfer from the enclaves back into the andesite host. For example, amphibole phenocrysts with simple zoning must have been transferred into the enclave-forming magma, where their Al-rich rims crystallised. However, they are now observed in the andesite magma. This may occur by disaggregation of magmatic enclaves during magma ascent or by shear within the chamber, as has been demonstrated at Soufrière Hills Volcano (Humphreys *et al.*, 2009). However, in the Mt. Lamington 1951 andesite, components that originated in the enclave-forming magma are rare and difficult to identify.

2.5.6. Trace element and isotope constraints on the petrogenesis of the Mt. Lamington magmas

2.5.6.1. Source of the 1951 andesite and enclave-forming magma

The high LILE/HFSE and LILE/LREE ratios of the 1951 andesites and enclaves indicate enrichment of fluid-mobile elements in the magma source region, and are thus consistent with slab-derived input of fluids/melts into the mantle source region of these magmas. This supports previous work indicating that, although there is apparently no active subduction in the region at present, magma generation is primarily driven by subduction-related processes (Johnson *et al.*, 1978; Arculus *et al.*, 1983).

The overlapping Sr-Nd isotope compositions of the enclaves and the andesite indicate that the 1951 andesite and enclave-forming magma originated from a common source. This also rules out significant partial melting or assimilation of lower crustal material, as this is dominated by the Emo Metamorphics, with $^{143}Nd/^{144}Nd$ spanning a wide compositional range from 0.512744±13 to 0.513107±18 (Worthing & Crawford, 1996) that is distinct from the Mt. Lamington compositions. To explore this further, we considered trace element ratios that do not vary significantly with crustal-level fractional crystallization, and may therefore indicate the source of the parental magmas, e.g., Zr/Nb (Elliott *et al.*, 1997). The 1951 andesites have Zr/Nb ratios in the range 27.7-34.3, while the enclaves overlap but display a larger Zr/Nb variation (15.0-33.3, **Fig. 2.17**). Zr/Nb is insensitive to fractional crystallisation of olivine, pyroxenes and plagioclase, but amphibole can fractionate Zr from Nb as a result of differences in ionic charge and site preferences, with the relative partition coefficients for Zr and Nb depending on the composition of both amphibole and melt (Tiepolo *et al.*, 2001). Ba/La ratios of amphiboles from Mt. Pinatubo, Mt. St. Helens and Mt. Hood eruption products vary from approximately 2-8 for magnesiohornblende and 6-28 for tschermakite, whereas Zr/Nb ratios typically range from 5-20 (**Fig. 2.17**; Loewen, 2013). Therefore, fractionation or incorporation of amphibole, particularly of magnesiohornblende or tschermakite composition, could in principle significantly affect the trace element ratios of the bulk-rocks. We suggest that the differences in Zr/Nb and Ba/La between the enclave and andesite rock suites can be explained either by more extensive fractional crystallisation of hornblende from the andesites, pushing their trace element ratios to higher values, and/or by incorporation of foreign amphibole crystals, including earlier fractionated cumulate amphibole, by the enclaves, dragging their trace element ratios to lower values. This process could also explain the variations of trace element concentrations with Rb (**Fig. 2.8**), which is strongly depleted in amphibole but enriched in biotite.

2.5.6.2. Formation of the 1951 andesite and enclave-forming magma

Formation of intermediate magmas is typically ascribed to either shallow fractional crystallisation of mantle-derived mafic magmas, deep fractionation of wet mantle-derived mafic magmas, dehydration

melting of amphibolitic lower crust, or mixing between mafic and felsic magmas, as summarised by Annen *et al*. (2006). The lack of isotopic heterogeneity among the andesites and enclaves, and their dissimilarity to the Emo Metamorphics precludes the possibility that significant dehydration partial melting of amphibolitic lower crust gave rise to the Mt. Lamington andesites. Therefore, to understand the formation of the 1951 andesite we must consider fractional crystallisation and mixing processes.

While there is clear evidence of bimodal magmatism and mixing, and some degree of hybridisation between the mafic enclaves and the andesite clearly does occur, incorporation and hybridisation of enclave material into the andesite is not considered to have a significant effect on bulk-rock compositions, based on petrology and offsets in geochemical trends. Hence, fractional crystallization is required to explain the geochemistry of the 1951 andesite.

The 1951 andesite has low MgO and low Cr and Ni concentrations, which suggests that previous fractionation of ferromagnesian mineral phases, such as olivine, pyroxenes, Fe-Ti oxides and amphibole, has taken place from the parental melt. There is no significant Eu anomaly in the chondrite-normalised REE patterns (**Fig. 2.12b**), indicating that plagioclase is not a major phase in the fractionating assemblage. Lack of fractionation between the MREE and HREE suggests amphibole rather than garnet is involved in the fractionation assemblage. We suggest that the xenocrysts of ol+sp ± cpx ± amph observed in the diktytaxitic enclaves may represent remnants of this earlier phase of fractionation. This is consistent with recent experimental studies showing that deep crystallisation of hydrous basalt produces ol + cpx + amph + plag (Melekhova *et al.*, 2015), as well as the presence of cumulate nodules in Lesser Antilles lavas that contain these phases (Arculus & Wills, 1980). Thus we conclude that at Mt. Lamington, mafic cumulates are produced in the lower crust and sampled by the replenishing enclave-forming magma (**Fig. 2.16**).

The andesites themselves show limited geochemical variations and thus provide little direct evidence of an earlier differentiation history. However, extensions to the linear trend lines in plots of major elements versus SiO_2 intersect the tie-lines between the amphibole and plagioclase compositional groups (**Fig. 2.7**). Thus the compositional variations of the andesites are consistent with fractionation of a mineral assemblage involving amphibole and plagioclase (amphibole > plagioclase). We suggest that this represents a second stage of shallow-level fractional crystallisation (**Fig. 2.16**).

On the other hand, the magmatic enclaves are hybrids of foreign components and original melt in various proportions, having assimilated olivine. This explains the unsystematic variations within the diktyatxitic and plutonic enclaves in trace element plots (**Fig. 2.8**) and the S-shaped REE patterns of the plutonic enclaves (**Fig. 2.9b**), which cannot be reproduced by numerical modelling assuming that the enclaves represent magmatic liquids. It also explains why the observed modal assemblages of the plutonic-textured enclaves (dominated by amphibole + plagioclase) do not match what is expected for a magma of basaltic bulk composition.

2.6. CONCLUSIONS

Two major types of mafic-intermediate magmatic enclaves are identified within the andesitic dome lavas produced during the 1951eruption of Mt. Lamington: diktytaxitic and plutonic-textured. Diktytaxitic enclaves are formed when the enclave magma is quenched against the overlying andesite magma and generates a foam layer, which floats upward into the andesite magma. In contrast, the plutonic-textured enclaves represent slow-cooling crystallization products of the enclave-forming magma away from the direct contact zone with the andesite magma.

Both andesite and enclaves contain abundant olivine crystals with amphibole reaction rims, which appear to be responsible for the high Cr and Ni concentrations in the Mt. Lamington magmas. Contamination of the magmas by the PUB is not necessary and would seem to require an unreasonable thermal budget. The olivines are euhedral and do not show deformation textures, as observed in the PUB olivines; additionally their geochemical signatures are inconsistent with the PUB harzburgite and dunite xenoliths. Therefore the olivines cannot have an ophiolite origin, and instead

are suggested to be products of earlier fractional crystallization from magmas that may have been precursor(s) to the 1951 andesite and/or pre-1951 shoshonite. Their presence, as well as that of xenocrysts of clinopyroxene and amphibole, are probably a result of remobilization and recycling by the enclave-forming magma.

Evidence for crystal exchange between the enclaves and the andesite host is seen in the petrology and further confirmed with mineral data. Isotopic data constrain the 1951 andesite and enclave-forming magma to have the same magma source; trace element signatures indicate a subduction-related component. We interpret variable trace element ratios to be a result of significant fractionation or assimilation of amphibole. The dominant processes that led to forming the 1951 andesite and enclave-bearing magma are likely to be deep fractional crystallization of mafic phases followed by shallow fractionation of amphibole ± plagioclase.

2.7. ACKNOWLEDGEMENTS

We thank Richard Arculus for providing the samples and background information. Ian Chaplin and Chris Ottley are thanked for their help during sample preparation and ICP-MS analysis, Leon Bowen and Chris Hayward for help in SEM imaging and EPMA. Yaoling Niu, Helen Williams and members of the Durham Volcanology research group are thanked for constructive discussions. Reviews by Brandon Browne and two anonymous reviewers are gratefully acknowledged.

2.8. FUNDING

This work forms part of the first author's PhD research, which is funded by a Durham Doctoral Studentship (Durham University) and the China Scholarship Council (201206170178). M.C.S.H. was supported by a Royal Society University Research Fellowship.

2.9. REFERENCES

Annen, C., Blundy, J. D. & Sparks, R. S. J. (2006). The genesis of intermediate and silicic magmas in deep crustal hot zones. *Journal of Petrology* 47, 505–539.

Arculus, R. J., Johnson, R. W., Chappell, B. W., Mc Kee, C. O. & Sakai, H. (1983). Ophiolite-contaminated andesites, trachybasalts, and cognate inclusions of Mount Lamington, Papua New Guinea: anhydrite-amphibole-bearing lavas and the 1951 cumulodome. *Journal of Volcanology and Geothermal Research* 18, 215-247.

Arculus, R. J. & Wills, K. J. A. (1980). The Petrology of Plutonic Blocks and Inclusions from the Lesser Antilles Island Arc. *Journal of Petrology* 21, 743-799.

Bacon, C. R. (1986). Magmatic inclusions in silicic and intermediate volcanic rocks. *Journal of Geophysical Research* 91, 6091-6112.

Baldwin, S. L., Fitzgerald, P. G. & Webb, L. E. (2012). Tectonics of the New Guinea Region. *Annual Review of Earth and Planetary Sciences* 40, 495-520.

Ban, M., Takahashi, K., Horie, T. & Toya, N. (2005). Petrogenesis of Mafic Inclusions in Rhyolitic Lavas from Narugo Volcano, Northeastern Japan. *Journal of Petrology* 46, 1543-1563.

Browne, B. L., Eichelberger, J. C., Patino, L. C., Vogel, T. A., Dehn, J., Uto, K. & Hoshizumi, H. (2006). Generation of porphyritic and equigranular mafic enclaves during magma recharge events at Unzen volcano, Japan. *Journal of Petrology* 47, 301-328.

Coombs, M. L. & Gardner, J. E. (2004). Reaction rim growth on olivine in silicic melts: Implications for magma mixing. *American Mineralogist* 89, 748-758.

Davidson, J. P. (1996). Deciphering mantle and crustal signatures in subduction zone magmatism. In: Bebout, G. E., Scholl, D. W., Kirby, S. H. & Platt, J. P. (eds.) *Subduction Top to Bottom*. Washington, D. C.: American Geophysical Union, 251-262.

Davidson, J. P., Boghossian, N. D. & Wilson, M. (1993). The Geochemistry of the Igneous Rock Suite of St Martin, Northern Lesser Antilles. *Journal of Petrology* 34, 839-866.

Davies, H. L. (2012). The geology of New Guinea - the cordilleran margin of the Australian continent. *Episodes* 35, 87-102.

Davies, H. L. & Jaques, A. L. (1984). Emplacement of ophiolite in Papua New Guinea. *Geological Society, London, Special Publications* 13, 341-349.

Davies, H. L. & Smith, I. E. (1971). Geology of Eastern Papua. *Geological Society of America Bulletin* 82, 3299-3312.

Di Muro, A., Pallister, J., Villemant, B., Newhall, C., Semet, M., Martinez, M. & Mariet, C. (2008). Pre-1991 sulfur transfer between mafic injections and dacite magma in the Mt. Pinatubo reservoir. *Journal of Volcanology and Geothermal Research* 175, 517-540.

Dirksen, O., Humphreys, M. C. S., Pletchov, P., Melnik, O., Demyanchuk, Y., Sparks, R. S. J. & Mahony, S. (2006). The 2001-2004 dome-forming eruption of Shiveluch volcano, Kamchatka: Observation, petrological investigation and numerical modelling. *Journal of Volcanology and Geothermal Research* 155, 201-226.

Dosso, L., Bougault, H., Beuzart, P., Calvez, J. Y. & Joron, J. L. (1988). The Geochemical Structure of the Southeast Indian Ridge. *Earth and Planetary Science Letters* 88, 47-59.

Edmonds, M., Humphreys, M. C. S., Hauri, E. H., Herd, R. A., Wadge, G., Rawson, H., Ledden, R., Plail, M., Barclay, J., Aiuppa, A., Christopher, T. E., Giudice, G. & Guida, R. (2014). Pre-eruptive vapour and its role in controlling eruption style and longevity at Soufriere Hills Volcano. *Geological Society, London, Memoirs* 39, 291-315.

Eichelberger, J. C. (1980). Vesiculation of Mafic Magma during Replenishment of Silicic Magma Reservoirs. *Nature* 288, 446-450.

Elliott, T., Plank, T., Zindler, A., White, W. & Bourdon, B. (1997). Element transport from slab to volcanic front at the Mariana arc. *Journal of Geophysical Research* 102, 14991-15019.

England, R. N. & Davies, H. L. (1973). Mineralogy of Ultramafic Cumulates and Tectonites from Eastern-Papua. *Earth and Planetary Science Letters* 17, 416-425.

Hall, R. & Spakman, W. (2002). Subducted slabs beneath the eastern Indonesia-Tonga region: insights from tomography. *Earth and Planetary Science Letters* 201, 321-336.

Hegner, E. & Smith, I. E. (1992). Isotopic compositions of late Cenozoic volcanics from southeast Papua New Guinea-- Evidence for multi-component sources in arc and rift environments. *Chemical Geology* 97, 233-249.

Hill, K. C. & Raza, A. (1999). Arc-continent collision in Papua Guinea: Constraints from fission track thermochronology. *Tectonics* 18, 950-966.

Holness, M. B., Anderson, A. T., Martin, V. M., Maclennan, J., Passmore, E. & Schwindinger, K. (2007). Textures in Partially Solidified Crystalline Nodules: a Window into the Pore Structure of Slowly Cooled Mafic Intrusions. *Journal of Petrology* 48, 1243-1264.

Humphreys, M. C. S., Christopher, T. & Hards, V. (2009). Microlite transfer by disaggregation of mafic inclusions following magma mixing at SoufriSre Hills volcano, Montserrat. *Contributions to Mineralogy and Petrology* 157, 609-624.

Ito, E., White, W. M. & Gopel, C. (1987). The O, Sr, Nd and Pb Isotope Geochemistry of Morb. *Chemical Geology* 62, 157-176.

Jakeš, P. & Smith, I. E. (1970). High potassium calc-alkaline rocks from Cape Nelson, Eastern Papua. *Contributions to Mineralogy and Petrology* 28, 259-271.

Jaques, A. L. & Chappell, B. W. (1980). Petrology and trace element geochemistry of the Papuan Ultramafic belt. *Contributions to Mineralogy and Petrology* 75, 55-70.

Johnson, R. W. (1982). Papua New Guinea. In: Thorpe, R. S. (ed.) *Andesites*. London: John Wiley & Sons, 225-244.

Johnson, R. W., Mackenzie, D. E. & Smith, I. E. (1978). Delayed partial melting of subduction-modified mantle in Papua New Guinea. *Tectonophysics* 46, 197-216.

Krawczynski, M. J., Grove, T. L. & Behrens, H. (2012). Amphibole stability in primitive arc magmas: effects of temperature, H2O content, and oxygen fugacity. *Contributions to Mineralogy and Petrology* 164, 317-339.

Le Maitre, R. W. (2002). *Igneous rocks: A Classification and Glossary of Terms*: Cambridge University Press, Blackwell.

Leake, B. E., Woolley, A. R., Arps, C. E. S., Birch, W. D., Gilbert, M. C., Grice, J. D., Hawthorne, F. C., Kato, A., Kisch, H. J., Krivovichev, V. G., Linthout, K., Laird, J., Mandarino, J. A., Maresch, W. V., Nickel, E. H., Rock, N. M. S., Schumacher, J. C., Smith, D. C., Stephenson, N. C. N., Ungaretti, L., Whittaker, E. J. W. & Guo, Y. Z. (1997). Nomenclature of amphiboles: Report of the subcommittee on amphiboles of the International Mineralogical

Association, Commission on New Minerals and Mineral Names. *Canadian Mineralogist* 35, 219-246.
Loewen, M. W. (2013). Volatile mobility of trace metals in volcanic systems. PhD thesis, Oregon State University, 177-200.
Lus, W. Y., McDougall, I. & Davies, H. L. (2004). Age of the metamorphic sole of the Papuan Ultramafic Belt ophiolite, Papua New Guinea. *Tectonophysics* 392, 85-101.
Mahoney, J. J., Natland, J. H., White, W. M., Poreda, R., Bloomer, S. H., Fisher, R. L. & Baxter, A. N. (1989). Isotopic and Geochemical Provinces of the Western Indian-Ocean Spreading Centers. *Journal of Geophysical Research-Solid Earth and Planets* 94, 4033-4052.
Martin, V. M., Holness, M. B. & Pyle, D. M. (2006). Textural analysis of magmatic enclaves from the Kameni Islands, Santorini, Greece. *Journal of Volcanology and Geothermal Research* 154, 89-102.
Matthews, S. J., Jones, A. P. & Bristow, C. S. (1992). A Simple Magma-Mixing Model for Sulfur Behavior in Calc-Alkaline Volcanic-Rocks - Mineralogical Evidence from Mount-Pinatubo 1991 Eruption. *Journal of the Geological Society* 149, 863-866.
Matthews, S. J., Jones, A. P. & Gardeweg, M. C. (1994). Lascar Volcano, Northern Chile - Evidence for Steady-State Disequilibrium. *Journal of Petrology* 35, 401-432.
McCulloch, M. T. & Gamble, J. A. (1991). Geochemical and geodynamical constraints on subduction zone magmatism. *Earth and Planetary Science Letters* 102, 358-374.
Melekhova, E., Blundy, J., Robertson, R. & Humphreys, M. (2015). Experimental evidence for polybaric differentiation of primitive arc basalt beneath St. Vincent, Lesser Antilles. *Journal of Petrology* 56, 161-192.
Michard, A., Montigny, R. & Schlich, R. (1986). Geochemistry of the Mantle beneath the Rodriguez Triple Junction and the Southeast Indian Ridge. *Earth and Planetary Science Letters* 78, 104-114.
Moore, G. & Carmichael, I. S. E. (1998). The hydrous phase equilibria (to 3 kbar) of an andesite and basaltic andesite from western Mexico: constraints on water content and conditions of phenocryst growth. *Contributions to Mineralogy and Petrology* 130, 304-319.
Murphy, M. D., Sparks, R. S. J., Barclay, J., Carroll, M. R. & Brewer, T. S. (2000). Remobilization of andesite magma by intrusion of mafic magma at the Soufriere Hills Volcano, Montserrat, West Indies. *Journal of Petrology* 41, 21-42.
Nakamura, M. (1995). Continuous Mixing of Crystal Mush and Replenished Magma in the Ongoing Unzen Eruption. *Geology* 23, 807-810.
Ottley, C. J., Pearson, D. G. & Irvine, G. J. (2003). A routine method for the dissolution of geological samples for the analysis of REE and trace elements via ICP-MS. In: Holland, J. G. & Tanner, S. D. (eds.) *Plasma Source Mass Spectrometry: Applications and Emerging Technologies*. Cambridge: Royal Society of Chemistry, 221-230.
Pallister, J. S., Hoblitt, R. P. & Reyes, A. G. (1992). A Basalt Trigger for the 1991 Eruptions of Pinatubo Volcano. *Nature* 356, 426-428.
Pearce, J. A. & Peate, D. W. (1995). Tectonic Implications of the Composition of Volcanic Arc Magmas. *Annual Review of Earth and Planetary Sciences* 23, 251-285.
Plail, M., Barclay, J., Humphreys, M. C. S., Edmonds, M., Herd, R. A. & Christopher, T. E. (2014). Characterization of mafic enclaves in the erupted products of Soufriere Hills Volcano, Montserrat, 2009 to 2010. *Geological Society, London, Memoirs* 39, 343-360.
Reagan, M. K., Gill, J. B., Malavassi, E. & Garcia, M. O. (1987). Changes in magma compostion at Arenal volcano, Costa Rica, 1968–1985: real-time monitoring of open-system differentiation. *Bulletin of Volcanology* 49, 415-434.
Richard, P., Shimizu, N. & Allegre, C. J. (1976). $^{143}Nd/^{146}Nd$, a natural tracer: an application to oceanic basalts. *Earth and Planetary Science Letters* 31, 269-278.
Smith, I. E. (1982). Volcanic evolution in eastern Papua. *Tectonophysics* 87, 315-333.
Smith, I. E. & Milsom, J. S. (1984). Late Cenozoic volcanism and extension in Eastern Papua. *Geological Society, London, Special Publications* 16, 163-171.
Smith, I. E. M. (2013a). High-magnesium andesites: the example of the Papuan Volcanic Arc. *Geological Society, London, Special Publications* 385, 117-135.

Smith, I. E. M. (2013b). The chemical characterization and tectonic significance of ophiolite terrains in southeastern Papua New Guinea. *Tectonics* 32, 159-170.

Smith, I. E. M. & Compston, W. (1982). Strontium Isotopes in Cenozoic Volcanic-Rocks from Southeastern Papua-New-Guinea. *Lithos* 15, 199-206.

Smith, I. E. M., Taylor, S. R. & Johnson, R. W. (1979). REE-fractionated trachytes and dacites from Papua New Guinea and their relationship to andesite petrogenesis. *Contributions to Mineralogy and Petrology* 69, 227-233.

Sparks, S. R. J., Sigurdsson, H. & Wilson, L. (1977). Magma mixing: a mechanism for triggering acid explosive eruptions. *Nature* 267, 315-318.

Staudigel, H., McCulloch, M. T., Zindler, A. & Perfit, M. R. (1987). Complex ridge subduction and island arc magmatism: an isotopic study of the New Georgia Forearc and the Woodlark Basin. In: Taylor, B. & Exon, N. F. (eds). *Marine Geology, Geophysics, and Geochemistry of the Woodlark Basin-Solomon Islands (Earth Science Series)*, 7, 227–240.

Sun, S. S. & McDonough, W. F. (1989). Chemical and isotopic systematics of oceanic basalts: implications for mantle composition and processes. *Geological Society, London, Special Publications* 42, 313-345.

Tatsumi, Y., Hamilton, D. L. & Nesbitt, R. W. (1986). Chemical characteristics of fluid phase released from a subducted lithosphere and origin of arc magmas: Evidence from high-pressure experiments and natural rocks. *Journal of Volcanology and Geothermal Research* 29, 293-309.

Taylor, B., Goodliffe, A., Martinez, F. & Hey, R. (1995). Continental Rifting and Initial Sea-Floor Spreading in the Woodlark Basin. *Nature* 374, 534-537.

Taylor, B., Goodliffe, A. M. & Martinez, F. (1999). How continents break up: insights from Papua New Guinea. *Journal of Geophysical Research* 104, 7497-7512.

Taylor, G. A. (1958). The 1951 eruption of Mount Lamington, Papua. *Bureau of Mineral Resources, Geology and Geophysics* 38.

Tiepolo, M., Bottazzi, P., Foley, S. F., Oberti, R., Vannucci, R. & Zanetti, A. (2001). Fractionation of Nb and Ta from Zr and Hf at mantle depths: the role of titanian pargasite and kaersutite. *Journal of Petrology* 42, 221-232.

Ubide, T., Gale, C., Larrea, P., Arranz, E., Lago, M. & Tierz, P. (2014). The Relevance of Crystal Transfer to Magma Mixing: a Case Study in Composite Dykes from the Central Pyrenees. *Journal of Petrology* 55, 1535-1559.

van der Plas, L. & Tobi, A. C. (1965). A chart for judging the reliability of point counting results. American Journal of Science 263, 87-90.

Wallace, L. M., Stevens, C., Silver, E., McCaffrey, R., Loratung, W., Hasiata, S., Stanaway, R., Curley, R., Rosa, R. & Taugaloidi, J. (2004). GPS and seismological constraints on active tectonics and arc-continent collision in Papua New Guinea: Implications for mechanics of microplate rotations. *Journal of Geophysical Research-Solid Earth* 109, B05404.

Weissel, J. K., Taylor, B. & Karner, G. D. (1982). The Opening of the Woodlark Basin, Subduction of the Woodlark Spreading System, and the Evolution of Northern Melanesia since Mid-Pliocene Time. *Tectonophysics* 87, 253-277.

Worthing, M. A. & Crawford, A. J. (1996). The igneous geochemistry and tectonic setting of metabasites from the Emo Metamorphics, Papua New Guinea; A record of the evolution and destruction of a backarc basin. *Mineralogy and Petrology* 58, 79-100.

Zellmer, G. F., Sakamoto, N., Iizuka, Y., Miyoshi, M., Tamura, Y., Hsieh, H. H. & Yurimoto, H. (2014). Crystal uptake into aphyric arc melts: insights from two-pyroxene pseudo-decompression paths, plagioclase hygrometry, and measurement of hydrogen in olivines from mafic volcanics of SW Japan. Orogenic Andesites and Crustal Growth 385, 161-184.

2.10. FIGURES

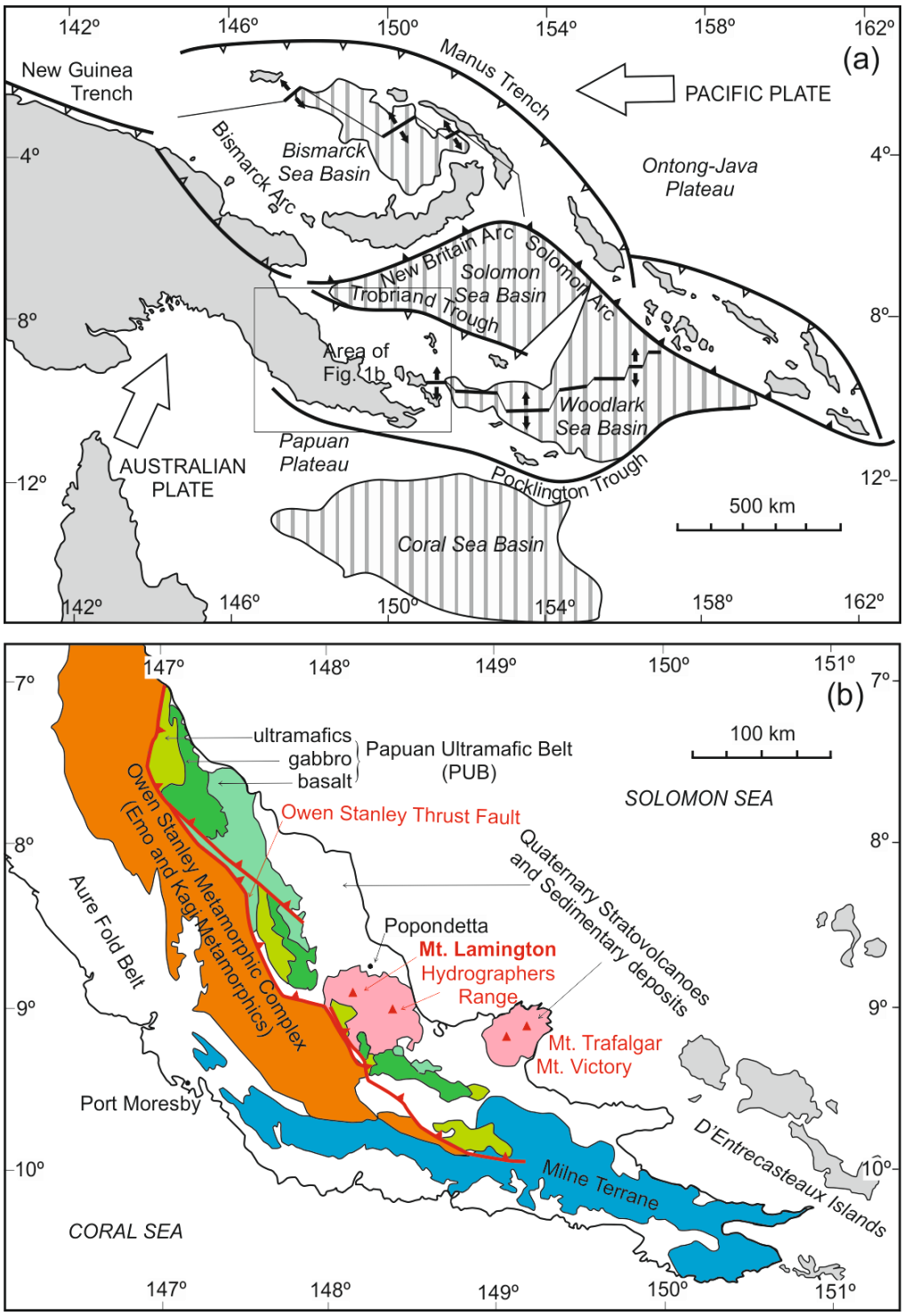

Fig. 2.1. (a) Regional map of the Papuan Peninsula, surrounding basins, subduction zones (both active and inactive) and seafloor spreading centres (after Baldwin *et al.*, 2012; Davies, 2012); (b) simplified geological map of the Papuan Peninsula (after Davies, 2012; Smith, 2013a), indicating the position of Mt. Lamington and three other major volcanic edifices, the Papuan Ultramafic Belt (PUB), Owen Stanley Metamorphic Complex, Milne Terrane and Aure Fold Belt.

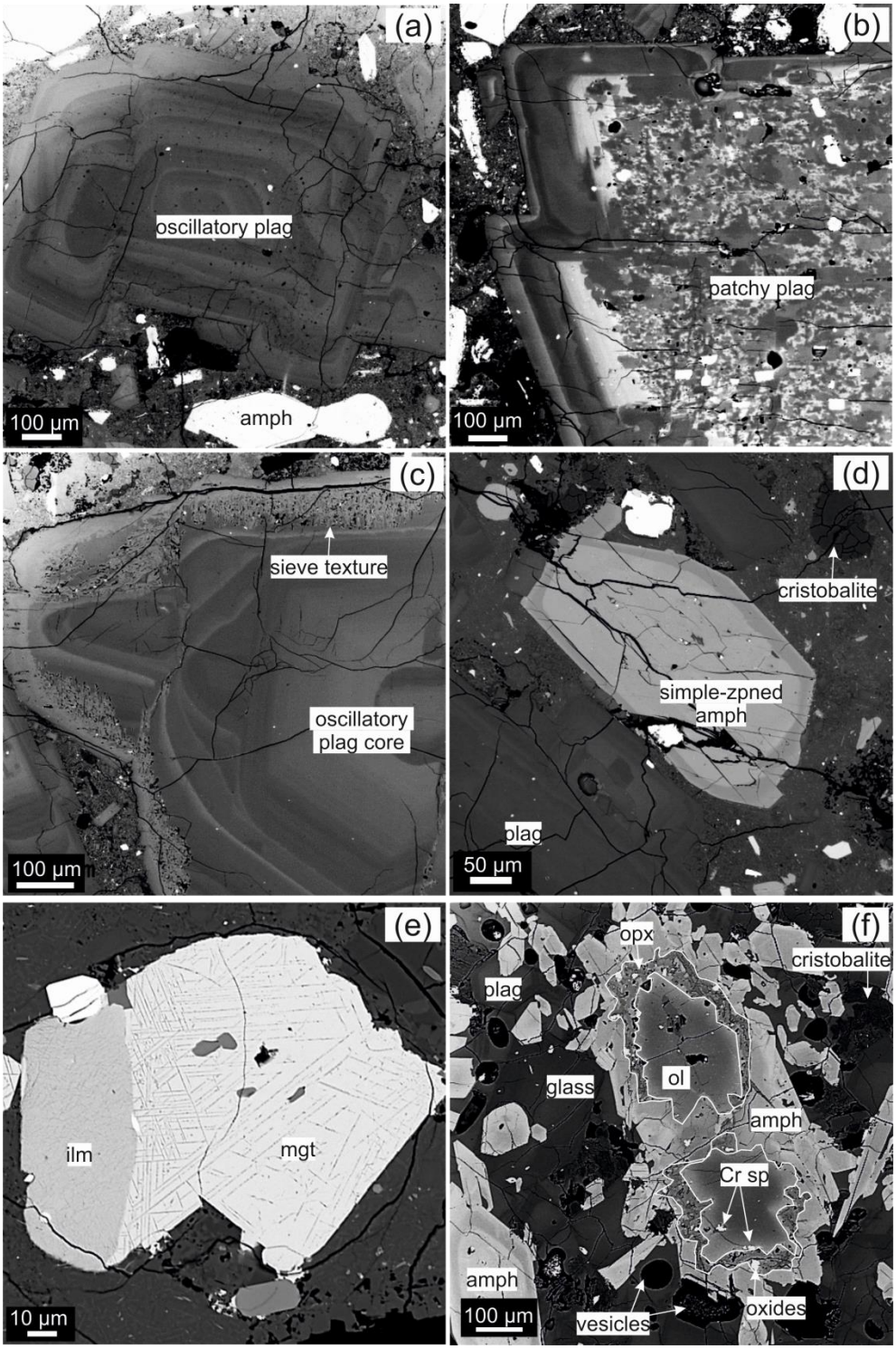

Fig. 2.2. Backscattered SEM images illustrating the mineralogical and textural features of the 1951 andesite (a-e) and diktytaxitic enclave (f): (a) oscillatory zoned plagioclase phenocryst; (b) patchy-zoned plagioclase; (c) sieve-textured plagioclase; (d) simple-zoned amphibole phenocryst; (e) an ilmenite-magnetite pair, the magnetite crystal contains exsolution lamellae of ilmenite; (f) an olivine xenocryst from a diktytaxitic enclave, showing a reaction rim of opx+ Fe-Ti oxides and amphibole, and inclusions of chromian spinel. The greyscale variation within the olivine relict corresponds to the compositional variation: the darker core and brighter rim represent $Fo_{88.2}$ and $Fo_{81.2}$, respectively. *plag* – plagioclase; *amph* – amphibole; *mgt* – magnetite; *ilm* – ilmenite; *ol* – olivine; *Cr sp* – chromian spinel.

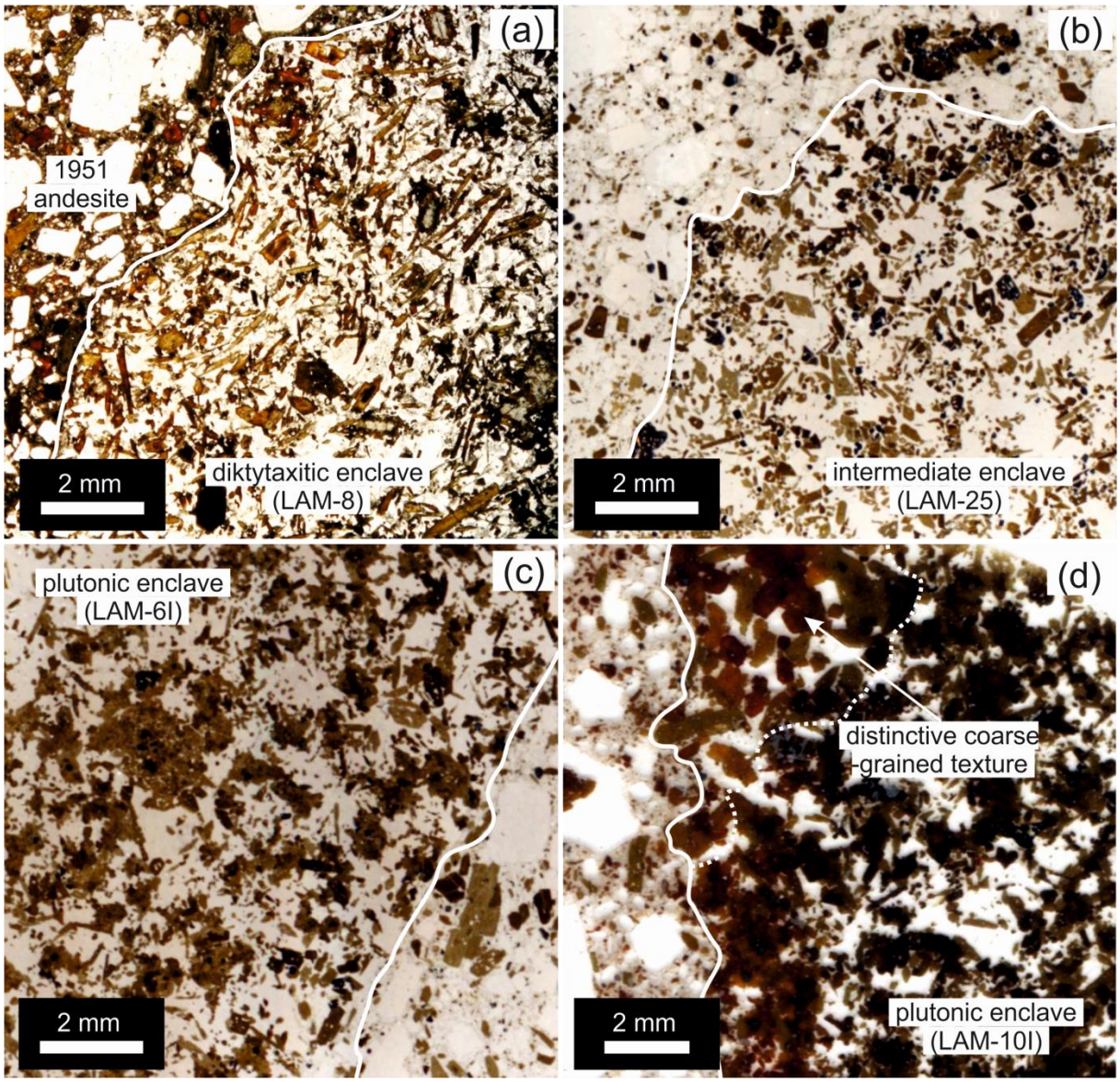

Fig. 2.3. Magmatic enclaves hosted in the 1951 andesite displaying textural variations. (a) diktytaxitic enclave LAM-8; (b) enclave intermediate between diktytaxitic texture and plutonic texture, LAM-25; (c) plutonic enclave (LAM-6I); (d) plutonic enclave with up to 69% amphibole (LAM-10I); this also contains an amphibole-rich region with a distinctive coarse-grained texture. See text for details.

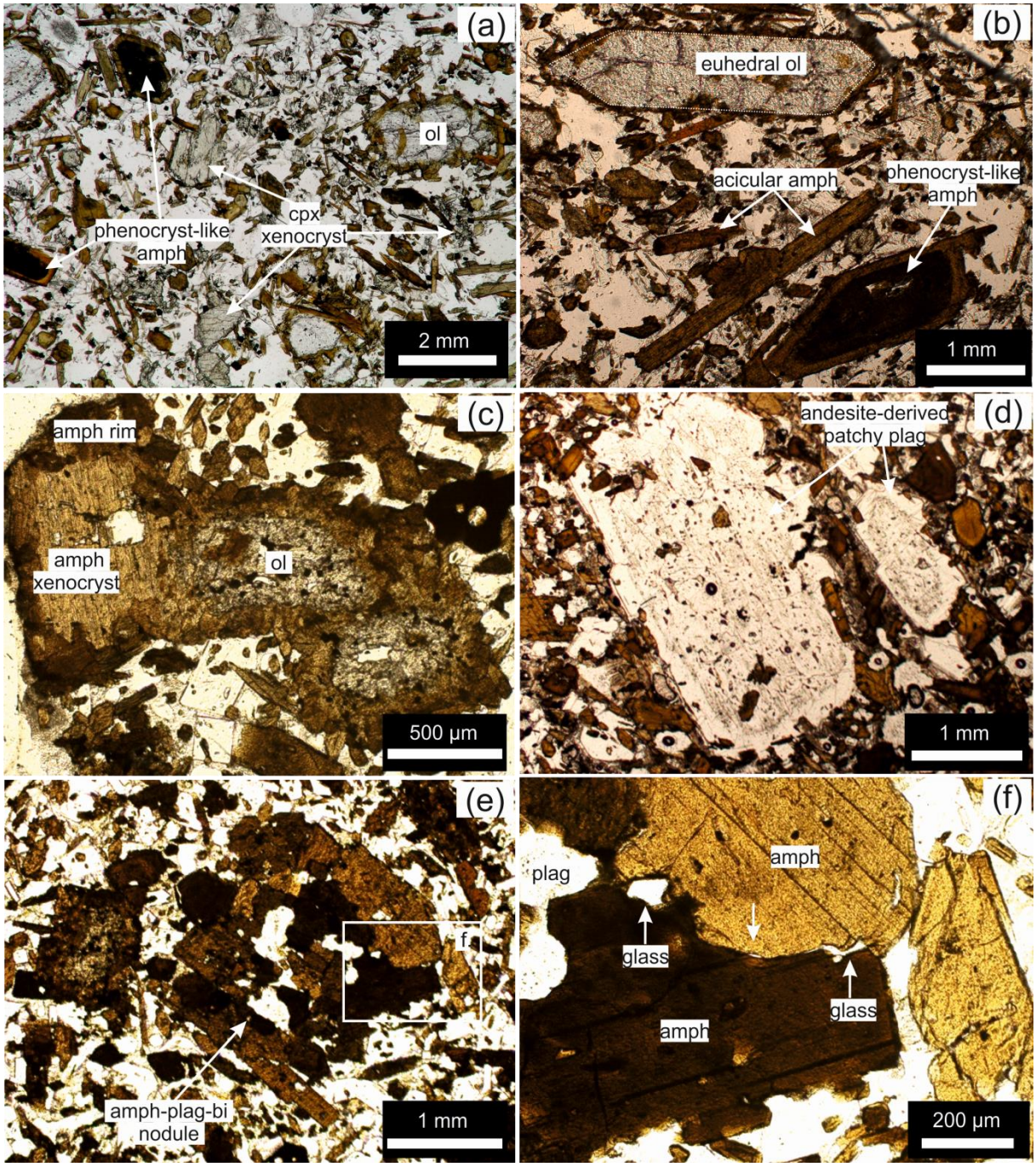

Fig. 2.4. Photomicrographs illustrating the mineralogical features of the diktytaxitic enclaves: (a) xenocrysts of clinopyroxene and olivine; (b) euhedral olivine xenocryst and acicular and phenocryst-like amphiboles; (c) amphibole xenocryst attached to olivine reaction relics, rimmed by secondary amphibole; (d) andesite-derived patchy-zoned plagioclase, with grain size contrasting to crystals from the diktytaxitic enclaves; (e,f) an amph-plag-bi nodule found in a diktytaxitic enclave; amphibole crystals are cumulus with an embayed texture, with minor glass present along the grain boundaries (indicated by white arrows).

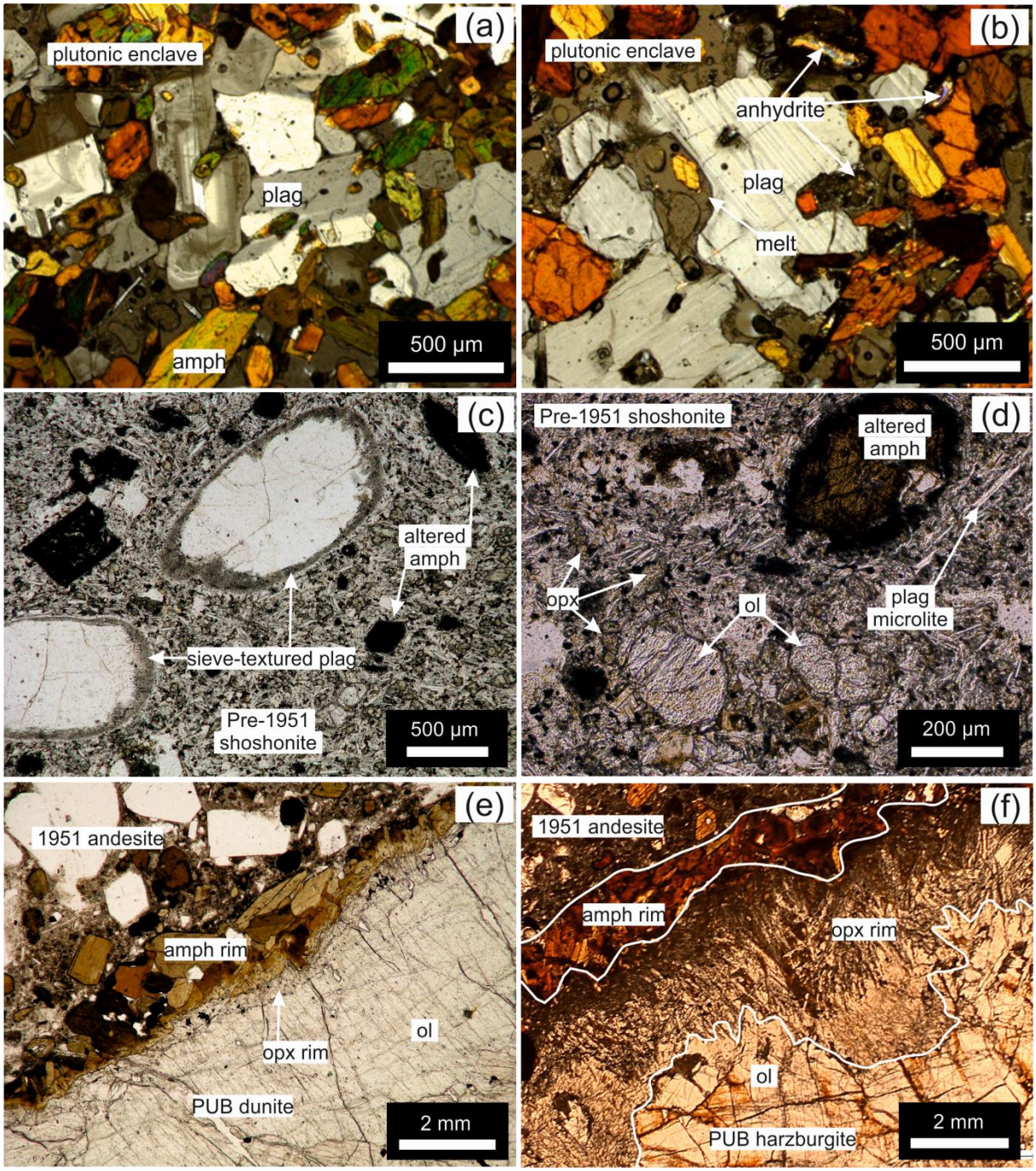

Fig. 2.5. Photomicrographs of plutonic enclave (a,b), pre-1951 shoshonite (c,d) and PUB xenoliths hosted in the 1951andesite (e,f). (a) Overgrowth of granular plagioclase with progressive crystallization; (b) Anhedral plagioclase in contact with melt (glass) in an anhydrite-bearing plutonic enclave (LAM-17I); (c) altered amphibole and sieve-textured plagioclase phenocrysts in a microcrystalline groundmass; (d) altered amphibole and olivine microphenocrysts, and orthopyroxene and plagioclase microlites; (e,f) dunite and harzburgite xenoliths from the PUB incorporated in the 1951 andesite; the xenoliths are rimmed by orthopyroxene and amphibole ± phlogopite.

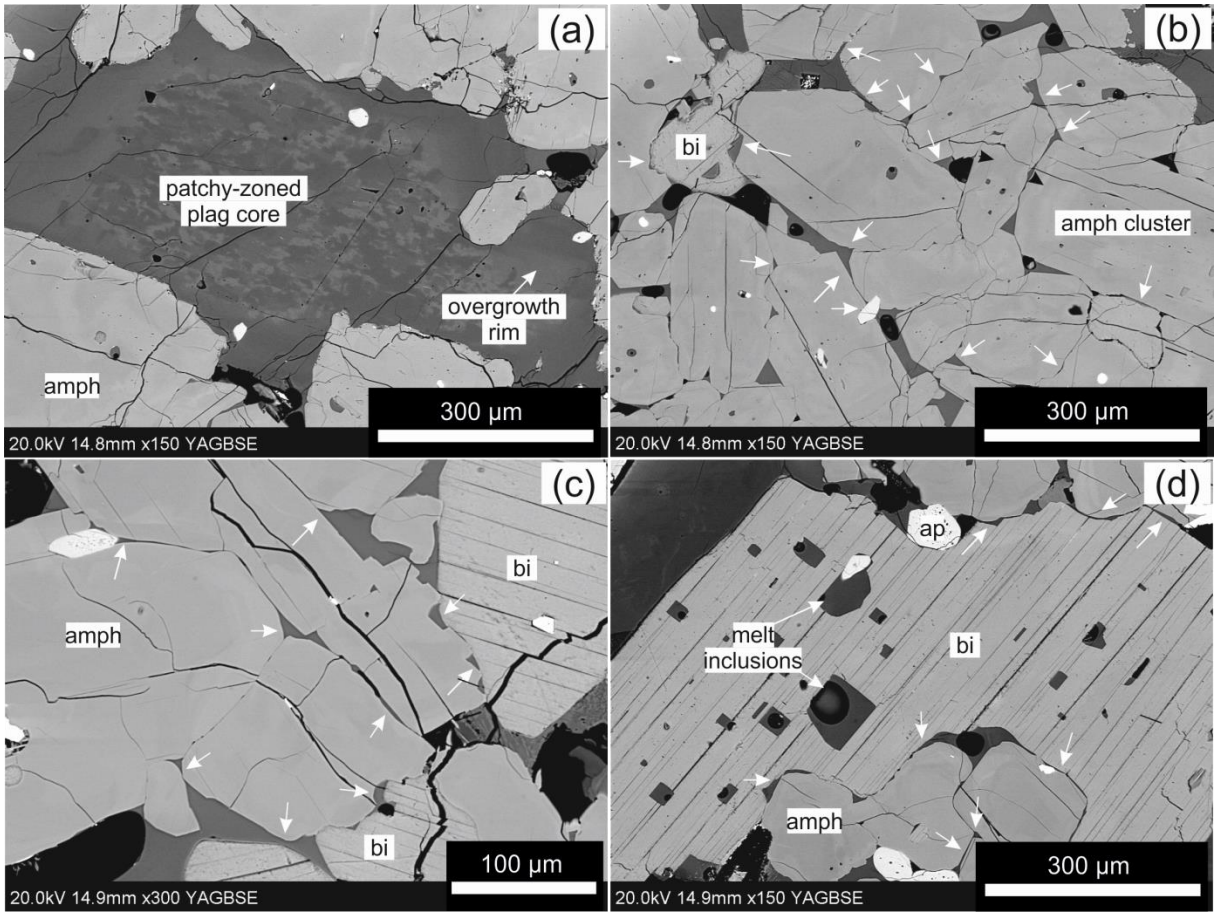

Fig. 2.6. Backscattered SEM images showing the textural features of the plutonic enclaves: (a) a spongy-cored plagioclase grain with zoned interstitial overgrowth; (b-d) amphibole-biotite clusters composed of subhedral-anhedral crystals and melt (glass) entrapped by the overgrowth of crystal grains. These features demonstrate the process of formation of a crystalline mush which has been observed in cumulates previously (e.g., Holness *et al.*, 2007).

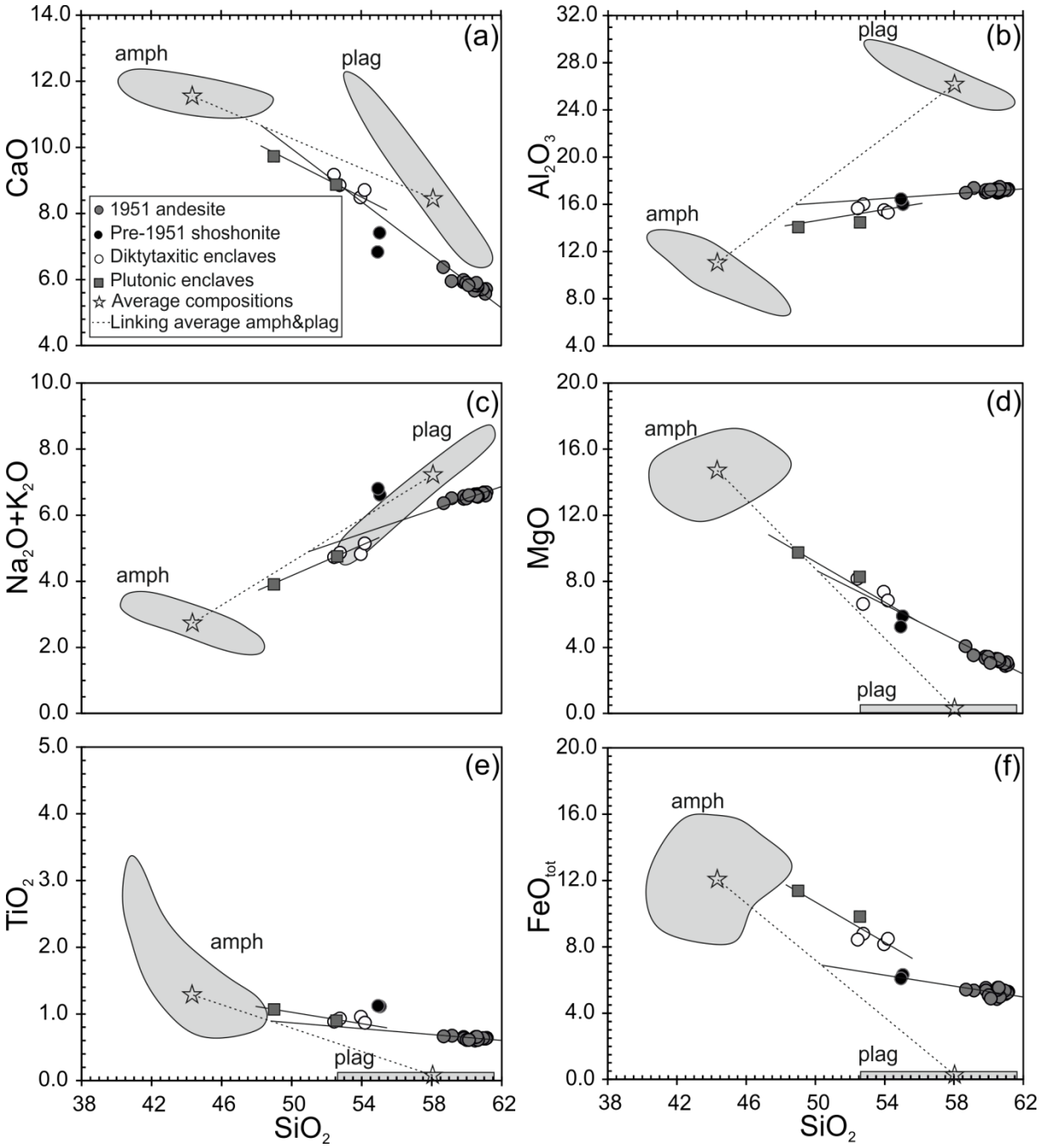

Fig. 2.7. Major element variation diagrams for Mt. Lamington volcanic samples; data from Arculus *et al*. (1983). Analytical uncertainties are overlapped by the symbol sizes. Grey fields labelled as *amph* and *plag* represent amphibole and plagioclase compositions determined by EPMA; stars represent the average composition of amphibole and plagioclase; solid lines demonstrate the variation trends of enclaves and andesites; extrapolation of the trend lines of the andesites intersect the dashed line, linking average compositions of amphibole and plagioclase, suggesting that fractional crystallization of amphibole and plagioclase gives rise to the 1951 andesite compositional variations. See text for details.

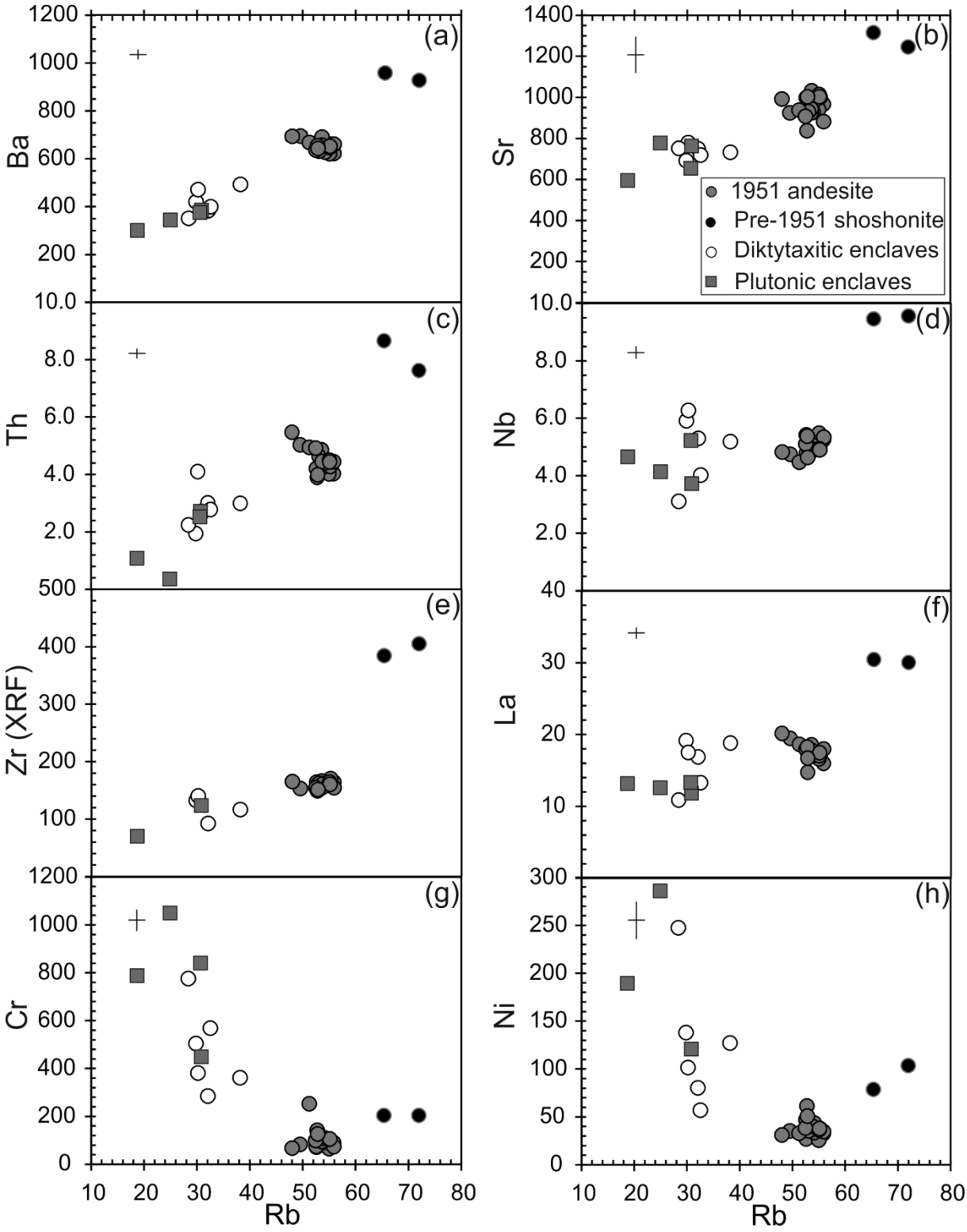

Fig. 2.8. Trace element (ppm) variation diagrams for the Mt. Lamington volcanic samples. Representative analytical uncertainties of ICP-MS data are shown by the error bars on each plot; analytical uncertainties for Zr (XRF; Arculus *et al.*, 1983) are unknown.

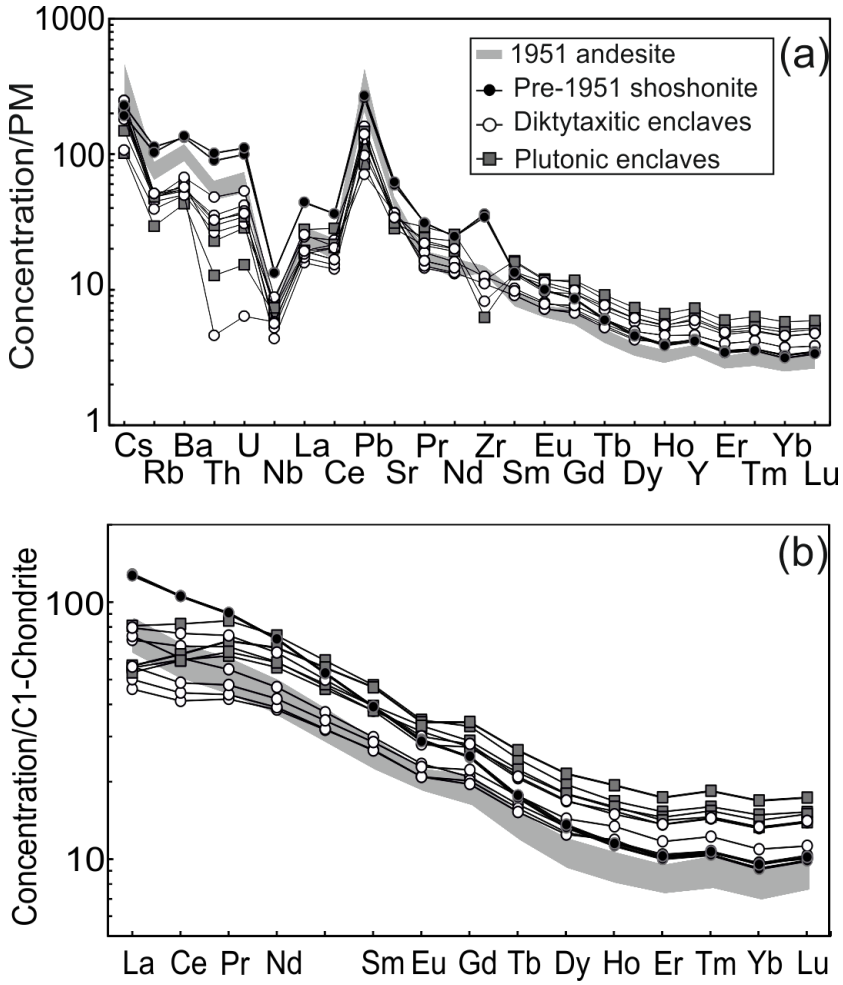

Fig. 2.9. (a) Primitive mantle normalized incompatible trace element patterns and (b) Chondrite normalized REE patterns for the 1951 andesite, magmatic enclaves and pre-1951 shoshonite. Normalization values from Sun & McDonough (1989).

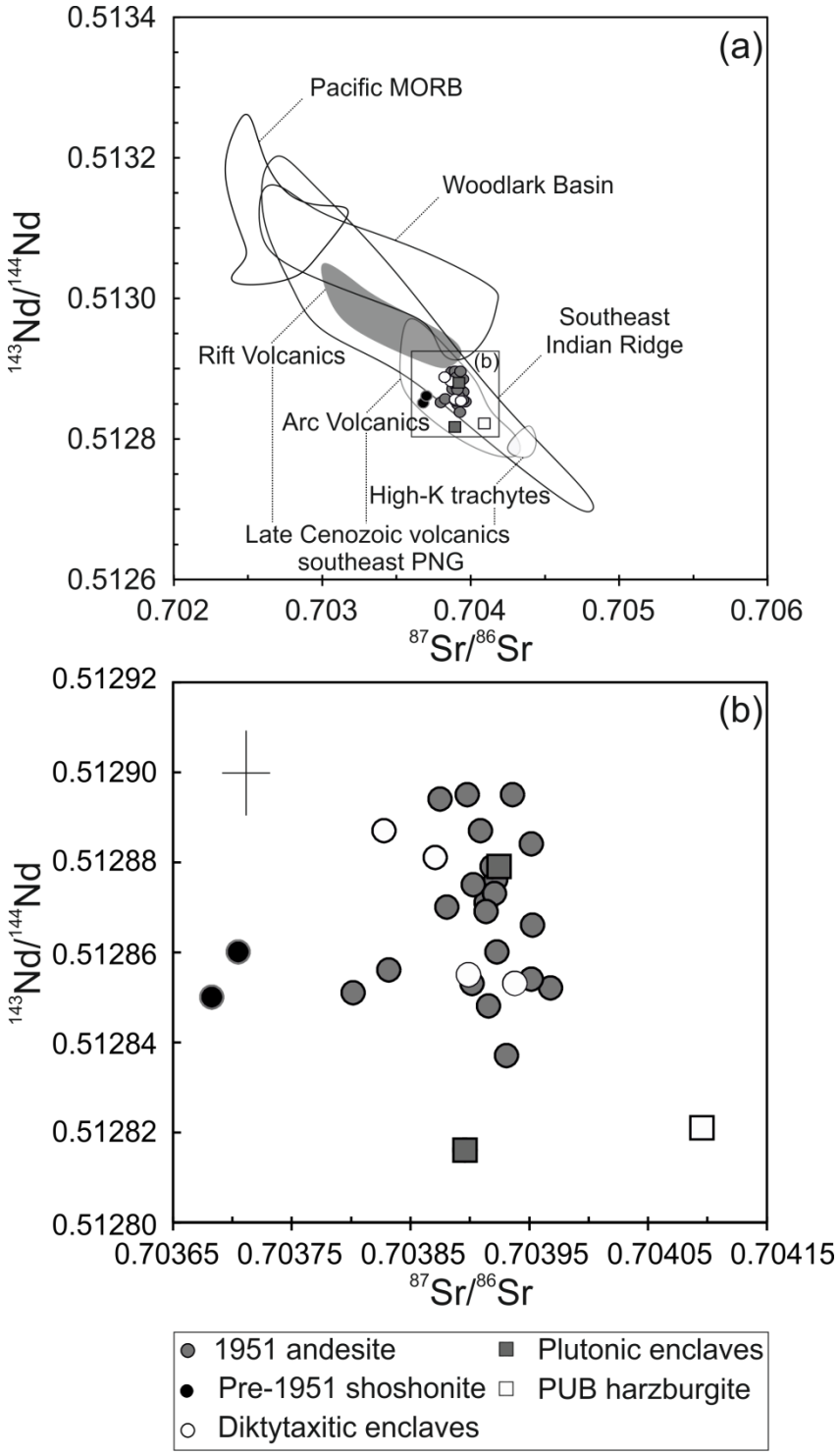

Fig. 2.10. (a,b) Sr-Nd isotopic compositions of the Mt. Lamington 1951 andesites, pre-1951 shoshonites, diktytaxitic enclaves, plutonic enclaves and the PUB harzburgite xenolith; (b) is an enlargement of the data shown in (a). Shown for comparison are fields for Pacific MORB, Woodlark Basin and Southeast Indian Ridge MORB: data from Michard *et a*l. (1986), Ito *et al*. (1987), Staudigel *et al*. (1987), Dosso *et al*. (1988) and Mahoney *et al*. (1989). Also shown is a field for Late Cenozoic rocks from southeast PNG (including rift volcanics, arc volcanics and high-K trachytes, data from Hegner & Smith, 1992).

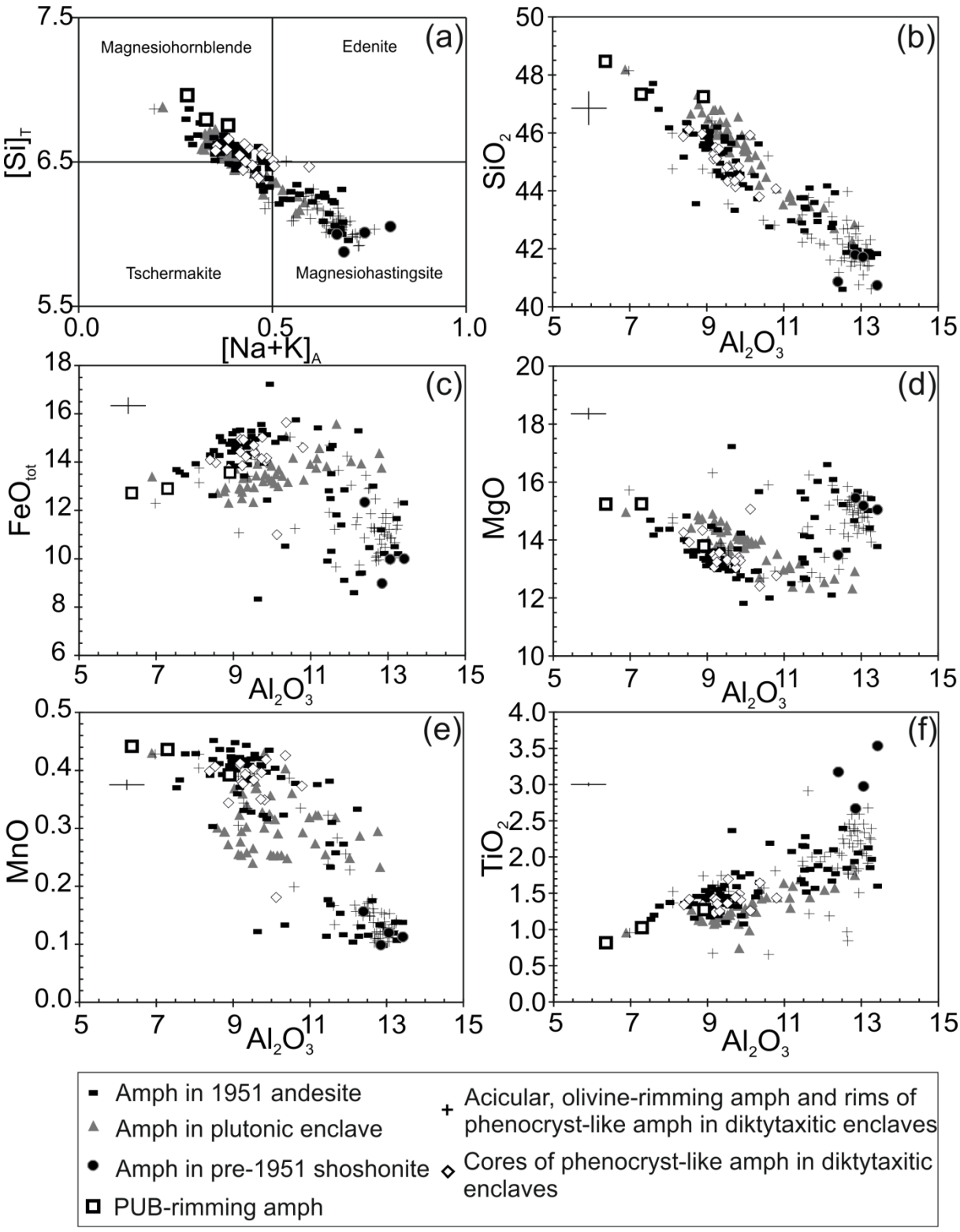

Fig. 2.11. (a) Amphibole compositions plotted in the classification diagram of Leake *et al.* (1997); $[Na+K]_A$ and $[Si]_T$ are calculated according to the amphibole stoichiometry procedure of Leake *et al.* (1997); (b-f) Chemical variations (wt %) of amphiboles from Mt. Lamington volcanic samples; representative 1 σ analytical uncertainties are illustrated as error bars.

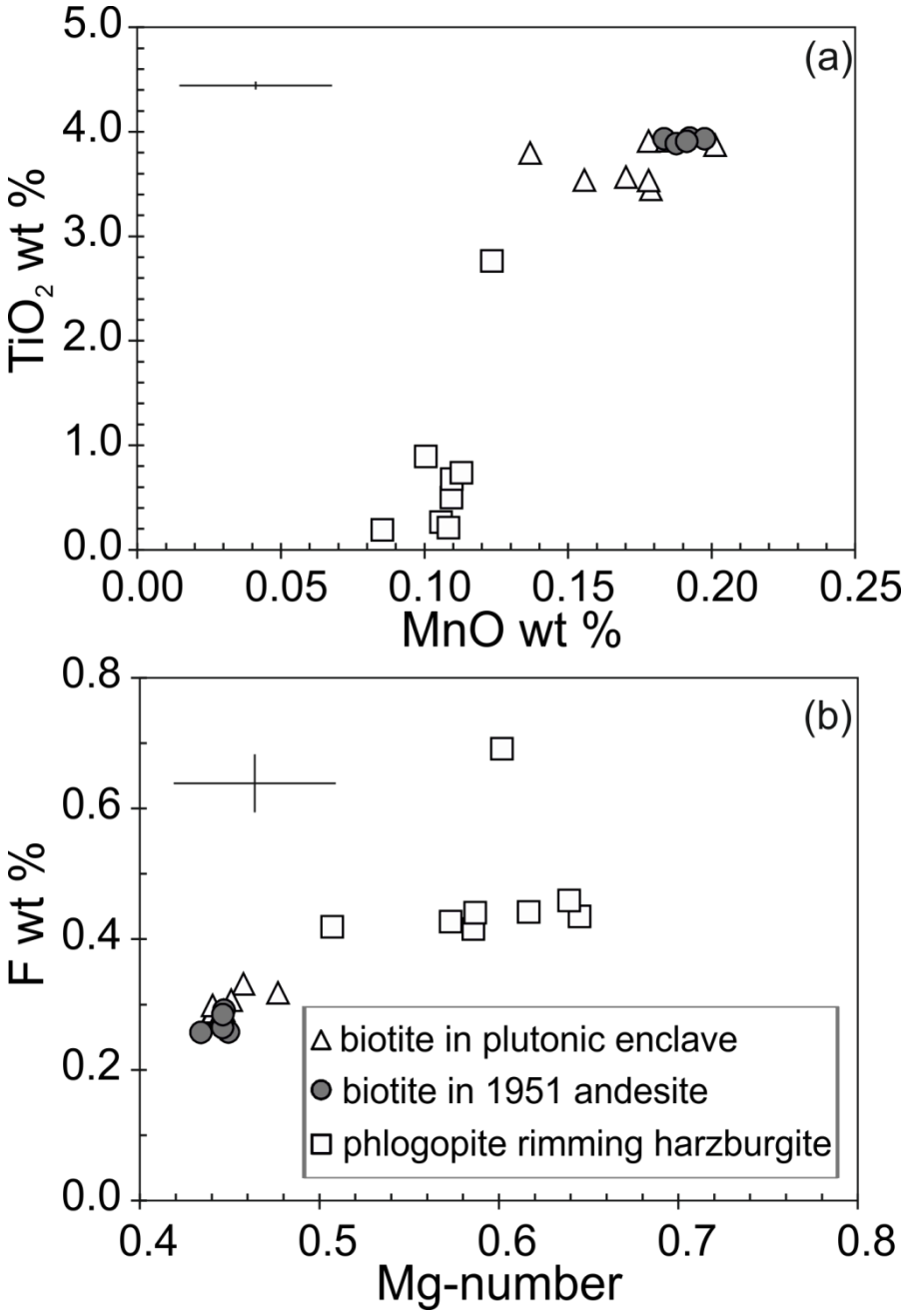

Fig. 2.12. Variation of TiO_2 versus MnO (a) and F versus Mg-number (b) for biotite from the 1951 andesite and plutonic enclaves. These have contrasting compositions to the phlogopite rimming the PUB harzburgite. Mg-number = $Mg/(Mg+Fe^{2+})$; representative 1 σ errors are indicated.

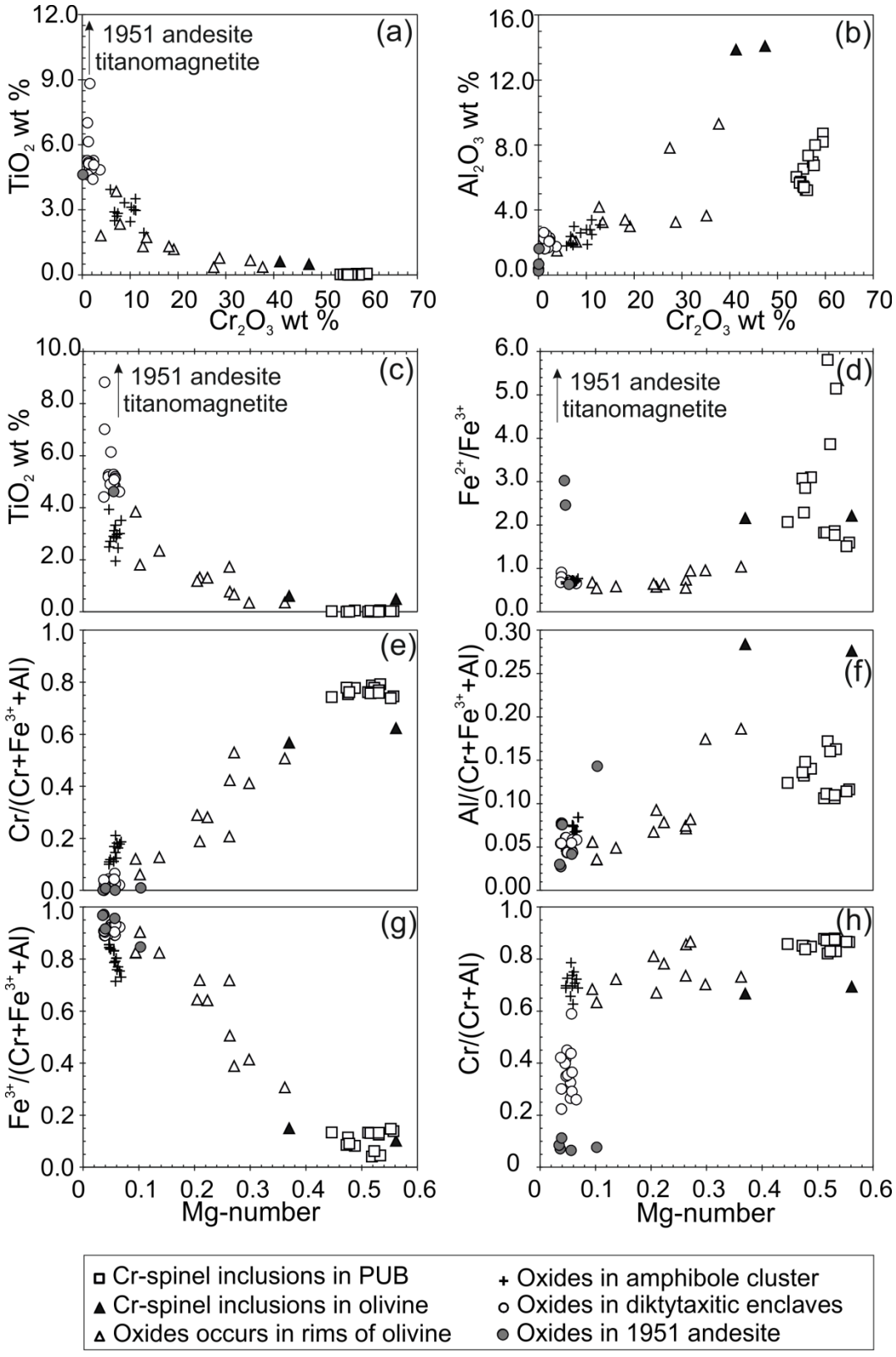

Fig. 2.13. Compositional variations of Fe-Ti-Cr oxides from Mt. Lamington volcanic samples and PUB xenoliths. Molecular percentages of Fe^{3+}, Cr and Al are calculated according to the spinel stoichiometry; Mg-number = $Mg/(Mg+Fe^{2+})$. Analytical uncertainties are overlapped by the symbol sizes. See text for details.

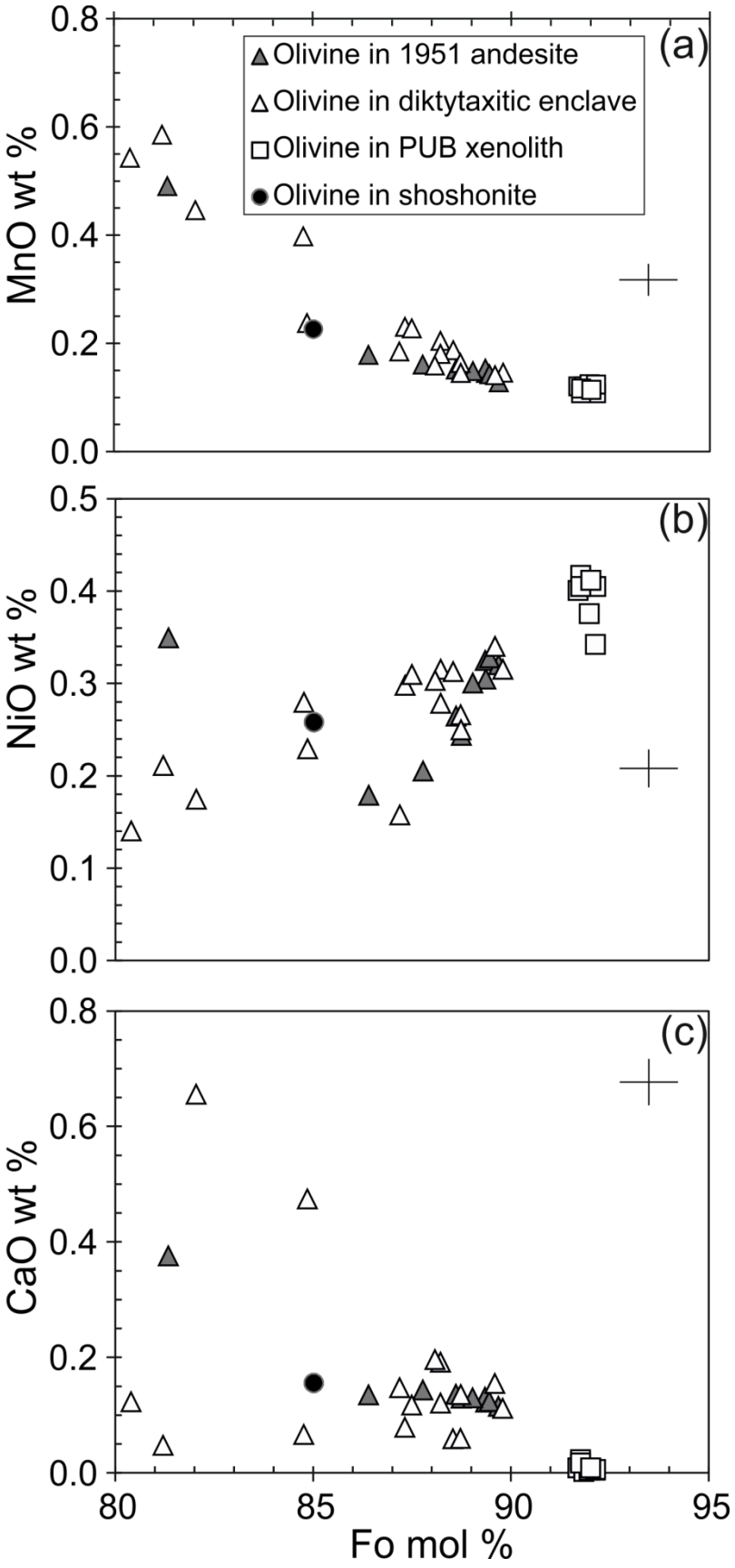

Fig. 2.14. Compositional variations of olivines from the Mt. Lamington volcanic samples and PUB xenoliths; representative 1 σ errors are given in the plots. See text for details. (a) MnO, (b) NiO and (c) CaO versus forsterite mol%.

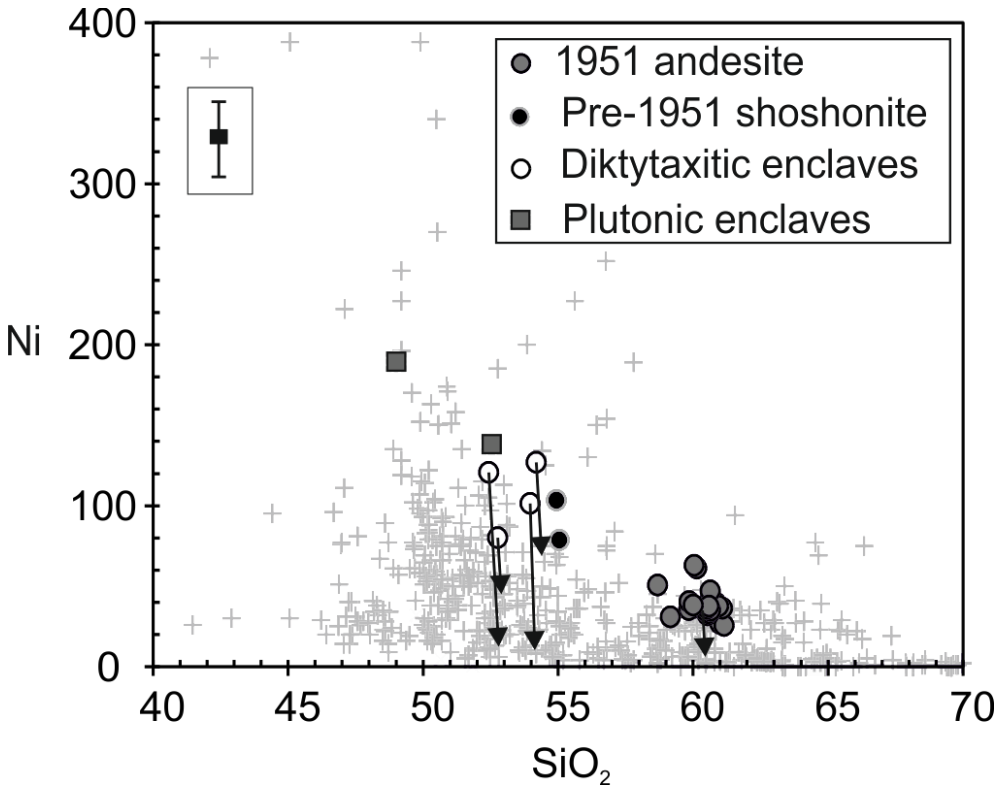

Fig. 2.15. Ni (ppm) variations versus SiO_2 (wt %) for the 1951 andesite, pre-1951 shoshonite and the magmatic enclaves. Grey pluses are comparison data for the Bismarck Arc-New Britain Arc (GEOROC, http://georoc.mpch-mainz.gwdg.de). The arrows on the enclaves and andesite indicate the effect of subtracting the observed amount of olivine (from vesicle-free modal analysis, Table 2), and point towards the inferred original composition before olivine assimilation. Magmatic enclaves with Ni > 200 ppm (LAM-9I, -19I and 20I) are not shown on this plot due to unavailable major element data of those samples (see Table 1).

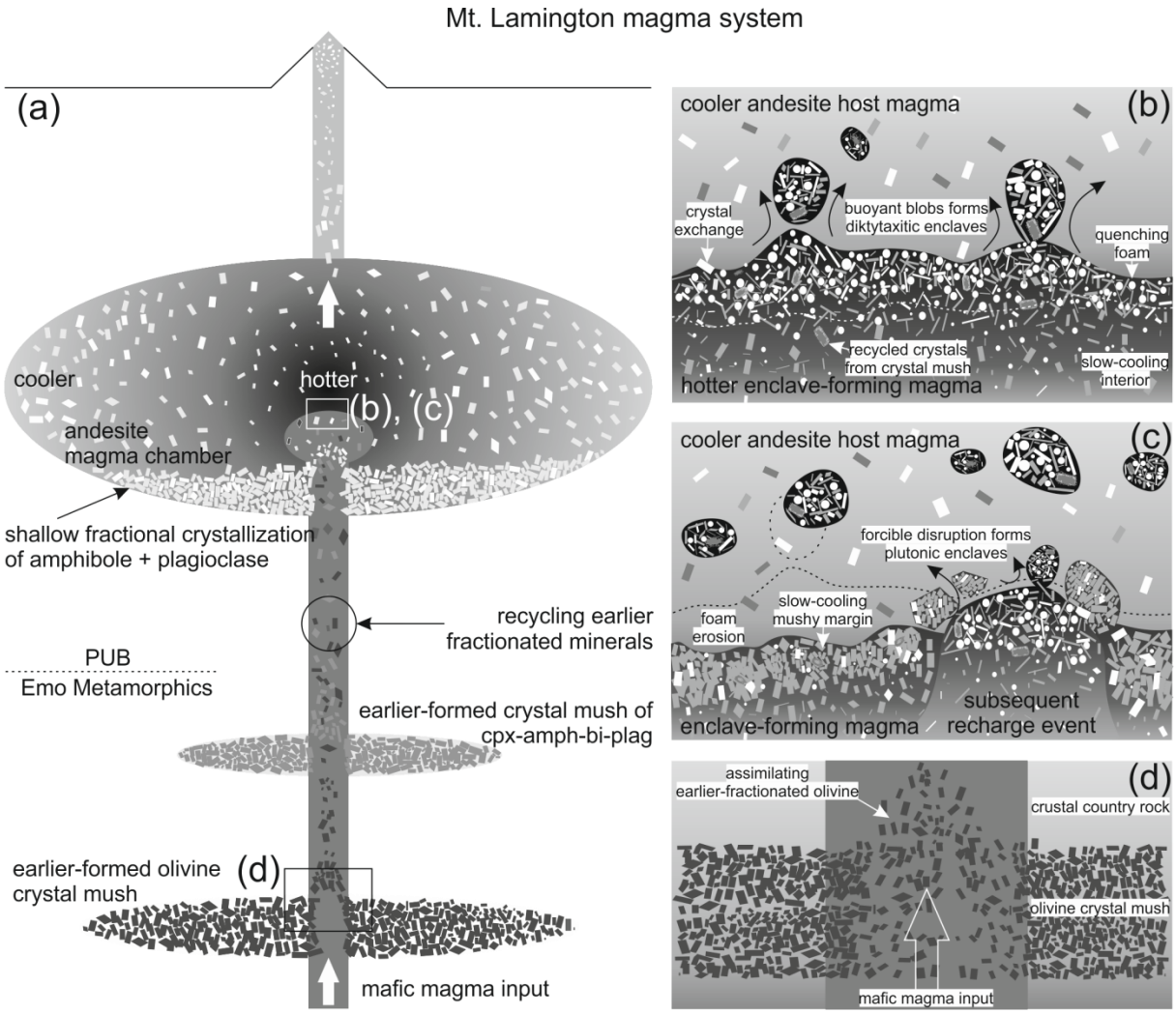

Fig. 2.16. Schematic cartoons of the Mt. Lamington magma system: (a) the compositional evolution of 1951 andesite is represented by shallow fractional crystallization of amphibole+plagioclase; the interrelationship between the magmatic enclaves and the andesite host is represented by enclave-forming magma intrusion into the andesite magma; earlier-fractionated crystals recycle through the recharging magma percolating crystal mushes; (b,c) the formation of diktytaxitic and plutonic-textured enclaves; (d) recycling of earlier-fractionated olivines from an old crystal mush through enclave-forming magma percolation; (b) and (c) are after Browne *et al.* (2006). See text for details.

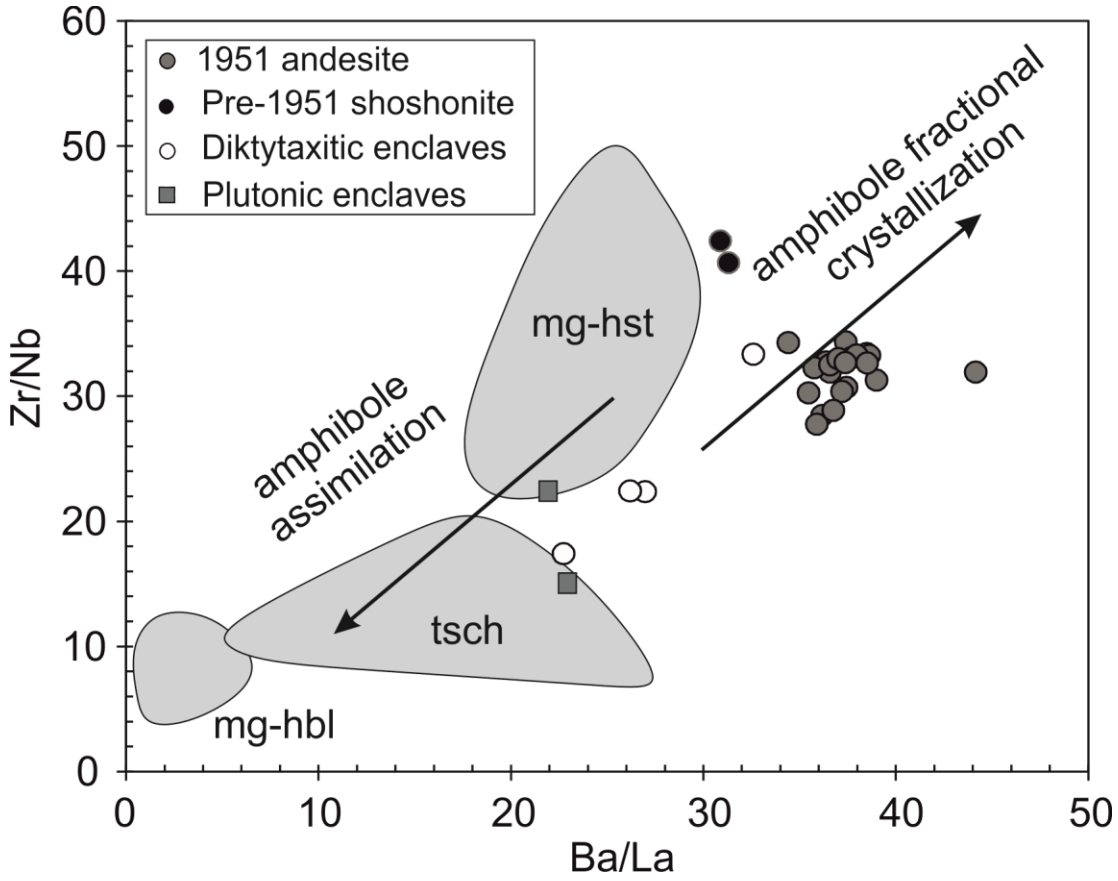

Fig. 2.17. Zr/Nb versus Ba/La for the 1951 andesite, pre-1951 shoshonite and the magmatic enclaves. The shaded fields illustrate the range of Zr/Nb and Ba/La ratios in amphiboles from Mt. Pinatubo, Mt. Hood and Mt. St. Helens (Lowen, 2013), which have compositions of magnesiohornblende (mg-hbl), tschermakite (tsch) and magnesiohastingsite (mg-hst). The difference in Zr/Nb and Ba/La ratios between the magmatic enclaves and the 1951 andesite can be explained either by more extensive fractional crystallisation of amphibole from the andesites, pushing their trace element ratios to higher values, or by recycling foreign amphibole crystals, including earlier fractionated cumulate amphibole, by the enclaves, reducing their trace element ratios to lower values.

2.11. TABLES

Table 1: Major and trace element and Sr-Nd isotopic compositions of samples from Mt. Lamington, Papua New Guinea

	1951 Andesite								
Samples	LAM-2	LAM-3	LAM-4	LAM-5	LAM-6H	LAM-8H	LAM-9H	LAM-10H	LAM-11
SiO_2	*61.00*	*60.65*	*60.54*	*61.15*	*60.02*	*61.10*	*60.66*	*60.86*	*60.49*
TiO_2	*0.63*	*0.61*	*0.65*	*0.64*	*0.61*	*0.63*	*0.63*	*0.63*	*0.60*
Al_2O_3	*17.29*	*17.31*	*16.97*	*17.30*	*17.22*	*17.19*	*17.03*	*17.16*	*17.35*
FeO_{tot}	*5.15*	*4.97*	*5.53*	*5.28*	*5.04*	*5.23*	*5.35*	*5.37*	*4.85*
MnO	*0.10*	*0.11*	*0.11*	*0.11*	*0.11*	*0.10*	*0.10*	*0.10*	*0.11*
MgO	*2.86*	*3.24*	*3.30*	*2.94*	*3.38*	*3.09*	*3.13*	*3.05*	*3.31*
CaO	*5.71*	*5.76*	*5.84*	*5.71*	*5.90*	*5.56*	*5.80*	*5.70*	*5.66*
Na_2O	*4.50*	*4.43*	*4.44*	*4.53*	*4.46*	*4.45*	*4.47*	*4.45*	*4.49*
K_2O	*2.18*	*2.14*	*2.15*	*2.16*	*2.10*	*2.14*	*2.17*	*2.18*	*2.14*
P_2O_5	*0.23*	*0.24*	*0.23*	*0.22*	*0.23*	*0.17*	*0.26*	*0.24*	*0.25*
Total	*99.66*	*99.46*	*99.75*	*100.04*	*99.07*	*99.67*	*99.58*	*99.74*	*99.25*
Cr	70	74	89	64	94	96	109	98	73
Ni	27	47	32	25	37	36	43	40	35
Co	33	57	36	40	32	31	37	37	30
Cu	17	17	13	13	18	12	14	23	13
Ga	20	20	20	20	19	20	20	20	20
Sc	11.8	12.5	13.5	13.1	12.7	11.7	12.4	12.8	13.3
V	99	105	114	102	121	107	112	110	115
Cs	2.45	2.49	2.74	2.51	2.62	2.73	2.72	2.56	2.58
Rb	52.7	52.6	55.9	55.0	53.6	52.9	54.2	54.0	55.9
Ba	664	650	622	621	690	650	656	639	660
Sr	997	922	965	940	942	934	985	926	881
Th	4.21	4.19	4.03	4.01	4.86	4.81	4.44	4.26	4.44
U	1.23	1.12	1.09	1.12	1.26	1.36	1.22	1.24	1.28
Pb	15.72	15.40	14.64	14.75	15.54	15.79	15.62	15.77	15.72
Nb	4.78	5.42	5.25	5.47	5.07	5.02	4.91	5.14	5.34
Zr	*164*	*154*	*164*	*168*	*154*	*160*	*162*	*164*	*154*
Y	15.70	15.81	16.48	15.81	17.43	15.01	15.96	16.49	16.88
La	17.76	17.96	15.96	16.59	18.55	14.72	17.41	17.46	17.97
Ce	36.54	36.85	33.18	34.05	38.34	30.13	36.05	36.28	37.23
Pr	5.06	5.00	4.70	4.64	5.20	4.13	5.02	5.00	5.10
Nd	20.31	19.95	19.01	18.56	20.66	16.73	20.23	19.93	20.31
Sm	3.95	3.86	3.75	3.62	4.03	3.38	3.95	3.88	3.95
Eu	1.17	1.13	1.11	1.06	1.15	1.06	1.17	1.14	1.14
Gd	4.07	3.70	3.87	3.53	3.69	3.32	4.13	3.80	3.79
Tb	0.51	0.49	0.49	0.45	0.52	0.44	0.52	0.49	0.51
Dy	2.72	2.66	2.58	2.44	2.81	2.43	2.74	2.65	2.74
Ho	0.54	0.52	0.52	0.48	0.55	0.48	0.55	0.54	0.53
Er	1.40	1.36	1.34	1.27	1.47	1.28	1.41	1.38	1.42
Tm	0.23	0.22	0.22	0.21	0.24	0.21	0.23	0.23	0.23
Yb	1.38	1.33	1.34	1.23	1.45	1.29	1.40	1.35	1.39
Lu	0.22	0.21	0.21	0.20	0.23	0.21	0.22	0.21	0.22
$^{87}Sr/^{86}Sr$	0.703968	0.703914	0.703802	0.703875	0.703953	0.703922	0.703881	0.703832	0.703952
$^{143}Nd/^{144}Nd$	0.512852	0.512871	0.512851	0.512894	0.512866	0.512876	0.512870	0.512856	0.512854

I in the column headings refers to the enclave sample separated from the corresponding andesite host sample (H).
Italic **data are from Arculus et al. (1983), as well as unpublished data; non-Italic trace element/Mn data are derived from ICP-MS analysis at Durham University.**
Two batches of ICP-MS analysis were carried out, LAM-1, -6H, -8I, -13, -27A and -27D were analyzed in batch 1, and the rest were analyzed in batch 2.
Multiple analyses of W2 and BHVO-1 standards are shown as averaged values and relative standard deviations (values in brackets); S value refers to standard error of W2, BHVO-1 and AGV-1 regression line.
Sr-Nd isotope compositions are analyzed at UCLA (SRM987 $^{87}Sr/^{86}Sr = 0.710248 \pm 17$; La Jolla $^{143}Nd/^{144}Nd = 0.511840 \pm 11$).
LAM-6I, -10I, -21I are plutonic enclaves; LAM-19I, -20I are intermediate enclaves; the rest of the magmatic enclaves are diktytaxitic enclaves.

Table 2.1

Table 1: continued

Samples	LAM-13	LAM-14	LAM-17	LAM-19H	LAM-20H	LAM-21H	LAM-22H	LAM-23	LAM-24
SiO_2	*60.66*	*58.70*	*60.95*	*60.54*	*60.57*	*59.85*		*59.86*	*60.52*
TiO_2	*0.61*	*0.66*	*0.63*	*0.65*	*0.65*	*0.65*		*0.63*	*0.65*
Al_2O_3	*17.47*	*16.98*	*17.27*	*17.03*	*17.14*	*16.98*		*17.19*	*17.24*
FeO_{tot}	*4.98*	*5.41*	*5.35*	*5.49*	*5.43*	*5.52*		*5.36*	*5.40*
MnO	*0.11*	*0.12*	*0.10*	*0.11*	*0.11*	*0.11*	0.10	*0.11*	*0.10*
MgO	*3.16*	*4.07*	*3.03*	*3.27*	*3.23*	*3.44*		*3.32*	*3.26*
CaO	*5.81*	*6.37*	*5.70*	*5.79*	*5.86*	*5.92*		*5.98*	*5.83*
Na_2O	*4.42*	*4.24*	*4.47*	*4.41*	*4.45*	*4.38*		*4.45*	*4.44*
K_2O	*2.13*	*2.12*	*2.19*	*2.16*	*2.14*	*2.11*		*2.12*	*2.15*
P_2O_5	*0.25*	*0.24*	*0.26*	*0.28*	*0.24*	*0.25*		*0.22*	*0.23*
Total	*99.60*	*98.91*	*99.96*	*99.73*	*99.80*	*99.19*		*99.24*	*99.81*
Cr	82	126	92	110	91	108	252	108	104
Ni	35	51	38	39	33	35	33	40	36
Co	43	65	38	36	30	37	15	33	31
Cu	31	21	18	14	15	13	20	20	14
Ga	19	21	20	20	20	20	20	21	20
Sc	11.5	15.1	12.0	13.3	13.5	12.7	12.6	13.2	12.9
V	112	131	111	115	116	117	119	117	115
Cs	2.47	1.28	2.42	2.72	2.75	2.65	2.79	2.61	2.68
Rb	49.6	52.9	55.3	53.6	54.2	53.1	51.3	53.7	55.1
Ba	695	642	660	656	627	631	667	657	647
Sr	924	1002	1000	924	982	929	936	1031	1013
Th	5.02	3.98	4.28	4.86	4.39	4.63	4.94	4.45	4.49
U	1.32	1.13	1.25	1.28	1.24	1.23	1.30	1.12	1.16
Pb	16.45	31.15	15.58	16.28	14.76	15.00	16.53	15.56	15.39
Nb	4.74	4.63	5.09	4.99	4.95	4.99	4.46	4.85	4.93
Zr	*153*	*151*	*170*	*166*	*162*	*162*		*160*	*164*
Y	16.42	16.97	16.08	16.26	16.28	16.56	15.96	16.56	15.99
La	19.44	16.68	17.15	16.99	17.23	17.25	18.62	17.75	17.04
Ce	39.95	35.21	35.64	35.05	35.18	35.93	37.83	36.49	35.27
Pr	5.27	5.05	4.99	4.86	4.91	4.95	5.14	5.14	4.94
Nd	20.97	20.80	20.11	19.58	19.61	19.69	20.48	20.85	20.03
Sm	4.07	4.17	3.92	3.89	3.83	3.87	3.97	4.06	3.90
Eu	1.17	1.25	1.14	1.16	1.13	1.14	1.18	1.21	1.15
Gd	3.64	4.35	4.06	3.83	3.88	3.79	3.89	4.29	4.10
Tb	0.51	0.56	0.51	0.50	0.50	0.49	0.51	0.53	0.51
Dy	2.79	2.95	2.67	2.72	2.65	2.68	2.72	2.83	2.70
Ho	0.55	0.60	0.54	0.54	0.53	0.52	0.55	0.57	0.56
Er	1.45	1.53	1.39	1.42	1.38	1.39	1.42	1.47	1.40
Tm	0.24	0.25	0.22	0.23	0.22	0.23	0.23	0.24	0.23
Yb	1.43	1.52	1.37	1.42	1.37	1.40	1.40	1.44	1.38
Lu	0.23	0.24	0.22	0.22	0.22	0.22	0.22	0.23	0.22
$^{87}Sr/^{86}Sr$	0.703921	0.703931	0.703916	0.703919	0.703952	0.703902		0.703903	0.703923
$^{143}Nd/^{144}Nd$	0.512873	0.512837	0.512848	0.512879	0.512884	0.512853		0.512875	0.512860

Table 2.1 continued

Table 1: continued

					Magmatic Enclaves				
Samples	LAM-25	LAM-26	LAM-27A	LAM-27C	LAM-6I	LAM-7	LAM-8I	LAM-9I	LAM-10I
SiO_2	*60.60*	*60.01*	*59.17*	*60.14*	*52.57*	*52.77*	*53.97*		*49.01*
TiO_2	*0.65*	*0.61*	*0.67*	*0.61*	*0.90*	*0.93*	*0.95*		*1.07*
Al_2O_3	*17.22*	*17.06*	*17.37*	*17.24*	*14.46*	*16.01*	*15.50*		*14.06*
FeO_{tot}	*5.53*	*5.07*	*5.36*	*4.87*	*9.81*	*8.78*	*8.15*		*11.38*
MnO	*0.11*	*0.11*	*0.11*	*0.11*	0.24	0.18	0.14	0.16	0.24
MgO	*3.27*	*3.42*	*3.51*	*3.05*	*8.27*	*6.62*	*7.35*		*9.74*
CaO	*5.89*	*5.90*	*5.95*	*5.82*	*8.87*	*8.85*	*8.48*		*9.72*
Na_2O	*4.43*	*4.40*	*4.34*	*4.46*	*3.41*	*3.33*	*3.34*		*2.83*
K_2O	*2.14*	*2.10*	*2.17*	*2.14*	*1.34*	*1.52*	*1.48*		*1.07*
P_2O_5	*0.24*	*0.24*	*0.27*	*0.23*	*0.30*	*0.23*	*0.30*		*0.16*
Total	*100.08*	*98.92*	*98.92*	*98.67*	*100.17*	*99.22*	*99.66*		*99.27*
Cr	105	99	66	141	504	284	380	775	787
Ni	38	38	31	61	138	80	101	247	189
Co	32	90	55	69	67	51	64	42	111
Cu	17	15	20	20	26	45	47	72	317
Ga	21	20	19	19	20	20	19	18	20
Sc	13.1	13.4	12.7	13.1	26.1	26.7	21.9	31.9	31.3
V	119	110	120	113	193	202	196	240	258
Cs	2.70	2.67	2.45	2.15	1.18	1.71	1.72	1.58	0.80
Rb	55.2	52.5	48.0	52.8	29.9	32.1	30.2	28.4	18.7
Ba	652	636	693	654	420	383	471	351	302
Sr	1002	906	991	837	690	748	778	750	594
Th	4.43	4.91	5.47	3.89	1.94	3.00	4.10	2.24	1.08
U	1.13	1.25	1.56	1.08	0.60	0.88	1.12	0.65	0.32
Pb	15.42	15.59	16.27	14.38	8.02	9.40	11.40	6.95	5.97
Nb	4.90	5.09	4.82	5.37	5.90	5.29	6.27	3.10	4.66
Zr	*160*	*154*	*165*	*149*	*132*	*92*	*140*		*70*
Y	16.44	16.53	18.01	16.58	30.06	25.29	19.53	19.41	27.94
La	17.44	17.93	20.14	18.23	19.13	16.85	17.46	10.84	13.15
Ce	35.96	36.63	42.48	37.65	50.24	41.14	37.04	25.15	36.39
Pr	5.08	5.01	5.75	5.13	8.03	6.36	5.18	3.97	5.86
Nd	20.51	20.01	22.97	20.55	34.51	27.29	21.72	17.74	25.93
Sm	4.02	3.91	4.50	4.00	7.24	5.75	4.54	4.06	5.76
Eu	1.18	1.15	1.30	1.14	2.01	1.61	1.36	1.21	1.81
Gd	4.21	3.78	4.08	3.82	6.73	5.58	4.27	4.12	5.58
Tb	0.53	0.50	0.56	0.51	0.91	0.77	0.61	0.59	0.81
Dy	2.77	2.70	3.03	2.75	4.93	4.24	3.38	3.21	4.52
Ho	0.56	0.53	0.60	0.54	0.95	0.86	0.66	0.66	0.89
Er	1.42	1.42	1.58	1.40	2.51	2.24	1.71	1.68	2.40
Tm	0.23	0.23	0.26	0.23	0.41	0.36	0.27	0.27	0.39
Yb	1.41	1.42	1.56	1.38	2.51	2.23	1.63	1.63	2.39
Lu	0.22	0.23	0.25	0.21	0.39	0.35	0.26	0.25	0.38
$^{87}Sr/^{86}Sr$	0.703905	0.703914	0.703898	0.703909	0.703896	0.703899	0.703938		0.703925
$^{143}Nd/^{144}Nd$		0.512869	0.512895	0.512887	0.512816	0.512855	0.512853		0.512879

Table 2.1 continued

Table 1: continued

						Shoshonite		ICP-MS Standards		S
Samples	LAM-18	LAM-19I	LAM-20I	LAM-21I	LAM-22I	LAM-1	LAM-27D	W2	BHVO-1	
SiO_2	*52.45*				*54.20*	*55.06*	*54.95*			
TiO_2	*0.88*				*0.86*	*1.11*	*1.12*			
Al_2O_3	*15.65*				*15.30*	*15.99*	*16.43*			
FeO_{tot}	*8.42*				*8.48*	*6.31*	*6.08*			
MnO	0.14	0.28	0.25	0.17	0.20	*0.12*	*0.12*	0.18(5.24%)	0.18(6.97%)	
MgO	*8.15*				*6.84*	*5.89*	*5.24*			
CaO	*9.16*				*8.70*	*7.41*	*6.83*			
Na_2O	*3.32*				*3.44*	*3.44*	*3.47*			
K_2O	*1.40*				*1.69*	*3.17*	*3.33*			
P_2O_5	*0.27*				*0.25*	*0.64*	*0.63*			
Total	*99.85*				*99.98*	*99.14*	*98.20*			
Cr	448	840	1049	567	361	203	203	98(4.42%)	295(3.54%)	1.57%
Ni	121	1271	286	57	127	79	103	95(8.01%)	128(3.13%)	11.84%
Co	57	35	46	32	47	43	51	46(3.70%)	46(4.85%)	0.25%
Cu	33	24	138	23	45	42	45	106(4.63%)	141(3.83%)	0.17%
Ga	19	22	20	19	20	20	20	17.3(2.57%)	21.2(2.54%)	4.22%
Sc	29.5	31.6	31.7	28.3	23.3	20.5	18.0	36.2(2.14%)	31.8(2.60%)	2.14%
V	217	243	239	235	172	173	161	255(14.32%)	239(41.90%)	19.36%
Cs	1.43	1.61	0.85	1.96	1.69	1.52	1.81	0.94(8.47%)	0.13(32.68%)	3.14%
Rb	30.8	30.7	24.9	32.6	38.2	65.4	72.0	20.1(2.42%)	9.4(2.64%)	0.38%
Ba	386	375	348	400	492	952	927	167(1.81%)	132(2.58%)	0.22%
Sr	763	654	777	718	732	1315	1244	292(25.16%)	423(5.30%)	9.46%
Th	2.70	2.53	0.39	2.77	2.99	8.64	7.62	2.11(1.99%)	1.21(2.60%)	0.28%
U	0.80	0.73	0.13	0.77	0.87	2.33	2.09	0.48(1.23%)	0.41(1.46%)	0.98%
Pb	9.17	10.45	5.03	9.95	10.32	19.20	18.21	7.38(2.40%)	1.97(2.58%)	0.66%
Nb	3.72	5.22	4.14	4.01	5.18	9.45	9.55	7.47(2.29%)	19.17(1.34%)	1.51%
Zr	*124*				*116*	*384*	*405*			
Y	19.25	33.26	26.98	21.10	25.60	18.97	19.50	22.52(0.92%)	27.45(1.83%)	3.06%
La	11.83	13.37	12.58	13.26	18.79	30.40	30.02	10.07(2.79%)	15.03(2.68%)	1.20%
Ce	27.08	38.22	36.11	29.61	46.15	64.51	64.44	21.69(2.53%)	36.2(2.33%)	1.97%
Pr	4.13	6.69	6.07	4.51	7.03	8.56	8.61	3.10(0.75%)	5.64(0.76%)	1.39%
Nd	18.11	30.92	27.13	19.56	29.60	33.45	33.45	13.52(0.84%)	25.95(1.32%)	0.77%
Sm	4.03	7.10	6.01	4.34	5.97	5.95	5.97	3.33(1.27%)	6.26(1.53%)	1.44%
Eu	1.20	1.97	1.91	1.32	1.73	1.68	1.66	1.10(1.54%)	2.09(2.27%)	3.78%
Gd	4.00	6.98	5.90	4.55	5.74	5.09	5.13	3.69(3.11%)	6.30(5.11%)	12.23%
Tb	0.57	0.99	0.83	0.66	0.78	0.64	0.66	0.63(1.65%)	0.98(2.33%)	0.61%
Dy	3.15	5.43	4.54	3.62	4.27	3.35	3.44	3.82(0.92%)	5.33(1.60%)	1.53%
Ho	0.67	1.09	0.90	0.75	0.84	0.63	0.65	0.79(0.80%)	1.00(1.25%)	0.88%
Er	1.65	2.86	2.33	1.93	2.25	1.65	1.69	2.11(0.64%)	2.42(1.42%)	1.77%
Tm	0.27	0.47	0.37	0.31	0.37	0.26	0.27	0.35(0.59%)	0.36(1.84%)	4.30%
Yb	1.61	2.85	2.25	1.85	2.25	1.55	1.61	2.07(1.23%)	2.02(2.24%)	1.47%
Lu	0.26	0.44	0.35	0.28	0.36	0.25	0.26	0.33(1.03%)	0.30(1.09%)	3.73%
$^{87}Sr/^{86}Sr$	0.703871				0.703828	0.703683	0.703705			
$^{143}Nd/^{144}Nd$	0.512881				0.512887	0.512850	0.512860			

Table 2.1 continued

Table 2: Representative point counting results

	1951 andesite														
Sample	LAM-3			LAM-5			LAM-6H			LAM-9H			LAM-23		
Counts/prop./std.	n	%	σ	n	%	σ	n	%	σ	n	%	σ	n	%	σ
Olivine	2	0.7	*0.5*	0	0.0	*0.0*	5	1.7	*0.7*	1	0.3	*0.3*	9	1.1	*0.4*
Amphibole	54	18.0	*2.2*	59	19.7	*2.3*	79	26.3	*2.5*	73	24.3	*2.5*	172	21.5	*1.5*
Plagioclase	104	34.7	*2.7*	108	36.0	*2.8*	90	30.0	*2.6*	98	32.7	*2.7*	292	36.5	*1.7*
Oxides	4	1.3	*0.7*	8	2.7	*0.9*	3	1.0	*0.6*	4	1.3	*0.7*	26	3.3	*0.6*
Biotite	3	1.0	*0.6*	3	1.0	*0.6*	3	1.0	*0.6*	4	1.3	*0.7*	15	1.9	*0.5*
Clinopyroxene	0	0.0	*0.0*	0	0.0	*0.0*	0	0.0	*0.0*	0	0.0	*0.0*	0	0.0	*0.0*
Melt	112	37.3	*2.8*	101	33.7	*2.7*	99	33.0	*2.7*	112	37.3	*2.8*	268	33.5	*1.7*
Bubble	21	7.0	*1.5*	21	7.0	*1.5*	21	7.0	*1.5*	8	2.7	*0.9*	18	2.3	*0.5*
Total	300	100		300	100		300	100		300	100		800	100	
Bubble-free Crystallinity %		59.9			63.8			64.5			61.6			65.7	

The point counting does not differentiate phenocryst/antecryst/xenocryst;
In 1951 andesite and diktytaxitic enclaves, orthopyroxene countings are included in the olivine group;
Bubble-free crystallinity = 100(ol+amph+plag+ox+bi+cpx)/(ol+amph+plag+ox+bi+cpx+melt);
Standard deviation σ = (P(100-P)/N)0.5, where P = the proportion of each phase in percent, and N = the total counts, according to van der Plas & Tobi (1965).

Table 2.2

Table 2: continued

	Diktytaxitic enclave												Intermediate			Plutonic enclave					
Sample	LAM-7			LAM-8I			LAM-9I			LAM-18			LAM-22I			LAM-19I			LAM-6I			LAM-10I		
Counts/prop./std.	n	%	σ	n	%	σ	n	%	σ	n	%	σ	n	%	σ	n	%	σ	n	%	σ	n	%	σ
Olivine	4	1.3	*0.7*	11	3.7	*1.1*	13	4.3	*1.2*	12	4.0	*1.1*	6	2.0	*0.8*	0	0.0	*0.0*	0	0.0	*0.0*	0	0.0	*0.0*
Amphibole	133	44.3	*2.9*	138	46.0	*2.9*	121	40.3	*2.8*	129	43.0	*2.9*	140	46.7	*2.9*	171	48.0	*2.6*	167	47.7	*2.7*	691	69.1	*1.5*
Plagioclase	62	20.7	*2.3*	77	25.7	*2.5*	80	26.7	*2.6*	78	26.0	*2.5*	94	31.3	*2.7*	81	22.8	*2.2*	127	36.3	*2.6*	217	21.7	*1.3*
Oxides	1	0.3	*0.3*	7	2.3	*0.9*	6	2.0	*0.8*	9	3.0	*1.0*	0	0.0	*0.0*	3	0.8	*0.5*	4	1.1	*0.6*	10	1.0	*0.3*
Biotite	1	0.3	*0.3*	0	0.0	*0.0*	0	0.0	*0.0*	0	0.0	*0.0*	4	1.3	*0.7*	3	0.8	*0.5*	7	2.0	*0.7*	9	0.9	*0.3*
Clinopyroxene	0	0.0	*0.0*	0	0.0	*0.0*	6	2.0	*0.8*	23	7.7	*1.5*	0	0.0	*0.0*	0	0.0	*0.0*	0	0.0	*0.0*	0	0.0	*0.0*
Melt	58	19.3	*2.3*	50	16.7	*2.2*	25	8.3	*1.6*	8	2.7	*0.9*	45	15.0	*2.1*	49	13.8	*1.8*	17	4.9	*1.1*	24	2.4	*0.5*
Bubble	41	13.7	*2.0*	17	5.7	*1.3*	49	16.3	*2.1*	41	13.7	*2.0*	11	3.7	*1.1*	49	13.8	*1.8*	28	8.0	*1.5*	49	4.9	*0.7*
Total	300	100		300	100		300	100		300	100		300	100		356	100		350	100		1000	100	
Bubble-free Crystallinity %		77.6			82.3			90.0			96.9			84.4			84.0			94.7			97.5	

Table 2.2 continued

Table 2.3

Table 3: Representative amphibole compositions

	1951 andesite						Diktytaxitic enclave							Plutonic enclave		Shoshonite		PUB dunite		
Type	unzoned		normal-zoned		reverse-zoned		phenocryst-like			acicular		ol-rimming		amph cluster		phenocryst		amph rim		1 σ error
Sample	LAM-10-0023		LAM-23-0001		LAM-23-0002		LAM-8I-0011			LAM-8I-0010		LAM-8I-0015		LAM-10I-0008		LAM-27D-0050		LAM-23		
Analysis	27/1.	29/1.	37/1.	38/1.	27/1.	28/1.	14/1.	15/1.	16/1.	2/1.	4/1.	21/1.	23/1.	4/1.	5/1.	50/1.	51/1.	9/1.	13/1.	
Position	core	core	core	rim	core	rim	core	inner	outer	core	core	core	core	core	core	core	core	core	core	
SiO_2	47.70	42.96	42.94	44.68	45.43	41.90	44.84	41.57	41.82	42.76	42.98	42.30	42.35	45.92	43.66	41.79	40.73	47.24	48.46	0.57
TiO_2	1.20	2.07	1.88	1.55	1.45	2.13	1.49	2.33	2.22	1.50	0.96	2.24	2.00	1.09	1.60	2.67	3.53	1.27	0.82	0.03
Al_2O_3	7.54	11.12	11.81	9.20	8.90	13.11	9.83	13.09	12.92	12.95	12.64	13.25	11.72	9.25	11.22	12.86	13.43	8.91	6.37	0.49
Cr_2O_3	0.01	0.04	0.13	0.01	0.01	0.06	0.03	0.03	0.01	0.01	0.00	0.04	0.00	0.66	0.09	0.30	0.05	0.00	0.25	0.02
FeO	13.59	15.41	12.85	14.82	14.87	10.49	14.03	10.86	11.09	11.44	11.27	11.38	13.64	13.34	14.57	8.97	9.99	13.57	12.71	0.28
MgO	14.17	12.49	13.65	12.98	13.30	15.01	13.39	14.79	15.00	14.91	15.04	14.27	12.86	13.80	12.39	15.45	15.04	13.79	15.23	0.16
CaO	11.37	11.24	11.77	11.31	11.49	12.04	11.59	12.21	11.90	11.79	11.86	12.03	11.78	11.43	11.34	11.87	11.66	11.02	11.45	0.28
MnO	0.38	0.38	0.27	0.42	0.41	0.12	0.35	0.15	0.13	0.15	0.18	0.14	0.28	0.36	0.32	0.10	0.11	0.39	0.44	0.01
Na_2O	1.54	2.23	2.25	1.89	1.81	2.47	2.05	2.56	2.48	2.47	2.51	2.49	2.21	1.71	2.09	2.57	2.50	1.96	1.59	0.13
K_2O	0.52	0.77	0.73	0.62	0.62	0.66	0.66	0.67	0.63	0.61	0.52	0.67	0.67	0.44	0.71	1.30	1.00	0.86	0.41	0.23
F	0.15	0.17	0.18	0.18	0.15	0.15	0.10	0.14	0.15	0.17	0.14	0.15	0.14	0.19	0.16	0.32	0.19	0.24	0.17	0.05
Cl	0.05	0.06	0.01	0.07	0.06	0.02	0.05	0.01	0.02	0.02	0.01	0.01	0.04	0.03	0.05	0.01	0.01	0.06	0.04	0.01
Total	98.22	98.99	98.47	97.74	98.51	98.17	98.43	98.42	98.41	98.82	98.14	98.99	97.72	98.24	98.24	98.23	98.28	99.31	97.95	
T Si	6.866	6.241	6.224	6.542	6.589	6.035	6.509	6.002	6.009	6.103	6.168	6.073	6.221	6.619	6.371	6.050	5.875	6.754	6.962	
T Al(IV)	1.134	1.759	1.776	1.458	1.411	1.965	1.491	1.998	1.991	1.897	1.832	1.927	1.779	1.381	1.629	1.950	2.125	1.246	1.038	
Total	8.00	8.00	8.00	8.00	8.00	8.00	8.00	8.00	8.00	8.00	8.00	8.00	8.00	8.00	8.00	8.00	8.00	8.00	8.00	
M1-3 Al(VI)	0.146	0.145	0.241	0.130	0.111	0.262	0.190	0.229	0.197	0.281	0.306	0.316	0.251	0.190	0.301	0.244	0.158	0.256	0.040	
M1-3 Ti	0.130	0.227	0.205	0.171	0.158	0.230	0.163	0.253	0.240	0.161	0.104	0.242	0.221	0.119	0.175	0.290	0.383	0.137	0.088	
M1-3 Cr	0.002	0.005	0.015	0.001	0.001	0.007	0.003	0.004	0.002	0.002	0.000	0.005	0.000	0.075	0.011	0.034	0.005	0.000	0.028	
M1-3 Fe^{3+}	0.696	0.886	0.686	0.785	0.785	0.709	0.669	0.643	0.841	0.889	0.877	0.606	0.622	0.787	0.693	0.444	0.708	0.644	0.749	
M1-3 Mg	3.041	2.705	2.949	2.832	2.876	3.223	2.898	3.184	3.213	3.173	3.217	3.055	2.816	2.965	2.695	3.334	3.235	2.938	3.262	
M1-3 Fe^{2+}	0.940	0.986	0.871	1.029	1.019	0.555	1.035	0.668	0.491	0.476	0.475	0.760	1.054	0.820	1.085	0.642	0.497	0.978	0.778	
M1-3 Mn	0.047	0.046	0.033	0.052	0.051	0.015	0.043	0.019	0.016	0.018	0.022	0.017	0.035	0.044	0.040	0.012	0.014	0.047	0.054	
Total	5.00	5.00	5.00	5.00	5.00	5.00	5.00	5.00	5.00	5.00	5.00	5.00	5.00	5.00	5.00	5.00	5.00	5.00	5.00	
M4 Ca	1.753	1.749	1.828	1.774	1.786	1.858	1.803	1.889	1.832	1.804	1.824	1.851	1.854	1.766	1.774	1.842	1.802	1.687	1.763	
M4 Na	0.247	0.251	0.172	0.226	0.214	0.142	0.197	0.111	0.168	0.196	0.176	0.149	0.146	0.234	0.226	0.158	0.198	0.313	0.237	
Total	2.00	2.00	2.00	2.00	2.00	2.00	2.00	2.00	2.00	2.00	2.00	2.00	2.00	2.00	2.00	2.00	2.00	2.00	2.00	
A Na	0.183	0.377	0.460	0.311	0.297	0.548	0.379	0.604	0.523	0.487	0.522	0.544	0.483	0.245	0.366	0.564	0.502	0.229	0.206	
A K	0.095	0.143	0.136	0.117	0.114	0.120	0.122	0.123	0.116	0.112	0.095	0.122	0.126	0.080	0.133	0.241	0.183	0.156	0.074	
Total	0.278	0.521	0.596	0.427	0.411	0.669	0.502	0.727	0.639	0.599	0.617	0.666	0.609	0.325	0.499	0.805	0.685	0.386	0.281	
Classification	Mg-Hbl	Mg-Hst	Mg-Hst	Mg-Hbl	Mg-Hbl	Mg-Hst	Mg-Hbl	Mg-Hst	Mg-Hst	Mg-Hst	Mg-Hst	Mg-Hst	Mg-Hst	Mg-Hbl	Tsch-Prg	Mg-Hst	Mg-Hst	Mg-Hbl	Mg-Hbl	

normal-zoned - high Al core and low Al rim; reverse-zoned - low Al core and high Al rim; inner - inner rim; outer - outer rim; Classification is based on the nomentclature of Leake et al. (1997).

Table 2.4

Table 4: Representative plagioclase compositions

	1951 andesite									Diktytaxitic enclave					Plutonic enclave			Shoshonite			
Type	Oscillatory		Sieve-textured			Patchy-zoned				Normal-zoned		Patchy-zoned			Oscillatory			Oscillatory			1 σ
Sample	LAM-23-0002		LAM-23-0009			LAM-23-0013				LAM-8I-0010		LAM-8I-0014			LAM-10I-0008			LAM-27D-0050			error
Analysis	29/1.	30/1.	49/1.	50/1.	51/1.	67/1.	69/1.	71/1.	73/1.	11/1.	12/1.	66/1.	67/1.	69/1.	17/1.	19/1.	20/1.	58/1.	59/1.	60/1.	
Position	core	rim	core	inner	outer	bright	dark	inner	outer	core	rim	bright	dark	rim	core	inner	outer	core	inner	outer	
SiO_2	55.33	60.12	56.39	52.95	58.06	57.35	58.77	56.52	59.54	53.99	59.91	49.69	63.57	57.81	57.12	59.77	61.35	54.29	55.46	58.91	0.14
Al_2O_3	27.59	24.59	27.67	29.70	26.13	26.48	25.91	27.72	25.69	28.05	24.15	30.78	22.22	26.84	27.54	25.36	24.90	28.05	27.62	24.95	0.16
FeO	0.24	0.24	0.22	0.48	0.32	0.20	0.20	0.18	0.19	0.42	0.25	0.44	0.54	0.33	0.24	0.27	0.29	0.22	0.21	0.23	0.001
CaO	10.48	6.69	9.93	12.53	8.22	8.91	8.00	10.15	7.10	10.99	6.71	14.69	5.93	8.88	9.42	7.05	6.51	11.10	10.56	7.56	0.03
SrO	0.38	0.26	0.39	0.28	0.25	0.27	0.30	0.27	0.22	0.32	0.21	0.26	0.18	0.30	0.32	0.25	0.24	0.43	0.38	0.27	0.003
Na_2O	5.55	7.62	5.93	4.41	6.82	6.64	7.12	6.04	7.30	5.39	7.63	3.49	7.10	6.35	6.34	7.42	7.77	5.17	5.51	7.04	0.05
K_2O	0.23	0.50	0.24	0.17	0.39	0.35	0.38	0.26	0.45	0.20	0.60	0.11	1.47	0.29	0.30	0.44	0.48	0.22	0.32	0.80	0.004
Total	99.82	100.01	100.78	100.61	100.22	100.19	100.69	101.16	100.50	99.41	99.48	99.47	101.17	100.82	101.30	100.56	101.55	99.50	100.10	99.77	
Si	2.502	2.683	2.520	2.389	2.596	2.566	2.612	2.513	2.647	2.452	2.687	2.276	2.825	2.578	2.533	2.656	2.697	2.468	2.502	2.643	
Al	1.470	1.294	1.457	1.579	1.377	1.396	1.357	1.453	1.346	1.501	1.277	1.662	1.164	1.411	1.439	1.328	1.290	1.502	1.468	1.319	
Fe	0.009	0.009	0.008	0.018	0.012	0.007	0.007	0.007	0.007	0.016	0.009	0.017	0.020	0.012	0.009	0.010	0.011	0.009	0.008	0.009	
Ca	0.508	0.320	0.476	0.606	0.394	0.427	0.381	0.483	0.338	0.535	0.323	0.721	0.282	0.424	0.448	0.336	0.307	0.541	0.510	0.363	
Na	0.487	0.659	0.514	0.386	0.591	0.576	0.613	0.521	0.629	0.474	0.664	0.310	0.612	0.549	0.545	0.639	0.662	0.456	0.482	0.613	
K	0.013	0.028	0.014	0.010	0.022	0.020	0.021	0.015	0.025	0.011	0.034	0.006	0.083	0.017	0.017	0.025	0.027	0.013	0.018	0.046	
Sr	0.010	0.007	0.010	0.007	0.007	0.007	0.008	0.007	0.006	0.008	0.005	0.007	0.005	0.008	0.008	0.006	0.006	0.011	0.010	0.007	
Total	4.999	5.000	4.999	4.996	4.999	5.000	4.999	4.999	5.000	4.997	4.999	4.999	4.991	4.999	4.999	4.999	4.999	4.999	4.998	4.999	
An	50.4	31.8	47.4	60.5	39.1	41.7	37.5	47.4	34.1	52.4	31.6	69.5	28.9	42.8	44.3	33.6	30.8	53.6	50.5	35.6	
Ab	48.3	65.4	51.2	38.5	58.7	56.3	60.4	51.1	63.4	46.5	65.0	29.9	62.6	55.5	54.0	64.0	66.5	45.2	47.7	60.0	
Or	1.3	2.8	1.4	1.0	2.2	2.0	2.1	1.5	2.5	1.1	3.4	0.6	8.5	1.7	1.7	2.5	2.7	1.3	1.8	4.5	

bright - bright core; dark - dark core; inner - inner rim; outer - outer rim; total iron displayed as Fe^{2+}; An = 100Ca/(Ca+Na+K); Ab = 100Na/(Ca+Na+K); Or = 100K/(Ca+Na+K).

Table 5: Representative mica compositions

	1951 andesite		Plutonic enclave		PUB rim		1 σ
Sample	LAM23		LAM-10I		LAM-12		error
Analysis	17-13	30-19	16-53	16-57	29	30	
SiO_2	37.36	37.55	37.30	37.29	39.20	39.78	0.54
TiO_2	3.93	3.94	3.80	3.87	0.50	0.68	0.04
Al_2O_3	14.47	13.93	14.45	14.65	14.33	13.50	0.57
Cr_2O_3	0.02	0.03	0.05	0.02	0.12	0.15	0.02
FeO	16.02	15.24	14.51	15.58	11.58	11.51	0.28
MgO	14.71	14.90	15.84	14.71	19.60	19.56	0.17
MnO	0.18	0.19	0.14	0.20	0.11	0.11	0.01
Na_2O	0.90	0.90	0.90	0.92	1.11	0.57	0.10
K_2O	8.69	8.63	9.00	8.85	8.65	9.20	0.43
F	0.26	0.26	0.32	0.29	0.42	0.44	0.05
Cl	0.11	0.10	0.07	0.11	0.07	0.07	0.01
Total	96.64	95.72	96.39	96.53	95.69	95.62	
T Si	5.549	5.611	5.529	5.542	5.741	5.836	
T Al(IV)	2.451	2.389	2.471	2.458	2.259	2.164	
Total	8.000	8.000	8.000	8.000	8.000	8.000	
M1-3 Al(VI)	0.081	0.065	0.054	0.108	0.214	0.170	
M1-3 Ti	0.439	0.442	0.423	0.433	0.055	0.075	
M1-3 Cr	0.002	0.004	0.006	0.002	0.013	0.017	
M1-3 Fe	1.990	1.905	1.798	1.937	1.419	1.412	
M1-3 Mg	3.257	3.319	3.500	3.260	4.280	4.278	
M1-3 Mn	0.023	0.024	0.017	0.025	0.014	0.014	
Total	5.792	5.759	5.799	5.765	5.994	5.965	
Na	0.259	0.260	0.258	0.266	0.314	0.162	
K	1.647	1.646	1.702	1.678	1.616	1.723	
Total	1.906	1.906	1.960	1.945	1.930	1.885	
Mg-number	0.43	0.45	0.48	0.44	0.59	0.59	

total iron displayed as Fe^{2+}; Mg-number = Mg/(Mg+Fe).

Table 2.5

Table 2.6

Table 6: Representative oxides compositions

	1951 andesite			Diktytaxitic enclave							Plutonic enclave				PUB xenoliths				Shoshonite	1 σ error
Type	Phenocryst		Cr-sp in ol	Microhenocryst		Reaction rim phase of olivines				Cr-sp in ol	inclusion in amph cluster				Cr-sp inclusions				Phenocryst	
Sample	LAM-23		LAM-23	LAM-8H		LAM-8I				LAM-8I	LAM-10I				LAM-23		LAM-12		LAM-27D	
Analysis	002-23	002-24	036-26	011-20	017-55	012-33	015-15	015-17	016-43	008-72	004-13	004-23	004-24	004-25	2	3	1	10	050-55	
SiO_2	0.06	0.09	0.11	0.08	0.10	0.08	0.11	0.09	0.08	0.15	0.08	0.08	0.08	0.10	0.06	0.08	0.06	0.18	0.06	0.001
TiO_2	32.26	4.61	0.49	4.84	4.41	0.77	0.35	2.34	1.30	0.61	3.93	3.12	2.71	1.94	0.02	0.05	0.02	0.02	31.87	0.02
Al_2O_3	0.25	1.61	14.08	1.74	2.07	3.25	9.30	2.04	3.39	13.87	1.79	1.88	1.83	3.08	6.53	6.94	8.71	6.04	0.66	0.006
Cr_2O_3	0.05	0.16	47.38	3.72	2.24	28.72	37.70	7.90	18.12	41.31	5.90	10.24	7.23	12.90	55.40	57.38	59.48	53.96	0.08	0.009
Fe_2O_3	4.69	58.70	8.08	53.97	54.26	36.04	23.99	53.72	43.46	11.43	52.91	50.37	53.89	45.96	8.80	6.38	3.27	10.18	6.03	0.08*
FeO	57.65	33.42	16.07	33.41	33.04	23.97	22.38	28.30	24.82	22.19	32.75	31.96	31.60	30.02	18.10	17.79	17.11	18.96	54.14	
MgO	1.32	1.12	11.55	1.13	0.72	4.81	7.13	2.52	4.01	7.31	0.90	1.06	0.91	1.04	9.21	9.51	10.33	8.57	3.49	0.001
CaO	0.00	0.02	0.01	0.04	0.13	0.04	0.02	0.15	0.11	0.09	0.04	0.01	0.07	0.14	0.00	0.00	0.00	0.00	0.01	0.01
MnO	0.48	0.66	0.28	0.65	0.57	0.86	0.79	0.58	0.72	0.48	0.64	0.70	0.63	0.59	0.33	0.32	0.35	0.43	0.29	0.001
NiO	0.01	0.02	0.16	0.04	0.02	0.21	0.14	0.20	0.22	0.06	0.06	0.06	0.06	0.04	0.08	0.08	0.04	0.14	0.01	0.001
Norm. total	96.77	100.42	98.21	99.61	97.55	98.75	101.91	97.83	96.24	97.51	98.99	99.48	99.03	95.83	98.52	98.53	99.37	98.46	96.64	
Si	0.002	0.003	0.004	0.003	0.004	0.003	0.004	0.003	0.003	0.005	0.003	0.003	0.003	0.004	0.002	0.003	0.002	0.006	0.002	
Ti	0.924	0.130	0.012	0.137	0.128	0.021	0.009	0.067	0.037	0.016	0.112	0.088	0.077	0.057	0.000	0.001	0.000	0.001	0.897	
Al	0.011	0.071	0.543	0.077	0.094	0.139	0.368	0.091	0.150	0.556	0.080	0.083	0.082	0.141	0.264	0.279	0.343	0.246	0.029	
Cr	0.001	0.005	1.226	0.111	0.068	0.826	1.001	0.237	0.539	1.111	0.177	0.305	0.217	0.396	1.504	1.549	1.570	1.476	0.002	
Fe^{3+}	0.134	1.657	0.199	1.531	1.575	0.986	0.606	1.532	1.231	0.293	1.512	1.428	1.540	1.342	0.227	0.164	0.082	0.265	0.170	
Fe^{2+}	1.836	1.048	0.440	1.053	1.065	0.729	0.629	0.897	0.781	0.631	1.040	1.007	1.003	0.974	0.520	0.508	0.478	0.548	1.695	
Mg	0.075	0.063	0.564	0.064	0.041	0.261	0.357	0.143	0.225	0.371	0.051	0.060	0.052	0.060	0.471	0.484	0.514	0.442	0.195	
Ca	0.000	0.001	0.000	0.001	0.006	0.002	0.001	0.006	0.004	0.003	0.002	0.000	0.003	0.006	0.000	0.000	0.000	0.000	0.000	
Mn	0.015	0.021	0.008	0.021	0.019	0.027	0.022	0.019	0.023	0.014	0.021	0.022	0.020	0.019	0.010	0.009	0.010	0.012	0.009	
Ni	0.000	0.001	0.004	0.001	0.001	0.006	0.004	0.006	0.007	0.002	0.002	0.002	0.002	0.001	0.002	0.002	0.001	0.004	0.000	
Total charge	7.866	6.343	7.801	6.469	6.425	7.014	7.394	6.468	6.769	7.707	6.488	6.572	6.460	6.658	7.773	7.836	7.918	7.735	7.830	
Mg-number	0.04	0.06	0.56	0.06	0.04	0.26	0.36	0.14	0.22	0.37	0.05	0.06	0.05	0.06	0.48	0.49	0.52	0.45	0.10	
Cr-number	0.11	0.06	0.69	0.59	0.42	0.86	0.73	0.72	0.78	0.67	0.69	0.79	0.73	0.74	0.85	0.85	0.82	0.86	0.07	

Fe_2O_3 wt % calculated from AB_2O_4 spinel stoichiometry; number of ions calculated on the basis of total cations = 3; Mg-number = $Mg/(Mg+Fe^{2+})$; Cr-number = $100Cr/(Cr+Al)$.

*** 1 σ error refers to analytical error of FeOtot as FeO.**

Table 7: Representative olivine compositions

	1951 andesite				Diktytaxitic enclave				PUB xenoliths		Shoshonite	
Type	Xenocryst				Xenocryst				Dunite ol		Phenocryst	1 σ
Sample	LAM-10H			LAM-23	LAM-8I				LAM-23		LAM-27D	error
Analysis	016-61	021-10	021-11	002-21	016-27	016-28	016-29	016-30	4	5	050-56	
Position	core	core	core	core	core		rim		random	random	core	
SiO_2	40.84	40.40	40.77	39.52	40.48	40.50	40.02	39.54	40.94	41.20	40.26	0.08
FeO_T	11.45	12.56	10.66	16.70	11.04	11.77	14.17	17.12	8.05	7.96	13.93	0.03
MnO	0.16	0.18	0.15	0.49	0.18	0.23	0.40	0.59	0.12	0.12	0.23	0.001
MgO	47.51	46.05	47.95	43.26	48.18	47.70	45.77	43.11	50.70	51.09	45.73	0.04
CaO	0.14	0.13	0.14	0.38	0.19	0.12	0.07	0.05	0.01	0.00	0.16	0.01
NiO	0.20	0.18	0.26	0.35	0.28	0.31	0.28	0.21	0.40	0.41	0.26	0.001
Total	100.36	99.56	100.00	100.78	100.44	100.67	100.75	100.65	100.23	100.79	100.64	
Si	1.006	1.010	1.005	0.995	0.994	0.996	0.994	0.998	0.993	0.993	1.001	
Fe	0.236	0.263	0.220	0.352	0.227	0.242	0.294	0.361	0.163	0.161	0.290	
Mn	0.003	0.004	0.003	0.010	0.004	0.005	0.008	0.013	0.002	0.002	0.005	
Mg	1.745	1.716	1.762	1.624	1.763	1.748	1.695	1.622	1.833	1.836	1.694	
Ca	0.004	0.004	0.004	0.010	0.005	0.003	0.002	0.001	0.000	0.000	0.004	
Ni	0.004	0.004	0.005	0.007	0.005	0.006	0.006	0.004	0.008	0.008	0.005	
Total	2.999	2.999	2.999	2.999	2.998	2.999	2.999	2.999	3.000	3.000	2.999	
Fo	87.8	86.4	88.6	81.3	88.2	87.5	84.8	81.2	91.7	91.8	85.0	

number of ions calculated on the basis of total cations = 3; total iron displayed as Fe^{2+}; Fo = 100Mg/(Mg+Fe).

Table 2.7

Table 8: Representative pyroxene compositions

Type	Shoshonite		Diktytaxitic enclave				PUB		1 σ error	
	Cpx phenocryst		Cpx xenocryst		ol reaction rim phase (Opx)		PUB reaction rim phase (Opx)			
Sample	LAM-27D		LAM-18		LAM-8I		LAM-12		Cpx	Opx
Analysis	70	71	2	3	015-18	016-32	20	24		
SiO_2	51.62	51.30	53.15	51.23	55.96	55.89	54.09	55.67	0.08	0.09
TiO_2	0.68	0.80	0.27	0.49	0.08	0.06	0.02	0.01	0.004	0.001
Al_2O_3	2.99	3.19	1.85	3.64	0.36	0.51	3.86	0.20	0.006	0.003
Cr_2O_3	0.07	0.07	0.48	0.30	0.06	0.04	0.39	0.03	0.001	0.001
FeO	6.34	5.82	4.40	5.25	12.35	12.17	9.42	11.86	0.03	0.03
MnO	0.16	0.15	0.12	0.11	0.79	0.78	0.32	0.79	0.001	0.001
MgO	15.76	15.68	17.16	15.76	30.56	30.79	30.96	30.14	0.02	0.03
CaO	21.21	21.46	21.40	21.96	0.41	0.38	0.98	1.17	0.02	0.01
NiO	0.03	0.02	0.25	0.33	0.04	0.06	0.20	0.19	0.001	
Na_2O	0.35	0.35	0.01	0.01					0.001	
Total	99.22	98.85	99.09	99.08	100.61	100.69	100.26	100.05		
T Si	1.949	1.945	1.983	1.939	1.976	1.971	1.931	1.975		
T Al(IV)	0.051	0.055	0.017	0.061	0.007	0.011	0.069	0.004		
T Fe^{3+}	0.000	0.000	0.000	0.000	0.011	0.010	0.000	0.020		
total	2.000	2.000	2.000	2.000	1.994	1.992	2.000	2.000		
M1-2 Al(VI)	0.015	0.016	0.024	0.020	0.000	0.000	0.012	0.000		
M1-2 Ti	0.019	0.023	0.007	0.014	0.002	0.002	0.000	0.000		
M1-2 Cr	0.001	0.001	0.007	0.004	0.001	0.001	0.006	0.000		
M1-2 Fe^{3+}	0.000	0.000	0.000	0.000	0.000	0.000	0.000	0.010		
M1-2 Fe^{2+}	0.200	0.184	0.137	0.166	0.354	0.349	0.281	0.322		
M1-2 Mn	0.005	0.005	0.004	0.004	0.023	0.023	0.010	0.024		
M1-2 Mg	0.887	0.886	0.955	0.889	1.609	1.618	1.648	1.594		
M1-2 Ca	0.858	0.871	0.856	0.891	0.015	0.014	0.038	0.044		
M1-2 Na	0.013	0.013	0.009	0.012						
M1-2 Ni	0.001	0.000	0.000	0.000	0.001	0.002	0.006	0.005		
Total	2.000	2.000	2.000	2.000	2.006	2.008	2.000	2.000		
En	45.6	45.6	49.0	45.7	80.9	81.3	83.8	80.1		
Wo	44.1	44.9	43.9	45.8	0.8	0.7	1.9	2.2		
Fs	10.3	9.5	7.0	8.5	18.3	18.0	14.3	17.7		

number of ions calculated on the basis of 6 oxygen;
En = 100Mg/(Ca+Mg+Fe^{2+}); Wo = 100Ca/(Ca+Mg+Fe^{2+});
Fs = 100Fe^{2+}/(Ca+Mg+Fe_{2+}).

Table 2.8

Table 9: Representative glass compositions

Sample	Diktytaxitic enclave				Plutonic enclave		1 σ error
	LAM-8I				LAM-10I		
Analysis	012-39	014-58	015-11	017-60	#28	#29	
SiO_2	75.93	77.76	76.08	73.29	78.27	76.96	0.43
Al_2O_3	13.01	13.13	13.14	15.90	12.56	12.96	0.16
Na_2O	3.12	2.61	3.31	5.05	2.16	2.27	0.06
MgO	0.07	0.03	0.07	0.04	0.09	0.07	0.01
K_2O	6.36	5.82	6.34	4.49	5.91	5.69	0.06
CaO	0.45	0.49	0.39	1.51	0.69	0.71	0.02
FeO	0.69	0.86	0.82	0.50	0.35	0.44	0.06
P_2O_5	0.02	0.02	0.02	0.02	0.02	0.01	0.01
TiO_2	0.16	0.13	0.13	0.11	0.11	0.12	0.001
MnO	0.03	0.04	0.03	0.01	0.01	0.02	0.001
Cl	0.12	0.15	0.09	0.04	0.01	0.01	0.01
F	0.02	0.00	0.00	0.01	0.00	0.01	0.01
Total	99.98	101.02	100.43	100.98	100.17	99.29	

Table 2.9

CHAPTER 3

Open-System Processes Revealed by Melt Major Element Inversion from Calcic Amphiboles

J. ZHANG*, M. C. S. HUMPHREYS, G. F. COOPER, J. P. DAVIDSON, C. G. MACPHERSON

DEPARTMENT OF EARTH SCIENCES, UNIVERSITY OF DURHAM, DURHAM, DH1 3LE, UK

*Corresponding author. E-mail: jing.zhang5@durham.ac.uk

ABSTRACT

Calibrations of back-calculated melt major element compositions (SiO_2, TiO_2, Al_2O_3, FeO, MgO, CaO and K_2O in weight percent, wt %) with calcic amphibole formula proportions ± temperature are provided, and chemometric empirical equations are derived. The calibrations are achieved with data from 130 published experiments, which are conducted on a wide range of pressure-temperature conditions (200-2,500 MPa; 750-1,100 °C) on melts of basanitic-rhyolitic compositions. The experiments produce wide range of amphibole chemical variations, which allow us to review the crystallization conditions of different amphibole species. The crystallization of calcic amphiboles generally follow the trend of liquid line of descent, pargsite and magnesiohastingsite are prone to crystallize in high-temperature, mafic melt; while tschermakite and magnesiohornblende tend to crystallize in low-temperature, felsic melt, despite of a significant overlapping in intermediate thermal and compositional conditions. The independent test with another 74 experiments demonstrates robust accuracy of the chemometric equations, and improved precision compared to previous pressure-dependent models (Ridolfi & Renzulli, 2012). We apply the chemometric equations to amphiboles from pumice clasts of the Ongatiti ignimbrite and the yielded melt compositions are in good agreement with the measured matrix glass compositions, suggesting the equilibrium between amphibole rims and the glassy melt is achieved. The predicted melt compositions from the amphibole cores which display large compositional variation and disequilibrium textures show large variation, and we propose this variation is probably due to different degrees of equilibration between amphiboles recycled from crystal mushes and evolved melts. We also apply the model to amphiboles from plutonic xenoliths in Grenada, and the most silicic predicted melt compositions are in agreement with the most silicic melt inclusions hosted in those plutonic xenoliths. We suggest that the variation in the predicted melt compositions and melt inclusions evidence either the equilibration of the mafic cumulates with a later recharged relatively evolved melt or in situ melt evolution through extensive crystallization of the cumulate mineral phases.

KEY WORDS: Calcic amphibole; Chemometrics; Melt compositions; Multiple regression; Ongatiti ignimbrite; Plutonic xenoliths.

This chapter is prepared as a paper manuscript to be submitted to *Contributions to Mineralogy and Petrology* or *American Mineralogist*.

3.1. INTRODUCTION

Amphibole is a common mineral phase present in water-bearing arc magmas. Importantly, according to existing experimental studies, the crystallization of amphibole can occur over a large pressure (P) – temperature (T) range from melts of basanitic-rhyolitic compositions (0.2 -2.5 GPa, 750-1,100 ºC; details see below; **Fig. 3.1a-d**). The crystal chemistry of amphibole is sensitive to various magma intensive variables (e.g. pressure, temperature, oxygen fugacity fO_2), melt volatile contents and melt compositions (Ridolfi *et al.*, 2008; Ridolfi & Renzulli, 2012; Ridolfi *et al.*, 2010). Amphibole-related thermobarometry has been well represented over decades (e.g. Anderson & Smith, 1995; Blundy & Cashman, 2008; Blundy & Holland, 1990; Ernst & Liu, 1998; Hammarstrom & Zen, 1986; Holland & Blundy, 1994; Hollister *et al.*, 1987; Krawczynski *et al.*, 2012; Molina *et al.*, 2015; Putirka, 2016; Putirka, 2008; Ridolfi & Renzulli, 2012; Ridolfi *et al.*, 2010; Schmidt, 1992). Amphibole-related thermometer models with reasonable error estimates in the range 22-45 °C are generally accepted (Molina et al., 2015; Putirka, 2016; Ridolfi & Renzulli, 2012; Ridolfi et al., 2010). In the past, the calibrations of amphibole-related barometers were mainly based on the presence of extensive equilibrium assemblage, e.g. the Al-in-hornblende barometer requires the presence of quartz + alkali feldspar + plagioclase + hornblende + biotite + Fe-Ti oxides + titanite + melt + fluid (Anderson & Smith, 1995; Hammarstrom & Zen, 1986; Hollister *et al.*, 1987); while more recently attempts are to make amphibole-only barometers (Ridolfi & Renzulli, 2012; Ridolfi *et al.*, 2010). However, applying these amphibole-only barometers should be treated with caution since a large offset (e.g. up to 1,100 MPa) between predicted pressure and experimental pressure still exists after numerous recalibrations (Erdmann *et al.*, 2014; Putirka, 2016; Shane & Smith, 2013). This has led to a conclusion that amphibole crystal chemistry (e.g. tetrahedral Al content, Al_T) is more sensitive to temperature and melt compositions, and less dependent on pressure (Putirka, 2016).

Recently, the links between amphibole crystal chemistry and anhydrous melt compositions have been described by empirical chemometric equations provided by Ridolfi & Renzulli (2012); see Eqs 5-11 therein). Those pressure-dependent empirical relationships enable us to calculate melt SiO_2, TiO_2, Al_2O_3, FeO, MgO, CaO, K_2O contents from knowledge of amphibole major element formula proportions and pressure. However, for natural amphiboles crystallized from magma plumbing systems, pressure is an unknown parameter, and using the pressure value estimated from amphibole-only barometer models (e.g. Ridolfi & Renzulli, 2012) could cause large uncertainties in the inferred melt compositions. For example, we observe large offset between the predicted and experimental melt MgO content, using predicted amphibole crystallization pressure > 1,000 MPa yielded from the amphibole-only barometer of Ridolfi & Renzulli (2012) (see below). The strong exponential correlation between the predicted melt MgO and pressure > 1,000 MPa demonstrates the fundamental problem of including pressure as a calibration parameter. Furthermore, although test results from Erdmann *et al.* (2014)'s study demonstrate that Ridolfi & Renzulli (2012)'s model yields reasonable melt SiO_2 content estimates for calcic amphiboles crystallized from melts with 55-75 wt % SiO_2 content, when we apply the equation to calcic amphiboles crystallized from more mafic melts, this equation gives overestimation of the melt SiO_2 content up to 15 wt % (see below). Different degrees of disagreements between the experimental melt compositions and predictions also exist in calculating melt TiO_2, FeO, CaO and K_2O contents (see below).

In order to improve the reliability of the amphibole-melt chemometric equations and better constrain the relative importance of temperature and melt compositions in controlling the crystal chemistry of calcic amphiboles, we compile results from previously published experimental studies. Using this dataset we first review the crystallization conditions of each specific calcic amphibole species, and then re-examine the amphibole-melt compositional correlations using multiple regression analysis. The accuracy of the recalibrated chemometric equations are demonstrated by testing with experimental data independent from those used in the calibrations. Finally, the implications of applying the recalibrated chemometric equations to calcic amphiboles from igneous systems are discussed.

3.2. SELECTING P-T-X DATA FROM LITERATURE

Experimental data from Library of Experimental Phase Relations (LEPR; Hirschmann *et al.*, 2008) and other studies are considered. We first split the data into two groups (**Fig. 3.1a, c**): one group for calibration (n=130; data from Adam & Green, 1994; Alonso-Perez *et al.*, 2009; Barclay & Carmichael, 2004; Bogaerts *et al.*, 2006; Costa *et al.*, 2004; Dalpé & Baker, 2000; Gardner *et al.*, 1995; Green & Pearson, 1985; Grove *et al.*, 2003; Hilyard *et al.*, 2000; Klein *et al.*, 1997; Martel *et al.*, 2013; Moore & Carmichael, 1998; Nandedkar, 2014; Nekvasil *et al.*, 2004; Nicholls & Harris, 1980; Pichavant *et al.*, 2009; Pichavant *et al.*, 2002; Rutherford & Devine, 2003; Sato *et al.*, 2005; Scaillet & Evans, 1999; Sisson, 1994; Sisson & Grove, 1993; Tiepolo *et al.*, 2000); and one group for test (n= 74; data from Adam & Green, 2006; Adam *et al.*, 1993; Blatter & Carmichael, 2001; Carroll & Wyllie, 1989; Ernst & Liu, 1998; Fujinawa & Green, 1997; Grove *et al.*, 1997; Holtz *et al.*, 2005; Kawamoto, 1996; Naney, 1983; Patino-Douce & Beard, 1995; Prouteau & Scaillet, 2003; Prouteau *et al.*, 1999; Skjerlie & Johnston, 1996; Springer & Seck, 1997; Xiong *et al.*, 2005). The split of the experimental data from different references is random, and the two groups are largely overlapping in experimental running P-T conditions, melt compositions and also the crystal chemistry of experimentally produced amphiboles, demonstrating good representativeness of the test group. A part of the calibration group overlaps those used in Ridolfi & Renzulli (2012)'s initial calibrations (**Table 3.1**), whereas all the data from the test group were not employed by Ridolfi & Renzulli (2012) and Erdmann *et al.* (2014)'s study before. Therefore, the test group can also be used in testing Ridolfi & Renzulli (2012)'s results. Details of the selected experimental running conditions, materials and products are listed in **Table 3.1**. We then use two criteria to filter the data: 1) the amphibole compositions must be calcic according to International Mineralogical Association (IMA; Hawthorne *et al.*, 2012); 2) there must be amphibole-melt equilibrium as tested using the Fe-Mg exchange coefficient.

First, all the selected amphibole compositional data from literature are recalculated from wt% oxide to formula proportions (atoms per formula unit/apfu), following the amphibole stoichiometry calculation procedure (13eCNK) recommended by IMA (Leake *et al.*, 1997). Si, Al, Ti, Cr, Fe, Mn, Mg are allocated to the tetrahedral (T) and small octahedral (M1-3) sites and adjusted to 13 cations, Fe^{3+} and Fe^{2+} proportions are determined separately by charge balance; and Ca, Na and K are allocated to large octahedral (M4) and vacant/partially-filled (A) sites. According to the nomenclature recommended by IMA (Hawthorne *et al.*, 2012), our compiled data are classified as calcic (Ca_{M4}>1.5 apfu) and non-calcic (low-Ca) amphiboles; the former is subcategorized into pargasite (Parg), magnesiohastingsite (MgHst), kaersutite (Kaer), tschmakite (Tsch) and magnesiohornblende (MgHbl) (**Table 3.1**; **Fig. 3.2**). Only calcic amphiboles are considered in this study, and the non-calcic amphiboles and those amphiboles that fail to meet the standard of stoichiometry calculation are excluded.

Second, following Roeder & Emslie (1970) and Putirka (2016), we employ the Fe-Mg exchange coefficient $K_D(\text{Fe-Mg})^{\text{Amph-melt}}$ (simply K_D) to test whether the equilibrium are achieved between amphiboles and coexisting melts during the experiments. K_D, expressed as:

$$K_D = \frac{X_{FeOt}^{Amph}}{X_{MgO}^{Amph}} \Big/ \frac{X_{FeOt}^{Melt}}{X_{MgO}^{Melt}}$$

(FeOt is total Fe as FeO) is independent of temperature, pressure and co-crystallizing mineral phases (Putirka, 2016; Roeder & Emslie, 1970). Like Putirka (2016), we consider K_D values in the range of 0.28±0.11 as test for equilibrium. Any experimentally produced amphibole and melt compositions that fail to sit within this range are considered inappropriate for recalibration and are removed from the original dataset (**Fig. 3.3**). The samples that fail to meet this test for equilibrium do not fall into any particular range of experimental running P-T conditions or melt chemistry (**Fig. 3.1**)

3.3. CALCIC AMPHIBOLE CRYSTALLIZATION CONDITIONS

Calcic amphiboles selected from the experimental studies (Parg, MgHst, Kaer, Tsch and MgHbl), display large compositional variability ($1.2 < Al_T < 2.4$; $0 < (Na+K)_A < 1.0$) over the wide range of P-T-melt chemistry (X) conditions (200-2,500 MPa; 750-1,100 °C; basanitic-rhyolitic melt compositions; **Fig. 3.1a-d**). This enables us to review the crystallization conditions of different amphibole species and constrain the relative importance of P-T-X in controlling amphibole crystal chemistry. The relationships between amphibole compositions and experimental running conditions and melt compositions are illustrated in **Fig. 3.1e-f**. The selected experiments generally represent evolving amphibole crystallization conditions in a magmatic environment, from hot, mafic melt (950-1,100 °C, c.a. 40-60 wt % SiO_2) to cooler, felsic melt (800-950 °C, c.a. 60-78 wt % SiO_2) over a large pressure variation range (200-2500 MPa; **Fig. 3.1c-d**). The relationship between temperature and melt SiO_2 content of the selected experiments generally follows the trend of liquid line of descent (**Fig. 3.1c-d**). However outliers decoupled from the relationship are also present, for example, in Sisson (1994)'s experiments, two MgHbl crystallize from rhyolitic melts (77.4-79.2 wt % SiO_2) under temperature up to 1,050 °C. The crystallization of calcic amphiboles occurs over a large temperature range (750-1,050 °C) at low pressure conditions (200-400 MPa), while under high pressure conditions (2,000-2,500 MPa), the crystallization of calcic amphiboles are linked to the highest temperatures (1,050-1,100 °C; **Fig. 3.1b**). The P-T window of calcic amphibole crystallization is outlined in **Fig. 3.1b**.

Parg crystallization occurs from the hottest (1,100 ºC) and most mafic (basanitic) melt with c.a. 40 wt % SiO_2, and continues to intermediate melt at 900-950 ºC (**Fig. 3.1d, 3.4**). MgHst crystallizes in basaltic to dacitic melts at ~900-1,050 ºC (**Fig. 3.1d, 3.4**), as well as (rarely) at lower temperature (800-850 ºC) in more evolved melts with >65 wt% SiO_2. Kaer crystallizes from melts with similar SiO_2 and Al_2O_3 contents to those MgHst-bearing melts, but with higher TiO_2 and lower CaO and MgO contents (**Fig. 3.4a-b, d-e**). Tsch crystallizes primarily at lower temperatures (800-950 ºC) in dacitic-rhyolitic melts with >60 wt % SiO_2 (**Fig. 3.1d**) and decreasing Al_2O_3, TiO_2, CaO and MgO (**Fig. 3.4a-b, d-e**). MgHbl only crystallizes from the most silicic melt with c.a. > 70 wt % SiO_2, over a range of temperatures.

The compiled dataset also demonstrates that MgHst, MgHbl and Tsch can all crystallize at the same pressure (e.g. 200 MPa; **Fig. 3.1b**). The poor correlations between pressure and amphibole tetrahedral Al content (Al_T) demonstrate the weak control by pressure on amphibole crystal chemistry (Putirka, 2016); in contrast, amphibole Al_T are strongly correlated with melt SiO_2 and TiO_2 contents (e.g., **Fig. 3.1f**), and intermediately correlated with temperature (**Fig. 3.1e**), suggesting that melt compositions and temperature are more important controlling factors to amphibole compositions than pressure. The stronger correlation of amphibole Al_T against melt SiO_2 content than against temperature gives us a hint that melt chemistry is probably more important than temperature in controlling amphibole crystal chemistry. However, the melt chemistry and temperature from the selected experiments are also inter-correlated, we cannot further quantify this issue here, and we will come back to this question later.

3.4. MULTIPLE REGRESSION ANALYSIS

In order to retrieve the correlations between melt major element compositions and amphibole crystal chemistry and temperature, we carry out a multiple regression analysis (MR) using the Data Analysis functions in Microsoft Excel. The MR analysis is a way of predicting values (dependent variables) based on multiple input parameters (independent variables). The SiO_2, TiO_2, Al_2O_3, FeO, MgO, CaO, K_2O contents in the melt, normalized to 100% anhydrous, are treated as dependent variables, respectively. For TiO_2, FeO, MgO, CaO, we also try with their values in natural logarithmic scale (e.g. $lnTiO_2$) as dependent variables. For independent variables, we try both amphibole-only and amphibole+T approaches. This enables us to decipher how significant is the role of temperature in modifying the recalibration results, and thus infer the effect of temperature on controlling amphibole crystal chemistry. Amphibole formula proportions including tetrahedral site Si (Si_T), M1-3 site Al

(Al_{VI}), Fe^{3+}, Mg, Ti and Fe^{2+}, and M4 site Ca (Ca_{M4}), and A site Na (Na_A), are considered as dependent variable choices. Tetrahedral site Al (Al_T), which has commonly been treated as one of the key parameters in previous amphibole thermobarometry studies, is not considered, in order to avoid the issue of multicollinearity. This is because amphibole SiO_2 or Si_T are strongly correlated with melt SiO_2 content (e.g. **Fig. 3.1f**), while Al doesn't really correlate with melt Al_2O_3, and Al_T strongly depends on the silica content of amphibole according to stoichiometric calculations ($Si_T + Al_T = 8$ apfu). M4 site Na is also not considered for the same reason (Ca + Na = 2 apfu in M4 site). M1-3 site Cr and Mn and A site K are also not considered due to their minor abundances in amphibole.

The output of each MR analysis is given as the intercept and the coefficients of nominated independent variable, on which basis a multiple regression function can be derived (**Table 3.2**). For example, *Eq. 1* used for calculating the SiO_2 content in the melt is written as:

$$SiO_2\ (wt\ \%) = -239.3567 - 0.0308T + 36.6276Si + 22.0010Al_{VI} + 26.6213Fe^{3+} + 5.6001Fe^{2+} + 48.2461Ti + 31.8979Ca + 14.9367Na_A \quad (Eq.\ 1)$$

Evaluation of the function is based on parameters including the coefficient of determination (R^2), standard error of the estimate (SE), number of objects/observations (N), and confidence of the coefficients for each independent variable and constant (p-value). A correlation that we deem to be statistically significant is reflected by $N \geq 30$, $R^2 \geq 0.6$ and p-value of each determined coefficient < 0.01. In **Table 3.2**, we use the normal font to denote that the p-values of the MR-derived independent variables and the constants are < 0.01 (>99% confidence), the bold font to denote that the p-values of the corresponding independent variable/constant are 0.01-0.03 (97-99% confidence), and the bold italic font to denote >0.03 p-value (<97% confidence). The MR analysis is performed following a trial-and-error procedure: all independent variables mentioned above were included in the MR analyses in the first place, then the ones with p-value over 0.03 were progressively removed until all/most of the remaining independent variables and constants are statistically significant (<0.03 in our calibrations).

To test the accuracy of the results of the MR analysis, we apply the MR-derived equations to the data of the test group. Agreement with the experimental melt compositions (r^2) and standard error of the estimate (se) are calculated and compared with the results of the MR analysis.

3.5. RESULTS

The experimental melt major element compositions can in general be linked with amphibole formula components ± experimental run temperature, with moderately robust R^2 and reasonable SE (**Table 3.2**). First of all, except for prediction of melt Al_2O_3 content, adding temperature as one of the independent variables in the calibrations of other melt major elements improves the precision and accuracy of the MR analyses slightly as revealed by decreasing SE and se, respectively (see below);, but the enhancement is very insignificant (e.g. decrease of SE from 0.46 to 0.41 in the prediction of lnMgO, *Eq. 11-12* and corresponding decrease of se from 1.47 to 1.07 wt %), and the confidence of other independent variables may be compromised by adding T (e.g. compare *Eq. 9* with *Eq. 10*, the p-value of the constant, Al_{VI}, Mg, Fe^{3+}, Fe^{2+} and Ca in *Eq. 9* are >0.01). Second, our independent variables in the MR analyses are the 13eCNK stoichiometric calculation results ± temperature, and our MR analyses results demonstrate the variable significance of amphibole major element formula proportions as the independent variables. In contrast, Ridolfi & Renzulli (2012)'s study uses the total formula proportions of the major elements unassigned to different crystallographic sites, e.g. Al_{total} instead of Al_T and Al_{VI}, Fe_{total} instead of Fe^{2+} and Fe^{3+}, Na_{total} instead of Na_{M4} and Na_A. Although the stoichiometric calculation based on charge-balance method may generate large errors in the calculated Fe^{2+}/Fe^{3+} ratio, our MR analyses results demonstrate the different significance of the major element, or even the same element in different oxidation state (Fe^{3+} may be removed from the MR analyses due to large p-values, but Fe^{2+} may be still significant for the MR analysis, e.g. *Eq. 3-4* for predicting melt SiO_2 content).

Melt SiO_2 content can be predicted with two main groups of independent variables robustly: Si + Al_{VI} + Fe^{3+} + Fe^{2+} + Ti + Ca + Na_A ± T (Mg-absent group; *Eq. 1-2*; **Fig. 3.6a-b**), and Si + Mg + Fe^{2+} + Ti + Ca + Na_A ± T (Al_{VI}, Fe^{3+}-absent group; *Eq. 3-4*). The estimates yielded with the two different groups of independent variables are also in excellent agreement (R^2 = 0.992). The predicted melt SiO_2 range of the test data points (n=74), which largely overlaps the experiments used for calibration, also reproduce the experiments very well, except two outliers from Xiong *et al.* (2005) (**Fig. 3.6a-b**). Moreover, the new equations (*Eq. 1-4*) are able to reproduce samples with low experimental melt SiO_2 content (<55 wt%, data from Adam & Green, 2006; Adam & Green, 1994; Adam *et al.*, 1993; Dalpé & Baker, 2000; Fujinawa & Green, 1997) which failed to be reproduced with Ridolfi & Renzulli (2012)'s equation (**Fig. 3.6a-b**).

Similarly, melt TiO_2 content in natural logarithmic scale ($lnTiO_2$) can also be predicted with two main groups of independent variables robustly: Si + Al_{VI} + Fe^{3+} + Fe^{2+} + Ti + Ca + Na_A ± T (Mg-absent group; *Eq. 5-6*; **Fig. 3.6c-d**), and Si + Mg + Fe^{2+} + Ca + Na_A ± T (Al_{VI}, Fe^{3+}, Ti-absent group; *Eq. 7-8*). The Mg-absent group works slightly better than the Al_{VI}, Fe^{3+}, Ti-absent group (R^2 = 0.843, 836, respectively; *Eq. 5-6*). But in general, the calibration results and test results are in excellent agreement with each other (R^2 = 0.986), and with experimental melt TiO_2 content (**Fig. 3.6c-d**). No obvious outliers is present in the test data points. Our equations also manage to reproduce the TiO_2 content of both calibration and test data points from the low-melt SiO_2 content experiments, where Ridolfi & Renzulli (2012)'s equation generates a large offset (**Fig. 3.6c-d**).

Melt FeO content in natural logarithmic scale (lnFeO) can only be predicted with one group of independent variables: Si + Al_{VI} + Mg + Fe^{3+} + Fe^{2+} + Ca ± T (Ti, Na_A-absent group; *Eq. 9-10*; **Fig. 3.6e-f**). However, the calibrations are less robust than the results of predicting SiO_2 and TiO_2 (R^2 = 0.767, 0.728, respectively; *Eq. 9-10*). The accuracy of our FeO calibrations is not significantly improved compared to the Ridolfi & Renzulli (2012)'s equation as illustrated in **Fig. 3.6e-f**, but the prediction of the test and calibration data points from the low-melt SiO_2 content experiments as mentioned above are apparently improved.

As mentioned earlier, pressure plays an important role as an independent variable in Ridolfi & Renzulli (2012)'s model of estimating melt MgO content (**Fig. 3.5**). The effect of pressure in misrepresenting melt MgO content is most obvious when the pressure is above 1 GPa calculated using Ridolfi & Renzulli (2012)'s barometer model (**Fig. 3.5**). Under these conditions, the predicted melt MgO is exponentially controlled by pressure, and the prediction can give overestimations of melt MgO up to several orders of magnitude higher (**Fig. 3.5**). Even when the calculated pressure is <1 GPa and in good agreement with the experiment pressure setup, the Ridolfi & Renzulli (2012)'s model still produce significant scatter which are in disagreement with the melt MgO content (**Fig. 3.5, 3.6g-h**). In contrast, the results of our MR analyses suggest that the melt MgO content in natural logarithmic scale (lnMgO) can be predicted with the independent variables of Si + Al_{VI} + Mg ± T robustly (Si, Al, Mg-group; *Eq. 11-12*; **Fig. 3.6g-h**). Our MgO predictions are in much greater agreement with calibration (R^2 = 0.846, 0.798, respectively; *Eq. 11-12*; **Fig. 3.6g-h**), compared to Ridolfi & Renzulli (2012)'s model which uses all amphibole major elements and pressure as independent variables, and this is confirmed with the comparable *se* calculated from the test data points.

When the pressure is above 1 GPa as calculated using Ridolfi & Renzulli (2012)'s barometer, Ridolfi & Renzulli (2012)'s equation for predicting melt CaO content produces a significant proportion of negative melt CaO contents (**Fig. 3.6i-j**). Our recalibrations improve the accuracy of predicting melt CaO content significantly (R^2 = 0.715-0.738; *Eq. 13-16*; **Fig. 3.6i-l**). We derive two groups of calibrations using CaO content and lnCaO, respectively. The former is related to Si + Fe^{3+} + Fe^{2+} + Ti + Na_A ± T (Al_{VI}, Mg, Ca-absent group, *Eq. 13-14*; **Fig. 3.6i-j**), while the latter is linked with Si + Mg + Fe^{3+} + Fe^{2+} + Ca ± T (Al_{VI}, Ti, Na_A-absent group; *Eq. 15-16*; **Fig. 3.6k-l**). The two groups of calibrations are basically in agreement with each other (R^2 = 0.860) and both can reproduce the experiments with standard error of estimate ≤ 1.56 wt %. However, calibrations with CaO also can

give negative estimates when the melt CaO content is low and underestimations at high melt CaO contents (*Eq. 13-14*; **Fig. 3.6i-j**), therefore we recommend using *Eq. 15-16* to calculate melt CaO content although their SE are slightly higher than *Eq. 13-14* (1.50 and 1.56 for *Eq. 15* and *Eq. 16*).

Ridolfi & Renzulli (2012)'s equation in predicting melt K_2O content fails to reproduce the test and calibration data points from the low-melt SiO_2 content experiments as mentioned above (**Fig. 3.6m-n**). Our recalibrations produce moderate correlations (R^2 = 0.628-0.652; SE = 0.70-0.72 wt %) with K_2O content in the experimental melt, using Si + Al_{VI} + Mg + Fe^{2+} + Ti + Ca + Na_A ± T (Fe^{3+} - absent group; *Eq. 17-18*; **Fig. 3.6m-n**). However, Eq. 17-18 underestimate melt K_2O at high melt K_2O contents (> 4.0 wt %) slightly.

For predicting melt Al_2O_3 content, our best calibration is achieved with Al_{VI} + Mg + Fe^{2+} + Ti + Na_A (T, Si, Fe^{3+}, Ca-absent group, *Eq. 19*; **Fig. 3.6o**), while Si and temperature are insignificant. However, our calibration does not significantly improve the accuracy of the predicted melt Al_2O_3 content (R^2 = 0.604; SE = 1.21 wt %), compared to Ridolfi & Renzulli (2012)'s model.

Na_2O content in the melt does not correlate with amphibole crystal formula proportions ± T ± P from either this study or Ridolfi & Renzulli (2012)'s study and we therefore do not attempt to predict melt Na_2O. As suggested by Ridolfi & Renzulli (2012), this may be due to the Na loss in glass caused by beam damage during electron probe microanalysis (e.g. Humphreys *et al.*, 2006b), which increases the analytical uncertainties of Na_2O and hinders robust multiple regression analysis.

3.6. DISCUSSION

3.6.1. Accuracy and precision of the chemometric equations

The estimates of precision and accuracy of the recalibrated chemometric equations are given as the standard error of estimate (SE) generated in the MR analyses, and in the application of test data (se), respectively (**Table 3.2**). For predicting melt TiO_2, FeO, MgO and CaO contents, since our calibrations are based on the values in natural logarithmic scale (ignore *Eq. 13-14*), the SE are therefore also given as the precision in natural logarithmic scale (SE ≤ 0.46). We calculate the corresponding melt contents for each data point and then give estimates of the real precision in wt % (**Table 3.2**). It is worth noting that in this scenario, the SE in wt % is strongly dependent on the range of the calculated melt content (e.g. SE[TiO_2] = SE[lnTiO_2] × TiO_2 wt %), and they are given here for the readers to make comparisons with the estimated se from the test data.

The *se* values for the test data are generally larger than SE for the calibration dataset, except for estimating melt TiO_2 in natural logarithmic scale. The TiO_2 variation range of the test experiments is slightly smaller than the calibration experiment group, and it probably accounts for the smaller calculated se of the test experiment group (± 0.45-0.54 wt %) relative to SE derived in the MR analyses (± 0.57-0.60 wt %). Our temperature-independent equations for estimating melt SiO_2 content have an absolute precision of better than < ± 3.6 wt % (*Eq. 2, 4*), and adding temperature into the independent variables can improve the precision slightly to ± 3.4 wt % (*Eq. 1, 3*). The calibrations of melt K_2O and Al_2O_3 contents are least robust among all calibrated elements (R^2 = 0.63-0.65, 0.60, respectively; *Eq. 17-19*). For melts with < 5.0 wt % K_2O, our precision of estimating melt K_2O content without temperature is ± 0.72 wt % (± 0.65 wt % for temperature-dependent equation, *Eq. 17*). While for melts with 11.4-21.5 wt % Al_2O_3, our precision of estimating melt Al_2O_3 content without temperature is ± 1.21 wt % (*Eq. 19*).

3.6.2. P-T-X control over amphibole crystal chemistry

Experiments conducted on a wide range of P-T-X conditions suggest that calcic amphiboles can only crystallize within a certain P-T window (**Fig. 3.1b**). Furthermore, the melt compositions and temperature from the experiments carried out within this P-T window largely follow a trend of liquid

line of descent except a few outliers (e.g. **Fig. 3.1d**; Sisson (1994). This suggests that the P-T window outlines the crystallization conditions of calcic amphiboles in natural igneous systems (**Fig. 3.1b**). More specifically, Parg and MgHst tend to crystallize in high-temperature, mafic melts and in contrast, Tsch and MgHbl are prone to crystallize in low-temperature, felsic melts (**Fig. 3.1d**).

Using pressure-independent chemometric equations derived from multiple regression analyses from this study yields improved precision in calibrating the major element compositions of melts from which calcic amphiboles are crystallized, relative to (Ridolfi & Renzulli, 2012)'s model. This reaffirms previous recognition that the dependence of amphibole crystal chemistry on pressure is less significant than melt compositions and temperature (Putirka, 2016). Moreover, the results of our multiple regression analyses demonstrate that temperature has a minor impact on improving the precision of calibrating melt compositions with amphibole crystal chemistry. This also explains the presence of MgHbl in rhyolitic melt, but at 1,050 ºC (Sisson, 1994). We believe this suggests that temperature is less important than melt compositions in controlling amphibole crystal chemistry; this is a major advantage in applying our results to natural systems, in which crystallisation temperature is commonly not known.

3.7. IMPLICATIONS

Here we present two case studies to demonstrate the implications of applying our chemometric equations to volcanic and plutonic amphiboles: amphiboles in pumice clasts from the Ongatiti ignimbrite, and in plutonic nodules from Grenada lavas.

3.7.1. Applications to amphiboles from the Ongatiti ignimbrite

3.7.1.1. Testing for equilibrium between amphibole rims and matrix glasses in pumice clasts

To date, tests for equilibrium between amphibole and coexisting melt with known major element compositions might involve calculation of K_D or application of thermometer models. For example, we might require a K_D value within the range of 0.28 ± 0.11, and consistency of amphibole crystallization temperatures estimated using different thermometer models (e.g. amphibole-only thermometer vs. liquid-only thermometer; Molina *et al.*, 2015; Putirka, 2016). Our recalibrations of melt compositions provide an additional way of testing for equilibrium between amphiboles and coexisting melts, when their compositional data are both available.

We take measured amphibole-glass pairs in pumice clasts of rhyolitic compositions from the Ongatiti ignimbrite, New Zealand, as an example. The coexisting amphibole and glass major element compositional data are taken from Cooper and Wilson (2014), where detailed background information is given, including geological setting, petrological and geochemical characteristics of the pumice samples, mineral textures and crystal major and trace element compositions, etc. According to Cooper and Wilson (2014)'s study, amphiboles in pumice clasts of the Ongatiti ignimbrite show textural complexity coupled with geochemical diversity, which offers a good opportunity to study open-system magmatic processes which have attributed to it, as well as silicic super-eruptions. In this study, we focus on attempting to reconstruct the melt compositions (matrix glasses) in equilibrium with the rims of amphiboles from pumice clasts GC1, P2023, P2026, P2027 and P2184. This effectively also represents a test for equilibrium between amphibole rims and matrix glasses, using the major element compositions of the amphiboles and temperature-independent equations from **Table 3.2**.

The amphibole crystals from the rhyodacitic-rhyolitic pumice clasts of the Ongatiti ignimbrite show complex mineral textures coupled with varying chemical compositions. The majority of the amphiboles (83%) have resorbed, patchy zoned cores (termed as Type B cores, in contrast to Type A cores, see below) with heterogeneous major and trace element compositions ($1.16 < Al_T < 2.10$, dominantly MgHst and MgHbl compositions and rare presence of Tsch), which are overgrown by oscillatory zoned rims with relatively homogeneous chemistry (MgHbl, $1.20 < Al_T < 1.42$; **Fig. 3.7b, c**). A lesser proportion (17%) of amphibole crystals have unzoned or weakly patchy zoned cores with compositions that are not distinct from the oscillatory zoned rims (Type A cores, MgHbl; **Fig. 3.7a**).

The rhyolitic matrix glasses which coexist with amphiboles are also geochemically homogeneous (e.g. SiO_2 = 77.75 -78.63 wt % in the 5 measured pumice clasts; **Table 3.3**; **Fig. 3.8**). It is suggested that the patchy zoned, resorbed amphibole cores are sourced from chemically variable crystal mushes spanning a large pressure and temperature range, and they are extracted by a later-stage melt replenishment event and ascended to a final storage region (Cooper & Wilson, 2014). The crystallization of homogeneous rims may then occur during the homogenization process of the stalled melt (Cooper & Wilson, 2014). We will provide further discussions on the formation of the chemical and textural variations in the Ongatiti amphiboles and implications to the magma plumbing system of the Mangakino Volcano later in this chapter (section 3.7.1.2).

We calculate major element compositions of the melts in equilibrium with the amphibole rims, using the MR-derived temperature-independent equations, and compare the results with the measured compositions of the matrix glasses. The results are listed in **Table 3.3** and plotted in **Fig. 3.8**. It is demonstrated that our predictions of melt SiO_2, TiO_2, CaO and K_2O are in good agreement with the measured glass compositions within the SE of corresponding MR equations (**Fig. 3.8a, e, f**), although the predicted melt SiO_2 and K_2O content show larger and smaller variation ranges compared to the matrix glasses, respectively. Our predictions of melt Al_2O_3 contents are systematically higher than the glass compositions (**Fig. 3.8b**), and this is probably related to the overestimation of melt Al_2O_3 with *Eq. 19* at lower melt Al_2O_3 content (**Fig. 3.5o**). The disparity between predicted and measured FeO and MgO in P2026, P2027 and P2184, and K_2O in P2023 are larger than the SE of the MR analyses (**Table 3.3**). Possible explanations for the offset between the predictions of FeO and MgO contents in P2026, P2027 and P2184 and measurements include the lower abundances of FeO and MgO in those melts and consequently large analytical uncertainties in the electron probe microanalyses, and the general overestimations of FeO and MgO contents with *Eq. 10* and *Eq. 12* at lower melt FeO and MgO contents (**Fig. 3.5f, h**).

In general, we think that the application of our MR results on amphibole rims of MgHbl compositions (data for which are least abundant among all calcic amphibole species used for calibrations) demonstrates good reliability of our chemometric equations in predicting melt major element compositions. It also demonstrates the equilibrium between amphibole rims and matrix glasses in at least the pumice clasts of GC1 and P2023. This result reaffirms the conclusion derived by Cooper & Wilson (2014)'s study that the homogeneous rims of amphiboles are crystallized/re-equilibrated with the melts prior to the eruption.

3.7.1.2. Implications of the variations in melt compositions predicted from amphibole cores

We now use our MR-derived chemometric equations to predict compositions of melts in equilibrium with amphibole cores, which display complex patchy zoning texture and large compositional variations. The results are plotted in **Fig. 3.8**. It is demonstrated that the cores of Ongatiti amphiboles are in equilibrium with melts spanning a large range of variations (63.18-81.88 wt % SiO_2, 1.89-4.99 wt % K_2O; **Fig. 3.8**). Cooper & Wilson (2014) concluded that the large compositional diversity in Ongatiti amphiboles is related to source variations. This conclusion was based on the assumption that equilibrium has been achieved between amphiboles and melts from which they are crystallized. However, the presence of patchy zoning and resorption/equilibration textures are obvious evidences of disequilibrium which may be ascribed to re-equilibration with melts of matrix glass composition shortly before the eruption. Therefore, we need to reconsider the meanings of the melt compositions predicted from Ongatiti amphibole cores, whether they represent the source variations or different degrees of equilibration.

Interestingly, large compositional variations are also present across different patches in single amphibole crystals and multiple amphibole crystals in single pumice clasts (e.g. **Fig. 3.7b, c**), as reported by Cooper & Wilson (2014). Cooper & Wilson (2014) argued that the large chemical variations in the cores of Ongatiti amphiboles (particularly Type B cores) are contributed by recycling crystals sourced from chemically extremely heterogeneous crystal mushes stalled at different depths and thermal conditions. We think that although this can be a possible process contributing to the

overall amphibole compositional and textural variations in theory, it can hardly explain the equally large variation range observed in crystals in each pumice clasts or even in individual crystals. Moreover, silicic super-eruptions tend to be chemically homogeneous (Cooper & Wilson, 2014, Huber *et al.*, 2009), and therefore extensive magma hybridization processes over long timescales are required to even out the heterogeneous compositions of multiple components; however, in such a scenario we would expect that the crystal disequilibrium textures are eliminated by diffusion-driven equilibration (e.g. **Fig. 3.7b**). In contrast, the crystal-scale compositional variations are coupled with the greyscale variations across brighter patches and darker patches and the resorption/dissolution textures, clearly indicating equilibration with a later melt after the crystals are formed (e.g. **Fig. 3.7b, c**; Humphreys *et al.*, 2006a, Streck, 2008).

Therefore, we propose an additional insight complementary to Cooper & Wilson (2014)'s conclusion, to explain the diversity of core compositions in Ongatiti amphiboles, which is caused by different degrees of equilibration with melts of probably matrix glass compositions (**Fig. 3.8e**). The different degrees of equilibration can be attributed to different timescales of equilibration, depending on the position of the amphiboles in the magma plumbing system. For example, we expect longer timescales of crystal interaction with melt in ponded melt-enriched magma bodies and therefore higher degree of equilibration, which can explain the formation of Type A cores with similar compositions to rims; while in the passageways of the magma plumbing system which are episodically infilled with ascending melts, various degrees of interaction from low to high can occur simultaneously, and this help explain the formation of Type B cores. Source variations related to the formation of crystal mushes may be still present over a range of depths, as evidenced by the presence of amphibole and plagioclase dominated microcrystalline clots with more scattered crystal and glass chemistry (Cooper & Wilson, 2014), but they can be overprinted by different degrees of equilibration of the recycled crystals with evolved melts and thus not directly observable. We suggest that the mafic melt where least silicic patches in Type B cores are probably sourced from have < 62 wt % SiO_2 and > 4 wt % CaO (**Fig. 3.8e**), more silicic patches are resulted from partial equilibration with melt of pumice matrix glass compositions in various degrees (**Fig. 3.8e**). This is also evidenced by partial diffusive re-equilibration texture observed in a Type B core in **Fig. 3.7b**.

Therefore we interpret that the compositional variations in plutonic-derived amphiboles may not represent source variations, instead they might be due to different degrees of equilibration with evolved melts during processes such as recycling earlier-fractionated crystal mush components to magma plumbing system (Zhang *et al.*, 2015), which is also termed as 'petrological cannibalism' (Cashman & Blundy, 2013). Consistently, the melt compositions reconstructed from amphiboles with disequilibrium textures (patchy zoning, resorption/dissolution textures) may not represent the original melt from which the amphiboles are crystallized. In contrast, the predicted melt compositions intermediate between a mafic source (grey star in **Fig. 3.8e**) and matrix glasses may have never existed. Therefore, to infer open magmatic processes causing the amphibole compositional diversity with disequilibrium textures, textural information must also be considered.

3.7.2. Applications to amphiboles in plutonic nodules from Grenada

The partial melting of the basic lower crust at convergent margins subjected to the underplating of hot, mantle-derived magmas is believed to be an important way of producing basaltic andesite melt or even more fractionated melt compositions, and leaving amphibole/garnet-bearing cumulates behind (e.g. Carroll & Wyllie, 1989; Springer & Seck, 1997; Xiong *et al.*, 2005). Fractional crystallization of amphiboles from arc magmas in global subduction systems is also suggested, despite it being absent as a phenocryst phase ('cryptic amphibole fractionation'; Davidson *et al.*, 2007); this process would also produce amphibole-bearing cumulates (e.g. Arculus & Wills, 1980; Stamper *et al.*, 2014). Amphibole-bearing cumulates would be prone to melting and/or assimilation if later replenishing magma percolated through the amphibole crystal mushes (Smith, 2014). Recycling of such cumulate crystals, followed by ascent and transport to a shallower storage zone where they might coexist with amphiboles that crystallized under lower temperatures and pressures, would contribute to crystal

textural and compositional heterogeneity (Zhang *et al.*, 2015). An ability to distinguish such crystals from phenocrysts, and then apply the chemometric equations, will yield information about their parental melt compositional variations, and thus contribute to our understandings of the intra-crustal processes involving the amphibole phase.

Some of the experiments for calibrating chemometric equations use plutonic samples, e.g. tonalite (Carroll & Wyllie, 1989) and granodiorite (Naney, 1983), and metamorphic samples, e.g. metabasalt (Ernst & Liu, 1998), metavolcanoclastic rocks (Skjerlie & Johnston, 1996) and granulite (Springer & Seck, 1997). The results show good agreement between our predictions and the measured melt compositions, and no difference from results yielded from volcanic samples. We believe this suggests the reliability of the application of the chemometric equations to amphiboles from plutonic and metamorphic source rocks. Below we provide a case study using amphiboles in plutonic xenoliths in lavas from Grenada, Lesser Antilles (Stamper *et al.*, 2014).

The petrological and mineralogical details and amphibole compositions of the plutonic xenoliths are described by (Stamper *et al.*, 2014). The majority of the plutonic xenoliths in Grenada are interpreted as having a cumulate origin (Stamper *et al.*, 2014). Olivine, clinopyroxene, amphibole, plagioclase and spinel are the most common mineral phases in the xenoliths and the proportions of different mineral phases display a diverse range (see Stamper et al. 2014, Fig. 2 therein). Amphiboles are abundant in the majority of the xenoliths and in the andesitic lavas, and most of the major element analyses suggest MgHst compositions, with occasional presence of Tsch and Parg. Texturally, amphiboles are present as either poikilitic crystals with inclusions of olivine, clinopyroxene, spinel and plagioclase, or as euhedral and equant crystals. Both types of amphiboles can be found in the amphibole-bearing cumulate nodules and lavas. To quantify the melt compositions that were in equilibrium with the cumulate crystals, we select amphiboles from three representative types of xenoliths and calculated their corresponding melt compositions. The samples chosen are clinopyroxenite (GRN17, GRN24, GR17, GR29, GR5-1), hornblendite (GR15, GR25, GR11, GR52) and hornblende gabbro (GRN6, GRN 21, GRN5, GR42).

Although the crystal chemistry of the amphiboles from the 3 selected types of xenoliths is largely overlapping, we observe a general difference in the calculated melt SiO_2 contents (**Fig. 3.9a**). With similar amphibole crystal SiO_2 content (between 40 and 44 wt %), melts yielded from amphiboles in clinopyroxenite, hornblendite and hornblende gabbro are progressively more silicic. For example, melts in equilibrium with amphibole of 42 wt % SiO_2 from clinopyroxenite contain 58-60 wt % SiO_2, while in the melts in equilibrium with amphiboles from hornblende gabbro, SiO_2 is $\geq$ 61.6 wt %. This results from variations in predicted melt FeO, MgO and CaO compositions (**Fig. 3.9e-g**). Although the difference is within the precision of our method of predicting melt SiO_2 content, the predicted SiO_2 contents in the melts display robust correlations with the amphibole crystal SiO_2 contents and show increasing R^2 and slope from clinopyroxenite to hornblendite and hornblende gabbro. The variation trends of the predicted melt FeO, MgO, CaO and K_2O content for amphiboles from the 3 types of xenoliths may also be distinguishable with increasing melt SiO_2 content (**Fig. 3.9e-h**). Furthermore, the most evolved melt compositions with 60.88-70.81 wt % SiO_2 inferred from most silicic amphiboles in hornblende gabbro are in agreement with the compositions of most silicic melt inclusions found in hornblende and clinopyroxene in these gabbros (Stamper *et al.*, 2014), especially in terms of SiO_2, TiO_2, FeO, MgO and CaO contents (**Fig. 3.9**). The predicted melt compositions also fit best with C-series lavas, consistent with low-pressure fractionation trend derived from MELTS modelling (Stamper *et al.*, 2014; see Fig. 22 therein; **Fig. 3.9b**).

Stamper *et al.* (2014) suggests that the source melts related to the formation of clinopyroxenite, hornblendite, hornblende gabbro and plagioclase hornblendite probably contain 47.5-51.3 wt % SiO_2 and 4.4-9.7 wt % MgO based on previous experimental studies (see Table 13 therein), far more mafic than our predicted melt compositions and the majority of the measured melt inclusions hosted in cumulate mineral phases (Stamper *et al.*, 2014). We propose two possible reasons to explain this offset as follows. First, the large spread in our predicted melt compositions and the melt inclusions may reflect *in situ* melt evolution during extensive crystallization of the cumulate mineral

phases. Stamper *et al.* (2014) demonstrates that the appearance of the major mineral phases in the plutonic xenoliths follows the sequence order of olivine, clinopyroxene, amphibole and plagioclase with decreasing temperature. Our melt major element estimates suggest that from clinopyroxenite to hornblendite and hornblende gabbro, with decreasing clinopyroxene proportion and increasing plagioclase proportion and thus decreasing temperature, the melts are slightly shifted to more silicic compositions. This is in agreement with the trend of liquid line of descent (**Fig. 3.2c-d**). Moreover, the most mafic melt inclusion with 49.41 wt % SiO_2 is hosted in a clinopyroxene crystal (Stamper *et al.*, 2014), and hence following the crystallization sequence of olivine, clinopyroxene and amphibole, by the time that amphibole starts to crystallize (even in the clinopyroxenite nodules), the melt has evolved more than its original mafic parental melt. Second, the variation between the predicted melt compositions and melt inclusions may be due to equilibration of the cumulate fragments with later evolved melts, which may be parental to the observed host lavas, rather than variations in source melts. This is consistent with the textural evidence that the plutonic nodules are fragmented and interacted with the host lavas during magma ascent and explosive eruptions (Stamper *et al.*, 2014). However, with little knowledge of the textural information of the crystals on which chemical data are collected, we are uncertain which one is the primary cause of the variation in amphibole crystal chemistry and the associated melt compositions. A combination of the two proposed causes is also likely.

3.8. CONCLUSIONS

We have used multiple-regression methods to recalibrate empirical chemometric equations used to calculate the major element composition of basanitic-rhyolitic melts in equilibrium with calcic amphibole. The equations are based on amphibole formula proportions ± temperature from published experimental P-T-X data, and are independent of pressure. Compared with the pressure-dependent equations of Ridolfi & Renzulli (2012), the new equations yield improved precision and accuracy. The results of multiple regression analyses demonstrate that temperature has a minor impact on improving the precision of calibrating melt compositions with amphibole crystal chemistry, which suggests that temperature is less important than melt compositions in controlling amphibole crystal chemistry. This is convenient for application of the equations to natural amphiboles where temperature is typically unknown. Using the chemometric equations, reconstructed melt compositions in equilibrium with the rims of amphiboles in pumice clasts of the Ongatiti ignimbrite are in good agreement with the matrix glass compositions. This suggests that equilibrium between the amphibole rims and melts of matrix glass compositions is achieved. The cores of amphiboles from the Ongatiti ignimbrite show large compositional variation as well as disequilibrium textures (e.g. patchy zoning, resorption/dissolution texture), and the predicted melt compositions also display large compositional variations. We interpret that the variation in the predicted melt compositions from amphibole cores may be due to different degrees of equilibration of the amphiboles derived from crystal mushes with evolved melts over a range of timescales. This interpretation is an alternative to the model provided by Cooper & Wilson (2014) which instead suggests that source heterogeneity is a major contribution to the crystal chemical diversity in the Ongatiti ignimbrite. Our multiple regression model is also able to predict the compositional variations in the melts predicted from amphiboles in clinopyroxenite, hornblendite and hornblende gabbro xenoliths in Grenada lavas, which are consistent with melt inclusions hosted in those cumulates, as reported by Stamper *et al.* (2014). However, the predicted melts cover a wide range of compositional variations which may be a result of *in situ* melt evolution due to extensive crystallization of the cumulate mineral phases, or equilibration of the cumulate fragments with later evolved melts. In order to give unequivocal interpretations of these predicted melt compositions we would require detailed knowledge of the textural setting of the crystals from which the amphibole major element data are collected (Cooper & Wilson, 2014, Stamper *et al.*, 2014). Without this information, uncertainty remains as to the primary cause of the compositional variations in the predicted melts. Therefore, we propose that the melt compositions inferred from amphiboles displaying disequilibrium textures, such as patchy zoning as a result of resorption/ dissolution, should be interpreted carefully for revealing open magmatic processes which may be responsible for the diversity in amphibole crystal chemistry and textures.

3.9. REFERENCES

Adam, J. & Green, T. (2006). Trace element partitioning between mica- and amphibole-bearing garnet lherzolite and hydrous basanitic melt: 1. Experimental results and the investigation of controls on partitioning behaviour. *Contributions to Mineralogy and Petrology* **152**, 1-17.

Adam, J. & Green, T. H. (1994). The Effects of Pressure and Temperature on the Partitioning of Ti, Sr and Ree between Amphibole, Clinopyroxene and Basanitic Melts. *Chemical Geology* **117**, 219-233.

Adam, J., Green, T. H. & Sie, S. H. (1993). Proton Microprobe Determined Partitioning of Rb, Sr, Ba, Y, Zr, Nb and Ta between Experimentally Produced Amphiboles and Silicate Melts with Variable F Content. *Chemical Geology* **109**, 29-49.

Alonso-Perez, R., Muntener, O. & Ulmer, P. (2009). Igneous garnet and amphibole fractionation in the roots of island arcs: experimental constraints on andesitic liquids. *Contributions to Mineralogy and Petrology* **157**, 541-558.

Anderson, J. L. & Smith, D. R. (1995). The Effects of Temperature and F(O2) on the Al-in-Hornblende Barometer. *American Mineralogist* **80**, 549-559.

Arculus, R. J. & Wills, K. J. A. (1980). The Petrology of Plutonic Blocks and Inclusions from the Lesser Antilles Island Arc. *Journal of Petrology* **21**, 743-799.

Barclay, J. & Carmichael, I. S. E. (2004). A hornblende basalt from western Mexico: Water-saturated phase relations constrain a pressure-temperature window of eruptibility. *Journal of Petrology* **45**, 485-506.

Blatter, D. L. & Carmichael, I. S. E. (2001). Hydrous phase equilibria of a Mexican high-silica andesite: A candidate for a mantle origin? *Geochimica et Cosmochimica Acta* **65**, 4043-4065.

Blundy, J. & Cashman, K. (2008). Petrologic Reconstruction of Magmatic System Variables and Processes. *Minerals, Inclusions and Volcanic Processes* **69**, 179-239.

Blundy, J. D. & Holland, T. J. B. (1990). Calcic Amphibole Equilibria and a New Amphibole-Plagioclase Geothermometer. *Contributions to Mineralogy and Petrology* **104**, 208-224.

Bogaerts, M., Scaillet, B. & Auwera, J. V. (2006). Phase equilibria of the lyngdal granodiorite (Norway): Implications for the origin of metaluminous ferroan granitolds. *Journal of Petrology* **47**, 2405-2431.

Carroll, M. R. & Wyllie, P. J. (1989). Experimental Phase-Relations in the System Tonalite-Peridotite-H2o at 15 Kb - Implications for Assimilation and Differentiation Processes near the Crust-Mantle Boundary. *Journal of Petrology* **30**, 1351-1382.

Cashman, K. & Blundy, J. (2013). Petrological cannibalism: the chemical and textural consequences of incremental magma body growth. *Contributions to Mineralogy and Petrology* **166**, 703-729.

Cooper, G. F. & Wilson, C. J. N. (2014). Development, mobilisation and eruption of a large crystal-rich rhyolite: The Ongatiti ignimbrite, New Zealand. *Lithos* **198**, 38-57.

Costa, F., Scaillet, B. & Pichavant, M. (2004). Petrological and experimental constraints on the pre-eruption conditions of Holocene dacite from Volcan San Pedro (36 degrees S, Chilean Andes) and the importance of sulphur in silicic subduction-related magmas. *Journal of Petrology* **45**, 855-881.

Dalpé, C. & Baker, D. R. (2000). Experimental investigation of large-ion-lithophile-element-, high-field-strength-element- and rare-earth-element-partitioning between calcic amphibole and basaltic melt: the effects of pressure and oxygen fugacity. *Contributions to Mineralogy and Petrology* **140**, 233-250.

Davidson, J., Turner, S., Handley, H., Macpherson, C. & Dosseto, A. (2007). Amphibole "sponge" in arc crust? *Geology* **35**, 787-790.

Erdmann, S., Martel, C., Pichavant, M. & Kushnir, A. (2014). Amphibole as an archivist of magmatic crystallization conditions: problems, potential, and implications for inferring magma storage prior to the paroxysmal 2010 eruption of Mount Merapi, Indonesia. *Contributions to Mineralogy and Petrology* **167**.

Ernst, W. G. & Liu, J. (1998). Experimental phase-equilibrium study of Al- and Ti-contents of calcic amphibole in MORB - A semiquantitative thermobarometer. *American Mineralogist* **83**, 952-969.

Fujinawa, A. & Green, T. H. (1997). Experimental study of partitioning of Hf and Zr between amphibole, clinopyroxene, garnet, and silicate melts. *Journal of Mineralogy Petrology and Economic Geology* **2**, 69-89.

Gardner, J. E., Rutherford, M., Carey, S. & Sigurdsson, H. (1995). Experimental Constraints on Pre-Eruptive Water Contents and Changing Magma Storage Prior to Explosive Eruptions of Mount St-Helens Volcano. *Bulletin of Volcanology* **57**, 1-17.

Green, T. H. & Pearson, N. J. (1985). Experimental-Determination of Ree Partition-Coefficients between Amphibole and Basaltic to Andesitic Liquids at High-Pressure. *Geochimica et Cosmochimica Acta* **49**, 1465-1468.

Grove, T. L., DonnellyNolan, J. M. & Housh, T. (1997). Magmatic processes that generated the rhyolite of Glass Mountain, Medicine Lake volcano, N California. *Contributions to Mineralogy and Petrology* **127**, 205-223.

Grove, T. L., Elkins-Tanton, L. T., Parman, S. W., Chatterjee, N., Muntener, O. & Gaetani, G. A. (2003). Fractional crystallization and mantle-melting controls on calc-alkaline differentiation trends. *Contributions to Mineralogy and Petrology* **145**, 515-533.

Hammarstrom, J. M. & Zen, E. A. (1986). Aluminum in Hornblende: an Empirical Igneous Geobarometer. *American Mineralogist* **71**, 1297-1313.

Hawthorne, F. C., Oberti, R., Harlow, G. E., Maresch, W. V., Martin, R. F., Schumacher, J. C. & Welch, M. D. (2012). Nomenclature of the amphibole supergroup. *American Mineralogist* **97**, 2031-2048.

Hilyard, M., Nielsen, R. L., Beard, J. S., Patino-Douce, A. & Blencoe, J. (2000). Experimental determination of the partitioning behavior of rare earth and high field strength elements between pargasitic amphibole and natural silicate melts. *Geochimica et Cosmochimica Acta* **64**, 1103-1120.

Hirschmann, M. M., Ghiorso, M. S., Davis, F. A., Gordon, S. M., Mukherjee, S., Grove, T. L., Krawczynski, M., Medard, E. & Till, C. B. (2008). Library of Experimental Phase Relations (LEPR): A database and Web portal for experimental magmatic phase equilibria data. *Geochemistry, Geophysics, Geosystems* **9**, n/a-n/a.

Holland, T. & Blundy, J. (1994). Nonideal Interactions in Calcic Amphiboles and Their Bearing on Amphibole-Plagioclase Thermometry. *Contributions to Mineralogy and Petrology* **116**, 433-447.

Hollister, L. S., Grissom, G. C., Peters, E. K., Stowell, H. H. & Sisson, V. B. (1987). Confirmation of the Empirical Correlation of Al in Hornblende with Pressure of Solidification of Calc-Alkaline Plutons. *American Mineralogist* **72**, 231-239.

Holtz, F., Sato, H., Lewis, J., Behrens, H. & Nakada, S. (2005). Experimental petrology of the 1991-1995 Unzen dacite, Japan. Part I: Phase relations, phase composition and pre-eruptive conditions. *Journal of Petrology* **46**, 319-337.

Huber, C., Bachmann, O. & Manga, M. (2009). Homogenization processes in silicic magma chambers by stirring and mushification (latent heat buffering). *Earth and Planetary Science Letters* **283**, 38-47.

Humphreys, M. C. S., Blundy, J. D. & Sparks, R. S. J. (2006a). Magma Evolution and Open-System Processes at Shiveluch Volcano: Insights from Phenocryst Zoning. *Journal of Petrology* **47**, 2303-2334.

Humphreys, M. C. S., Kearns, S. L. & Blundy, J. D. (2006b). SIMS investigation of electron-beam damage to hydrous, rhyolitic glasses: Implications for melt inclusion analysis. *American Mineralogist* **91**, 667-679.

Kawamoto, T. (1996). Experimental constraints on differentiation and H2O abundance of calc-alkaline magmas. *Earth and Planetary Science Letters* **144**, 577-589.

Klein, M., Stosch, H. G. & Seck, H. A. (1997). Partitioning of high field-strength and rare-earth elements between amphibole and quartz-dioritic to tonalitic melts: An experimental study. *Chemical Geology* **138**, 257-271.

Krawczynski, M. J., Grove, T. L. & Behrens, H. (2012). Amphibole stability in primitive arc magmas: effects of temperature, H2O content, and oxygen fugacity. *Contributions to Mineralogy and Petrology* **164**, 317-339.

Leake, B. E., Woolley, A. R., Arps, C. E. S., Birch, W. D., Gilbert, M. C., Grice, J. D., Hawthorne, F. C., Kato, A., Kisch, H. J., Krivovichev, V. G., Linthout, K., Laird, J., Mandarino, J. A., Maresch, W. V., Nickel, E. H., Rock, N. M. S., Schumacher, J. C., Smith, D. C., Stephenson, N. C. N., Ungaretti, L., Whittaker, E. J. W. & Guo, Y. Z. (1997). Nomenclature of amphiboles: Report of the subcommittee on amphiboles of the International Mineralogical Association, Commission on New Minerals and Mineral Names. *Canadian Mineralogist* **35**, 219-246.

Martel, C., Champallier, R., Prouteau, G., Pichavant, M., Arbaret, L., Balcone-Boissard, H., Boudon, G., Boivin, P., Bourdier, J. L. & Scaillet, B. (2013). Trachyte Phase Relations and Implication for Magma Storage Conditions in the Chaine des Puys (French Massif Central). *Journal of Petrology* **54**, 1071-1107.

Molina, J. F., Moreno, J. A., Castro, A., Rodríguez, C. & Fershtater, G. B. (2015). Calcic amphibole thermobarometry in metamorphic and igneous rocks: New calibrations based on plagioclase/amphibole Al-Si partitioning and amphibole/liquid Mg partitioning. *Lithos* **232**, 286-305.

Moore, G. & Carmichael, I. S. E. (1998). The hydrous phase equilibria (to 3 kbar) of an andesite and basaltic andesite from western Mexico: constraints on water content and conditions of phenocryst growth. *Contributions to Mineralogy and Petrology* **130**, 304-319.

Nandedkar, R. H. (2014). Evolution of hydrous mantle-derived calc-alkaline liquids by fractional crystallization at 0.7 and 0.4 GPa – An experimental study. Ph.D. thesis, ETH.

Naney, M. T. (1983). Phase-Equilibria of Rock-Forming Ferromagnesian Silicates in Granitic Systems. *American Journal of Science* **283**, 993-1033.

Nekvasil, H., Dondolini, A., Horn, J., Filiberto, J., Long, H. & Lindsley, D. H. (2004). The origin and evolution of silica-saturated alkalic suites: an experimental study. *Journal of Petrology* **45**, 693-721.

Nicholls, I. A. & Harris, K. L. (1980). Experimental Rare-Earth Element Partition-Coefficients for Garnet, Clinopyroxene and Amphibole Coexisting with Andesitic and Basaltic Liquids. *Geochimica et Cosmochimica Acta* **44**, 287-308.

Patino-Douce, A. E. & Beard, J. S. (1995). Dehydration-Melting of Biotite Gneiss and Quartz Amphibolite from 3 to 15 Kbar. *Journal of Petrology* **36**, 707-738.

Pichavant, M., Di Carlo, I., Le Gac, Y., Rotolo, S. G. & Scaillet, B. (2009). Experimental Constraints on the Deep Magma Feeding System at Stromboli Volcano, Italy. *Journal of Petrology* **50**, 601-624.

Pichavant, M., Martel, C., Bourdier, J. L. & Scaillet, B. (2002). Physical conditions, structure, and dynamics of a zoned magma chamber: Mount Pelee (Martinique, Lesser Antilles Arc). *Journal of Geophysical Research-Solid Earth* **107**.

Prouteau, G. & Scaillet, B. (2003). Experimental constraints on the origin of the 1991 Pinatubo dacite. *Journal of Petrology* **44**, 2203-2241.

Prouteau, G., Scaillet, B., Pichavant, M. & Maury, R. C. (1999). Fluid-present melting of ocean crust in subduction zones. *Geology* **27**, 1111-1114.

Putirka, K. A. (2016). Amphibole thermometers and barometers for igneous systems, and some implications for eruption mechanism of felsic magmas at arc volcanoes. *American Mineralogist* **in press**.

Putirka, K. D. (2008). Thermometers and Barometers for Volcanic Systems. *Minerals, Inclusions and Volcanic Processes* **69**, 61-120.

Ridolfi, F., Puerini, M., Renzulli, A., Menna, M. & Toulkeridis, T. (2008). The magmatic feeding system of El Reventador volcano (Sub-Andean zone, Ecuador) constrained by texture, mineralogy and thermobarometry of the 2002 erupted products. *Journal of Volcanology and Geothermal Research* **176**, 94-106.

Ridolfi, F. & Renzulli, A. (2012). Calcic amphiboles in calc-alkaline and alkaline magmas: thermobarometric and chemometric empirical equations valid up to 1,130°C and 2.2 GPa. *Contributions to Mineralogy and Petrology* **163**, 877-895.

Ridolfi, F., Renzulli, A. & Puerini, M. (2010). Stability and chemical equilibrium of amphibole in calc-alkaline magmas: an overview, new thermobarometric formulations and application to subduction-related volcanoes. *Contributions to Mineralogy and Petrology* **160**, 45-66.

Roeder, P. L. & Emslie, R. F. (1970). Olivine-Liquid Equilibrium. *Contributions to Mineralogy and Petrology* **29**, 275-&.

Rutherford, M. J. & Devine, J. D. (2003). Magmatic conditions and magma ascent as indicated by hornblende phase equilibria and reactions in the 1995-2002 Soufriere Hills magma. *Journal of Petrology* **44**, 1433-1454.

Sato, H., Holtz, F., Behrens, H., Botcharnikov, R. & Nakada, S. (2005). Experimental petrology of the 1991-1995 Unzen dacite, Japan. Part II: Cl/OH partitioning between hornblende and melt and its implications for the origin of oscillatory zoning of hornblende phenocrysts. *Journal of Petrology* **46**, 339-354.

Scaillet, B. & Evans, B. W. (1999). The 15 June 1991 eruption of Mount Pinatubo. I. Phase equilibria and pre-eruption P-T-fO(2)-fH(2)O conditions of the dacite magma. *Journal of Petrology* **40**, 381-411.

Schmidt, M. W. (1992). Amphibole Composition in Tonalite as a Function of Pressure - an Experimental Calibration of the Al-in-Hornblende Barometer. *Contributions to Mineralogy and Petrology* **110**, 304-310.

Shane, P. & Smith, V. C. (2013). Using amphibole crystals to reconstruct magma storage temperatures and pressures for the post-caldera collapse volcanism at Okataina volcano. *Lithos* **156-159**, 159-170.

Sisson, T. W. (1994). Hornblende-Melt Trace-Element Partitioning Measured by Ion Microprobe. *Chemical Geology* **117**, 331-344.

Sisson, T. W. & Grove, T. L. (1993). Experimental Investigations of the Role of H2O in Calc-Alkaline Differentiation and Subduction Zone Magmatism. *Contributions to Mineralogy and Petrology* **113**, 143-166.

Skjerlie, K. P. & Johnston, A. D. (1996). Vapour-absent melting from 10 to 20 kbar of crustal rocks that contain multiple hydrous phases: Implications for anatexis in the deep to very deep continental crust and active continental margins. *Journal of Petrology* **37**, 661-691.

Smith, D. J. (2014). Clinopyroxene precursors to amphibole sponge in arc crust. *Nature Communications* **5**.

Springer, W. & Seck, H. A. (1997). Partial fusion of basic granulites at 5 to 15 kbar: Implications for the origin of TTG magmas. *Contributions to Mineralogy and Petrology* **127**, 30-45.

Stamper, C. C., Blundy, J. D., Arculus, R. J. & Melekhova, E. (2014). Petrology of Plutonic Xenoliths and Volcanic Rocks from Grenada, Lesser Antilles. *Journal of Petrology* **55**, 1353-1387.

Streck, M. J. (2008). Mineral Textures and Zoning as Evidence for Open System Processes. *Minerals, Inclusions and Volcanic Processes* **69**, 595-622.

Tiepolo, M., Vannucci, R., Bottazzi, P., Oberti, R., Zanetti, A. & Foley, S. (2000). Partitioning of rare earth elements, Y, Th, U, and Pb between pargasite, kaersutite, and basanite to trachyte melts: Implications for percolated and veined mantle. *Geochemistry Geophysics Geosystems* **1**.

Xiong, X. L., Adam, J. & Green, T. H. (2005). Rutile stability and rutile/melt HFSE partitioning during partial melting of hydrous basalt: Implications for TTG genesis. *Chemical Geology* **218**, 339-359.

Zhang, J., Davidson, J. P., Humphreys, M. C. S., Macpherson, C. G. & Neill, I. (2015). Magmatic Enclaves and Andesitic Lavas from Mt. Lamington, Papua New Guinea: Implications for Recycling of Earlier-fractionated Minerals through Magma Recharge. *Journal of Petrology* **56**, 2223-2256.

3.10. FIGURES

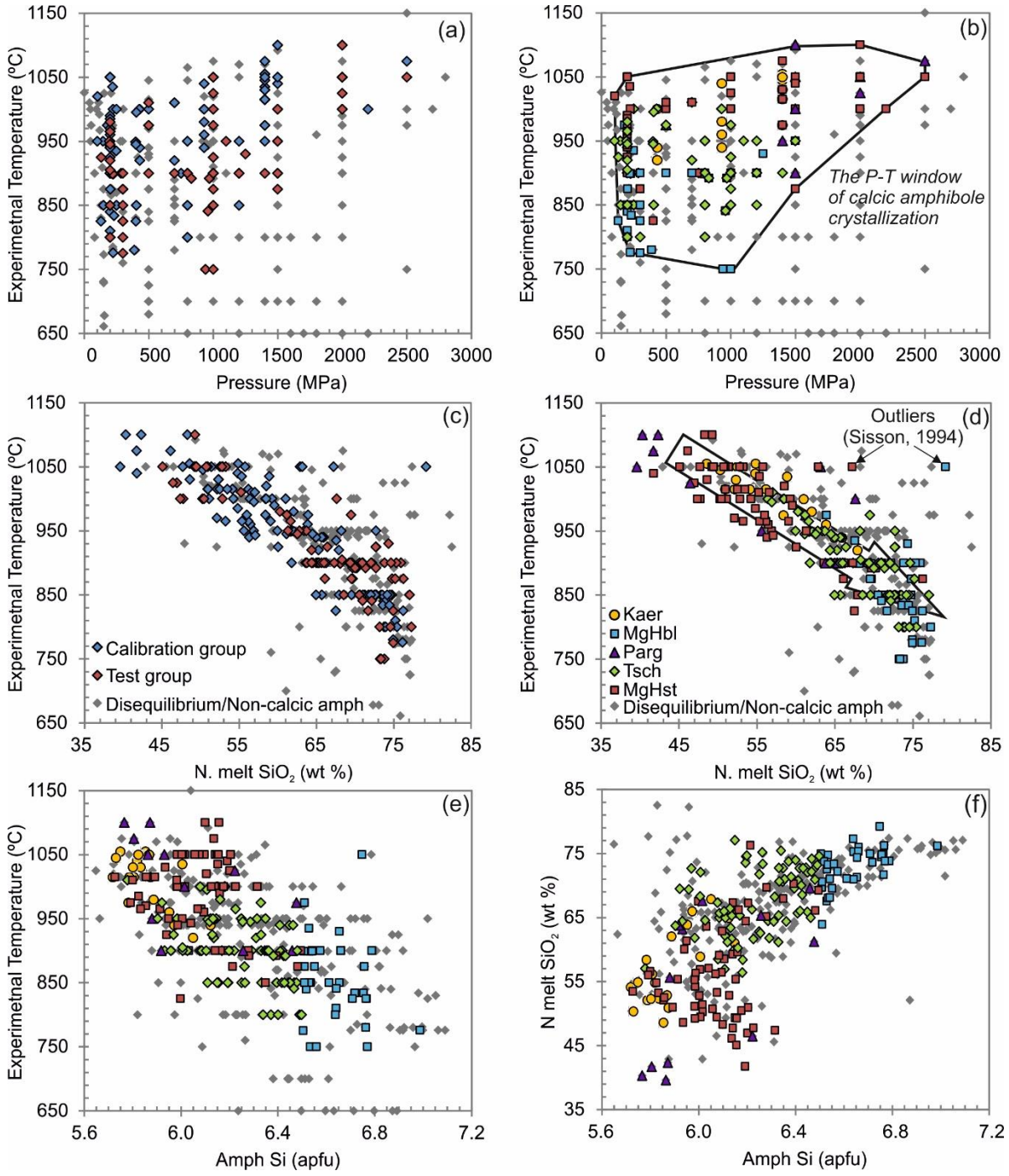

Fig. 3.1 (a-b) Experimental running pressure-temperature conditions, and (c-d) the temperature-melt SiO_2 content relationship of the selected experiments. (a) and (c) illustrate the overlapping P-T-X conditions between the studies selected for calibrating chemometric equations and others for testing the accuracy of the equations, while (b) and (d) illustrate the corresponding amphibole species in terms of MgHst (magnesiohastingsite), MgHbl (magnesiohornblende), Parg (pargasite), Tsch (tschermakite) and Kaer (kaersutite), as well as amphiboles which are either non-calcic or with compositions out of equilibrium with the melt. The area outlined in (b) denotes the P-T window within which calcic amphiboles can crystallize and equilibrate with the melt. The big balck arrow in (d) outlines the trend of liquid line of descent by eye. (e-f) The relationships between amphibole crystal chemistry (tetrahedral Si, in apfu) and temperature and melt SiO_2 content (melt SiO_2 contents are normalized to 100% anhydrous phase). See text for details.

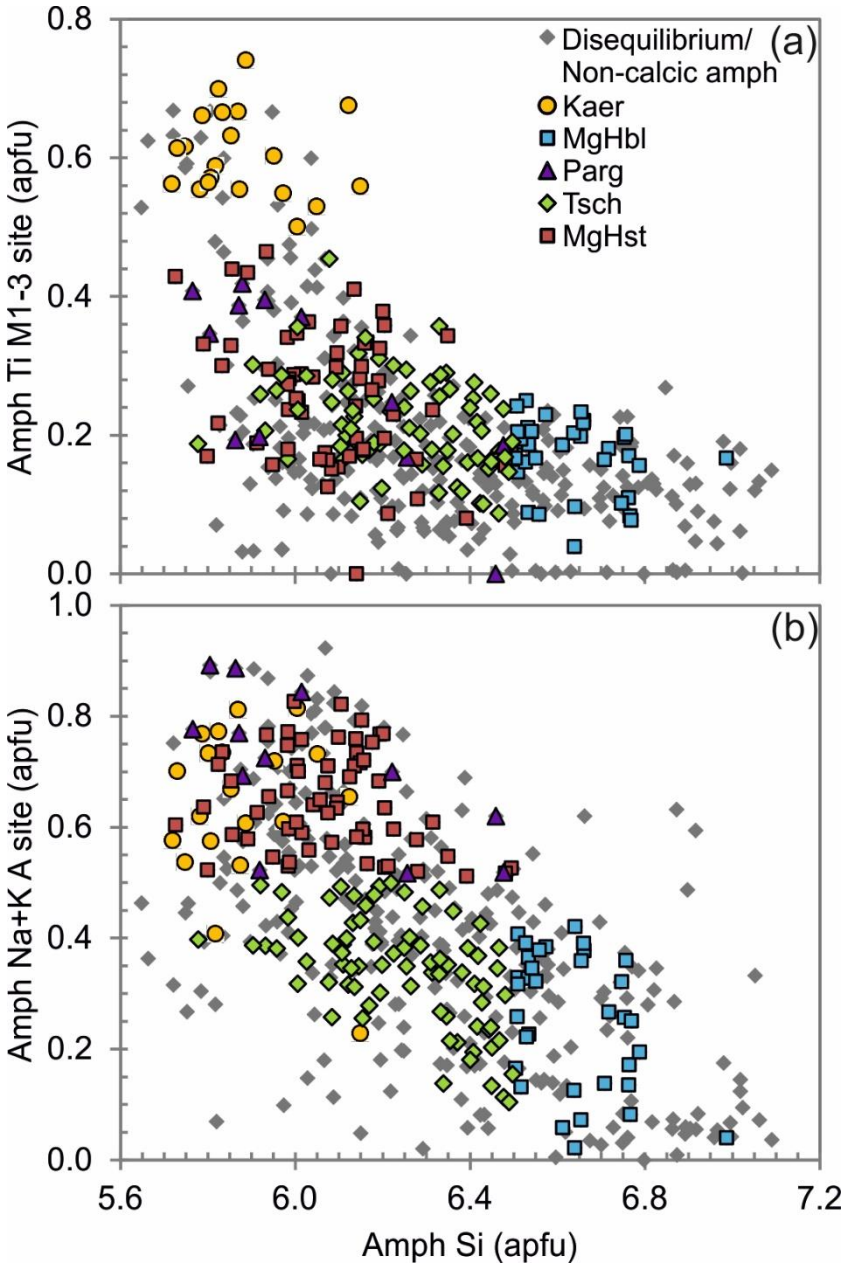

Fig. 3.2 Calcic amphibole formula proportions of Parg, MgHst, Kaer, Tsch and MgHbl from the selected experimental studies.

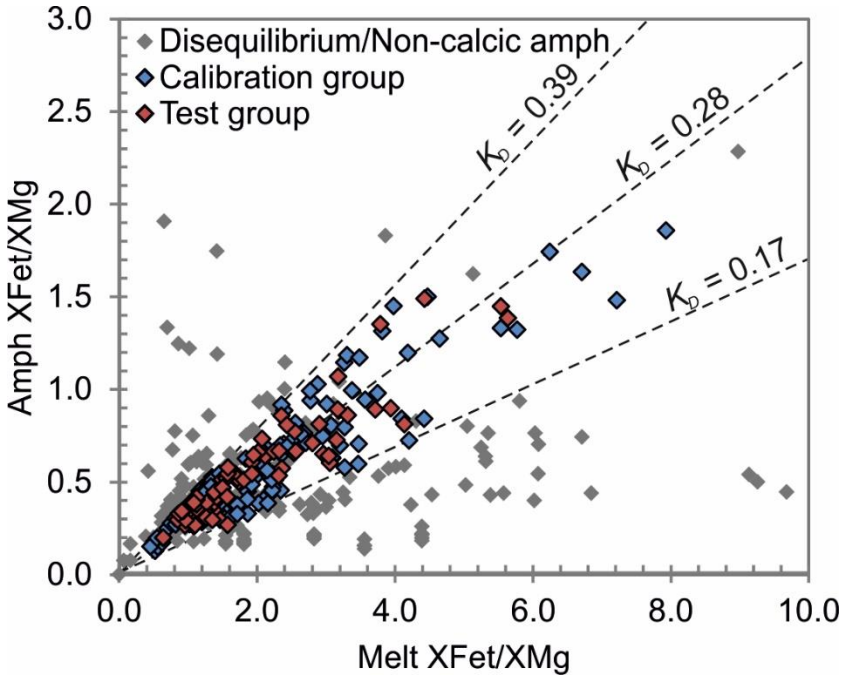

Fig. 3.3 Amphibole-melt equilibrium test based on the Fe-Mg exchange coefficient (K_D). The amphibole and melt compositions are regarded as in equilibrium when K_D is within the range of 0.28 ± 0.11. See text for details.

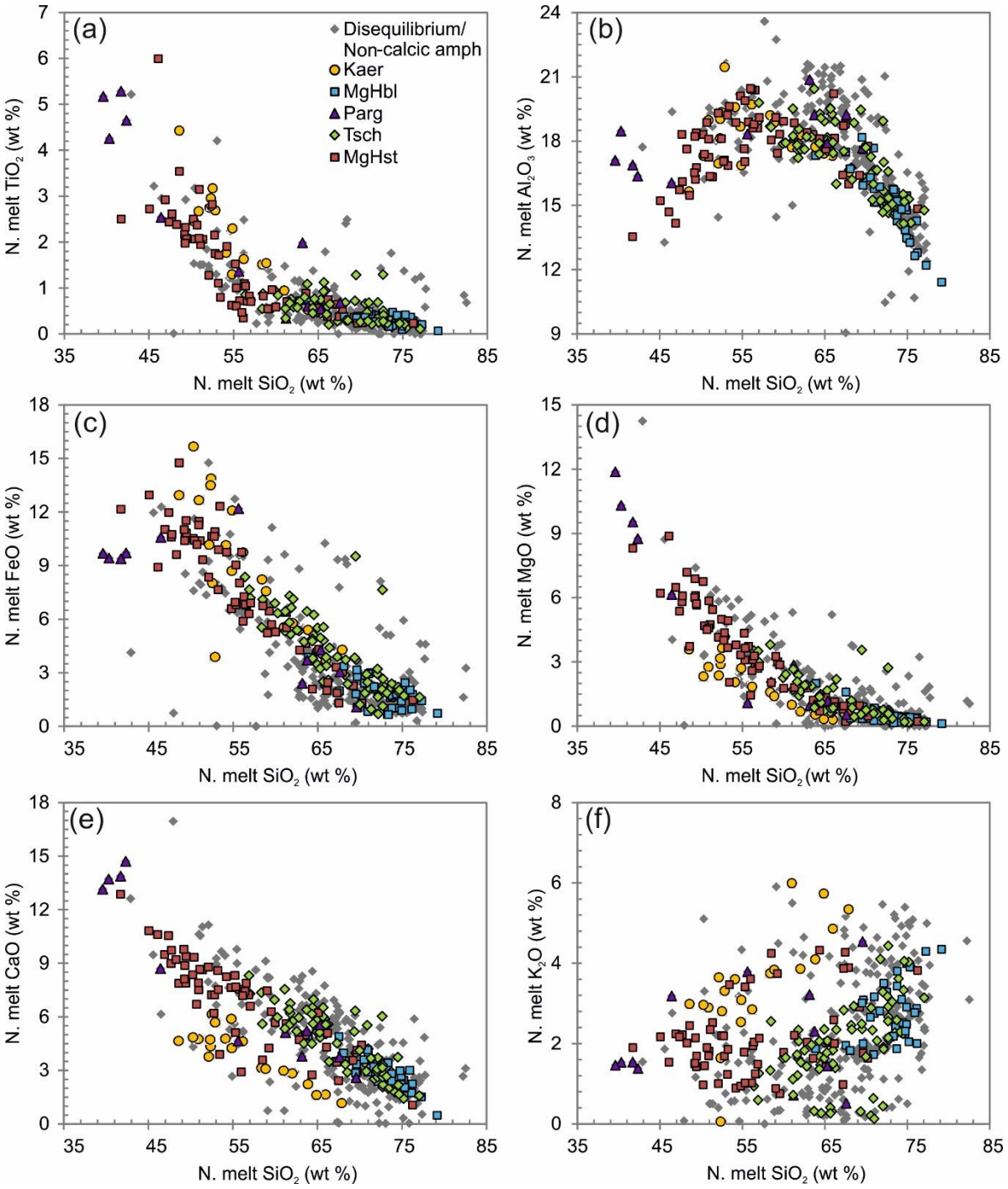

Fig. 3.4 Major element compositions of melts from the selected experimental studies (normalized to 100% anhydrous phase).

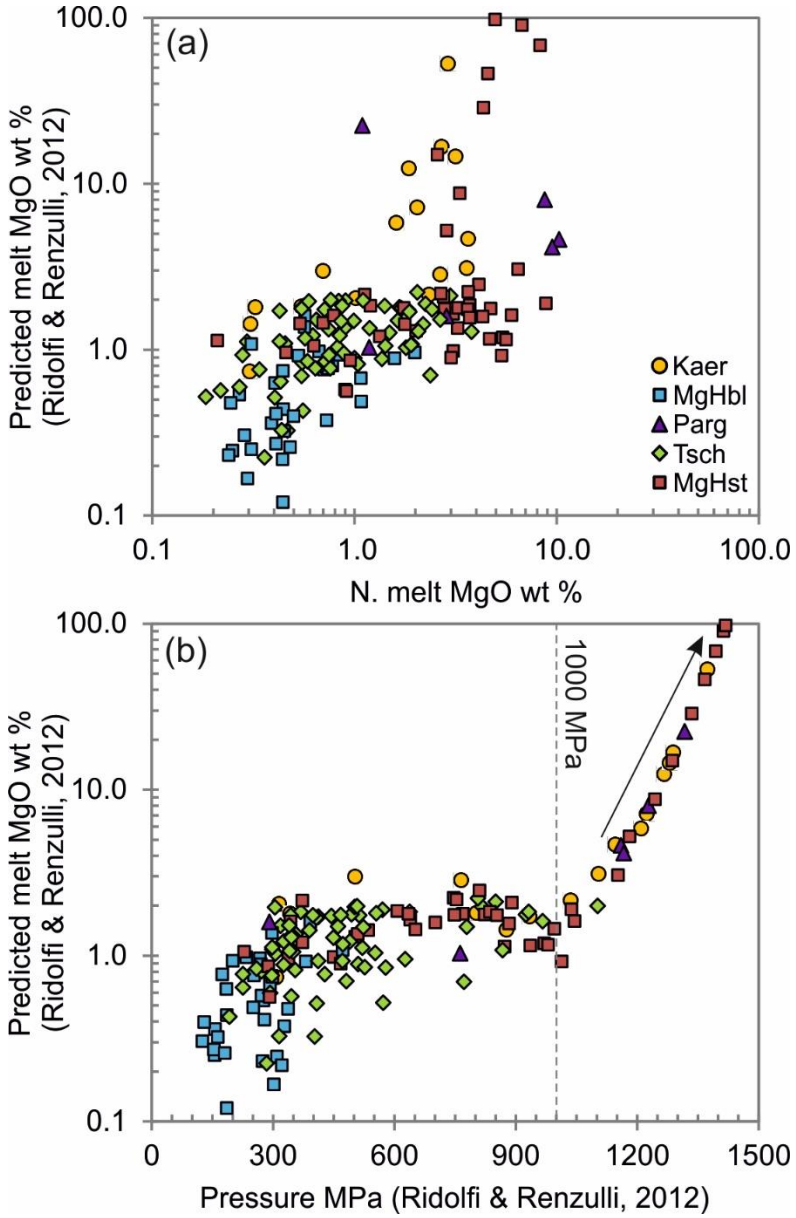

Fig. 3.5 (a) Predicted melt MgO using Ridolfi and Renzulli (2012)'s model vs. measured MgO; (b) the overestimated predicted melt MgO (> 3 wt %) is strongly dependent on the calculated pressure (> 1,000 MPa) with Ridolfi and Renzulli (2012)'s barometer model. See text for discussions.

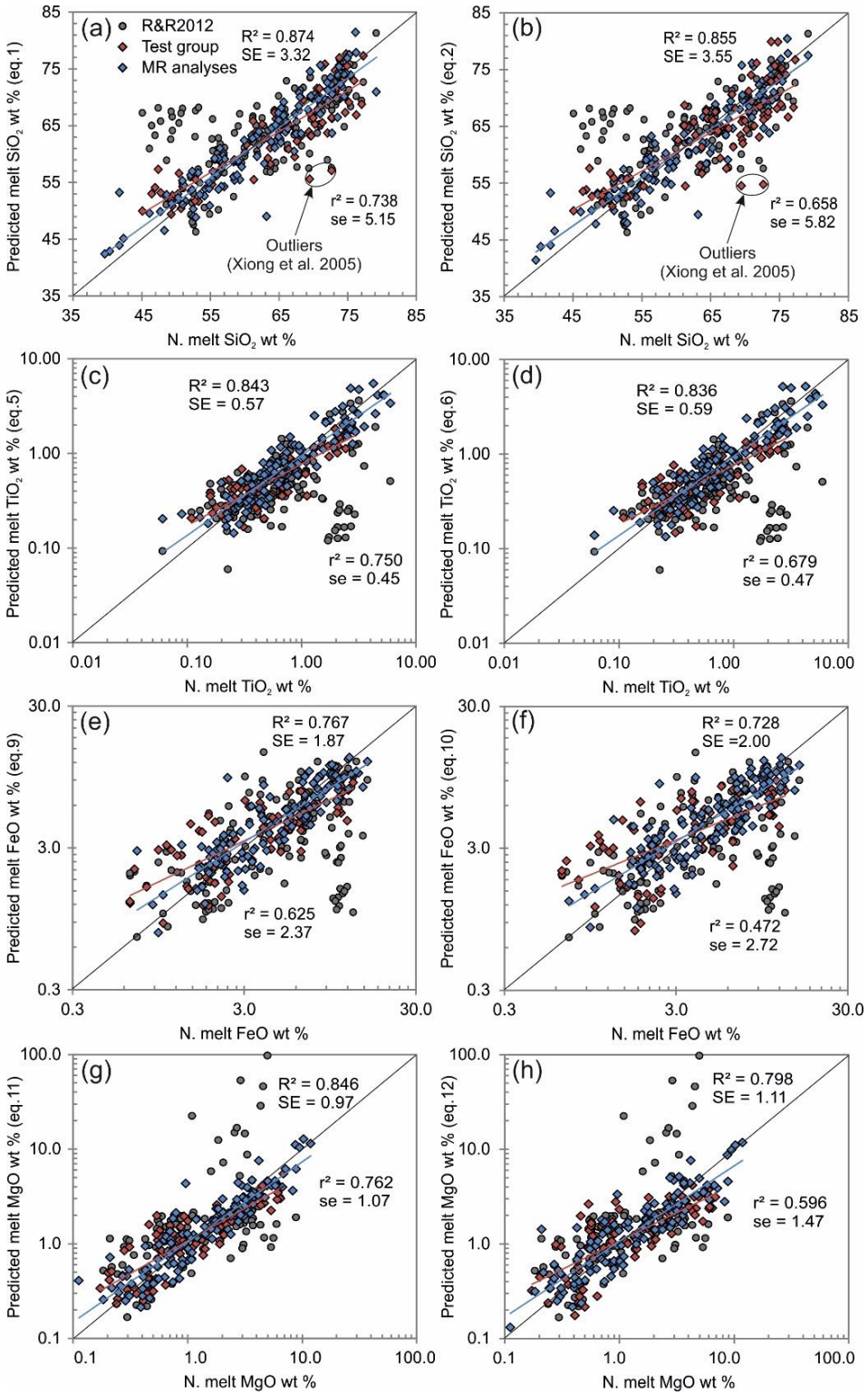

Fig. 3.6 Comparison between experimental melt compositions and predictions for the calibration group (blue; results of the multiple regress analyses), test group (red) using equations from Table 1, and results calculated using Ridolfi & Renzulli (2012)'s chemometric equations (grey). The multiple regression analysis can reproduce the melt major element compositions with better agreement than Ridolfi & Renzulli (2012)'s model, which generates large offset from measured melt compositions especially in the low-SiO_2 group. The offset are also seen in the predictions of TiO_2, FeO, MgO, CaO and K_2O with Ridolfi & Renzulli (2012)'s model. The accuracy of our calibrated chemometric equations are tested with good agreement between the experimental melt compositions and the results

yielded from the test group. Correlation coefficients and standard error of estimates are given in each plot for the calibration results (R^2 and SE) and test results (r^2 and se). See text for details.

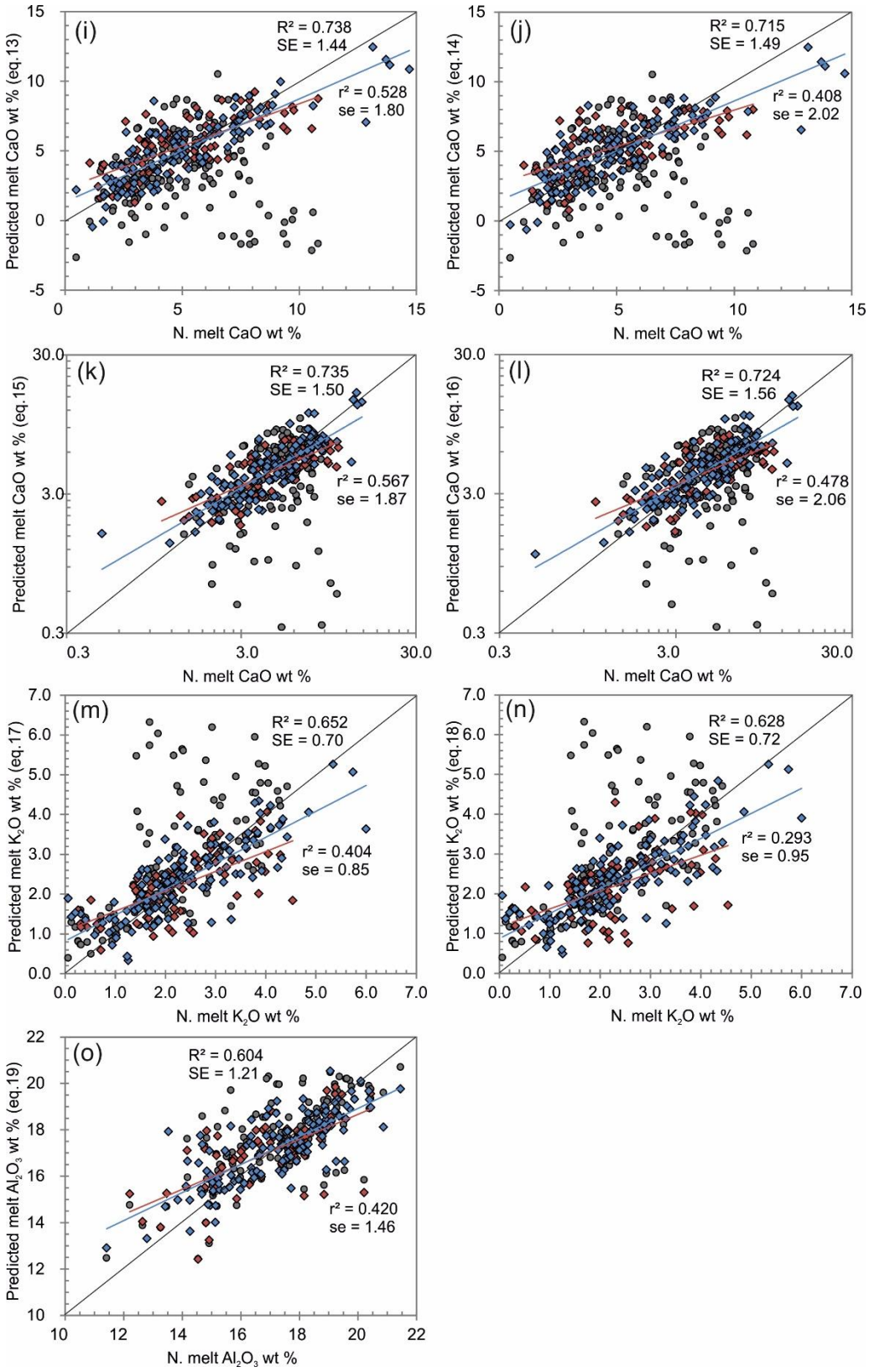

Fig. 3.6 continued.

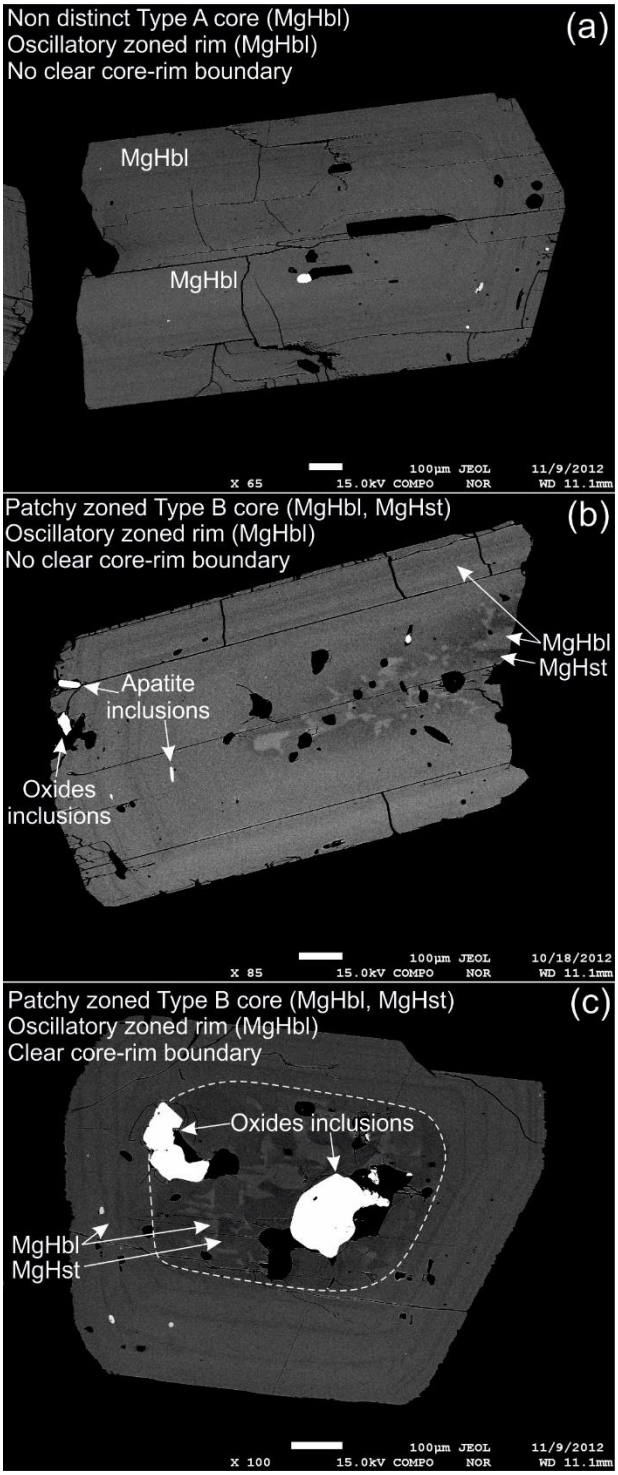

Fig. 3.7 SEM images (personal communications with C. G. Cooper) of amphibole crystals from the Ongatiti ignimbrite. (a) Type A crystal with non-distinct core and oscillatory zoned rim (no compositional contrast). (b-c) Type B crystals with patchy zoned core (brighter patches of MgHbl compositions and dark patches of MgHst compositions) and oscillatory zoned rim (MgHbl), and with the presence of apatite and Fe-Ti oxides inclusions. The crystal in panel (c) has a clearer core-rim boundary than the crystal in panel (b). We interpret that Type A crystal cores are in equilibration with melts of matrix glass compositions due to longer timescales of interaction with the rim-crystallizing melt, while Type B cores clearly showing disequilibrium textures have interacted with the rim-crystallizing melt in relatively shorter timescales. See text for further details.

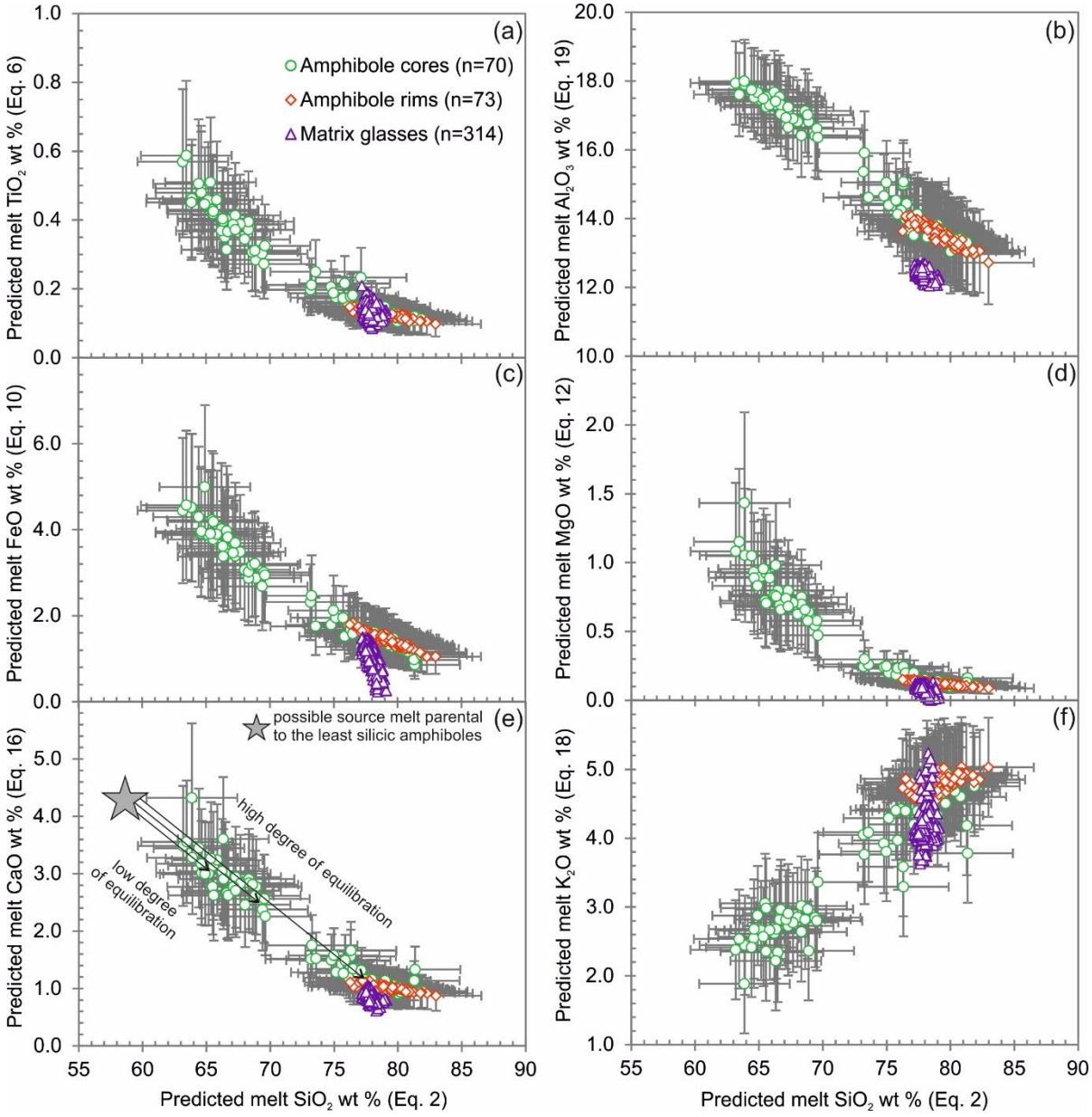

Fig. 3.8 The predicted melt compositions from cores and rims of amphiboles in the Ongatiti ignimbrite, and the measured compositions of matrix glasses of pumice clasts in the Ongatiti ignimbrite. The grey star in (e) illustrates a possible source melt parental to the least silicic amphiboles, different degrees of equilibration (shown by arrows with different lengths) with silicic melt of matrix glass compositions (purple triangles) may be responsible for producing the spread in the crystal chemistry of Type B cores and hence predicted melt compositions. Type A cores have compositions similar to rims and we interpret that they are formed by full equilibration with the melt of matrix glass compositions. See text for discussions.

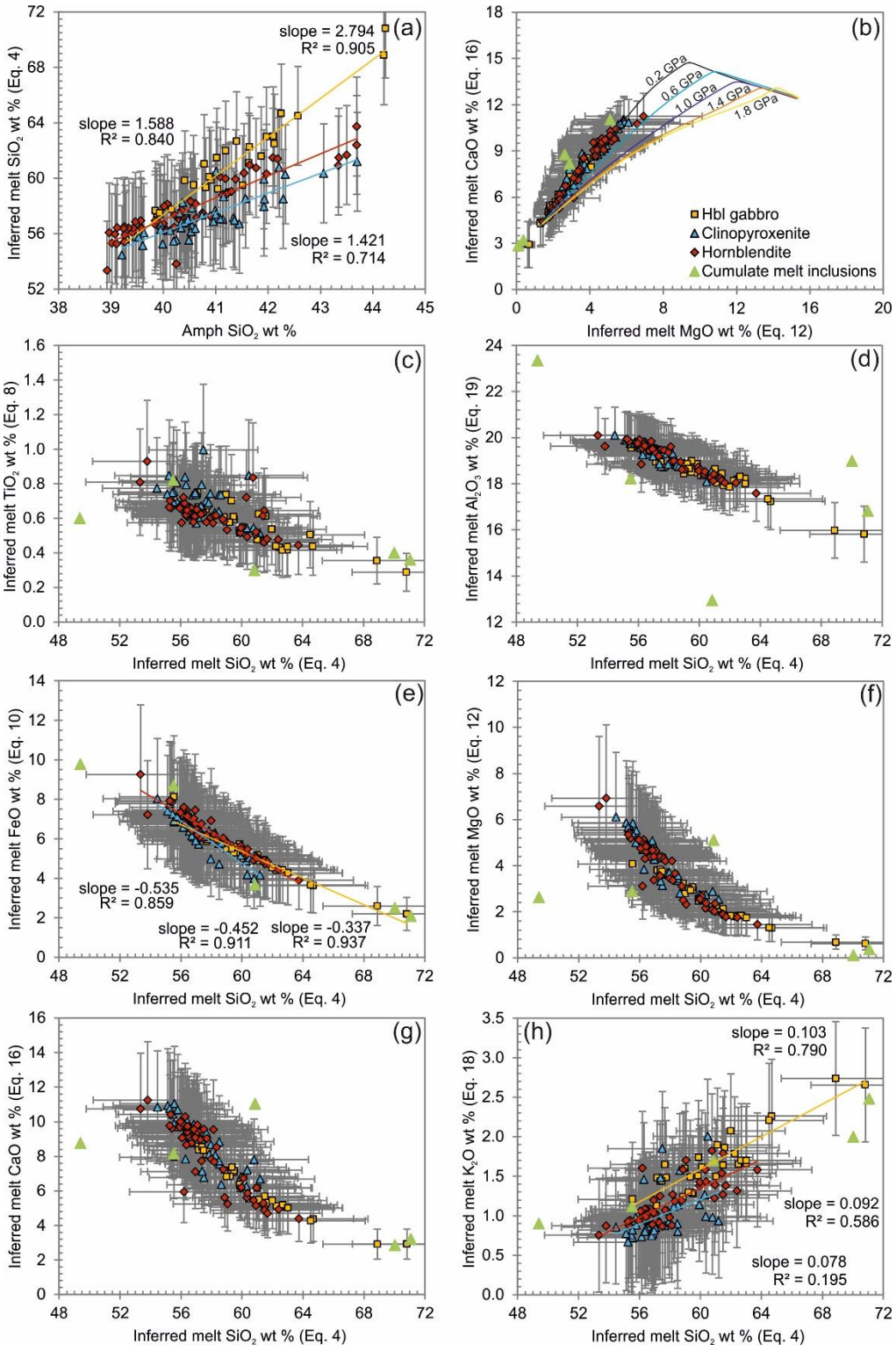

Fig. 3.9 (a) Inferred melt SiO_2 content vs SiO_2 content in amphibole from clinopyroxenite, hornblendite and hornblende gabbro (Hbl gabbro) xenoliths from Grenada; (b-h) inferred major element compositions in the melts in equilibrium with the plutonic amphiboles from Grenada. Curves in (b) illustrate the results of MELTS modelling with a range of pressure input (Stamper et al., 2014). The variations of the predicted melt CaO content and MgO content are consistent with low-pressure fractionation. With similar amphibole crystal SiO_2 content (between 40 and 44 wt %), melts in equilibrium with clinopyroxenite, hornblendite and hornblende gabbro are progressively more silicic (a) and the variations of melt FeO and K_2O contents against SiO_2 also display different slopes (e, h).

3.11. TABLES

Table 1 Materials, conditions and run products of the selected experimental studies

References for calibration	Rock type	*N* (130)	*P* MPa	*T* °C	Amphibole Species	RR2012	E2014
Adam & Green 1994	basanite	5	500-2,000	1,000-1,100	MgHst	Y	
Alonso-Perez et al., 2009	andesite	12	800-1,200	800-950	Tsch		
Barclay & Carmichael 2004	trachybasalt	3	104-223	1000-1035	MgHst		Y
Bogaerts et al. 2006	granodiorite	2	404	850	Tsch		Y
Costa et al. 2004	dacite	4	200-206	850-900	MgHbl, MgHst	Y	Y
Dalpé & Baker, 2000	basanite-basalt	7	1,500-2,500	1,000-1,100	MgHst, Parg	Y	
Gardner et al., 1995	dacite	6	150-250	850	Tsch, MgHbl	Y	
Green & Pearson 1985	andesite	4	750-2,000	900-1,050	MgHst, Parg, Tsch		
Grove et al. 2003	Mg andesite	1	200	990	MgHst		
Hilyard et al. 2000	dacite-tonalite	5	200-500	900-945	MgHst, MgHbl, Parg, Tsch		
Klein et al. 1997	dacite	2	1,000	850-900	Tsch		
Martel et al. 2013	trachyte	2	200-400	825-900	MgHst		Y
Moore & Carmichael, 1998	basaltic andesite-andesite	6	101-250	900-1,000	MgHbl, Tsch	Y	
Nandedkar 2014	basaltic andesite-rhyolite	3	700	920-1,010	Tsch, MgHst		
Nekvasil et al., 2004	basalt-dacite	8	430-930	920-1040	Kaer, Tsch	Y	
Nicholls & Harris 1980	basalt-andesite	1	1,000	900	Tsch		
Pichavant et al. 2002	basaltic andesite	6	399-427	945-1,000	Tsch	Y	Y
Pichavant et al. 2009	quartz diorite	3	200	850	MgHst, Tsch		
Rutherford & Devine 2003	andesite	3	200	810-840	MgHbl	Y	Y
Sato et al. 2005	dacite	5	200	850	MgHbl, Tsch	Y	Y
Scaillet & Evans 1999	dacite	7	224-389	776-899	MgHbl, Tsch	Y	Y
Sisson 1994	basalt-andesite-dacite	4	200	1050	MgHbl, MgHst		
Sisson & Grove 1993	high-Al basalt	11	200	925-970	MgHst		Y
Tiepolo et al. 2000	basalt-andesite	20	1400	950-1075	Kaer, MgHst, Parg		

References for test	Rock type	*N* (74)	*P* MPa	*T* °C	Amphibole Species	RR2012	E2014
Adam & Green 2006	basanite	1	1,000	1,025	MgHst		
Adam et al. 1993	basanite-basalt	4	1,000-2,000	1,000-1,050	MgHst, Parg		
Blatter & Carmichael, 2001	andesite	2	132-194	925-950	Tsch		
Carroll & Wyllie, 1989	tonalite	2	1,500	900-950	MgHst, Parg		
Ernst & Liu, 1998	basalt	5	800-1,400	900-950	Tsch		
Fujinawa & Green, 1997	basalt-andesite	16	500-2,000	900-1,100	MgHst, Parg, Tsch		
Grove et al., 1997	basalt	5	200	905-980	Tsch		
Holtz et al., 2005	dacite	10	200-300	775-875	MgHst, Tsch, MgHbl		
Kawamoto, 1996	basaltic andesite	2	500	975	Parg, Tsch		
Naney, 1983	granodiorite	2	800	900	MgHst, Parg		
Patino-Douce & Beard, 1995	quartz amphibolite	6	300-1,250	875-930	MgHbl, Tsch		
Prouteau & Scaillet, 2003	dacite	9	830-970	750-892	MgHst, Tsch, MgHbl		
Prouteau et al., 1999	dacite	2	220-1,000	750-899	MgHbl		
Skjerlie & Johnston, 1996	andesitic metavolcanoclastics	4	1,000-1,500	850-900	MgHst, Tsch		
Springer & Seck, 1997	granulite	2	1,000-1,500	900-1,000	Tsch, Parg		
Xiong et al., 2005	basalt	2	1,000	925-975	Tsch		

Y indicates the data of the reference are also used in the calibrations of chemometric equations in Ridolfi and Renzulli (2012) and Erdmann et al. (2014)'s study.

Table 3.1

Table 2 Results of multiple linear regressions used for estimating melt major element compositions on the basis of temperature and calcic-amphibole component

Eq.	Dependent variable	Range of variation	N	Constant	Independent variable coefficients									R^2	SE	SE in wt %	se of test
					T °C	Si	Al (vi)	Mg	Fe3+	Fe2+	Ti	Ca	Na (A)				
1	SiO2 (wt %)	39.6 - 79.2	130	-239.3567	-0.0308	36.6276	22.0010		26.6213	5.6001	48.2461	31.8979	14.9367	0.874		3.32	5.15
2	SiO2 (wt %)	39.6 - 79.2	130	-384.8195		48.3551	32.6767		36.7324	7.5620	64.7844	46.9687	18.5029	0.855		3.55	5.82
3	SiO2 (wt %)	39.6 - 79.2	130	-127.9320	-0.0300	39.3800		-27.7929		-23.1936	27.6206	34.5097	17.1069	0.871		3.36	5.22
4	SiO2 (wt %)	39.6 - 79.2	130	-214.8001		49.9275		-36.9481		-30.5601	33.2703	47.7379	20.2747	0.852		3.57	5.84
5	lnTiO2	-2.8 - 1.8	130	29.1200	**0.0018**	-3.2797	-2.3446		-3.0219	-0.8999	**-2.8339**	-3.2723	-2.5173	0.843	0.36	0.57	0.45
6	lnTiO2	-2.8 - 1.8	130	37.6762		-3.9695	-2.9726		-3.6167	-1.0153	-3.8067	-4.1588	-2.7270	0.836	0.37	0.59	0.47
7	lnTiO2	-2.8 - 1.8	130	14.9760	**0.0019**	-3.3595		2.8363		2.0537		-3.0194	-2.6671	0.834	0.37	0.57	0.50
8	lnTiO2	-2.8 - 1.8	130	19.3697		-3.8556		3.2213		2.3144		-3.5001	-2.7795	0.827	0.38	0.60	0.54
9	lnFeO	-0.3 - 2.8	130	**5.4751**	0.0034	-1.9576	**1.1926**	***1.8883***	**1.3685**	***1.9042***		**-1.9707**		0.767	0.35	1.87	2.37
10	lnFeO	-0.3 - 2.8	130	12.2163		-2.9194	1.5899	3.1038	1.7896	2.9239		-3.3256		0.728	0.38	2.00	2.72
11	lnMgO	-2.2 - 2.5	130	***3.2169***	0.0045	-1.6836	1.1277	1.0037						0.846	0.41	0.97	1.07
12	lnMgO	-2.2 - 2.5	130	13.2278		-2.7199	1.0381	1.2489						0.798	0.46	1.11	1.47
13	CaO (wt %)	0.5 - 14.7	130	51.4251	0.0092	-7.2727			-4.4674	-2.6473	-10.3050		-4.4228	0.738		1.44	1.80
14	CaO (wt %)	0.5 - 14.7	130	69.0838		-8.6230			-5.1598	-3.2876	-9.3680		-4.1935	0.715		1.49	2.02
15	lnCaO	-0.7 - 2.7	130	6.4750	0.0014	-0.4368		-1.6425	-1.1291	-2.2978		2.1915		0.735	0.29	1.50	1.87
16	lnCaO	-0.7 - 2.7	130	9.6837		-0.7807		-1.3717	-1.1206	-2.1177		1.7914		0.724	0.30	1.56	2.06
17	K2O (wt %)	<5.0	130	33.6113	-0.0043	-5.6238	-2.7212	6.3530		7.6216	-5.9949	-6.7867	-7.0326	0.652		0.70	0.85
18	K2O (wt %)	<5.0	130	20.5281		-4.0234	-2.6110	4.9890		6.5012	-5.0490	-4.7773	-6.5255	0.628		0.72	0.95
19	Al2O3 (wt %)	11.4 - 21.5	130	26.4045			2.9902	-3.6838		-4.5202	3.6620		8.4222	0.604		1.21	1.46

Bold font indicate the p-value of the parameter or the constant is 0.01 < p-value < 0.03; bold italic font indicate p-value > 0.03.

Table 3 Equilibrium test for amphibole-glass pairs from pumice clasts in Ongatiti ignimbrite

Pumice #		Am. wt %	Am.sd.	Gl. wt %	Gl.sd.	Pred. wt %	Pred.sd.	MR.se.	Diff.	Diff%	Diff.>MR.se?
GC1	SiO_2	44.62	0.33	77.75	0.16	77.88	0.91	5.84	0.13	0.2%	
(N.amph = 28)	TiO_2	1.77	0.04	0.13	0.02	0.14	0.01	0.05	0.01	7.9%	
(N.gl = 22)	Al_2O_3	7.68	0.16	12.34	0.11	13.75	0.14	1.46	1.41	11.4%	
	FeO	19.40	0.30	1.30	0.07	1.47	0.13	0.56	0.18	13.8%	
	MgO	10.17	0.19	0.11	0.01	0.13	0.01	0.06	0.02	18.2%	
	CaO	10.59	0.08	0.85	0.02	1.03	0.04	0.31	0.18	**20.6%**	
	K_2O	0.65	0.03	4.08	0.12	4.67	0.07	0.95	0.59	14.4%	
	Na_2O	1.98	0.05	3.41	0.17						
	MnO	0.48	0.03	0.04	0.02						
P2023	SiO_2	45.93	0.39	77.86	0.24	80.61	0.70	5.84	2.75	3.5%	
(N.amph = 15)	TiO_2	1.75	0.06	0.14	0.02	0.12	0.01	0.05	-0.02	-14.9%	
(N.gl = 28)	Al_2O_3	7.31	0.17	12.39	0.08	13.12	0.12	1.46	0.73	5.9%	
	FeO	19.33	0.64	1.20	0.19	1.14	0.08	0.43	-0.06	-5.1%	
	MgO	10.37	0.37	0.10	0.02	0.10	0.01	0.04	0.00	-1.4%	
	CaO	10.74	0.07	0.92	0.07	0.92	0.05	0.28	0.00	0.4%	
	K_2O	0.61	0.04	3.86	0.15	4.84	0.15	0.95	0.99	**25.5%**	Y
	Na_2O	1.81	0.06	3.50	0.11						
	MnO	0.41	0.02	0.03	0.02						
P2026	SiO_2	45.07	0.44	78.23	0.23	76.10	2.40	5.84	-2.13	-2.7%	
(N.amph = 5)	TiO_2	1.82	0.08	0.13	0.02	0.15	0.01	0.06	0.02	14.3%	
(N.gl = 28)	Al_2O_3	7.48	0.18	12.30	0.07	13.51	0.13	1.46	1.20	9.8%	
	FeO	20.11	0.29	0.73	0.27	1.65	0.25	0.63	0.92	**126.4%**	Y
	MgO	10.45	0.22	0.05	0.03	0.14	0.02	0.06	0.09	**173.5%**	Y
	CaO	10.79	0.04	0.74	0.06	1.03	0.05	0.31	0.29	**39.4%**	
	K_2O	0.63	0.04	4.65	0.33	4.89	0.08	0.95	0.24	5.2%	
	Na_2O	1.92	0.06	3.15	0.20						
	MnO	0.44	0.02	0.01	0.01						
P2027	SiO_2	45.15	0.46	77.97	0.43	79.57	1.32	5.84	1.60	2.1%	
(N.amph = 33)	TiO_2	1.82	0.06	0.13	0.01	0.13	0.01	0.05	0.00	1.5%	
(N.gl = 9)	Al_2O_3	7.23	0.22	12.50	0.14	13.15	0.23	1.46	0.64	5.2%	
	FeO	19.53	0.31	0.72	0.40	1.26	0.15	0.48	0.54	**75.3%**	Y
	MgO	10.24	0.25	0.04	0.03	0.11	0.01	0.05	0.07	**160.6%**	Y
	CaO	10.66	0.11	0.77	0.07	0.94	0.05	0.28	0.17	**21.6%**	
	K_2O	0.60	0.04	4.79	0.34	4.92	0.07	0.95	0.13	2.7%	
	Na_2O	1.78	0.09	3.06	0.19						
	MnO	0.37	0.02	0.01	0.01						
P2184	SiO_2	44.74	0.35	78.63	0.30	78.47	1.01	5.84	-0.16	-0.2%	
(N.amph = 30)	TiO_2	1.81	0.11	0.13	0.01	0.14	0.01	0.05	0.01	4.2%	
(N.gl = 29)	Al_2O_3	7.60	0.26	12.21	0.08	13.41	0.21	1.46	1.20	9.8%	
	FeO	19.97	0.54	0.74	0.30	1.41	0.12	0.54	0.67	**90.7%**	Y
	MgO	9.95	0.31	0.06	0.03	0.12	0.01	0.05	0.06	**95.6%**	Y
	CaO	10.64	0.11	0.79	0.02	0.99	0.07	0.30	0.19	**24.6%**	
	K_2O	0.64	0.04	4.09	0.13	4.88	0.17	0.95	0.79	19.3%	
	Na_2O	1.83	0.06	3.32	0.13						
	MnO	0.38	0.02	0.02	0.01						

Table 3.3

CHAPTER 4

New insights into trace element partitioning in calcic amphibole from multiple regression analysis

J. ZHANG*, M. C. S. HUMPHREYS, G. F. COOPER, J. P. DAVIDSON, C. G. MACPHERSON

DEPARTMENT OF EARTH SCIENCES, UNIVERSITY OF DURHAM, DURHAM, DH1 3LE, UK

*Corresponding author. E-mail: jing.zhang5@durham.ac.uk

ABSTRACT

We present a new multiple regression (MR) analysis of published amphibole-melt trace element partitioning data, with the aim of retrieving robust relationships between amphibole crystal-chemical compositions, temperature and trace element partition coefficients ($^{Amph/L}D$). We examined experimental data for calcic amphiboles of kaersutite (Kaer), pargasite (Parg), tschermakite (Tsch), magnesiohornblende (MgHbl) and magnesiohastingsite (MgHst) compositions crystallized from basanitic-rhyolitic melts. The MR analysis demonstrates the varying significance of temperature and amphibole major element components assigned to different crystallographic sites (T, M_{1-3}, M_4, A) as independent variables in controlling $^{Amph/L}D$, and it allows us to retrieve statistically significant relationships for Sr, Pb, HFSE (Ti, Zr, Hf, Nb and Ta), REE and Y ($n > 25$, $R^2 > 0.6$, p-value < 0.05). Reliability test indicates that $^{Amph/L}D$ of Sr, Pb, Ti, Zr, Nb, La, Ce, Nd, Sm, Dy and Er can be reproduced by the multiple regression equations with reasonable accuracy.

A significant advantage of our study over previous work linking $^{Amph/L}D$ to melt polymerization (e.g. Tiepolo et al., 2007) is the ability to recover $^{Amph/L}D$ and reconstruct melt compositions from *in situ* amphibole compositional analyses. Using compositional data of amphiboles from Mt. Pinatubo, Mt. Hood, Shiveluch Volcano, Mt. St. Helens and the Ongatiti ignimbrite of the Mangakino Volcano, we are able to distinguish the relative importance of melt trace element contents and $^{Amph/L}D$ in controlling amphibole trace element contents: melt compositions of Sr, Pb, Ti and Zr are the dominant factor governing their concentrations in amphibole; in contrast, Nb, REE and Y contents in amphiboles are more related to $^{Amph/L}D$ and less related to melt compositions. We also demonstrate that the inferred melt major and trace element compositions from amphibole crystal chemistry, combined with amphibole textural information, can be a powerful tool in decoding the magmatic processes occurring in magma plumbing systems. Magma mixing/mingling and recycling of earlier-fractionated crystals from crystal mushes are demonstrated to be responsible to amphibole compositional diversity in arc magmas.

KEY WORDS: Calcic amphibole; Trace element; Partitioning; Partition coefficient; Multiple regression; Magma mixing.

This chapter is prepared to be submitted to *Journal of Petrology*.

4.1. INTRODUCTION

Understanding trace element partitioning between minerals and coexisting melts during melt generation and evolution/crystallization is fundamental in understanding the nature of magmatic processes. Partition coefficient ($D = C_{mineral}/C_{melt}$) is a parameter which describes the preference of an element to partition into either mineral or liquid phases, and thus is widely used for modelling the evolution path of geochemistry during magmatic processes (Rollinson, 1993). Amphibole, one of the most important mineral phases in calc-alkaline magmas and plutons, and a major component of middle-lower crust (Davidson *et al.*, 2007; Rudnick & Fountain, 1995), is suggested to be widely crystallized and fractionated from mantle-derived magmas in subduction zones globally (Alonso-Perez *et al.*, 2009; Cawthorn & O'Hara, 1976; Davidson *et al.*, 2007; Kratzmann *et al.*, 2010; Krawczynski *et al.*, 2012; Larocque & Canil, 2010; Neill *et al.*, 2013). This process is thought to play a significant role in forming intermediate-felsic magmas and amphibole-bearing cumulates in subduction zones (Arculus & Wills, 1980; Hidalgo & Rooney, 2010; Nandedkar *et al.*, 2014; Stamper *et al.*, 2014). Amphibole is also a host for a diverse range of trace elements due to the large availability of distinct crystal sites, therefore, it has great potential for recording the melt compositions and the trace element capacity of the amphibole-abundant mid-lower crust. However, in order to retrieve this information, it is important to quantify the amphibole/melt partition coefficient ($^{Amph/L}D$) for a range of trace elements.

$^{Amph/L}D$ is controlled by a range of thermodynamic and geochemical parameters, such as melt and mineral compositions, temperature, pressure and oxygen fugacity (Blundy & Wood, 1994; Dalpé & Baker, 2000; Hilyard *et al.*, 2000; Nandedkar, 2014; Tiepolo *et al.*, 2007). Attempts to constrain $^{Amph/L}D$ have been made previously, either through analysing natural phenocryst-melt pairs in equilibrium, or through experimental studies carried out on natural magmatic samples under a range of pressure-temperature-melt geochemistry (p-T-X) conditions. The variation of $^{Amph/L}D$ values derived from these different natural systems or under different initial conditions can be up to one order of magnitude (e.g. $^{Amph/L}D_{Zr,\ Nb}$, see below). Therefore, understanding the controlling parameters of $^{Amph/L}D$ is a priority for choosing appropriate $^{Amph/L}D$ values for geochemical modelling. A previous review on trace element partitioning between amphibole and melt suggested that $^{Amph/L}D$ for a large range of geochemically important elements are strongly correlated with the degree of melt polymerization (Tiepolo *et al.* (2007), and this is confirmed by a more recent experimental study (Nandedkar, 2014). However, this observation still does not permit inverse retrieval of unknown melt compositions from analysis of amphiboles, a primary aim in many petrological studies.

Parameterizations of D have been reported for mineral phases including olivine, orthopyroxene, clinopyroxene, plagioclase (Bédard, 2005; Bédard, 2006; Bédard, 2007; Bédard, 2014; Sun & Liang, 2012), but an equivalent study for amphibole remains absent. Rather, to date the quantification of $^{Amph/L}D$ from the perspective of mineral compositions remains limited and unsystematic (e.g. Bottazzi *et al.*, 1999; Nandedkar, 2014). However, the amphiboles crystallizing from previous experimental $^{Amph/L}D$-determining studies and from natural melts display a progressive change in crystal chemistry over a series (basanitic to rhyolitic) of melt compositions (see below and **Fig. 4.1**). Therefore, we can test whether the changing $^{Amph/L}D$ values are also related to the compositions of amphibole and temperature. Moreover, the crystal lattice strain model demonstrates that the crystal structure is also important in incorporating a series of elements sharing similar ionic charge and radius (Blundy & Wood, 1994). Thus, the purpose of this study is to provide new insights into trace element partitioning in calcic amphiboles on the basis of known amphibole compositions, to allow the compositions of coexisting melts to be inferred from solid crystal phases.

In this study, we first report the results of multiple regression analysis for previously published $^{Amph/L}D$ values. A series of multiple linear regression equations is derived to predict $^{Amph/L}D$ from amphibole crystal chemistry and temperature. Then we carry out reliability tests to demonstrate the accuracy of the predicted $^{Amph/L}D$ using this method. We will explore whether the amphibole trace element variations observed are driven by variations in crystal chemistry (and hence $^{Amph/L}D$) or melt compositional differences, using compositional data of amphiboles and corresponding inferred melts

from Mt. Pinatubo, Mt. Hood, Shiveluch Volcano, Mt. St. Helens and the Ongatiti ignimbrite of the Mangakino Volcano. The magmatic processes that occurred in the magma plumbing systems of Pinatubo and Mangakino volcanoes associated with amphibole compositional diversity are then discussed on the basis of the inferred melt compositions.

4.2. BACKGROUND

4.2.1. Site preferences of trace elements in amphibole

The double-chain crystal structure of amphibole forms different types of crystallographic sites which can accommodate various geochemically significant trace elements, including large ion lithophile elements (Rb, Sr, Ba), Pb, U, Th, high field strength elements (Ti, Zr, Hf, Nb and Ta), rare earth elements (REE) and Y, as well as transitional metals (Sc, V, Cr, Ni, Zn, Cu). The crystallographic sites of calcic amphiboles include tetrahedral site (T), two major types of octahedral sites (small-medium M1-3 sites, and large M4 site), and a vacant/partially-filled site (A), and these are occupied by different major elements. Si and Al are the dominant components of the T site; Mg, Fe (both Fe^{2+} and Fe^{3+}), Ti, Mn and Al occupy the M1-3 sites; the larger octahedral M4 site is dominated by Ca and Na; and Na also sits in the A site together with K. Crystal-chemical control over the partitioning of trace element into mineral phases is constrained by the ionic charge and radius of the trace element and the major element being replaced (e.g. the crystal lattice strain model, see below).

Rb and Ba are only accommodated in amphibole A site due to their large ionic radius (**Table 4.1**, ionic radius data from (Shannon, 1976); Sr can be incorporated into both A site and M4 site theoretically; Pb mainly occurs as bivalent trace element phase in amphibole and is commonly preferred by the A site (Tiepolo *et al.*, 2007).

Site preference for HFSE in titanian pargasite and kaersutite is discussed by Oberti *et al.* (2000), Tiepolo *et al.* (2001) and Tiepolo *et al.* (2000b), according to which the distribution of Ti among octahedral M1-3 sites of amphibole is controlled by the following two exchange vectors: (1) $^{M1}Ti^{4+} + 2^{O3}O^{2-} = {}^{M1}(Mg, Fe, Mn)^{2+} + 2^{O3}OH^{1-}$; (2) $^{M2,M3}Ti^{4+} + 2^{T1,T2}Al^{3+} = {}^{M2,M3}(Mg, Fe, Mn)^{2+} + 2^{T1,T2}Si^{4+}$. Ti presence in M1 site is governed by the dehydrogenation (the presence of oxo component at O3 site, $^{O3}O^{2-}$), which is strongly dependent on the intensive parameters of temperature and oxygen fugacity (fO_2). Under high temperature and high fO_2 conditions (e.g. upper mantle), this exchange mechanism is thought to be more common (Tiepolo *et al.*, 2001). Ti presence in M2 site is correlated with the amount of tetrahedral Al, and this mechanism is more commonly known as 'Ti-Tschermak substitution'. The incorporation of Ti in M3 site is rare and only reported in a few examples of titanian pargasite and kaersutite with high octahedral Al ($\geq$ 2.0 apfu), and is negligible for the majority of calcic amphiboles. Incorporation of Zr and Hf (tetravalent HFSE) in amphibole is analogous to clinopyroxene, with their preferred site of M2 (equivalent to M1 site in clinopyroxene), and probably achieved by substitution for Ti due to the similarities in their ionic radii (Oberti *et al.*, 2000). In contrast, $^{Amph/L}D$ of Nb and Ta (pentavalent HFSE) are incorporated preferentially into the M1 site (Tiepolo *et al.*, 2000b).

REE and Y are commonly believed to be partitioned into the M4 site of amphibole because their cation radii (0.977-1.16Å, Table **1**; Shannon, 1976) are most similar to Ca (1.12Å; Brenan *et al.*, 1995; Hilyard *et al.*, 2000; Klein *et al.*, 1997). The ionic radius of REE decreases with increasing atomic number: light REE (LREE, La, Ce, Pr) have larger ionic radius than Ca, while heavy REE (HREE) and Y have smaller radius than Ca. Bottazzi *et al.* (1999) suggests that HREE and Y may also be incorporated in a smaller M4 site (M4') comprising Li, Mg and Fe^{2+} (also referred to as the cummingtonite component).

4.2.2. REE partitioning in amphiboles: the crystal lattice strain model

A theoretical way of predicting $^{Amph/L}D$ is given by the crystal lattice strain model of Blundy and Wood (1994). This model demonstrates that the maximum capacity for a given trace element in a mineral crystallographic site is related to the temperature, the charge and radius of the ion entering into the site, and the size and the elasticity of lattice site. For example, for an isovalent series of ions *i* with radius of r_i entering the lattice site with radius of r_0 and Young's Modulus *E*, the partition coefficient D_i can be calculated using the following equation:

$$D_i = D_0 \exp\left\{-4\pi N_A E\left[\frac{1}{2} r_0 (r_i - r_0)^2 + \frac{1}{3}(r_i - r_0)^3\right] / RT\right\}$$

where D_0 is the strain-compensated partition coefficient for an ion that perfectly fits the lattice (radius of r_0), N_A is the Avogadro's Number, *R* is the gas constant, and *T* is temperature in Kelvin. Application of the crystal lattice strain model results in a parabolic curve against ionic radius (also referred to as the Onuma curve following Onuma *et al.*, 1968), peaking at r_0. The Young's Modulus *E* controls the tightness of the curve, and D_0 decides the height of the curve. MREE generally have higher $^{Amph/L}D$ than LREE and HREE since the ionic radiuses of MREE are closer to the site radius than LREE and HREE. The results of a recent study that parameterizes D_0 as a function of pressure, temperature, amphibole and melt compositions shows that D_0 is negatively correlated with temperature, amphibole Mg and the mole fraction of Ca in the melt, and positively correlated with amphibole Ti, while *E* and r_0 remain relatively constant during parameterizations (Shimizu *et al.*, 2015).

4.2.3. Compositional and temperature control over $^{Amph/L}D$

The relationship between $^{Amph/L}D$ of various trace elements and the degree of melt polymerization (represented by the relative proportion of network-forming components, X_{nf}/X) is explored by Tiepolo et al. (2007). Their results demonstrate that the $^{Amph/L}D$ of most trace elements (except Sr and Ba) are exponentially correlated with X_{nf}/X, indicating that the degree of melt polymerization is the dominant controlling factor of $^{Amph/L}D$ for most trace elements. However, a compilation of data from the literature shows greater complexity than this would suggest (**Fig. 4.2**). With increasing SiO_2 content from mafic melts to felsic melts, $^{Amph/L}D$ of HFSE, Pb, REE and Y are increasing (**Fig. 4.2h, j, m, n, o**), while $^{Amph/L}D$ of Rb is decreasing (**Fig. 4.2a**). $^{Amph/L}D_{Rb}$ is also positively correlated with DK ($^{Amph}K_2O/^{Melt}K_2O$) due to replacement of K in A site (**Fig. 4.2b**), however, $^{Amph/L}D_{Rb}$ is not correlated with amphibole crystal chemistry (**Fig. 4.2c-d**). In contrast, $^{Amph/L}D_{Sr}$ does not correlate with melt SiO_2 content or DCa ($^{Amph}CaO/^{Melt}CaO$; **Fig. 4.2f-g**). We also observe that $^{Amph/L}D_{Sr}$ is negatively correlated with amphibole Mg# and positively correlated with amphibole Ti (**Fig. 4.2d-e**), although Mg, Fe^{2+} and Ti are M1-3 site components. $^{Amph/L}D_{Ba}$ does not correlate with the degree of melt polymerization, amphibole crystal chemistry, or DK. Therefore, it is unclear to us what is the dominant factor controlling $^{Amph/L}D_{Ba}$. $^{Amph/L}D_{Pb}$ does not correlate with DK, instead, it correlates with amphibole Mg# negatively and with amphibole octahedral Al positively (e.g. **Fig. 4.2i**). $^{Amph/L}D_{Ti}$ is not related to amphibole crystal chemistry (**Fig. 4.2l**), and is strongly dependent on the degree of melt polymerization. Interestingly, $^{Amph/L}D_{Ti}$ is negatively correlated with melt TiO_2 content (**Fig. 4.2k**). $^{Amph/L}D$ of Zr, Hf, Nb and Ta are also not related to amphibole crystal chemistry and they are solely controlled by melt compositions (**Fig. 4.2m-n**). $^{Amph/L}D_{REE, Y}$ are strongly correlated with melt SiO_2 content and DCa (**Fig. 4.2o, p**), and not correlated with amphibole crystal chemistry (**Fig. 4.2q, r**).

The published experimental data considered in Tiepolo et al. (2007)'s study also display a negative correlation between temperature and the degree of melt polymerization. Therefore, the relative importance of temperature and the degree of melt polymerization in controlling $^{Amph/L}D$ is actually not constrained. The results of a more recent study of Nandedkar (2014), which focuses on determining $^{Amph/L}D$ from experiments modelling liquid line of descent, are also unable to solve this issue.

4.3. METHODOLOGY

4.3.1. Selecting P-T-X-$^{Amph/L}$D data from literature

We consider $^{Amph/L}$D values determined from published experimental studies. Most of the references cited here (**Table 4.2**) are listed in the GERM Partition Coefficient Database (http://earthref.org/KDD/) and traceDs database (http://traceds.ofm-research.org/index.php; Nielsen *et al.*, 2015), and many of them overlap those included in a previous $^{Amph/L}$D review study (Tiepolo *et al.*, 2007). The experimental studies selected (Adam & Green, 1994; Dalpé & Baker, 2000; Green & Pearson, 1985; Hilyard *et al.*, 2000; Klein *et al.*, 1997; Latourrette *et al.*, 1995; Nicholls & Harris, 1980; Sisson, 1994; Tiepolo *et al.*, 2001; Tiepolo *et al.*, 2007; Tiepolo *et al.*, 2000a; Tiepolo *et al.*, 2000b) are carried out under a large variation of pressure-temperature conditions (200-2,500 MPa, 780-1,100 ºC), using melts of various compositions (basanite to rhyolite, **Fig. 4.1**, see details in **Table 2**). The temperature and melt compositions generally follow the trend of liquid line of descent by eye, except several outliers from Sisson (1994) and Green & Pearson (1985) (**Fig. 4.1c-d**). Amphibole examined from those experimental studies show large major element compositional variability, including compositions of pargasite (Parg), magnesiohastingsite (MgHst), kaersutite (Kaer), tschmakite (Tsch) and magnesiohornblende (MgHbl) (**Fig. 4.1b, d, f**).

Published amphibole major element compositions are converted from wt.% oxide to formula proportions (atoms per formula unit/apfu), following the amphibole stoichiometry calculation procedure recommended by International Mineralogical Association (IMA, (Leake *et al.*, 1997), in order to identify the amphibole species. Si, Al, Ti, Cr, Fe, Mn, Mg are allocated to the T and M1-3 sites and adjusted to 13 cations (13eCNK), and Fe^{3+} and Fe^{2+} are determined by the charge balance during the calculation. Ca, Na and K are allocated to the M4 and A sites. According to the nomenclature recommended by IMA (Hawthorne *et al.*, 2012), our compiled compositional data of amphibole classify themselves into non-calcic (low-Ca) and calcic group, and the latter is subcategorized into Parg, MgHst, Kaer, Tsch and MgHbl (**Table 4.2**). In this study we only consider $^{Amph/L}$D derived from calcic amphiboles for those that meet the standard of stoichiometry calculation (Leake *et al.*, 1997).

Errors on experimentally derived $^{Amph/L}$D data are usually provided by the original literature. Those errors are dominated by micro-analytical uncertainties. Another potential flaw in the experimentally determined $^{Amph/L}$D data is that co-crystallizing mineral phases may subtract some preferential elements, for example, Sr and Eu may be incorporated into plagioclase co-crystallized with amphibole during the experiments. This could be a cryptic bias in the validity of $^{Amph/L}$D for the corresponding element. Potential errors in $^{Amph/L}$D may also involve disequilibrium between the melt and the mineral assemblage as a result of insufficient experimental duration.

4.3.2. Multiple regression analysis

Although correlations between $^{Amph/L}$D and amphibole major element components are occasionally seen (for example, $^{Amph/L}D_{Sr}$ correlates with amphibole Ti content, see **Fig. 4.2e**), they are not ubiquitous for all of the considered trace elements, so we suspect that major element components of different sites might have a combined effect on $^{Amph/L}$D. In order to test this proposal, we carry out multiple regression (MR) analyses on the compiled $^{Amph/L}$D from calcic amphiboles, using the Data Analysis functions in Microsoft Excel. The MR analysis is a way of predicting values (dependent variables) based on multiple input parameters (independent variables). Temperature (T) and amphibole formula proportions including tetrahedral site Si (Si_T), M1-3 site Al (Al_{VI}), Ti, Fe^{3+}, Mg and Fe^{2+}, M4 site Ca (Ca_{M4}), and A site Na (Na_A) are considered as input parameters for the multiple regression analyses (**Tables 4.3-4.5**). The analyses are applied to LILE (Rb, Sr, Ba), Pb, U, Th, HFSE (Ti, Zr, Hf, Nb and Ta), REE and Y, for which sufficient partition coefficient data have been collected previously to allow statistically significant predictions (defined as number of available data $N \geq 30$).

For other elements such as light elements (Li, Be, B) and transitional metals there were insufficient available $^{Amph/L}D$ data, so the MR analyses are not performed and not discussed in this study.

The output of the multiple regression analysis is given as the intercept/constant and the coefficients of each independent variable, on which basis a multiple regression equation can be derived (**Tables 4.3-4.5**). For example, the equation for the prediction of $^{Amph/L}D_{Rb}$ (*Eq. 1*) is expressed as:

$$^{Amph/L}D_{Rb} = \exp\{-10.0892 + 0.0098 * T(^oC) - 3.1103 * Ti\ (apfu) - 1.4521 * Na_A\ (apfu)\}$$

Evaluation of the function is based on parameters including coefficient of determination (R^2), standard error (SE), number of objects/observations (N), and the confidence of the coefficients for each independent variable (p-value). A correlation that we deem to be statistically significant is reflected by $N \geq 30$, $R^2 \geq 0.6$ and p-values of all of the determined coefficients << 0.05. The multiple regression analysis for each element is performed following this procedure: all independent variables mentioned above were first included in the MR analyses, then independent variables with p-value over 0.05 were progressively removed until the remaining independent variables and constants are statistically significant. Occasional independent parameters and constants generated in the MR analyses may have a p-value larger than 0.01, and they are denoted in bold (0.01 < p-value < 0.05; 95-99% confidence) and bold italic (p-value > 0.05; <95% confidence) font in **Tables 4.3-4.5**. For each element, we produce MR equations both including and excluding temperature. This is because temperature may be co-correlated with other melt compositional parameters, so is likely an important variable. However, temperature is likely to be unknown for application of the MR results to retrieving melt compositions from natural systems; therefore it is useful to have parameterisations that exclude temperature.

4.3.3. Accuracy of the multiple regression analysis

Testing the reliability of the multiple regression results is achieved through applying $^{Amph/L}D$ data from an independent set of experimental studies covering a similar range in physical conditions (Adam & Green, 2006; Adam *et al.*, 1993; Brenan *et al.*, 1995; Nandedkar, 2014) and from analysing amphibole phenocryst-matrix pairs in equilibrium (Dostal *et al.*, 1983; Luhr & Carmichael, 1980; Luhr *et al.*, 1984; Nagasawa & Schnetzler, 1971). The compositions of amphiboles and melts from which they are crystallized and $^{Amph/L}D$ values from those studies also encompass large range of variations (**Fig. 4.1a, c, e**; **Table 4.2**), which adds credibility to their representability as test points. We compare the predicted results with measured $^{Amph/L}D$, giving an insight into the accuracy of the MR analyses. The results are presented in section 4.4.2.

4.4. RESULTS

4.4.1. Parameterizations of $^{Amph/L}D$ with temperature and amphibole crystal chemistry

The results of MR analyses are listed in **Tables 4.3-5** and representative plots are shown in **Fig. 4.3**. Using $^{Amph/L}D$ on a natural logarithmic scale (lnD), as the dependent variable yields much better results than using $^{Amph/L}D$ directly, therefore we present the results of calibrating $^{Amph/L}D$ in natural logarithmic scale only (one exception for Sr is given as *Eq. 5* in **Table 4.3**).

4.4.1.1. $^{Amph/L}D_{Rb, Sr, Ba}$

Rb behaves as an incompatible element in amphibole of Kaer, Parg, MgHst and Tsch compositions ($0.03 \leq {}^{Amph/L}D_{Rb} \leq 0.54$), with one exception ($^{Amph/L}D_{Rb} = 1.04 \pm 0.17$) from Parg in Dalpé and Baker (2000), which is excluded for the MR analysis (N = 28). $^{Amph/L}D_{Rb}$ data for MgHbl are not available. The results of MR analysis show that lnDRb can be modelled using a combination of either T+Ti±Na or Si+Mg+Fe^{2+}+Ca±T with intermediate correlations and reasonable errors (weighted $R^2 \geq 0.648$; weighted SE of $^{Amph/L}D_{Rb}$ = 0.055-0.068; *Eq. 1-4* in **Table 4.3**). However, the predicted $^{Amph/L}D_{Rb}$ for

Parg (analysis number of P-MT-43) from Dalpé and Baker (2000) is always lower than the measured value (measured $^{Amph/L}D_{Rb}$ = 0.54±0.14; **Fig. 4.3a-b**).

Sr behaves as a moderately incompatible element in calcic amphiboles (0.11 ≤ $^{Amph/L}D_{Sr}$ ≤ 0.90; N = 42). There is only one exception ($^{Amph/L}D_{Rb}$ =1.65±0.27) from MgHbl in Sisson (1994), and this data point is excluded for the MR analysis as it is also decoupled from the clear correlation between $^{Amph/L}D_{Sr}$ and Xnf/X (Tiepolo *et al.*, 2007). As mentioned earlier, $^{Amph/L}D_{Sr}$ correlates with amphibole Ti and Mg# closely (**Fig. 4.3d-e**), and in the MR analysis, $^{Amph/L}D_{Sr}$ are related to octahedral Al+Ti+Mg+Fe^{3+}+ Fe^{2+}, whereas temperature, Si_T and Ca_{M4} are insignificant (*Eq. 5;* **Fig. 4.3c**). Coefficients of those independent variables are positive while the intercept is negative. lnDSr is also related to Al+Ti+ Fe^{3+}+ Fe^{2+}+Ca (*Eq. 6;* **Fig. 4.3d**) or Al+Mg+ Fe^{3+}+ Fe^{2+}+Ca (*Eq. 7;* **Fig. 4.3e**). *Eq.5-7* suggest that temperature, Si_T and A site components are insignificant for calibrating lnDSr and $^{Amph/L}D_{Sr}$. The MR analysis carried out on $^{Amph/L}D_{Sr}$ yields best correlation with measured data and smallest weighted SE in *Eq. 5*. However, *Eq. 7* is the most precise as the p-values of the coefficients of independent variables and constant are all <0.01.

Ba is also moderately incompatible (0.08 ≤ $^{Amph/L}D_{Ba}$ ≤ 0.72). The MR analysis cannot find a good correlation of the $^{Amph/L}D_{Ba}$ with amphibole crystal formula components. $^{Amph/L}D_{Ba}$ also do not display clear correlations with melt compositions.

4.4.1.2. $^{Amph/L}D_{Pb, U, Th}$

Experimental studies show that Pb is strongly incompatible (0.032 ≤ $^{Amph/L}D_{Pb}$ ≤ 0.17). Although a relatively limited number of $^{Amph/L}D_{Pb}$ data are available for evaluation (N = 21), the results of the MR analysis suggest that $^{Amph/L}D_{Pb}$ is related to Al_{vi} and Mg, but with a relatively poor correlation (weighted R^2 = 0.482; *Eq. 8*; **Fig. 4.3f**). The coefficients of Alvi and Mg are less statistically significant than the independent variables involved in the parameterizations of $^{Amph/L}D$ for other trace elements (p-value of Al_{vi} and Mg are 0.053 and 0.045, respectively).

No correlation is found between $^{Amph/L}D_{U, Th}$ (0.01 ≤ $^{Amph/L}D_{U, Th}$ ≤ 0.03) and any of the independent variables. Moreover, calculation from phenocryst-matrix pairs give D values up to one order of magnitude higher, e.g. $^{Amph/L}D_{U}$ = 0.10, Tsch (Dostal *et al.*, 1983); 0.13 ≤ $^{Amph/L}D_{Th}$ ≤ 0.25, MgHst (Luhr & Carmichael, 1980), and error estimates on those data are not constrained. Therefore, calibrations of $^{Amph/L}D_{U, Th}$ are not discussed further in this study.

4.4.1.3. $^{Amph/L}D_{HFSE}$

Although Ti is a minor element phase rather than trace element phase in amphibole, it is allotted to M1 and M2 sites in calcic amphiboles and the ratio of $^{Amph}TiO_2/\,^{melt}TiO_2$ is often measured as $^{Amph/L}D_{Ti}$ in the $^{Amph/L}D$-determining studies. Therefore, we also treat Ti like other HFSE and carry out the multiple regression analysis on lnDTi.

HFSE show different compatibility when partitioning into amphibole. Ti behaves as a moderately incompatible to strongly compatible element (0.580 ≤ $^{Amph/L}D_{Ti}$ ≤ 18.0; N=66). Zr is incompatible in most measurements (0.08 ≤ $^{Amph/L}D_{Zr}$ ≤ 1.06, N = 46). Hf behaves as strongly incompatible to moderately compatible (0.07 ≤ $^{Amph/L}D_{Hf}$ ≤ 1.9, N = 39). Nb is also incompatible (0.062 ≤ $^{Amph/L}D_{Nb}$ ≤ 1.0, N = 41), with one exception of 1.63±0.13 (MgHst; Tiepolo *et al.*, 2000b). This data point is not included in the MR analysis because it plots off the exponential correlation between $^{Amph/L}D_{Nb}$ and Xnf/X (Tiepolo *et al.*, 2007). The compatibility of Ta is similar to Nb, which is generally incompatible (0.062 ≤ $^{Amph/L}D_{Ta}$ ≤ 1.00, N = 44), with one exception of 1.60±0.24 (Parg) from Hilyard *et al.* (2000), and this data point is also excluded from MR analysis.

The MR analysis results show lnDHFSE are related to 3 groups of independent variables (**Table 4.4**): temperature-dependent group (*Eq.9-11;* **Fig. 4.3g, i, k**), Si+Al_{vi}+Fe^{3+}+Fe^{2+}+Ti+Ca (*Eq. 12-16;* **Fig. 4.3h, l, n**) and Si+Mg+Fe^{2+}+Ti+Ca (*Eq. 17-21;* **Fig. 4.3j, m**). For Zr and Nb, the temperature-dependent MR analyses yield better correlations than those without temperature (higher

R^2 and lower SE in *Eq. 10-11* compared to those in *Eq. 13, 15, 18, 20*). However, the significances of the constants of the temperature-involved MR analysis are poorer than others. The results of calibrations through Mg-bearing, Al_{vi}, Fe^{3+}-absent independent variables generally agree with the Al_{vi}, Fe^{3+}- bearing, Mg-absent group in weighted R^2 and SE. *Eq. 18* and *Eq. 15* are slightly more accurate than *Eq. 13* and *Eq. 20* in predicting $^{Amph/L}D_{Zr, Nb.}$ The coefficients of Si, Ti and Ca are always positive while the coefficients of T and Mg are always negative in the MR analysis for the calibration of $^{Amph/L}D_{HFSE}$.

4.4.1.4. $^{Amph/L}D_{REE, Y}$

$^{Amph/L}D_{REE, Y}$ of Kaer, Parg, MgHst and Tsch are largely overlapping, while MgHbl crystallized from highly polymerized rhyolitic melt have much higher $^{Amph/L}D_{REE, Y}$ (e.g. Sisson (1994)'s experiments; **Fig. 4.3o-x**). Since there are very limited amount of $^{Amph/L}D_{REE, Y}$ data available for MgHbl from previous $^{Amph/L}$D-determining studies, the selected experimental studies do not include any MgHbl data for Gd, Yb and Lu. Therefore, we borrow $^{Amph/L}D_{Yb, Lu}$ data from (Nagasawa & Schnetzler, 1971) and add them to the MR calibrations (**Fig. 4.3u, v, w**). Also, the results of MR analyses for Pr, Tb, Ho and Tm can be biased by limited amount of available data, and therefore they are not presented in this article. The MR analysis also fails to calibrate $^{Amph/L}D_{Eu}$ data.

Statistically significant predictions for lnD of La, Ce, Nd, Sm, Gd, Dy, Er, Yb, Lu and Y are retrieved through the MR analyses ($N \geq 27$, weighted $R^2 \geq 0.804$, p-value of the coefficients of most independent variables and constants < 0.01, *Eq. 22-41* in **Table 4.5**), Temperature is insignificant during the parameterizations of lnDREE, Y and $^{Amph/L}D_{REE, Y}$. lnDREE, Y can be predicted with two main groups of independent variables: Si+Al_{vi}+Fe^{3+}+Fe^{2+}+Ti+Ca (Mg-absent; *Eq. 22-31*), and Si+Mg+Fe^{2+}+Ti+Ca (Al_{vi}, Fe^{3+}-absent; *Eq. 32-41*). The R^2 and SE are generally in agreement between the two groups. However, the MR analyses seem to underestimate the $^{Amph/L}$D data for the MgHbl group in general (**Fig. 4.3o-x**). Similar to the predictions of HFSE, the coefficients of Si, Ti and Ca are always positive while the coefficients of Mg and constants are always negative. The coefficients of Al_{vi}, Fe^{3+} and Fe^{2+} are always positive in the Mg-absent group, while the coefficients of Fe^{2+} are always negative for the Al_{vi}, Fe^{3+}-absent group.

In summary, our MR analyses reproduce measured $^{Amph/L}$D on a natural logarithmic scale for Rb, Sr, Pb, Ti, Zr, Hf, Nb, Ta, REE and Y with various degrees of agreements and reasonable errors. The MR analysis can predict lnDREE, Y with most robust correlation coefficients ($R^2 > 0.75$), while the predictions of lnD of Pb, Zr, Hf and Ta are least robust ($R^2 > 0.41$). The MR analysis demonstrates the varying significance of temperature and amphibole major element components assigned to different crystallographic sites as independent variables in affecting $^{Amph/L}$D. Temperature can be an important independent variable in predicting lnD of Rb and HFSE, but they can also be predicted, as well as lnD of Sr, Pb, REE and Y, without including temperature as an independent variable. Vacant/A site components seem to be insignificant in controlling $^{Amph/L}$D, except for Rb and Zr when temperature is also involved in the equations. The coefficients of Si and Ca are always positive in all equations.

4.4.2. Accuracy of the MR-derived equations

The prediction results of the selected test points are plotted together with the original MR analyses results against measurements data in **Fig. 4.3**. Lack of agreement (within uncertainty) of the test points with the predicted compositions (1:1 line) indicates a lower degree of reliability of the MR-derived $^{Amph/L}$D-calculating equation, or that the quality of the measured $^{Amph/L}$D data is questionable.

4.4.2.1 $^{Amph/L}D_{Rb, Sr, Pb}$

Eq. 1 and *Eq. 2* work better for predicting $^{Amph/L}D_{Rb}$ than *Eq. 3-4*, as shown by smaller weighted standard error of estimate (se). In the test results of applying Eq. 1-2 (e.g. **Fig. 4.3a**), the predicted $^{Amph/L}D_{Rb}$ for MgHst (RBN8 outer, 0.101±unknown error) and Tsch (RN8 inner, 0.089±0.001) from

the experiments of Nandedkar (2014), and for Parg (D-5, 0.13±0.02) from the experiment of (Brenan *et al.*, 1995), are always higher than the experimental results. In contrast, the predicted $^{Amph/L}D_{Rb}$ of MgHst (1393, 0.58±0.08) from Adam *et al.* (1993) are always lower than the measured data, and this is consistent with the failure of predicting Parg (P-MT-43; 0.54±0.14) from Dalpé and Baker (2000) during the calibrations. The rest of the test points show good agreement with the measured data. In contrast, *Eq. 3* and *Eq. 4* fail to predict $^{Amph/L}D_{Rb}$ with robust reliability (**Fig. 4.2b**).

For predicting $^{Amph/L}D_{Sr}$, the test results of applying *Eq. 5* show the predicted $^{Amph/L}D_{Sr}$ are generally lower than the measurements (se of 0.142), although robust positive correlation is displayed by the test points (R^2 = 0.802, **Fig. 4.3c**). In contrast, results yielded from *Eq. 6-7* are similar and both show better agreement between the predictions and the measurements compared to results from *Eq. 5* (se of 0.124 and 0.111, respectively), except outliers of MgHst (1951; 0.42±0.03) from Adam & Green (2006), Parg (D-5, 0.29±0.03) from Brenan *et al.* (1995), MgHst (1409, 0.44±0.04; 1388, 0.31±0.02) and Parg (1395; 0.38±0.02) from Adam *et al.* (1993) (**Fig. 4.3d-e**).

For predicting $^{Amph/L}D_{Pb}$, the 5 test points from Adam and Green (2006), Brenan *et al.* (1995) and Nandedkar (2014) show excellent agreement with the measured $^{Amph/L}D_{Pb}$ (se of 0.006)(**Fig. 4.3f**). This is despite the relatively small number of data points used for calibration, and the poor correlation coefficient and large uncertainties on the coefficients of the independent variables.

4.4.2.2. $^{Amph/L}D_{HFSE}$

For predicting $^{Amph/L}D_{Ti}$ with temperature, *Eq. 9* is only able to reproduce one data point (MgHst, RBN8 outer, 2.438±0.148; Nandedkar, 2014) out of the 5 data experimentally derived from Adam and Green (2006), Brenan *et al.* (1995) and Nandedkar (2014) (**Fig. 4.3g**). For predicting $^{Amph/L}D_{Ti}$ without temperature, *Eq. 12* and *Eq. 17* behave similarly (*Eq. 12* slightly more accurate with a smaller se than *Eq. 17*), and both are able to reproduce MgHst (1951; 1.35±0.05) from Adam & Green (2006), MgHst (6, 4.34±0.31; 15, 4.32±0.31) from Luhr & Carmichael (1980), and Tsch (RN11, 4.286±0.468) from Nandedkar (2014). However, Parg (D-5, 2.00±0.18) from (Brenan *et al.*, 1995), MgHst (2, 6.80±0.48; 7, 4.55±0.32; 17, 4.59±0.32) from (Luhr & Carmichael, 1980), MgHst (RBN8 outer, 2.438±0.148) and Tsch (RN8 inner, 2.582±0.103) from Nandedkar (2014) are plotted as outliers (**Fig. 4.3h**).

For predicting $^{Amph/L}D_{Zr}$ with temperature, *Eq. 10* is able to reproduce experimental results from Adam & Green (2006) and Nandedkar (2014), and Parg (1395, 0.18±0.04) and MgHst (1409, 0.31±0.07) from Adam *et al.* (1993). However, Parg (D-5, 0.22±0.03) from Brenan *et al.* (1995), MgHst (1388, 0.21±0.02; 1389, 0.22±0.04; 1393, 0.32±0.01) from Adam *et al.* (1993) are plotted as outliers (**Fig. 4.3i**). For predicting $^{Amph/L}D_{Zr}$ without temperature, *Eq. 13* and *Eq. 18* behave similarly (smaller se in *Eq. 13*), but both are less robust than *Eq. 10* (higher se) because these two equations also fail to reproduce MgHst (1951, 0.31±0.05) from Adam & Green (2006) and MgHst (1409, 0.31±0.07) from Adam *et al.* (1993) (**Fig. 4.3j**).

For predicting $^{Amph/L}D_{Hf}$ without temperature, *Eq. 14* and *Eq. 19* behave similarly (smaller se in *Eq. 19*). However, the two equations overestimate the measured $^{Amph/L}D_{Hf}$ through phenocryst-melt pairs from Dostal *et al.* (1983), Luhr & Carmichael (1980) and Luhr *et al.* (1984), and underestimate experimentally determined $^{Amph/L}D_{Hf}$ from Adam and Green (2006), Brenan *et al.* (1995) and Nandedkar (2014). The 1:1 line intersects the vertical error bars of MgHst (7, 0.45±0.06; 15, 0.36±0.05; 17, 4.59±0.32) from Luhr & Carmichael (1980), MgHst (0.76±0.02) from Luhr *et al.*, (1984), MgHst (1951, 0.59±0.15) from Adam & Green (2006), and Tsch (RN8 inner, 0.623±0.005) from Nandedkar (2014) (**Fig. 4.3m**).

For predicting $^{Amph/L}D_{Nb}$ with temperature, *Eq. 11* is only able to reproduce MgHst (1388, 1389, 0.07±0.01) from Adam *et al.* (1993), and MgHst (1951, 0.21±0.02) from Adam & Green (2006). However, *Eq. 11*overestimates measured $^{Amph/L}D_{Nb}$ of Parg (1395, 0.09±0.01), MgHst (1409, 0.09±0.01; 1393, 0.08±0.01) from Adam *et al.* (1993), and underestimates measured $^{Amph/L}D_{Nb}$ from Brenan *et al*. (1995) and Nandedkar (2014) (**Fig. 4.3k**). The test results for predicting $^{Amph/L}D_{Nb, Ta}$

without temperature using *Eq. 15, 16, 20, 21* are similar to the results of *Eq. 11*, and *Eq. 15, 16* have smaller se than *Eq. 20, 21* (**Fig. 4.3l, n**).

4.4.2.3. $^{Amph/L}D_{REE, Y}$

For $^{Amph/L}D$ prediction of LREE and MREE (La, Ce, Nd, Sm and Dy), the MR-derived equations work well for reproducing the test points of MgHst and Tsch compositions from Adam & Green (2006), Dostal *et al.* (1983), Luhr & Carmichael (1980), Luhr *et al.* (1984) and Nandedkar (2014), although outliers are still present (e.g. **Fig. 4.3c-d**). However, the MR-derived equations overestimate $^{Amph/L}D$ for the MgHbl group from Nagasawa & Schnetzler (1971) significantly (**Fig. 4.3o-p**). The Mg-absent group of equations (*Eq. 22-25, 27*) predict $^{Amph/L}D$ for the MgHbl group more accurately than the Al_{vi}, Fe^{3+}-absent group (*Eq. 32-35, 37*).

Eq. 26 and *Eq. 36* underestimate $^{Amph/L}D_{Gd}$ of MgHst (RBN8 outer, 1.617±0.005) and Tsch (RN11, 2.974±0.298) from Nandedkar (2014) (**Fig. 4.3q, r**).

Eq. 38 predicts $^{Amph/L}D_{Er}$ of the MgHbl group from Nagasawa & Schnetzler (1971) better than *Eq. 28*, which predicts lower values than the measured values (**Fig. 4.3s, t**).

Both *Eq. 29* and *Eq. 39* fail to predict $^{Amph/L}D_{Yb}$ accurately. The two equations underestimate $^{Amph/L}D_{Yb}$ of amphiboles with different compositions, however, the offset between the predicted $^{Amph/L}D_{Yb}$ and measured $^{Amph/L}D_{Yb}$ is smaller when *Eq. 39* is applied. Similarly, *Eq. 40* predicts $^{Amph/L}D_{Lu}$ of the MgHbl group from Nagasawa & Schnetzler (1971) with more accuracy than *Eq. 30* (**Fig. 4.3u, v, w**).

The prediction of $^{Amph/L}D_{Y}$ via *Eq. 31* and *Eq. 41* are less accurate than the prediction of $^{Amph/L}D_{REE}$. The predictions of the test points of Parg, MgHst and Tsch compositions from Adam & Green (2006), Adam *et al.* (1993) and Nandedkar (2014) display a positive variation trend against the measured values but with a shallower slope (**Fig. 4.3x**).

In summary, the MR-derived equations presented here can predict $^{Amph/L}D$ of Sr, Pb, LREE and MREE of MgHst, Parg and Tsch reasonable well, while the predictions for $^{Amph/L}D$ of Rb, HFSE, HREE and Y are less accurate. The predictions of $^{Amph/L}D_{REE}$ for MgHbl are the least accurate of the tested amphibole species.

4.5. DISCUSSION

4.5.1. A further test with MgHbl

The offsets of the predicted $^{Amph/L}D$ for test points from measurements may be due to poor accuracy of the MR-derived equations, and/or questionable quality of the $^{Amph/L}D$ data selected for tests. Furthermore, the predictions of $^{Amph/L}D$ for MgHbl are less accurate than the predictions for other amphibole species. However, the HFSE and REE $^{Amph/L}D$ data for MgHbl are only presented in several studies, e.g. Hilyard *et al.* (2000), Nagasawa & Schnetzler (1971) and Sisson (1994). Considering the limited $^{Amph/L}D$ data for MgHbl used for testing the reliability of our $^{Amph/L}D$-predicting models (e.g. $^{Amph/L}D$ for Ce, Nd, Sm, Dy and Er from Nagasawa & Schnetzler, 1971), here we apply a further test to demonstrate the accuracy of our $^{Amph/L}D$ models in application to MgHbl using amphibole-matrix glass pairs from pumice clasts from the Ongatiti ignimbrite

In Chapter 3, we demonstrated that amphibole rims and matrix glasses from the Ongatiti ignimbrite are in equilibrium, through the successful reconstruction of the matrix glass major element compositions with the chemical compositions of the amphibole rims. This allows us to calculate the $^{Amph/L}D$ data with the trace element compositions of amphiboles and matrix glasses, which are analysed with LA-ICPMS and results are reported by Cooper & Wilson (2014). The results of our calculated and predicted $^{Amph/L}D$ data are given in **Table 4.6** and plotted in **Fig. 4.4**. The errors of calculated $^{Amph/L}D$ based on measurements are given as the standard deviations of the multiple

analyses of amphibole and glass compositions, processed according to the error propagation approach, while the errors of the predicted $^{Amph/L}D$ are given as the averaged error values of individual predictions.

Our predictions yield $^{Amph/L}D$ for Ti, Zr, Nb and LREE-MREE (La, Ce, Nd, Sm, Dy and Er) which are in good agreement with the calculations. While for Sr, Pb and Y, the disparities between our predictions and the calculated $^{Amph/L}D$ are slightly higher than the error of predictions (**Fig. 4.4**).The $^{Amph/L}D$ for Rb, Hf and Ta are overestimated while the $^{Amph/L}D$ for Gd, Yb and Lu are underestimated, with large offsets (**Fig. 4.4**). The predicted results are generally comparable to the results of test experiments. Therefore, we regard our MR equations for predicting $^{Amph/L}D$ of Sr, Pb, Ti, Zr, Nb, LREE, MREE and Y work reasonably for all calcic amphibole compositions, and these elements are discussed in the following sections.

MgHbl, which crystallizes from highly polymerized silicic melt, is commonly found in evolved arc magmas (Plail *et al.*, 2014; Thornber *et al.*, 2008; Zhang *et al.*, 2015) and silicic supereruptions (Cooper, 2014; Cooper & Wilson, 2014), and has distinctively higher REE partition coefficients compared to other calcic amphibole species (Nagasawa & Schnetzler, 1971; Sisson, 1994). Therefore, in order to reconstruct magmatic processes involved in producing abundant MgHbl crystals in evolved arc magmas, a larger number of additional experimental constraints on the trace element partitioning behaviours in MgHbl are needed in the future. However, the MR-derived $^{Amph/L}D$-predicting models presented here provide a means to successfully estimate $^{Amph/L}D$.

4.5.2. Crystal vs. melt compositional control over amphibole trace element concentrations

Both melt trace element compositions and partition coefficients affect trace element abundances in amphibole, however, their relative importance may vary between elements. We will assess the influences of each element below. We take published major and trace element data of amphiboles from four stratovolcanoes (Mt. Pinatubo, Mt. Hood, Mt. St. Helens and Shiveluch volcano; data from Loewen, 2013), and one silicic super-eruption (the Ongatiti ignimbrite of the Mangakino Volcano; data from Cooper & Wilson, 2014) as case studies. The primary reason for choosing those five case studies is that they are historically relatively well studied and abundant amphibole compositional data are recently collected which ensure that we observe variation trends between amphibole trace element compositions and predicted $^{Amph/L}D$ and predicted melt compositions. Details of the analytical methods and accuracy of the results are reported by the corresponding study, respectively. We apply the empirical $^{Amph/L}D$-predicting equations and melt major element calibration models (Chapter 3) to amphibole major element crystal chemistry in order to calculate $^{Amph/L}D$ and melt major element compositions, and then with trace element data to infer corresponding melt trace element compositions. Results are illustrated in **Fig. 4.5**. The errors of the inferred melt trace element concentrations are calculated with the internal standard errors of the amphibole LA-ICP-MS analyses, i.e. 10% analytical uncertainty according to Loewen (2013) and Cooper & Wilson (2014), and the standard error of estimates of the MR analyses, following the error propagation principles.

4.5.2.1. Case studies from evolved arc magmas

Amphiboles of Mt. Pinatubo are from andesite and basaltic enclaves exposed during the 7^{th}-12^{th} June, 1991 eruption (Pallister *et al.*, 1996). The 1991 eruption of Mt Pinatubo has been heavily studied in the literature, and the petrogenetic processes that triggered the eruption are documented in detail by Kress (1997), Pallister *et al.* (1996) and Pallister *et al.* (1992), amongst others. The eruption initiated when a hybrid andesite was generated by mingling of dacite with ol-cpx basalt at 8-9 km depth. The hybrid andesite itself then mixed with shallowly stored dacite during ascent and triggered eruption of large quantities of the dacite magma. Both basalt and dacite contained amphibole phenocrysts, some of which were transferred into the andesite during mingling. The dataset of Loewen (2013) includes amphiboles from all three magma types: basalt inclusions, andesite and dacite; however, the data show a bimodal amphibole population with contrasting crystal chemistry (low-Si MgHst group vs. high-Si MgHbl group; e.g. **Fig. 4.5a1**). MgHst is not present in the dacite samples, while MgHbl can

be found in all three magma types (Loewen, 2013). The MgHst group has distinctively higher Sr and Ti, and lower Nb, REE and Y contents compared to the MgHbl group (**Fig. 5**). Pb concentrations in both groups are overlapping, while Zr in the MgHst group is slightly higher than the MgHbl group in general.

Amphiboles of Mangakino Volcano are from the pumice clasts of the Ongatiti ignimbrite, erupted at 1.21 ± 0.04 Ma (Cooper & Wilson, 2014). The crystal-rich Ongatiti ignimbrite is of rhyodacite and low-silica rhyolite composition, and the groundmass is of homogeneous rhyolitic composition, in contrast to crystal chemistry of major mineral phases (plagioclase, amphibole, orthopyroxene) which display large variability. Amphiboles in pumice clasts from the Ongatiti ignimbrite show contrasting core and rim textures and chemical compositions (Cooper & Wilson, 2014). The cores are very often patchy zoned, contain abundant melt and mineral inclusions and display a large compositional variation from MgHst to MgHbl. They are interpreted as derived from earlier-fractionated crystals and present as components of crystal mushes prior to the later magma replenishment event, which resorbed the crystals and recycled them to a shallower storage zone (Cooper & Wilson, 2014). In contrast, the rims of the amphiboles from the pumice clasts have a very limited range of compositional variation (MgHbl-only). The cores have lower Sr and higher Pb and Ti, and the rims have higher Pb, REE and Y, compared to amphiboles with similar Si content from the other case studies.

Amphiboles of Mt. Hood are from dacitic dome lavas and associated mafic enclaves, produced during the Old Maid eruptive period (1780 C.E.; Kent *et al.*, 2010; Koleszar, 2011; Koleszar *et al.*, 2012). Amphiboles from dacitic dome lavas are dominantly of MgHbl compositions, whiles in mafic enclaves they are mainly of Tsch compositions. Together, they comprise of continuous compositional variation from Tsch to MgHbl. With increasing Si from Tsch to MgHbl, Sr and Ti are decreasing, while Zr, Nb, REE and Y are increasing. Koleszar (2011) suggests that they form under a spectrum of pressure and temperature conditions, which are probably due to recharge-driven two-endmember magma mixing.

Amphiboles of Shiveluch Volcano are from the 2001 eruption (Dirksen *et al.*, 2006; Humphreys *et al.*, 2006; Humphreys *et al.*, 2008). Complex zonings of phenocrysts of plagioclase, amphibole and apatite in the andesite produced during this eruption suggest complicated magma evolution history, including mixing chemically and thermally variant magmas by incrememtal magma replenishment. Similar to amphiboles of Mt. Hood, amphiboles of Shiveluch Volcano also display a continuous variation from Tsch to MgHbl in major element compositions, however, their trace element compositions do not display obvious variation trend against amphibole Si content.

Amphiboles of Mt. St. Helens are from white pumice and dome block (grey dacite) samples produced during the 18th May, 1980 eruption (Cashman & McConnell, 2005). Cashman & McConnell (2005) suggests that the magma plumbing system of Mt. St. Helens probably comprise of multiple levels of magma storage regions, to explain the transition in eruption styles from explosive plinian eruption to subplinian and vulcanin eruptions with increasing pulsatility. Amphiboles from this eruption are dominated by Tsch compositions, with occasional presence of MgHbl. The compositional variations of Mt. St. Helens' amphiboles are relatively scattered compared to amphiboles from other locations. Sr and Ti concentrations display a weak negative correlation, and REE and Y show a weak positive correlation against amphibole Si content.

The textural information of amphiboles of Mt. Hood, Shiveluch Volcano and Mt. St. Helens on which compositional data are collected are not provided by Loewen (2013). Therefore, we only use those data to explore the relative importance of $^{Amph/L}D$ and melt compositions in controlling amphibole trace element compositions in section 4.5.3, and do not discuss open-system magmatic processes in section 4.5.4.

4.5.2.2. $^{Amph/L}D_{Sr, Pb}$

The calculated $^{Amph/L}D$ values of Sr for the MgHbl group from Mt. Pinatubo show a significant variation (0.18-0.33) relative to the limited Sr compositional variation within this group (24-52 ppm; **Fig. 4.5a2**). It is similar for amphiboles from other locations. In contrast, amphibole Sr concentrations are strongly related to the Sr contents in the calculated melt (e.g. $R^2 = 0.910$ amongst Mt. Hood's amphiboles; **Fig. 4.5a3**). This suggests that melt Sr contents is a more significant control over amphibole Sr contents than amphibole major element chemistry. Higher Sr contents in MgHst relative to Tsch and MgHbl are caused by higher Sr contents in the melt as well as higher $^{Amph/L}D_{Sr}$.

The Pb contents of amphiboles, regardless of the species, are generally similar. The predicted $^{Amph/L}D_{Pb}$ is also not distinguishable from each other (0.03-0.08; **Fig. 4.5b2**). However, the amphibole Pb contents are strongly correlated with the predicted melt Pb contents (e.g. $R^2 = 0.99$ within Mt. Hood's amphiboles; **Fig. 4.5b3**). This indicates that similar to Sr, melt contents of Pb is the determinant of amphibole Pb contents, rather than $^{Amph/L}D_{Pb}$.

4.5.2.3. $^{Amph/L}D_{Ti, Zr, Nb}$

The lower TiO_2 for the MgHbl group of Mt. Pinatubo is coupled with higher predicted $^{Amph/L}D$ of Ti (5.4-10.4) relative to the MgHst group (**Fig. 4.5c2**). For the Mt. Hood amphiboles, there is a weak negative correlation between the predicted $^{Amph/L}D_{Ti}$ and amphibole TiO_2 content (**Fig. 4.5c2**). Therefore, the lower TiO_2 in MgHbl must be related to lower TiO_2 content in the melt, and vice versa (**Fig. 4.5c3**), and $^{Amph/L}D_{Ti}$ is a less important controlling factor. The opposite effect of $^{Amph/L}D_{Ti}$ and melt TiO_2 content in controlling amphibole TiO_2 content is consistent with our expectations, since $^{Amph/L}D_{Ti}$ is strongly negatively correlated with melt TiO_2 content according to the $^{Amph/L}D$-determining studies (**Fig. 4.2k**).

Similarly, lower amphibole Zr concentrations in Mt. Pinatubo MgHbl group are coupled with higher predicted $^{Amph/L}D_{Zr}$ (**Fig. 4.5d2**). While for Mt. Hood and Mt. St. Helens amphiboles, there is no obvious correlation between the predicted $^{Amph/L}D_{Zr}$ and amphibole Zr concentrations (**Fig. 4.5d2**). Instead, the amphibole Zr concentrations are strongly linked with the inferred melt Zr contents (e.g. $R^2 = 0.662$ for Mt. Hood amphiboles; **Fig. 4.5d3**).

In contrast, the higher Nb concentrations in the Mt. Pinatubo MgHst group are consistent with higher predicted $^{Amph/L}D_{Nb}$ relative to the MgHbl group (**Fig. 4.5e2**). In Mt Hood amphiboles, with increasing Nb contents from Tsch to MgHbl, the predicted $^{Amph/L}D_{Nb}$ is progressively increasing from 0.3 to 1.6, displaying a robust positive correlation ($R^2 = 0.782$; **Fig. 4.5e2**). While the inferred melt compositions do not display any obvious variations against amphibole Nb concentrations in Mt. Hood amphiboles (**Fig. 4.5e3**). The Nb contents in Mt. St. Helens amphiboles show weak positive correlations with both $^{Amph/L}D_{Nb}$ and melt Nb contents. However, strong positive correlation between Mt. Hood amphiboles Nb contents and $^{Amph/L}D_{Nb}$ still indicates that $^{Amph/L}D_{Nb}$ is a more important parameter in controlling amphibole Nb contents.

4.5.2.4. $^{Amph/L}D_{REE, Y}$

Similar to Nb, the higher LREE and MREE (e.g. La and Sm) concentrations in the Mt. Pinatubo MgHst group are consistent with higher predicted $^{Amph/L}D$ relative to the MgHbl group (**Fig. 4.5f2**). While the inferred melt LREE and MREE concentrations from MgHst group and MgHbl group are largely overlapping (**Fig. 4.5f3**). This indicates that $^{Amph/L}D$ is a dominant parameter in controlling amphibole LREE and MREE contents. Moreover, in Mt. Hood amphiboles, the correlation pattern between the inferred melt LREE and MREE compositions and their abundances in amphibole is S-shaped, i.e. stronger positive correlations are found in Tsch with low REE and MgHbl with higher REE concentrations relative to amphiboles in between (**Fig. 4.5f3**). This also suggests that melt REE contents are also important in determining amphibole REE abundances, but maybe less significant than $^{Amph/L}D$. The Mt. St. Helens, Shiveluch Volcano and Ongatiti amphiboles display a more scattered variation of inferred LREE and MREE concentrations in the melts against their abundances

in the amphiboles, compared to Mt. Pinatubo and Mt. Hood amphiboles. We will discuss the implications in a later section (section 4.5.4.).

Although our MR predictions of $^{Amph/L}D$ for HREE (Yb and Lu) and Y are less accurate than LREE and MREE, the variation patterns of the inferred $^{Amph/L}D$ and their concentrations in melts against their abundances in amphiboles are similar to LREE and MREE (**Fig. 4.5g2, 3**). This suggests that for all REE and Y's partitioning between melts and amphiboles, $^{Amph/L}D$ is a more important control than melt REE concentrations.

In summary, for Sr, Pb and tetravalent HFSE (Ti, Zr), melt trace element compositions are the dominant factor governing their concentrations in amphiboles, but for pentavalent HFSE (Nb), REE and Y, partition coefficients instead are the primary control.

4.5.3. Insights from crystal-chemical control over trace element partitioning in amphibole

Our MR analyses results offer an insight into the relative importance of melt trace element contents and $^{Amph/L}D$ in controlling the trace element contents in amphibole, which varies from element to element. For example, $^{Amph/L}D_{Sr}$ is more dependent on amphibole Mg# and Ti and less dependent on melt major element compositions (**Fig. 4.2d-e**). Our MR analyses also prove the importance of M1-3 site components, including Mg, Fe^{2+}, Ti and Al_{VI} (*Eq. 5-7* in **Table 4.3**), in predicting $^{Amph/L}D_{Sr}$. However, amphibole Sr contents are more related to melt Sr concentrations and less correlated with $^{Amph/L}D_{Sr}$. This suggests that amphibole Sr contents, unlike $^{Amph/L}D_{Sr}$, are less correlated with M1-3 site components. This is consistent with the preference of Sr for A site and M4 site in amphibole crystal structure (Tiepolo *et al.*, 2007), which do not appear in the MR-derived equations. In other words, the absence of the preferred structural site components as statistically significant independent variables in the MR analyses explains the weaker correlation of amphibole Sr with $^{Amph/L}D_{Sr}$ than with melt Sr contents. This explanation is also applicable to Pb. On the contrary, the presence of Ti and Ca in the MR-derived $^{Amph/L}D$-predicting equations for Nb, Y and REE are consistent with the stronger correlation of amphibole Nb, Y and REE contents with predicted $^{Amph/L}D_{Nb,\ Y,\ REE}$ than with their melt contents.

This cannot explain the more important control of melt contents over amphibole Ti and Zr contents than $^{Amph/L}D$, with the presence of Ti in the MR equations. Therefore, additional explanations are needed. $^{Amph/L}D_{Ti}$ is strongly correlated with melt SiO_2 content positively and melt TiO_2 content negatively, and is not related to amphibole crystal chemistry (**Fig. 4.2j, l**). Ti contents in calcic amphiboles, in contrast, are commonly known to be strongly associated with amphibole tetrahedral Al contents as a function of the Ti-Tschermak exchange (Anderson & Smith, 1995; Bachmann & Dungan, 2002; Hammarstrom & Zen, 1986; Holland & Blundy, 1994; Ruprecht *et al.*, 2012; Thornber *et al.*, 2008). Our conclusion of Chapter 3 demonstrates that amphibole major element crystal chemistry is a function of amphibole crystallization temperature and melt major element compositions. Therefore, amphibole Ti content, more behaving like a major element rather than a trace element, is also related to melt compositions. Zr substitutes Ti in amphibole, therefore its contents in amphiboles should also be related to melt compositions, rather than $^{Amph/L}D_{Zr}$.

4.5.4. Implications to magmatic processes occurring in magma plumbing systems

With the robust predictions of melt major element compositions (Chapter 3) and trace element partition coefficients through the multiple regression analyses approach, we are now able to reconstruct major and trace element compositions of the melts from which calcic amphiboles are crystallized or re-equilibrated. The variations of the inferred major and trace element compositions of the melts can imply magmatic processes occurred during amphibole crystallization/equilibration. Below we provide our interpretations of magmatic processes occurring at Mt. Pinatubo and Mangakino Volcano.

4.5.4.1. Mt. Pinatubo

Application of the MR analysis indicates that the MgHst group crystallize from mafic melt with 54-62 wt % SiO_2, while the MgHbl group crystallize from felsic melts with >74 wt % SiO_2 (**Fig. 4.5a4**). The inferred SiO_2 content in felsic melts is in good agreement with compositions of matrix glasses in phenocryst-rich dacite (75-79 wt % SiO_2; Pallister *et al.*, 1996) and melt inclusions in plagioclase, amphibole and quartz crystals in dacite (~75 wt% SiO_2; Rutherford & Devine, 1996), and higher than the dacite bulk-rocks (~64 wt% SiO_2; Pallister *et al.*, 1996). In contrast, our predicted melt SiO_2 content from the MgHst group is more similar with bulk-rock basalt inclusions (50-52 wt% SiO_2; Pallister *et al.*, 1996), and distinguishable from matrix glasses in basalt inclusions which have 70-76 wt % SiO_2. Pallister *et al.* (1996) suggested that the high SiO_2 content in basaltic inclusions may be due to extensive crystallization of abundant amphibole, plagioclase and magnetite microlites during interaction in the andesite and dacite hosts. Hence we think amphibole crystallization in basalt inclusions probably occurs in melt of 54-62 wt % SiO_2. There are few intermediate amphibole compositions between these two populations, suggesting that amphiboles crystallized from completely different melt compositions, and probably under different pressure and temperature conditions. This is consistent with the petrographic evidence of magma mingling between basalt of 50-52 wt% SiO_2 and dacite with a rhyolitic melt of ~75 wt% SiO_2 (Pallister *et al.*, 1996).

The melt Sr, Pb, Zr, Nb, REE and Y contents inferred from the MgHbl group are in excellent agreement with trace element compositions measured in quartz-hosted melt inclusions in dacite pumices (Borisova *et al.*, 2008). Inferred Sr contents in the melts display no obvious negative correlations with inferred melt SiO_2 contents or positive correlations with CaO in the individual groups (**Fig. 4.5a4, a5**), suggesting that compositional variations within each group are not related to plagioclase co-crystallization with amphibole. With decreasing melt FeO content, the TiO_2 contents in the melts from which MgHst are crystallized do not drop rapidly, indicating limited ilmenite co-crystallization with MgHst (**Fig. 4.5c5**). This is consistent with the absence of ilmenite in basalt inclusions (Pallister *et al.*, 1996). The melts from which MgHbl are crystallized have very low FeO and TiO_2 contents, indicating significant ilmenite crystallization in dacite (**Fig. 4.5c5**; again this is consistent with the presence of ilmenite in dacite according to Pallister *et al.* (1996). No significant variation in the inferred melt Zr content against melt SiO_2 content in both groups implies that zircon has not achieved the saturation point in both melts (**Fig. 5d4, d5**). Rutile and ilmenite are the major hosts for magmatic Nb (Foley *et al.*, 2000; Green & Pearson, 1987; Jenner *et al.*, 1993; Xiong *et al.*, 2005), and since rutile is absent in Mt. Pinatubo magmas, the inferred decreasing Nb with decreasing melt TiO_2 within the MgHbl group indicate the simultaneous ilmenite crystallization with MgHbl, while this process is not important during MgHst crystallization (**Fig. 5e4, e5**). Apatite is a major host for magmatic REE and Y (Fujimaki, 1986; Luhr *et al.*, 1984; Nagasawa & Schnetzler, 1971), the crystallization of apatite can decrease their contents in the melt, together with CaO. Therefore, the coherent decreasing REE, Y and CaO contents and increasing SiO_2 content in the inferred melts suggest that apatite is a co-crystallization phase together with both MgHst and MgHbl (**Fig. 4.5f4, f5, g4, g5**). The predicted melt compositions are consistent with bulk trace element concentrations in Pinatubo whole rocks which show that the mafic inclusions are significantly more REE-enriched than the dacites (Pallister *et al.*, 1996). The interpretation that decreasing REE, Y and CaO are related to apatite crystallisation is also consistent with petrographic observations, which indicate that apatite is ubiquitous in Pinatubo eruptive products (Pallister *et al.*, 1996).

4.5.4.2. Mangakino Volcano

The Ongatiti eruption of the Mangakino Volcano occurred at 1.21 ± 0.04 Ma, and this eruption produced the Ongatiti ignimbrite dominated by rhyodacite to low-Si rhyolite compositions (Cooper & Wilson, 2014). Amphiboles from pumice clasts of the Ongatiti ignimbrite display different compositional variation trends from those of Mt Pinatubo. The majority of amphibole crystal cores (Type B cores) show patchy zoning and resorption texture, accompanied with significant compositional span in both major and trace elements from MgHst to MgHbl (Cooper & Wilson, 2014). In contrast, the rims are chemically homogeneous, with only MgHbl compositions (**Fig. 4.5a1**)

(Cooper & Wilson, 2014). It has previously been suggested that the patchy zoned cores are probably originated from crystal mushes at depth, and then equilibrated with more felsic melts and recycled to the melt in a shallower storage region where MgHbl rims are crystallized (Cooper & Wilson, 2014). Such process is also termed as 'petrological cannibalism' for explaining the textural and compositional complexity in plagioclase crystals from Mt. St. Helens in another recent study (Cashman & Blundy, 2013). The large compositional span in the cores may be either resulted from large source variations, i.e. chemically contrasting melts parental to the crystal mushes, or from equilibration with the rim-crystallizing melt, or both (see detailed discussions in Chapter 3). Application of our MR analysis to this dataset permits us to understand how the compositions of the crystal mush liquid compare with that of the more felsic host melt in equilibrium with the rims.

The rims are in equilibrium with the matrix glass of the pumice clasts, suggesting that the rims are crystallized from a rhyolitic melt of matrix glass compositions (76-82 wt % SiO_2; see Chapter 3). The inferred major and trace element compositions of the rim-crystallizing rhyolitic melts display variation trends (e.g. decreasing melt Zr, Nb, REE and Y against increasing melt SiO_2 content) which cannot be attributed to mixing with a less evolved melt of higher Zr, Nb, REE and Y (**Fig. 4.5a4, d4, e4, f4, g4**). Instead, they must reflect melt compositional evolution driven by crystallization of the phenocryst phases, such as amphibole, plagioclase, quartz, orthopyroxene, ilmenite, titanomagnetite, as well as accessory phases including apatite and zircon (Cooper & Wilson, 2014). Plagioclase is not a significant crystallization phase together with amphibole crystallization as suggested by inferred invariant low Sr and CaO contents in the melt (**Fig. 4.5a4, a5**), thus the large abundance of plagioclase phenocrysts in the melt must be crystallized prior to the amphibole rim growth. Ilmenite co-crystallization with amphibole may be minor, as suggested by insignificant variation of TiO_2 against FeO (**Fig. 4.5c5**), however, it may be responsible for the decreasing Nb content with increasing SiO_2 since rutile is not observed in the Ongatiti ignimbrite pumice clasts (Cooper & Wilson, 2014). The very low predicted TiO_2 and FeO contents in the melts suggest that the abundant ilmenite crystals and inclusions in amphiboles observed by Cooper & Wilson (2014) must be crystallized prior to amphibole (**Fig. 4.5c5**). The inferred Zr contents are decreasing with increasing SiO_2 contents in the melt, indicating zircon's co-crystallization together with amphibole rims (**Fig. 4.5d4**). This is consistent with the observation of zircons with core-rim textures in the Ongatiti ignimbrite (Cooper *et al.*, 2014). The inferred melt compositions also record decreasing REE and Y contents with increasing SiO_2 (**Fig. 4.5f4, g4**), suggesting apatite crystallization during amphibole rim growth. This is also consistent with the observations of apatite inclusions in amphibole crystals (e.g. see Fig. 7b in Chapter 3) (Cooper *et al.*, 2014).

The predicted melt Sr, Zr, Nb and Y contents and major element compositions yielded from cores of amphiboles do not display systematic variations (**Fig. 4.5a4, d4, e4, g4**), while Pb and La are moderately positively correlated with melt SiO_2 content (**Fig. 4.5b4, f4**). We interpreted that the variations in predicted melt major element variations are due to different degrees of equilibration of the crystals from mushes with felsic melt of matrix glass compositions in Chapter 3. This process can also explain the correlations of predicted melt Pb and La against melt SiO_2 (**Fig. 4.5b4, f4, f5**). The more complex patterns of other trace elements may be ascribed to equilibration process overprinted by co-crystallization of other mineral phases, as well as source heterogeneities suggested by Cooper *et al.* (2014).

In summary, the large amphibole compositional variations with the co-presence of multiple species in individual volcanic eruptions are mainly produced by mingling/mixing crystals from different sources, including different melts (e.g. Mt. Pinatubo) and/or crystal mushes (e.g. Mangakino Volcano). Within individual groups, co-crystallization of major/accessory mineral phases with amphiboles can also be recorded by systematic variation of the inferred melt major and trace element compositions.

4.6. CONCLUSION

Multiple regression (MR) analyses can be used to parameterize published $^{Amph/L}D$ of Rb, Sr, Pb, HFSE, REE and Y for calcic amphiboles of Parg, MgHst, Kaer, Tsch and MgHbl compositions. It is demonstrated that temperature and amphibole major element components assigned to different crystallographic sites show different significance in controlling $^{Amph/L}D$ of those elements (**Table 4.2**). Application of the multiple regression-derived $^{Amph/L}D$-estimating models to tests, including experimentally derived $^{Amph/L}D$ which are independent from those employed in the MR analyses, and those calculated from Ongatiti MgHbl-glass pairs, yields good agreement with measurements for predicting $^{Amph/L}D$ of Sr, Pb, Ti, Zr, Nb, LREE and MREE. This suggests that reasonable accuracy is achieved for predicting $^{Amph/L}D$ of those elements with MR analyses.

Published amphibole major and trace element compositional data from Mt. Pinatubo, Mt. Hood, Shiveluch Volcano, Mt. St. Helens and Ongatiti are applied as case studies. $^{Amph/L}D$ and major and trace element contents in the melt are inferred based on amphibole crystal chemistry. This enables us to constrain whether the differences of trace element concentrations in amphiboles with contrasting major element compositions are due to the differences of $^{Amph/L}D$ or melt trace element concentrations. We demonstrate that melt trace element contents are the dominant factor governing Sr, Pb, Ti and Zr concentrations in amphibole, but for Nb, REE and Y, partition coefficients instead are the primary control.

We then use case studies of Mt. Pinatubo and Mangakino Volcano to demonstrate that the inferred melt trace compositions have significant implications in decoding magmatic processes that contribute to amphibole compositional diversity in arc magma plumbing systems. Bimodal amphibole populations and hence inferred melt compositions in Mt. Pinatubo indicate magma mingling process, which is consistent with conclusions driven by earlier studies, e.g. Pallister *et al.* (1996). The inferred melt trace element compositions from bimodal groups also record co-crystallization of plagioclase, ilmenite, zircon and apatite together with amphiboles in various significances, and the interpretation can be generally supported by petrography evidences. For Ongatiti amphiboles, the melt Pb and La variations predicted from patchy zoned cores indicate recycling crystal mush components derived from a mafic melt followed by equilibration with a felsic rim-crystallizing melt. While the rims of the Ongatiti amphiboles record co-crystallization of zircon, apatite and minor ilmenite.

4.7. REFERENCES

Adam, J. & Green, T. (2006). Trace element partitioning between mica- and amphibole-bearing garnet lherzolite and hydrous basanitic melt: 1. Experimental results and the investigation of controls on partitioning behaviour. *Contributions to Mineralogy and Petrology* **152**, 1-17.

Adam, J. & Green, T. H. (1994). The Effects of Pressure and Temperature on the Partitioning of Ti, Sr and Ree between Amphibole, Clinopyroxene and Basanitic Melts. *Chemical Geology* **117**, 219-233.

Adam, J., Green, T. H. & Sie, S. H. (1993). Proton Microprobe Determined Partitioning of Rb, Sr, Ba, Y, Zr, Nb and Ta between Experimentally Produced Amphiboles and Silicate Melts with Variable F Content. *Chemical Geology* **109**, 29-49.

Alonso-Perez, R., Muntener, O. & Ulmer, P. (2009). Igneous garnet and amphibole fractionation in the roots of island arcs: experimental constraints on andesitic liquids. *Contributions to Mineralogy and Petrology* **157**, 541-558.

Anderson, J. L. & Smith, D. R. (1995). The Effects of Temperature and F(O2) on the Al-in-Hornblende Barometer. *American Mineralogist* **80**, 549-559.

Arculus, R. J. & Wills, K. J. A. (1980). The Petrology of Plutonic Blocks and Inclusions from the Lesser Antilles Island Arc. *Journal of Petrology* **21**, 743-799.

Bachmann, O. & Dungan, M. A. (2002). Temperature-induced Al-zoning in hornblendes of the Fish Canyon magma, Colorado. *American Mineralogist* **87**, 1062-1076.

Bédard, J. H. (2005). Partitioning coefficients between olivine and silicate melts. *Lithos* **83**, 394-419.

Bédard, J. H. (2006). Trace element partitioning in plagioclase feldspar. *Geochimica et Cosmochimica Acta* **70**, 3717-3742.

Bédard, J. H. (2007). Trace element partitioning coefficients between silicate melts and orthopyroxene: Parameterizations of D variations. *Chemical Geology* **244**, 263-303.

Bédard, J. H. (2014). Parameterizations of calcic clinopyroxene-Melt trace element partition coefficients. *Geochemistry Geophysics Geosystems* **15**, 303-336.

Blundy, J. & Wood, B. (1994). Prediction of Crystal-Melt Partition-Coefficients from Elastic-Moduli. *Nature* **372**, 452-454.

Borisova, A. Y., Freydier, R., Polve, M., Salvi, S., Candaudap, F. & Aigouy, T. (2008). In situ multi-element analysis of the Mount Pinatubo quartz-hosted melt inclusions by NIR femtosecond laser ablation-inductively coupled plasma-mass spectrometry. *Geostandards and Geoanalytical Research* **32**, 209-229.

Bottazzi, P., Tiepolo, M., Vannucci, R., Zanetti, A., Brumm, R., Foley, S. F. & Oberti, R. (1999). Distinct site preferences for heavy and light REE in amphibole and the prediction of D-Amph/L(REE). *Contributions to Mineralogy and Petrology* **137**, 36-45.

Brenan, J. M., Shaw, H. F., Ryerson, F. J. & Phinney, D. L. (1995). Experimental-Determination of Trace-Element Partitioning between Pargasite and a Synthetic Hydrous Andesitic Melt. *Earth and Planetary Science Letters* **135**, 1-11.

Cashman, K. & Blundy, J. (2013). Petrological cannibalism: the chemical and textural consequences of incremental magma body growth. *Contributions to Mineralogy and Petrology* **166**, 703-729.

Cashman, K. V. & McConnell, S. M. (2005). Multiple levels of magma storage during the 1980 summer eruptions of Mount St. Helens, WA. *Bulletin of Volcanology* **68**, 57-75.

Cawthorn, R. G. & O'Hara, M. J. (1976). Amphibole fractionation in calc-alkaline magma genesis. *American Journal of Science* **276**, 309-329.

Cooper, G. F. (2014). The dynamics of large-scale silicic magmatic systems: case studies from Mangakino Volcanic Centre, Taupo Volcanic Zone, New Zealand. Victoria University of Wellington.

Cooper, G. F. & Wilson, C. J. N. (2014). Development, mobilisation and eruption of a large crystal-rich rhyolite: The Ongatiti ignimbrite, New Zealand. *Lithos* **198**, 38-57.

Cooper, G. F., Wilson, C. J. N., Charlier, B. L. A., Wooden, J. L. & Ireland, T. R. (2014). Temporal evolution and compositional signatures of two supervolcanic systems recorded in zircons from Mangakino volcanic centre, New Zealand. *Contributions to Mineralogy and Petrology* **167**.

Dalpé, C. & Baker, D. R. (2000). Experimental investigation of large-ion-lithophile-element-, high-field-strength-element- and rare-earth-element-partitioning between calcic amphibole and basaltic melt: the effects of pressure and oxygen fugacity. *Contributions to Mineralogy and Petrology* **140**, 233-250.

Davidson, J., Turner, S., Handley, H., Macpherson, C. & Dosseto, A. (2007). Amphibole "sponge" in arc crust? *Geology* **35**, 787-790.

Dirksen, O., Humphreys, M. C. S., Pletchov, P., Melnik, O., Demyanchuk, Y., Sparks, R. S. J. & Mahony, S. (2006). The 2001-2004 dome-forming eruption of Shiveluch volcano, Kamchatka: Observation, petrological investigation and numerical modelling. *Journal of Volcanology and Geothermal Research* **155**, 201-226.

Dostal, J., Dupuy, C., Carron, J. P., Dekerneizon, M. L. & Maury, R. C. (1983). Partition-Coefficients of Trace-Elements - Application to Volcanic-Rocks of St-Vincent, West-Indies. *Geochimica et Cosmochimica Acta* **47**, 525-533.

Foley, S. F., Barth, M. G. & Jenner, G. A. (2000). Rutile/melt partition coefficients for trace elements and an assessment of the influence of rutile on the trace element characteristics of subduction zone magmas. *Geochimica et Cosmochimica Acta* **64**, 933-938.

Fujimaki, H. (1986). Partition-Coefficients of Hf, Zr, and Ree between Zircon, Apatite, and Liquid. *Contributions to Mineralogy and Petrology* **94**, 42-45.

Green, T. H. & Pearson, N. J. (1985). Experimental-Determination of Ree Partition-Coefficients between Amphibole and Basaltic to Andesitic Liquids at High-Pressure. *Geochimica et Cosmochimica Acta* **49**, 1465-1468.

Green, T. H. & Pearson, N. J. (1987). An Experimental-Study of Nb and Ta Partitioning between Ti-Rich Minerals and Silicate Liquids at High-Pressure and Temperature. *Geochimica et Cosmochimica Acta* **51**, 55-62.

Hammarstrom, J. M. & Zen, E. A. (1986). Aluminum in Hornblende: an Empirical Igneous Geobarometer. *American Mineralogist* **71**, 1297-1313.

Hawthorne, F. C., Oberti, R., Harlow, G. E., Maresch, W. V., Martin, R. F., Schumacher, J. C. & Welch, M. D. (2012). Nomenclature of the amphibole supergroup. *American Mineralogist* **97**, 2031-2048.

Hidalgo, P. J. & Rooney, T. O. (2010). Crystal fractionation processes at Baru volcano from the deep to shallow crust. *Geochemistry Geophysics Geosystems* **11**.

Hilyard, M., Nielsen, R. L., Beard, J. S., Patino-Douce, A. & Blencoe, J. (2000). Experimental determination of the partitioning behavior of rare earth and high field strength elements between pargasitic amphibole and natural silicate melts. *Geochimica et Cosmochimica Acta* **64**, 1103-1120.

Holland, T. & Blundy, J. (1994). Nonideal Interactions in Calcic Amphiboles and Their Bearing on Amphibole-Plagioclase Thermometry. *Contributions to Mineralogy and Petrology* **116**, 433-447.

Humphreys, M. C. S., Blundy, J. D. & Sparks, R. S. J. (2006). Magma Evolution and Open-System Processes at Shiveluch Volcano: Insights from Phenocryst Zoning. *Journal of Petrology* **47**, 2303-2334.

Humphreys, M. C. S., Blundy, J. D. & Sparks, R. S. J. (2008). Shallow-level decompression crystallisation and deep magma supply at Shiveluch Volcano. *Contributions to Mineralogy and Petrology* **155**, 45-61.

Jenner, G. A., Foley, S. F., Jackson, S. E., Green, T. H., Fryer, B. J. & Longerich, H. P. (1993). Determination of Partition-Coefficients for Trace-Elements in High-Pressure Temperature Experimental Run Products by Laser-Ablation Microprobe Inductively-Coupled Plasma-Mass Spectrometry (Lam-Icp-Ms). *Geochimica et Cosmochimica Acta* **57**, 5099-5103.

Kent, A. J. R., Darr, C., Koleszar, A. M., Salisbury, M. J. & Cooper, K. M. (2010). Preferential eruption of andesitic magmas through recharge filtering. *Nature Geoscience* **3**, 631-636.

Klein, M., Stosch, H. G. & Seck, H. A. (1997). Partitioning of high field-strength and rare-earth elements between amphibole and quartz-dioritic to tonalitic melts: An experimental study. *Chemical Geology* **138**, 257-271.

Koleszar, A. (2011). Controls on Eruption Style and Magma Compositions at Mount Hood, Oregon. Ph.D. thesis, Oregon State University, 1-199.

Koleszar, A. M., Kent, A. J. R., Wallace, P. J. & Scott, W. E. (2012). Controls on long-term low explosivity at andesitic arc volcanoes: Insights from Mount Hood, Oregon. *Journal of Volcanology and Geothermal Research* **219-220**, 1-14.

Kratzmann, D. J., Carey, S., Scasso, R. A. & Naranjo, J. A. (2010). Role of cryptic amphibole crystallization in magma differentiation at Hudson volcano, Southern Volcanic Zone, Chile. *Contributions to Mineralogy and Petrology* **159**, 237-264.

Krawczynski, M. J., Grove, T. L. & Behrens, H. (2012). Amphibole stability in primitive arc magmas: effects of temperature, H2O content, and oxygen fugacity. *Contributions to Mineralogy and Petrology* **164**, 317-339.

Kress, V. (1997). Magma mixing as a source for Pinatubo sulphur. *Nature* **389**, 591-593.

Larocque, J. & Canil, D. (2010). The role of amphibole in the evolution of arc magmas and crust: the case from the Jurassic Bonanza arc section, Vancouver Island, Canada. *Contributions to Mineralogy and Petrology* **159**, 475-492.

Latourrette, T., Hervig, R. L. & Holloway, J. R. (1995). Trace-Element Partitioning between Amphibole, Phlogopite, and Basanite Melt. *Earth and Planetary Science Letters* **135**, 13-30.

Leake, B. E., Woolley, A. R., Arps, C. E. S., Birch, W. D., Gilbert, M. C., Grice, J. D., Hawthorne, F. C., Kato, A., Kisch, H. J., Krivovichev, V. G., Linthout, K., Laird, J., Mandarino, J. A., Maresch, W. V., Nickel, E. H., Rock, N. M. S., Schumacher, J. C., Smith, D. C., Stephenson, N. C. N., Ungaretti, L., Whittaker, E. J. W. & Guo, Y. Z. (1997). Nomenclature of amphiboles: Report of the subcommittee on amphiboles of the International Mineralogical

Association, Commission on New Minerals and Mineral Names. *Canadian Mineralogist* **35**, 219-246.
Loewen, M. W. (2013). Volatile mobility of trace metals in volcanic systems. Ph.D. thesis, Oregon State University.
Luhr, J. F. & Carmichael, I. S. E. (1980). The Colima Volcanic Complex, Mexico: I. Post-Caldera Andesites From Volcfin Colima. *Contributions to Mineralogy and Petrology* **71**, 343-372.
Luhr, J. F., Carmichael, I. S. E. & Varekamp, J. C. (1984). The 1982 Eruptions of El-Chichon Volcano, Chiapas, Mexico: Mineralogy and Petrology of the Anhydrite-Bearing Pumices. *Journal of Volcanology and Geothermal Research* **23**, 69-108.
Nagasawa, H. & Schnetzler, C. C. (1971). Partitioning of rare earth, alkali and alkaline earth elements between phenocrysts and acidic igneous magma. *Geochimica et Cosmochimica Acta* **35**, 953-968.
Nandedkar, R. H. (2014). Evolution of hydrous mantle-derived calc-alkaline liquids by fractional crystallization at 0.7 and 0.4 GPa – An experimental study. Ph.D. thesis, ETH.
Nandedkar, R. H., Ulmer, P. & Muntener, O. (2014). Fractional crystallization of primitive, hydrous arc magmas: an experimental study at 0.7 GPa. *Contributions to Mineralogy and Petrology* **167**.
Neill, I., Kerr, A. C., Hastie, A. R., Pindell, J. L. & Millar, I. L. (2013). The Albian-Turonian Island Arc Rocks of Tobago, West Indies: Geochemistry, Petrogenesis, and Caribbean Plate Tectonics. *Journal of Petrology* **54**, 1607-1639.
Nicholls, I. A. & Harris, K. L. (1980). Experimental Rare-Earth Element Partition-Coefficients for Garnet, Clinopyroxene and Amphibole Coexisting with Andesitic and Basaltic Liquids. *Geochimica et Cosmochimica Acta* **44**, 287-308.
Nielsen, R., Ghiorso, M. S. & Trischman, T. (2015). V33C-3119: What We Have Learned About the Existing Trace Element Partitioning data During the Population Phase of traceDs. *AGU Fall Meeting abstracts*. San Francisco.
Oberti, R., Vannucci, R., Zanetti, A., Tiepolo, M. & Brumm, R. C. (2000). A crystal chemical re-evaluation of amphibole/melt and amphibole/clinopyroxene D-Ti values in petrogenetic studies. *American Mineralogist* **85**, 407-419.
Onuma, N., Higuchi, H., Wakita, H. & Nagasawa, H. (1968). Trace element partitioning between two pyroxenes and the host lava. *Earth and Planetary Science Letters* **5**, 47-51.
Pallister, J., Hoblitt, R., Meeker, G. P., Knight, R. J. & Siems, D. F. (1996). Magma Mixing at Mount Pinatubo: Petrographic and Chemical Evidence from the 1991 Deposits. In: Newhall, C. & Punongbayan, R. S. (eds.) *Fire and Mud: Eruptions and Lahars of Mount Pinatubo, Philippines*. Seattle: University of Washington Press, 687-731.
Pallister, J. S., Hoblitt, R. P. & Reyes, A. G. (1992). A Basalt Trigger for the 1991 Eruptions of Pinatubo Volcano. *Nature* **356**, 426-428.
Plail, M., Barclay, J., Humphreys, M. C. S., Edmonds, M., Herd, R. A. & Christopher, T. E. (2014). Chapter 18 Characterization of mafic enclaves in the erupted products of Soufriere Hills Volcano, Montserrat, 2009 to 2010. *Geological Society, London, Memoirs* **39**, 343-360.
Rollinson, H. R. (1993). *Using geochemical data: evaluation, presentation, interpretation*: Pearson Prentice Hall.
Rudnick, R. L. & Fountain, D. M. (1995). Nature and Composition of the Continental-Crust - a Lower Crustal Perspective. *Reviews of Geophysics* **33**, 267-309.
Ruprecht, P., Bergantz, G. W., Cooper, K. M. & Hildreth, W. (2012). The Crustal Magma Storage System of Volcan Quizapu, Chile, and the Effects of Magma Mixing on Magma Diversity. *Journal of Petrology* **53**, 801-840.
Rutherford, M. & Devine, J. D. (1996). Preeruption Pressure-Temperature Conditions and Volatiles in the 1991 Dacitic Magma of Mount Pinatubo. In: Newhall, C. & Punongbayan, R. S. (eds.) *Fire and Mud: Eruptions and Lahars of Mount Pinatubo, Philippines*. Seattle: University of Washington Press, 751-766.
Shannon, R. D. (1976). Revised Effective Ionic-Radii and Systematic Studies of Interatomic Distances in Halides and Chalcogenides. *Acta Crystallographica Section A* **32**, 751-767.

Shimizu, K., Liang, Y., Sun, C. G., Jackson, C. & Saal, A. (2015). V13A-3091: Parameterized Lattice Strain Models for REE Partitioning between Amphibole and Silicate Melt. *AGU Fall Meeting abstracts*. San Francisco.

Sisson, T. W. (1994). Hornblende-Melt Trace-Element Partitioning Measured by Ion Microprobe. *Chemical Geology* **117**, 331-344.

Stamper, C. C., Blundy, J. D., Arculus, R. J. & Melekhova, E. (2014). Petrology of Plutonic Xenoliths and Volcanic Rocks from Grenada, Lesser Antilles. *Journal of Petrology* **55**, 1353-1387.

Sun, C. G. & Liang, Y. (2012). Distribution of REE between clinopyroxene and basaltic melt along a mantle adiabat: effects of major element composition, water, and temperature. *Contributions to Mineralogy and Petrology* **163**, 807-823.

Thornber, C., Pallister, J. S., Lowers, H. A., Rowe, M. C., Mandeville, C. & Meeker, G. P. (2008). Chemistry, mineralogy and petrology of amphibole in Mount St. Helens 2004-2006 Dacite. In: Sherrod, D. R., Scott, W. E. & Stauffer, P. H. (eds.) *A volcano rekindled: the renewed eruption of Mount St Helens, 2004-2006*. Washington: U.S. Geological Survey Professional Paper.

Tiepolo, M., Bottazzi, P., Foley, S. F., Oberti, R., Vannucci, R. & Zanetti, A. (2001). Fractionation of Nb and Ta from Zr and Hf at mantle depths: the role of titanian pargasite and kaersutite. *Journal of Petrology* **42**, 221-232.

Tiepolo, M., Oberti, R., Zanetti, A., Vannucci, R. & Foley, S. F. (2007). Trace-element partitioning between amphibole and silicate melt. *Amphiboles: Crystal Chemistry, Occurrence, and Health Issues* **67**, 417-451.

Tiepolo, M., Vannucci, R., Bottazzi, P., Oberti, R., Zanetti, A. & Foley, S. (2000a). Partitioning of rare earth elements, Y, Th, U, and Pb between pargasite, kaersutite, and basanite to trachyte melts: Implications for percolated and veined mantle. *Geochemistry Geophysics Geosystems* **1**.

Tiepolo, M., Vannucci, R., Oberti, R., Foley, S., Bottazzi, P. & Zanetti, A. (2000b). Nb and Ta incorporation and fractionation in titanian pargasite and kaersutite: crystal-chemical constraints and implications for natural systems. *Earth and Planetary Science Letters* **176**, 185-201.

Xiong, X. L., Adam, J. & Green, T. H. (2005). Rutile stability and rutile/melt HFSE partitioning during partial melting of hydrous basalt: Implications for TTG genesis. *Chemical Geology* **218**, 339-359.

Zhang, J., Davidson, J. P., Humphreys, M. C. S., Macpherson, C. G. & Neill, I. (2015). Magmatic Enclaves and Andesitic Lavas from Mt. Lamington, Papua New Guinea: Implications for Recycling of Earlier-fractionated Minerals through Magma Recharge. *Journal of Petrology* **56**, 2223-2256.

4.8. FIGURES

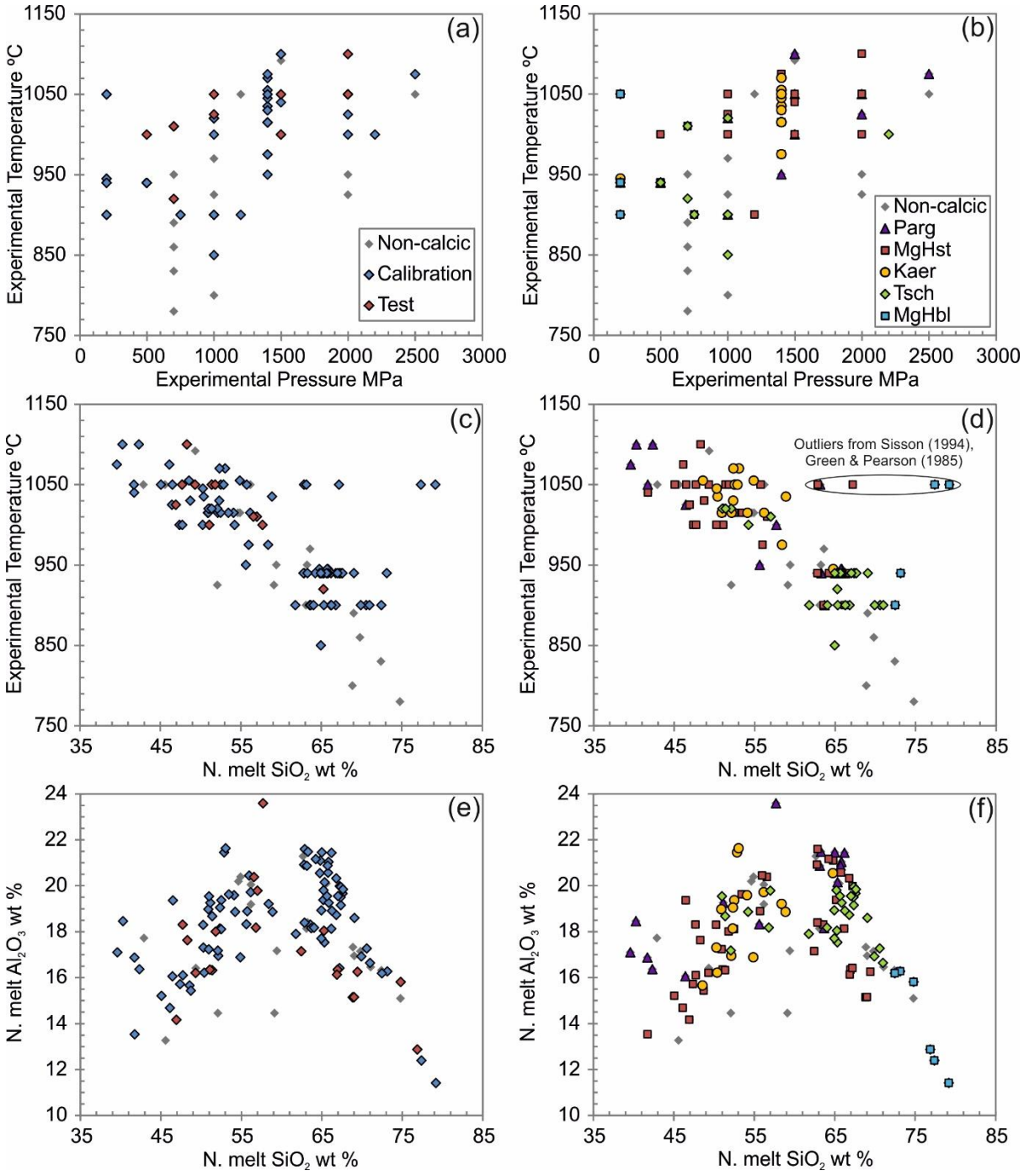

Fig. 4.1 P-T-X conditions of the selected $^{Amph/L}D$-determining studies. In (a), (c) and (e), blue symbols represent those experiments used for multiple regression analyses, while red symbols indicate those experiments used for tests. In (b), (d) and (f), the experiments are symbolled as the species of calcic amphiboles (and non-calcic amphiboles) produced in the experiments.

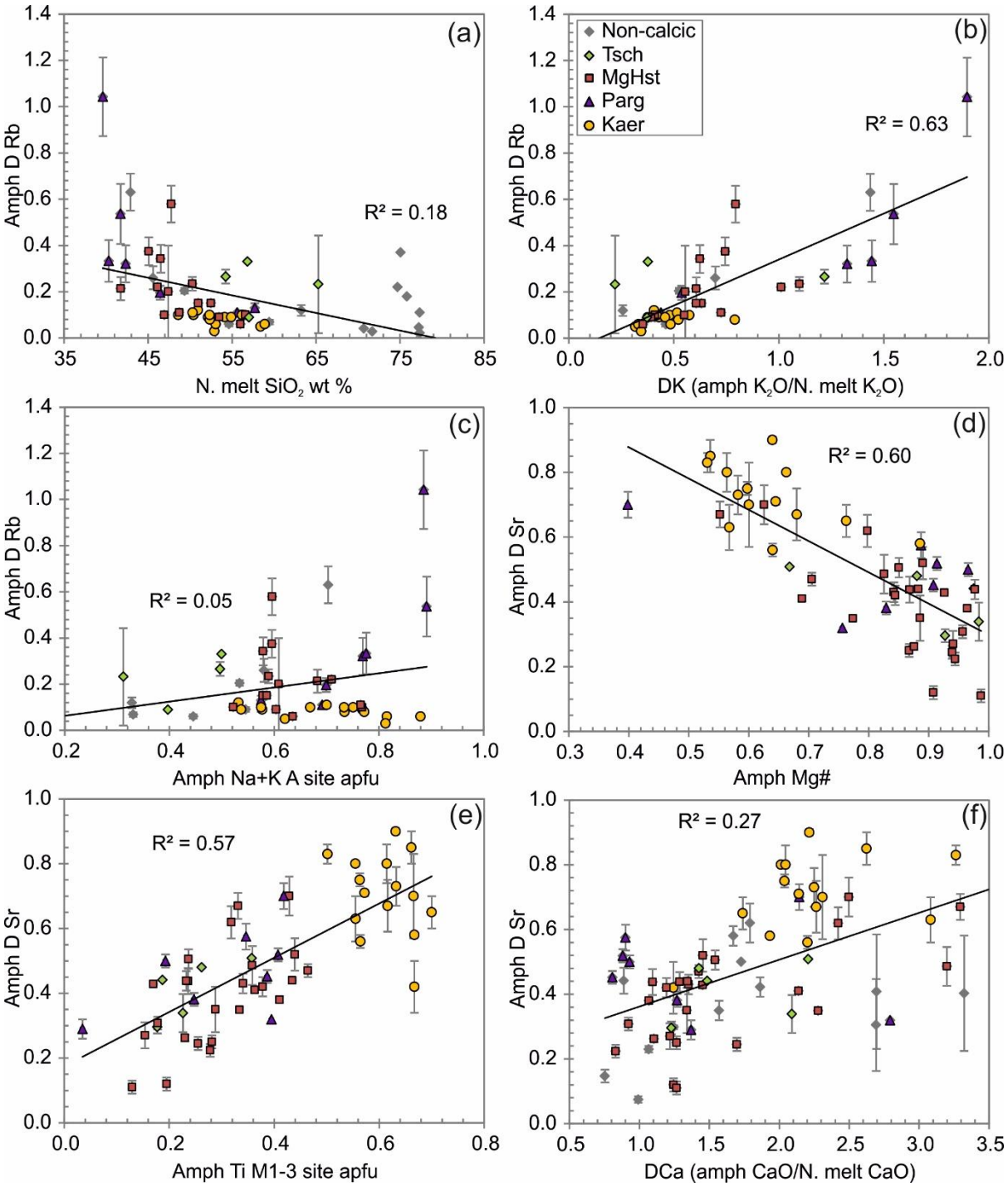

Fig. 4.2 $^{Amph/L}D$ of different trace elements plotted against melt compositions, amphibole crystal formula proportions, and major element partition coefficients. See text for details.

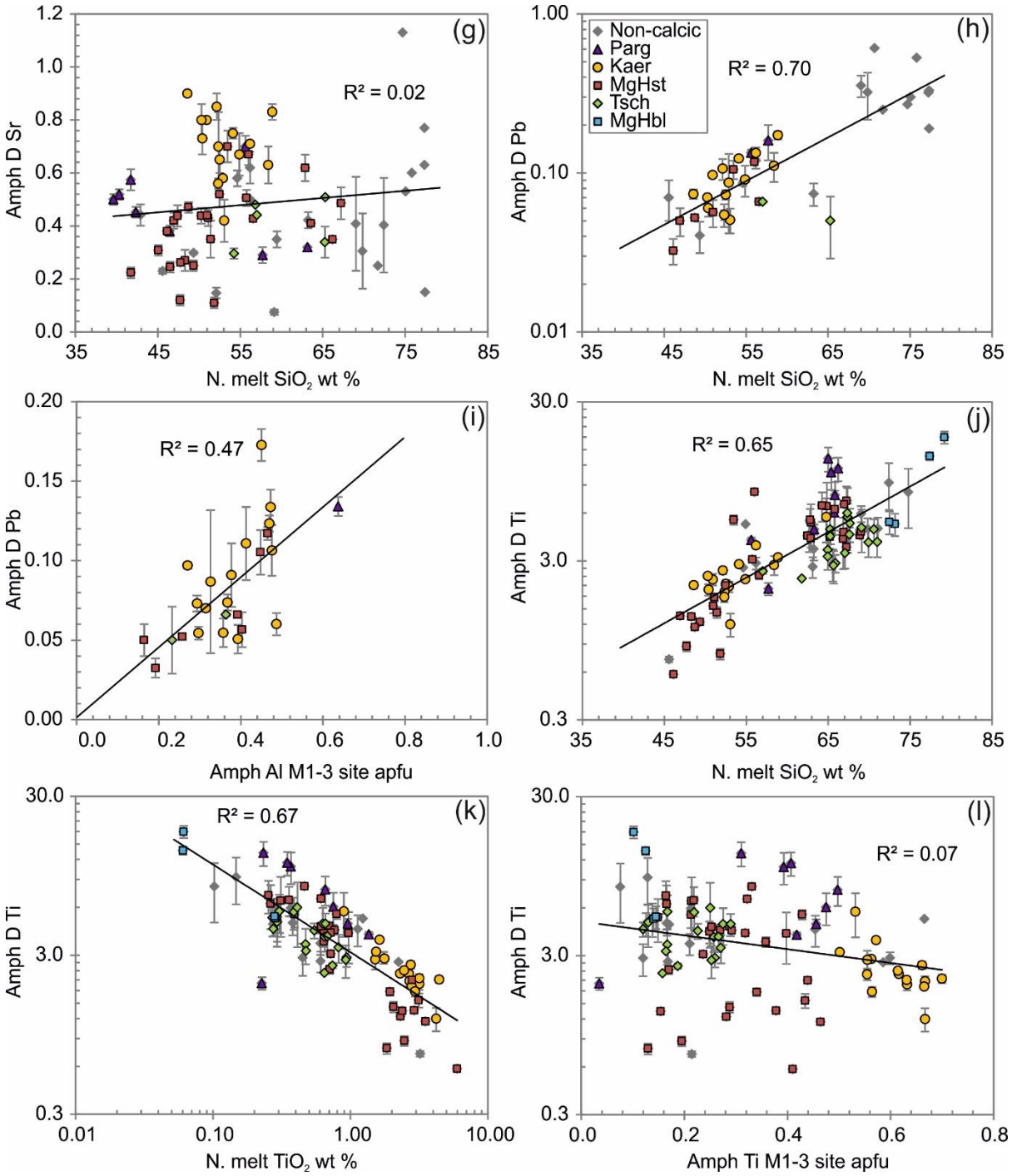

Fig. 4.2 continued

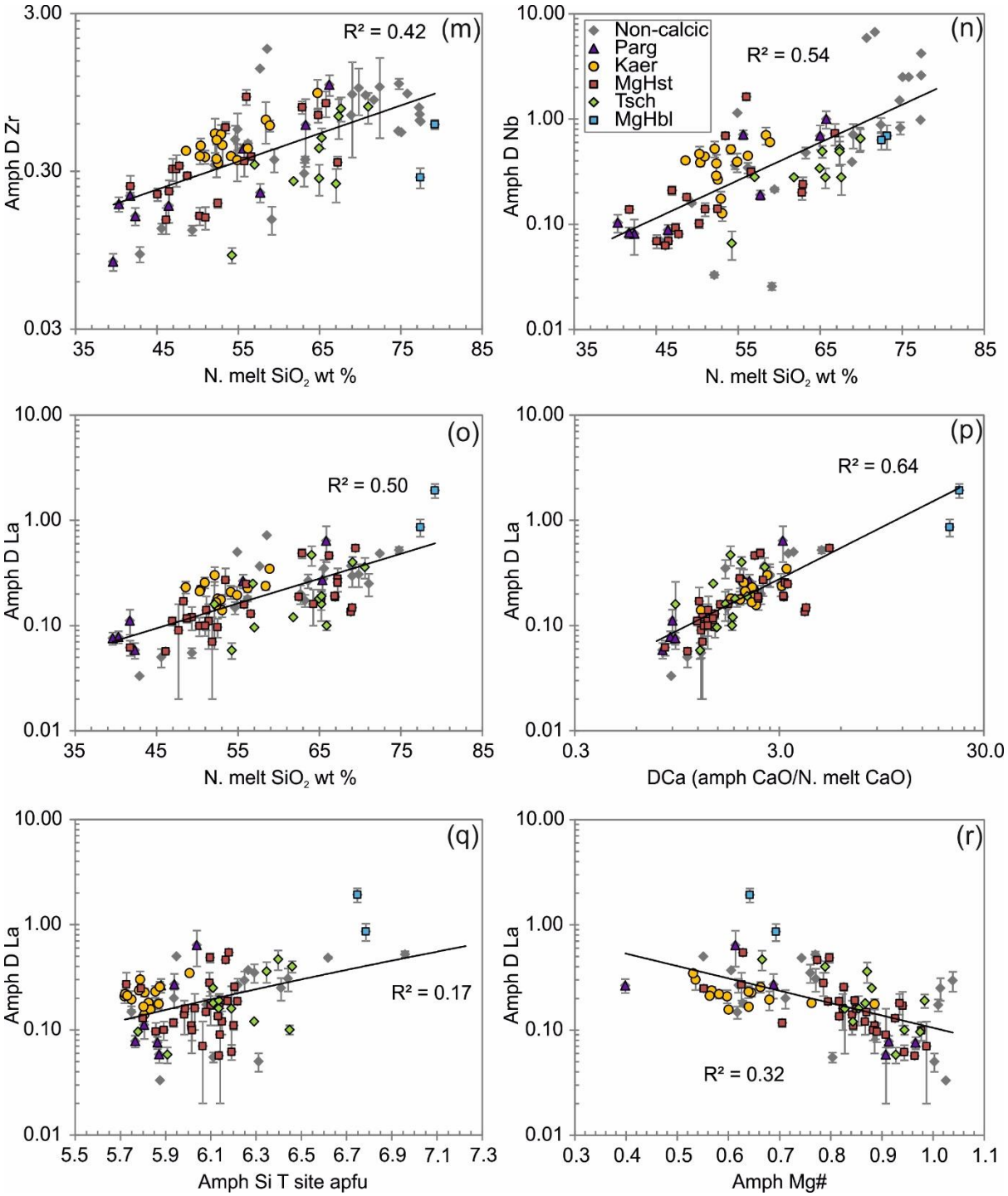

Fig. 4.2 continued.

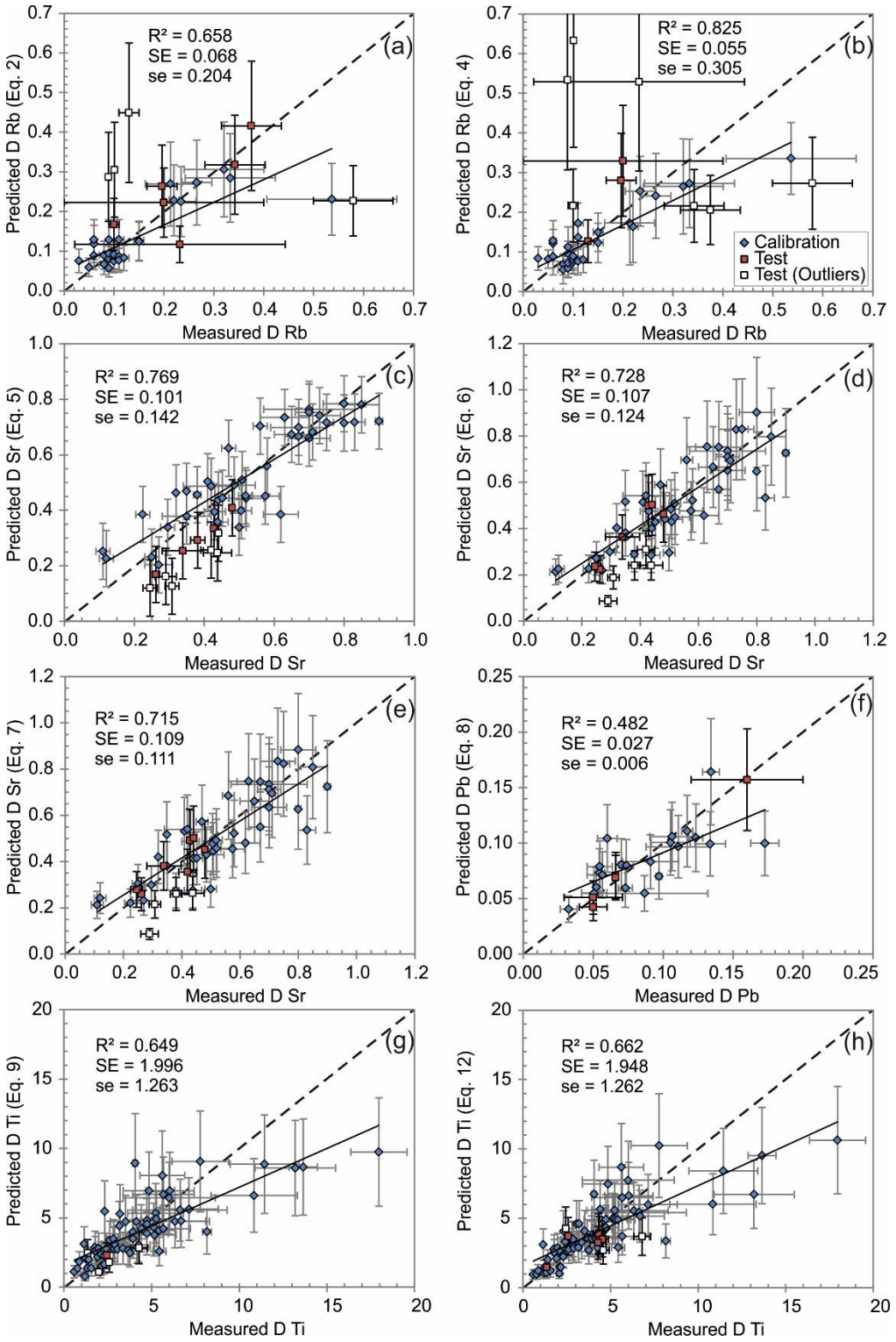

Fig. 4.3 Results of multiple regression analyses (blue) and tests (red and white) for calibrating and testing the accuracy of predicting $^{Amph/L}D$ with amphibole crystal chemistry ± temperature. The corresponding equations to each plot are given in Table 3-5. Test points shown in red suggest agreement with the measured $^{Amph/L}D$ is within the error of the predicted $^{Amph/L}D$; while symbols in white indicate that the offset between the predicted and measured $^{Amph/L}D$ is larger than the error of predicted $^{Amph/L}D$. R^2 and SE represent the correlation coefficient and standard error of estimate for the calibration data points, while se represents the standard error of estimate for the test points. The dashed line in each plot represents the 1:1 line.

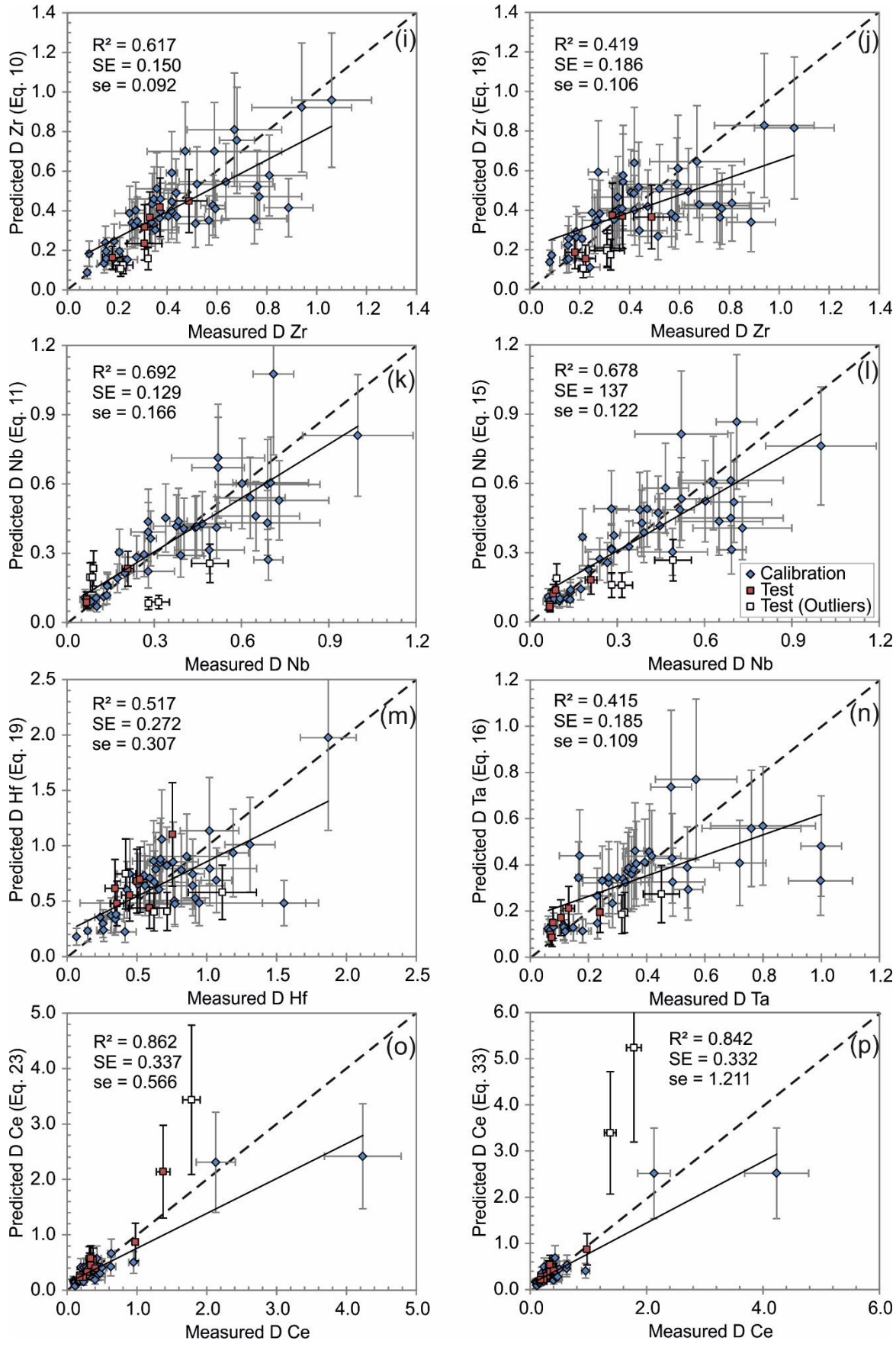

Fig. 4.3 continued

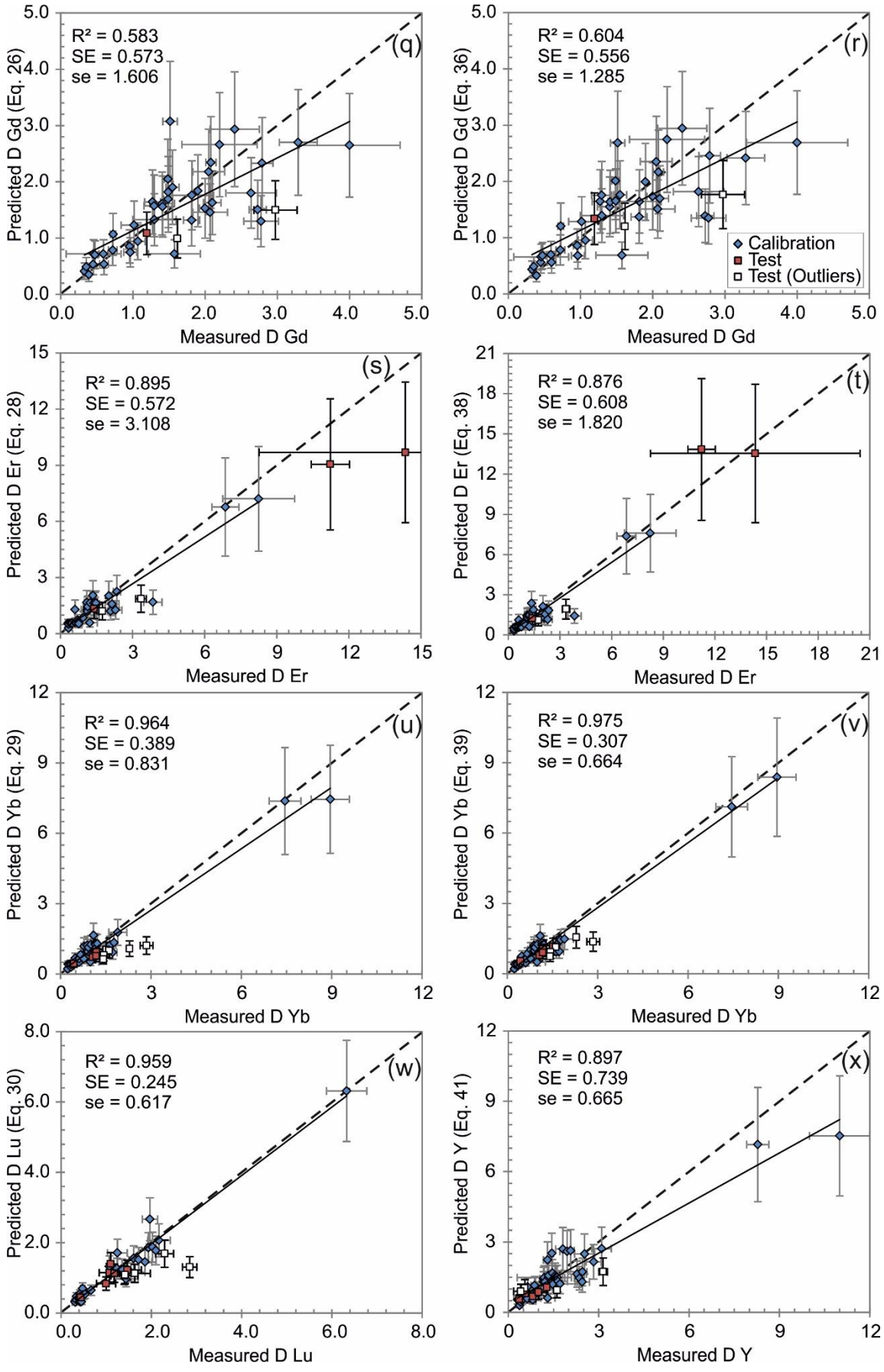

Fig. 4.3 continued

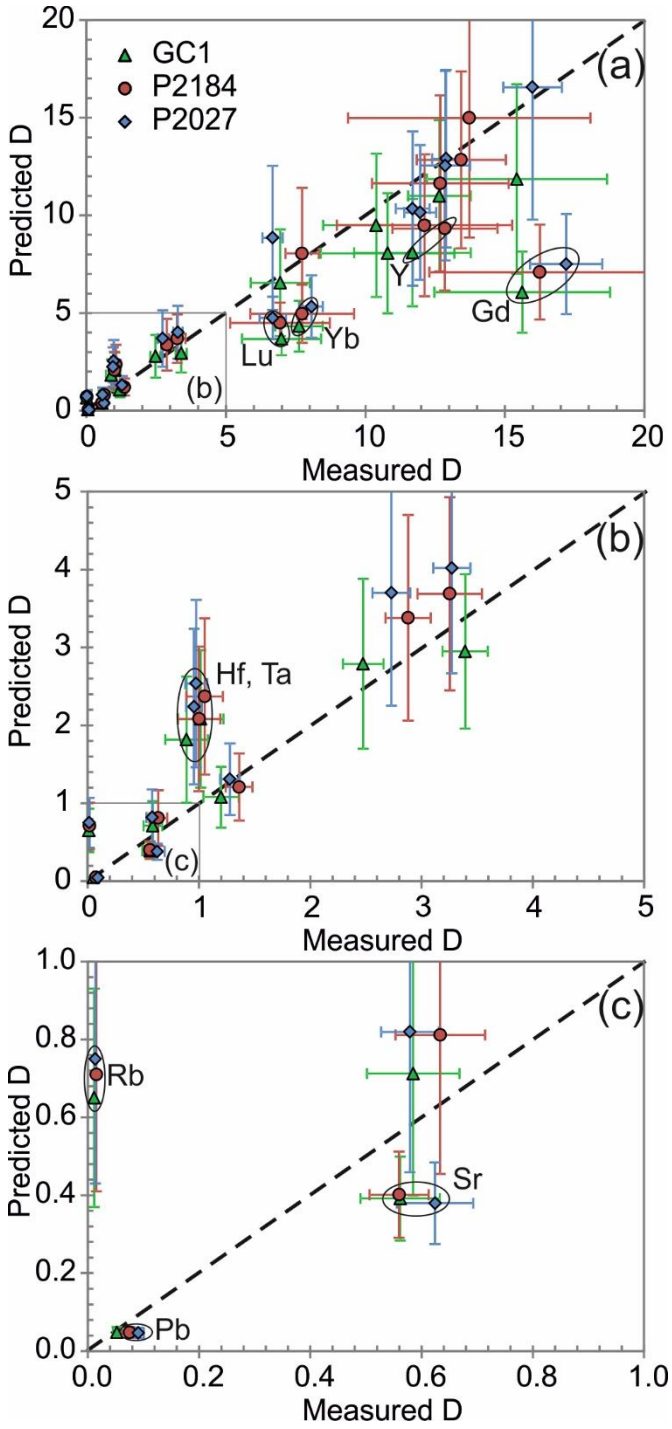

Fig. 4.4 Predicted $^{Amph/L}D$ against measured $^{Amph/L}D$ with Ongatiti amphibole and matrix glass compositions from Cooper & Wilson (2014); the results are given in Table 6. The data points outlined with ellipsoids are those showing disagreement with the measured $^{Amph/L}D$. The dashed line in each plot represents the 1:1 line.

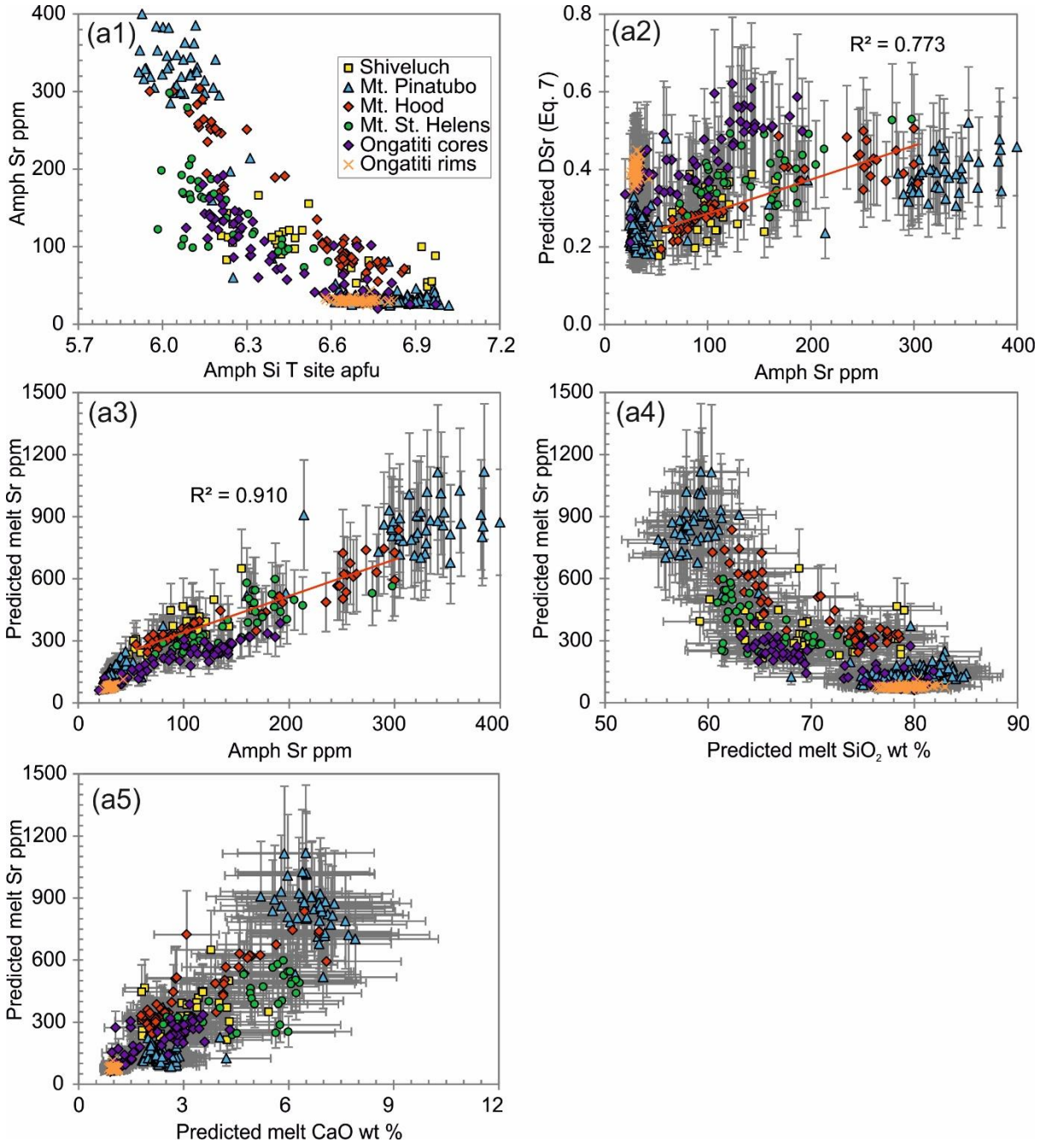

Fig. 4.5 Plots of amphibole trace elements, predicted $^{Amph/L}D$ and inferred melt major and trace element compositions for amphiboles from Mt. Pinatubo (blue), Mt. Hood (red), Mt. St. Helens (green), Shiveluch Volcano (yellow), and Ongatiti (purple for amphibole cores, orange for amphibole rims). The errors in the predicted $^{Amph/L}D$ are calculated based on the corresponding MR-derived equations in Table 3-5; the errors in the inferred melt trace element compositions are calculated with errors in predicted $^{Amph/L}D$ and 10% analytical uncertainties in the trace element analyses, according to Loewen (2013). White arrows in (d), (e), (f) and (g) indicate co-crystallization of other mineral phases (zircon, ilmenite/rutile and apatite) together with amphibole; purple stars in (b4), (f4) and (f5) illustrate the possible source melt which is parental to the least evolved patchy cores in Ongatiti amphiboles, and equilibration of less silicic amphiboles with rim-crystallizing melt may be responsible for producing the variations of predicted melt Pb and La against melt SiO_2 (purple arrows); (a) Sr; (b) Pb; (c) Ti; (d) Zr; (e) Nb; (f) La; (g) Y.

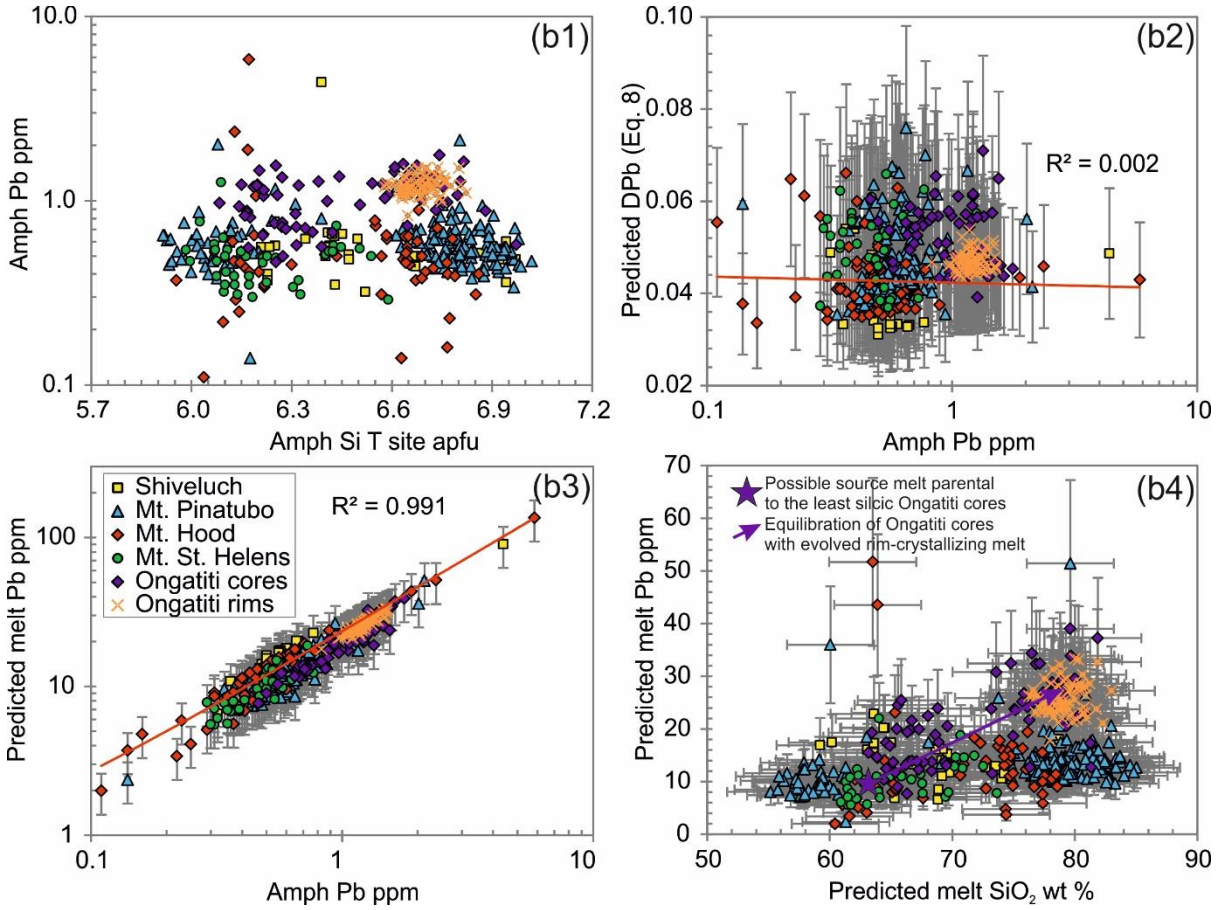
(b1)
Amph Pb ppm
Amph Si T site apfu
(b2)
Predicted DPb (Eq. 8)
R² = 0.002
Amph Pb ppm
(b3)
Shiveluch
Mt. Pinatubo
Mt. Hood
Mt. St. Helens
Ongatiti cores
Ongatiti rims
R² = 0.991
Predicted melt Pb ppm
Amph Pb ppm
(b4)
Possible source melt parental to the least silcic Ongatiti cores
Equilibration of Ongatiti cores with evolved rim-crystallizing melt
Predicted melt Pb ppm
Predicted melt SiO2 wt %

Fig. 4.5b

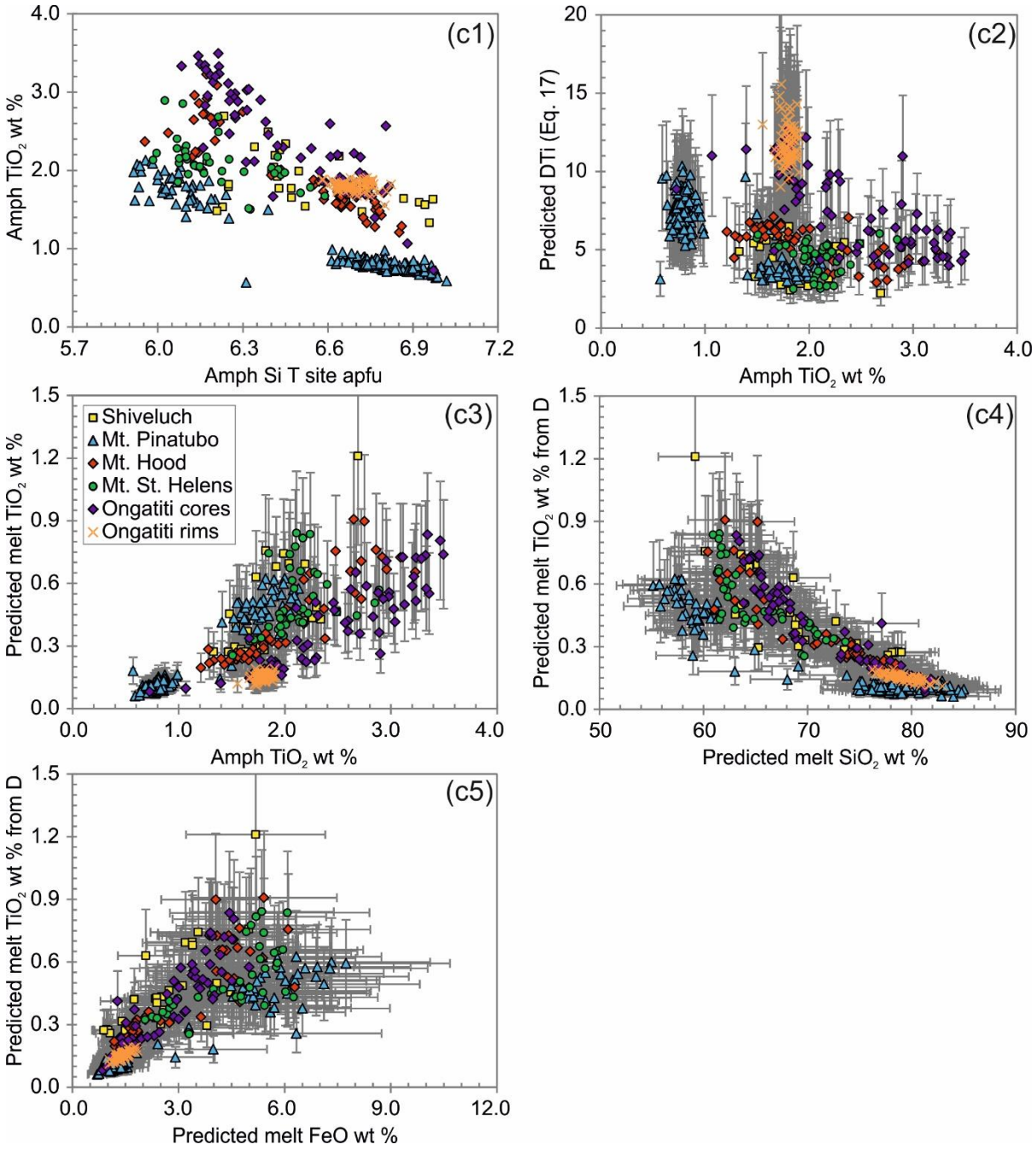
(c1)
Amph TiO2 wt %
Amph Si T site apfu
(c2)
Predicted DTi (Eq. 17)
Amph TiO2 wt %
(c3)
Shiveluch
Mt. Pinatubo
Mt. Hood
Mt. St. Helens
Ongatiti cores
Ongatiti rims
Predicted melt TiO2 wt %
Amph TiO2 wt %
(c4)
Predicted melt TiO2 wt % from D
Predicted melt SiO2 wt %
(c5)
Predicted melt TiO2 wt % from D
Predicted melt FeO wt %

Fig. 4.5c

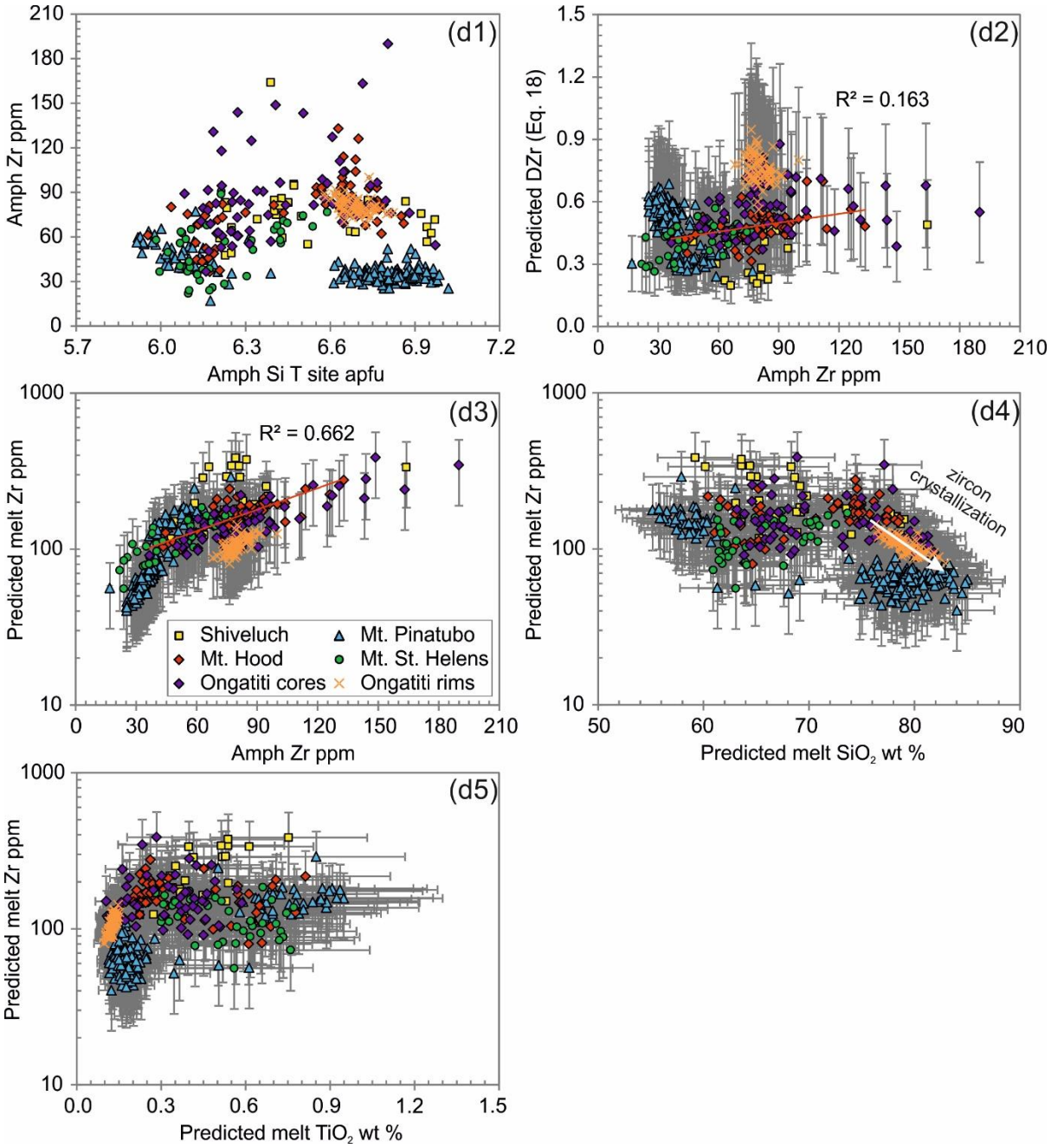
(d1)
Amph Zr ppm
Amph Si T site apfu
(d2)
R² = 0.163
Predicted DZr (Eq. 18)
Amph Zr ppm
(d3)
R² = 0.662
Predicted melt Zr ppm
Amph Zr ppm
Shiveluch
Mt. Pinatubo
Mt. Hood
Mt. St. Helens
Ongatiti cores
Ongatiti rims
(d4)
zircon crystallization
Predicted melt Zr ppm
Predicted melt SiO2 wt %
(d5)
Predicted melt Zr ppm
Predicted melt TiO2 wt %

Fig. 4.5d

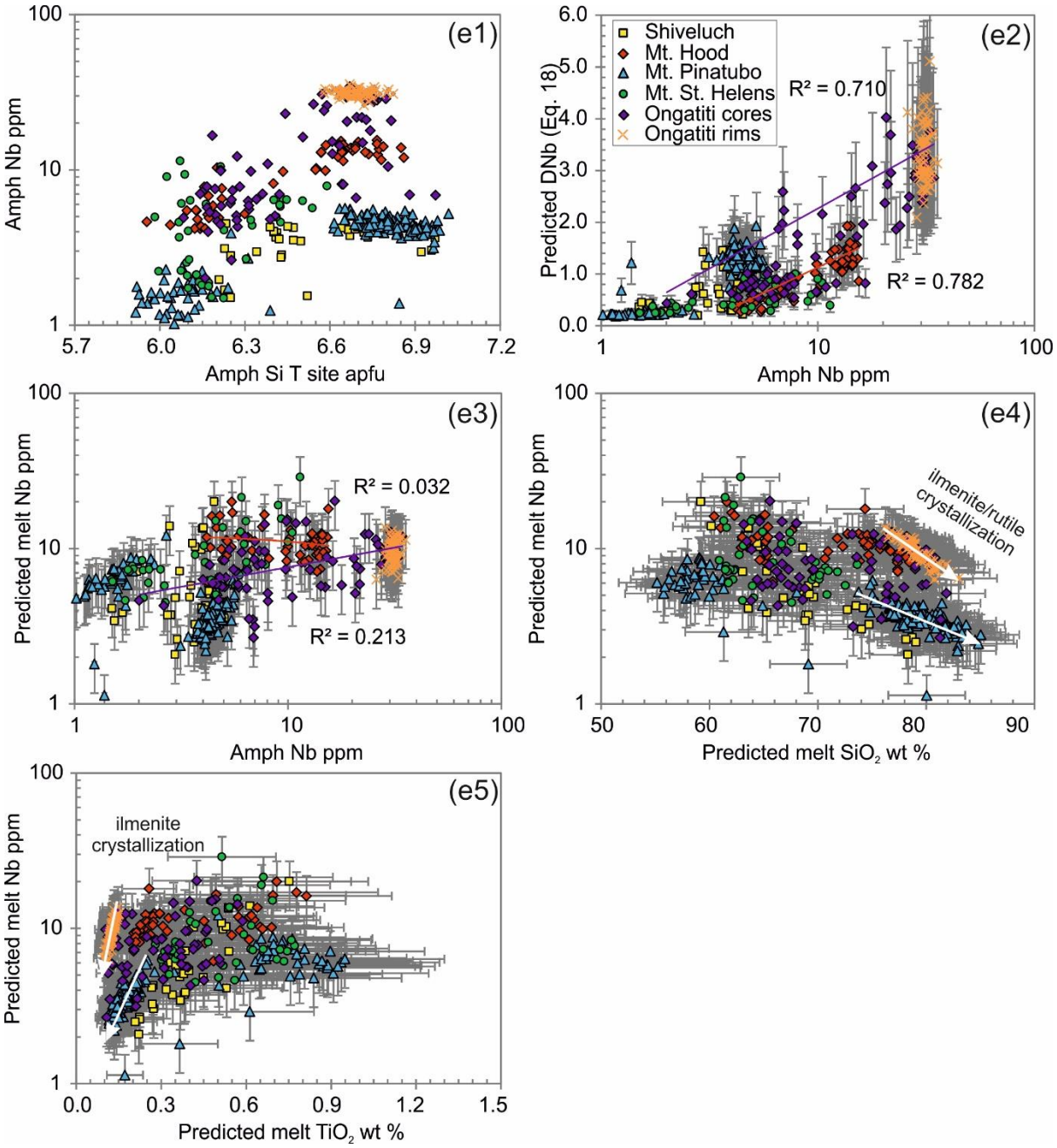
(e1)
Amph Nb ppm
Amph Si T site apfu
(e2)
Shiveluch
Mt. Hood
Mt. Pinatubo
Mt. St. Helens
Ongatiti cores
Ongatiti rims
R² = 0.710
R² = 0.782
Predicted DNb (Eq. 18)
Amph Nb ppm
(e3)
R² = 0.032
R² = 0.213
Predicted melt Nb ppm
Amph Nb ppm
(e4)
ilmenite/rutile crystallization
Predicted melt Nb ppm
Predicted melt SiO2 wt %
(e5)
ilmenite crystallization
Predicted melt Nb ppm
Predicted melt TiO2 wt %

Fig. 4.5e

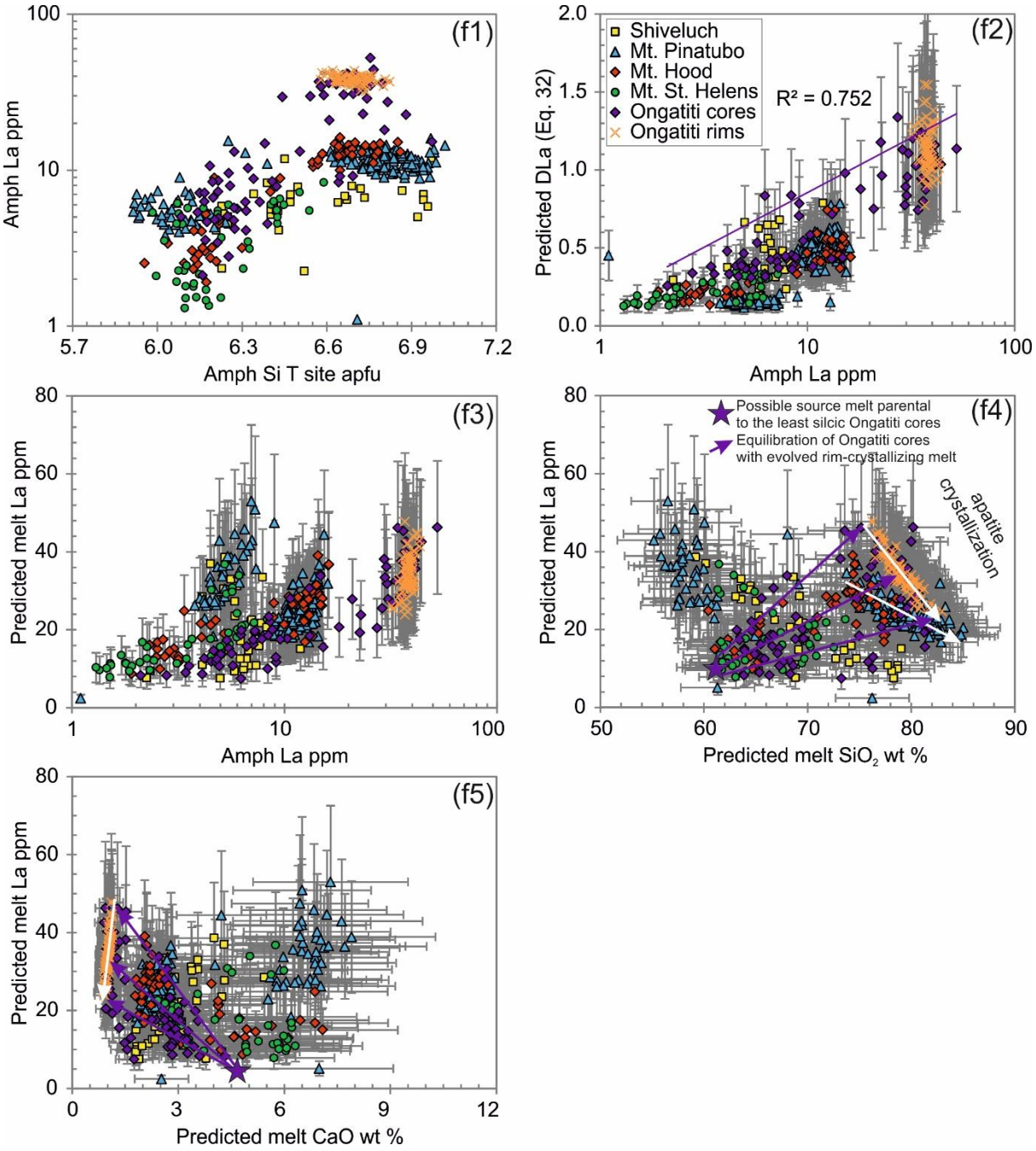
(f1)
Amph La ppm
Amph Si T site apfu
(f2)
Shiveluch
Mt. Pinatubo
Mt. Hood
Mt. St. Helens
Ongatiti cores
Ongatiti rims
R² = 0.752
Predicted DLa (Eq. 32)
Amph La ppm
(f3)
Predicted melt La ppm
Amph La ppm
(f4)
Possible source melt parental to the least silcic Ongatiti cores
Equilibration of Ongatiti cores with evolved rim-crystallizing melt
apatite crystallization
Predicted melt La ppm
Predicted melt SiO2 wt %
(f5)
Predicted melt La ppm
Predicted melt CaO wt %

Fig. 4.5f

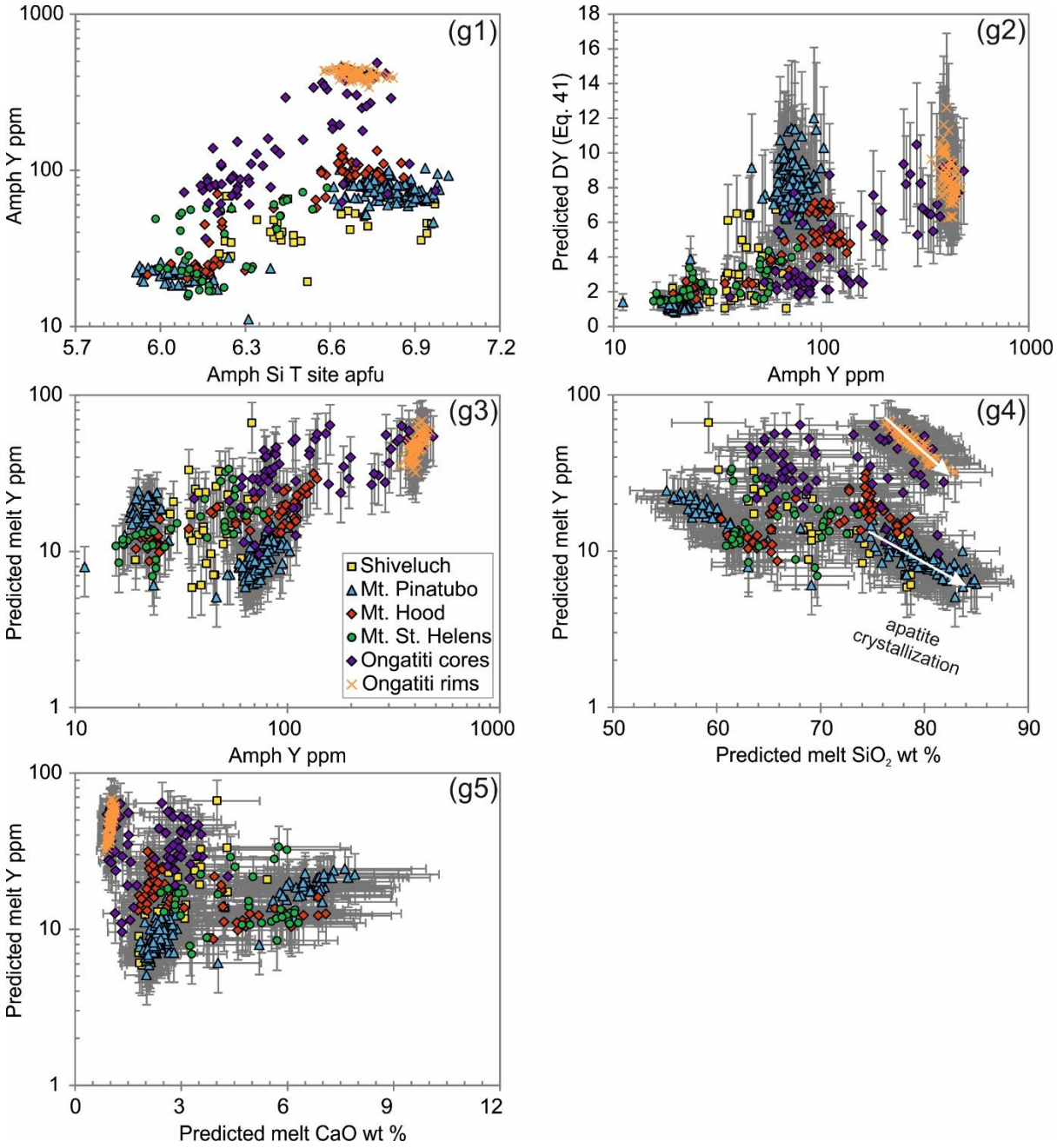
(g1)
Amph Y ppm
Amph Si T site apfu
(g2)
Predicted DY (Eq. 41)
Amph Y ppm
(g3)
Predicted melt Y ppm
Amph Y ppm
Shiveluch
Mt. Pinatubo
Mt. Hood
Mt. St. Helens
Ongatiti cores
Ongatiti rims
(g4)
Predicted melt Y ppm
apatite crystallization
Predicted melt SiO2 wt %
(g5)
Predicted melt Y ppm
Predicted melt CaO wt %

Fig. 4.5g

4.9. TABLES

Table 1 Major and trace element ionic radius (Å) and their site preferences in amphibole crystal structure.

T	IV	M1-3	VI	M4	VIII	A	XII
Si4+	0.26	Al3+	0.535	Ca2+	1.12	K+	1.64
Al3+	0.39	Ti4+	0.605	Na+	1.18	Na+	1.39
Ti4+	0.42	Cr3+	0.615	**REE**		**LILE**	
		Fe3+	0.645	La3+	1.16	Rb+	1.72
		Mg2+	0.72	Ce3+	1.143	Ba2+	1.61
		Fe2+	0.78	Pr3+	1.126	Sr2+	1.44
		Mn2+	0.83	Nd3+	1.109		
		HFSE		Sm3+	1.079	Pb2+	1.49
		Zr4+	0.72	Eu3+	1.066		
		Hf4+	0.71	Gd3+	1.053		
		Nb5+	0.64	Tb3+	1.04		
		Ta5+	0.64	Dy3+	1.027		
		Metals		Ho3+	1.015		
		Cr3+	0.615	Er3+	1.004		
		Ni2+	0.69	Tm3+	0.994		
		V4+	0.58	Yb3+	0.985		
		V3+	0.64	Lu3+	0.977		
		Sc3+	0.745				
		Co2+	0.745	Y3+	1.019		
		Zn2+	0.74	Sr2+	1.26		
		Cu2+	0.73	Th4+	1.05		
		Ga3+	0.62	U4+	1		

Roman numbers indicate the coordination numbers of the according site; ionic radius data are from Shannon (1976).

Table 4.1

Table 2 Materials, conditions and run products of the selected $^{Amph/L}D$-determining studies

No.	References	Melt compositions	N	P (MPa)	T (ºC)	Calcic-amph species	T2007
1*	Adam et al. 1993	basanite-basalt	8	1,000-2,000	925-1,050	MgHst, Parg	Y
2	Adam & Green 1994	basanite	6	500-2,000	1,000-1,100	MgHst	Y
3*	Adam & Green 2006	basanite	2	1,000-2,000	1,025-1,050	MgHst	
4*	Brenan et al. 1995	andesite	1	1,500	1,000	Parg	Y
5	Dalpé & Baker, 2000	basanite-basalt	8	1,500-2,500	1,000-1,100	MgHst, Parg, Tsch	Y
6	Green & Pearson 1985	andesite	5	750-2,000	900-1,050	MgHst, Parg, Tsch	
7	Hilyard et al. 2000	dacite-tonalite	35	200-500	900-945	MgHst, MgHbl, Parg, Tsch	Y
8	Klein et al. 1997	dacite	3	1,000	800-900	Tsch	Y
9*	Nandedkar 2014	basaltic andesite-rhyolite	8	700	780-1,010	Tsch, MgHst	
10	Nicholls & Harris 1980	basalt-andesite	9	1,000	900-1,020	Tsch, Parg	
11	Sisson 1994	basalt-andesite-dacite-rhyolite	5	200	1050	MgHbl, MgHst	Y
12	Tiepolo et al. 2000a, 2000b, 2001, 2007	basalt-andesite	25	1400	1070	Kaer, MgHst, Parg	Y
13*	Dostal et al. 1983	basalt-andesite	1	-	-	Tsch	
14*	Luhr & Carmichael 1980	andesite	5	-	-	MgHst	
15*	Luhr et al. 1984	andesite	1	-	-	MgHst	
16*	Nagasawa & Schnetzler 1971	dacite	2	-	-	MgHbl	

References No. 1-12 are experimental studies; 13-16 are measurements on natural samples (amphibole-melt pairs); Data in references marked with asterisks are used for test and not included in the multiple regression analysis, except $^{Amph/L}D$ of Yb and Lu from Nagasawa & Schnetzler 1971. Y in the column of T2007 indicate the references considered by the previous review study of Tiepolo et al. 2007.

Table 4.2

Table 4.3

Table 3 Results of multiple linear regressions used for estimating $^{amph/L}D$ on the basis of temperature and calcic-amphibole component

	Dependent				Independent variable coefficients											weighted	weighted	weighted
Eq.	variable	Range of D	N	Constant	T °C	Si	Al(vi)	Mg	Fe3+	Fe2+	Ti	Ca	Na (A)	R^2	SE	R^2	SE	se (test)
1*	lnD Rb	0.03-0.54	28	-10.0892	0.0098						-3.1103		***-1.4521***	0.701	0.371	0.648	0.068	0.170
2*	lnD Rb	0.03-0.54	28	-9.1404	0.0085						-3.4945			0.652	0.392	0.658	0.068	0.204
3*	lnD Rb	0.03-0.54	28	-29.7643	**0.0085**	3.2229		-3.3512		-2.9757		7.2540		0.708	0.383	0.738	0.059	0.303
4*	lnD Rb	0.03-0.54	28	-17.6767		**2.2658**		-2.3829		-2.2997		6.6579		0.624	0.425	0.825	0.055	0.305
5*	D Sr	0.11-0.90	42	**-24.2306**			**4.7934**	**4.8965**	4.9941	5.0659	5.3094			0.769	0.101	-	-	0.142
6*	lnD Sr	0.11-0.90	42	-8.4275			**0.9103**		1.3662	0.4240	3.5870	2.8574		0.730	0.263	0.728	0.107	0.124
7*	lnD Sr	0.11-0.90	42	9.9436			-2.6626	-3.6775	-2.3464	-3.2516		2.8064		0.704	0.275	0.715	0.109	0.111
8*	lnD Pb	0.032-0.17	21	-2.4949			***1.6909***	**-0.2709**						0.563	0.292	0.482	0.027	0.006

Asterisks indicate the multiple linear regression equation does not include magnesiohornblende; bold font indicate the p-value of the parameter is 0.01 < p-value < 0.05; bold italic font indicate > 0.05 p-value; weighted R2 denote the correlation coefficient between predicted D and measured D; weighted SE and se for test results are in wt %.

Table 4.4

Table 4 Results of multiple linear regressions used for estimating $^{amph/L}D$ on the basis of temperature and calcic-amphibole component

	Dependent				Independent variable coefficients											weighted	weighted	weighted
Eq.	variable	Range of D	N	Constant	T °C	Si	Al(vi)	Mg	Fe3+	Fe2+	Ti	Ca	Na (A)	R^2	SE	R^2	SE	se (test)
9	lnD Ti	0.580-18.0	66	**-5.3584**	-0.0037	1.3175		-0.9320				2.8551		0.692	0.401	0.649	1.996	1.263
10	lnD Zr	0.08-1.06	46	**8.6888**	-0.0038	1.9630	-4.1253	-6.5119	-3.5904	-5.8814		4.8775	2.3549	0.722	0.354	0.617	0.150	0.092
11	lnD Nb	0.062-1.0	41	**-9.1794**	-0.0060	2.1853		-0.9249			2.8891	**1.3637**		0.839	0.326	0.692	0.129	0.166
12	lnD Ti	0.580-18.0	66	-35.1877		2.7543	3.3290		3.6087	1.0878	6.1626	7.8006		0.753	0.364	0.662	1.948	1.262
13	lnD Zr	0.08-1.06	46	-34.0622		2.4693	2.9883		3.3919	0.7891	7.7102	6.8533		0.539	0.444	0.409	0.188	0.125
14	lnD Hf	0.07-1.9	39	-36.2125		3.1013	**2.2841**		3.1699	0.8538	7.6612	6.4069		0.628	0.426	0.511	0.274	0.368
15	lnD Nb	0.062-1.0	41	-42.1024		3.9181	2.5191		3.5446	1.3754	8.0374	6.0403		0.834	0.336	0.678	0.137	0.122
16	lnD Ta	0.062-1.00	44	-36.1952		3.3074	**2.3303**		2.9786	1.1491	6.4495	5.4145		0.641	0.452	0.415	0.185	0.109
17	lnD Ti	0.580-18.0	66	-17.0968		2.7487		-3.6875		-2.6407	2.8682	7.8158		0.765	0.352	0.666	1.925	1.832
18	lnD Zr	0.08-1.06	46	-16.8751		2.4066		-3.2096		-2.4751	4.3594	6.4472		0.536	0.440	0.419	0.186	0.106
19	lnD Hf	0.07-1.9	39	-20.9513		3.1517		-2.8788		-2.1204	4.6483	5.7256		0.622	0.423	0.517	0.272	0.307
20	lnD Nb	0.062-1.0	41	-25.8246		4.1209		-3.3842		-2.1321	4.8737	5.5398		0.831	0.334	0.623	0.152	0.138
21	lnD Ta	0.062-1.00	44	-21.7315		3.3665		-2.8397		**-1.7750**	3.6521	4.9879		0.641	0.446	0.400	0.188	0.123

Bold font indicate the p-value of the parameter is > 0.01 and <0.05; bold italic font indicate >0.05 p-value.

Table 4.5

Table 5 Results of multiple linear regressions used for estimating $^{amph/L}D$ on the basis of calcic-amphibole formular component

Eq.	Dependent variable	Range of D	N	Constant	Independent variable coefficients							R^2	SE	weighted R^2	weighted SE	weighted se (test)
					Si	Al(vi)	Mg	Fe3+	Fe2+	Ti	Ca					
22	lnD La	0.057-1.92	54	-27.6853	2.5704	**1.2790**		1.8251	1.0069	4.0482	3.9567	0.766	0.360	0.804	0.144	0.058
23	lnD Ce	0.093-4.23	36	-38.2268	3.5601	***1.8345***		3.1187	1.0077	6.9110	5.8340	0.801	0.392	0.924	0.337	0.566
24	lnD Nd	0.197-8.73	36	-40.4087	3.8697	***2.1971***		3.4314	1.0378	7.5835	6.1429	0.793	0.417	0.891	0.627	1.413
25	lnD Sm	0.27-11.3	60	-37.8156	3.5403	2.1975		3.3358	1.1328	6.8877	6.1645	0.795	0.386	0.865	0.700	0.824
26*	lnD Gd	0.33-4	41	-44.0408	4.2682	4.7387		3.8681	0.8387	8.8905	6.3062	0.759	0.347	0.846	0.573	1.606
27	lnD Dy	0.33-12.33	36	-46.5188	4.5209	3.3543		4.2393	0.9772	9.0382	7.0177	0.799	0.409	0.926	0.719	2.536
28	lnD Er	0.31-8.25	34	-40.5125	3.7462	**2.7824**		3.9121	0.9571	7.9964	6.6053	0.790	0.388	0.895	0.572	3.108
29	lnD Yb	0.24-8.95	35	-39.0189	4.0673	3.9037		3.4268	0.6640	7.9084	4.4606	0.872	0.309	0.964	0.389	0.831
30	lnD Lu	0.3-6.3	29	-39.6589	3.5026	3.4692		3.7985	0.8025	7.0851	6.8962	0.935	0.228	0.959	0.245	0.617
31	lnD Y	0.3-11	43	-39.3037	3.9645	3.1324		3.4732	0.9251	7.3236	5.3610	0.810	0.354	0.894	0.770	0.666
32	lnD La	0.057-1.92	54	-19.8905	2.7255		-1.8178		***-0.8579***	2.5304	3.9963	0.767	0.356	0.774	0.152	0.054
33	lnD Ce	0.093-4.23	36	-27.7753	4.3140		-3.3281		-2.3900	4.6699	6.2085	0.796	0.390	0.842	0.332	1.211
34	lnD Nd	0.197-8.73	36	-27.9831	4.5562		-3.6189		-2.6497	4.9855	6.4824	0.791	0.412	0.875	0.615	3.009
35	lnD Sm	0.27-11.3	60	-23.9916	3.9127		-3.3322		-2.3126	4.1799	6.1593	0.779	0.398	0.806	0.838	1.266
36*	lnD Gd	0.33-4	41	-21.4324	3.7334		-3.8797		-2.9731	4.6656	6.5134	0.759	0.342	0.799	0.556	1.285
37	lnD Dy	0.33-12.33	36	-27.7413	4.8381		-4.2880		-3.3683	5.3200	7.1244	0.804	0.396	0.917	0.728	4.998
38	lnD Er	0.31-8.25	34	-24.7713	4.2974		-4.0186		-3.1335	4.7875	6.7542	0.789	0.382	0.876	0.608	1.820
39	lnD Yb	0.24-8.95	35	-20.2659	3.7412		-3.4917		-2.7473	4.2831	4.9048	0.874	0.301	0.975	0.307	0.664
40	lnD Lu	0.3-6.3	29	-21.6358	3.7843		-3.4863		-3.0453	5.2504	5.4975	0.888	0.293	0.930	0.342	0.658
41	lnD Y	0.3-11	43	-21.8049	3.9247		-3.4093		-2.5304	4.0095	5.1674	0.819	0.340	0.897	0.739	0.665

Asterisks indicate the multiple regression equation does not include magnesiohornblende; bold font indicate the p-value of the parameter is 0.01 < p-value < 0.05; bold italic font indicate > 0.05 p-value.

Table 6 Amphibole and glass compositions from Cooper & Wilson (2014) used for calculating D, and our predictions based on MR equations.

	Amph compositions						Glass compositions					
	GC1		P2027		P2184		GC1		P2027		P2184	
	n=28		n=33		n=30		n=22		n=9		n=29	
	wt%	sd	wt%	sd	wt%	sd	wt%	sd	wt%	sd	wt%	sd
SiO_2	44.62	0.33	45.15	0.46	44.74	0.35	77.75	0.16	77.97	0.43	78.63	0.30
TiO_2	1.77	0.04	1.82	0.06	1.81	0.11	0.13	0.02	0.13	0.01	0.13	0.01
Al_2O_3	7.68	0.16	7.23	0.22	7.60	0.26	12.34	0.11	12.50	0.14	12.21	0.08
FeOt	19.40	0.30	19.53	0.31	19.97	0.54	1.30	0.07	0.72	0.40	0.74	0.30
MgO	10.17	0.19	10.24	0.25	9.95	0.31	0.11	0.01	0.04	0.03	0.06	0.03
CaO	10.59	0.08	10.66	0.11	10.64	0.11	0.85	0.02	0.77	0.07	0.79	0.02
MnO	0.48	0.03	0.37	0.02	0.38	0.02	0.04	0.02	0.01	0.01	0.02	0.01
Na_2O	1.98	0.05	1.78	0.09	1.83	0.06	3.41	0.17	3.06	0.19	3.32	0.13
K_2O	0.65	0.03	0.60	0.04	0.64	0.04	4.08	0.12	4.79	0.34	4.09	0.13
	n=20		n=15		n=18		n=7		n=1		n=8	
	ppm	sd	ppm	sd	ppm	sd	ppm	sd	ppm	sd	ppm	sd
Rb	1.82	0.16	2.09	0.38	2.24	0.67	158.96	8.63	152.40		144.85	3.63
Sr	29.94	1.90	31.09	3.41	30.35	2.09	53.30	5.87	49.80		54.24	3.53
Ba	134.79	12.24	142.04	15.18	138.42	11.19	936.14	38.19	853.00		831.13	25.54
Pb	1.14	0.13	1.29	0.14	1.29	0.13	21.79	1.83	14.20		17.17	2.74
Th	0.22	0.04	0.23	0.03	0.22	0.05	16.85	2.37	14.97		14.13	1.61
U	0.04	0.02	0.05	0.02	0.06	0.02	3.70	0.17	3.91		3.50	0.33
Ti	10327	396	10747	412	10492	387	816	65	834		781	88
Zr	79.89	4.91	78.01	6.96	78.65	4.03	136.53	17.46	134.70		124.14	14.43
Hf	4.25	0.39	3.90	0.40	4.09	0.48	4.19	0.75	4.00		3.89	0.40
Nb	31.05	1.37	31.42	1.61	31.23	2.13	9.15	0.37	9.60		9.60	0.55
Ta	0.88	0.09	0.92	0.07	0.88	0.10	0.99	0.19	0.96		0.88	0.14
La	38.45	2.19	37.83	2.64	37.35	2.15	32.09	3.81	29.60		27.45	1.86
Ce	171.48	9.76	177.17	11.00	170.81	9.28	69.26	3.26	64.90		59.30	2.68
Pr	34.41	1.84	33.40	2.01	33.23	2.29	7.37	0.76	7.01		6.10	0.48
Nd	195.63	10.75	186.77	10.14	190.72	12.86	28.17	4.03	28.00		24.68	0.93
Sm	66.17	3.57	64.30	4.43	64.51	5.20	6.37	1.12	5.00		5.09	0.89
Eu	3.96	0.20	4.07	0.28	4.01	0.43	0.56	0.12	0.51		0.48	0.09
Gd	81.68	5.85	73.93	5.56	74.94	5.75	5.23	0.99	4.30		4.61	1.07
Tb	13.48	0.94	12.27	0.87	12.88	1.21	0.92	0.17	0.72		0.76	0.12
Dy	85.50	6.90	78.34	5.13	82.50	7.17	5.54	1.07	4.90		6.01	1.83
Ho	16.80	0.68	15.87	1.05	15.73	1.72	1.37	0.32	1.05		1.01	0.23
Er	43.80	2.73	40.91	2.12	42.59	2.85	4.06	0.86	3.50		3.52	0.88
Tm	5.88	0.35	5.34	0.38	5.46	0.62	0.59	0.07	0.50		0.56	0.17
Yb	32.03	1.89	31.69	1.60	30.76	2.63	4.20	0.40	3.93		3.98	0.90
Lu	4.40	0.41	3.74	0.27	4.13	0.41	0.63	0.11	0.56		0.60	0.14
Y	418.38	24.65	385.18	18.45	404.19	22.33	35.81	6.04	32.20		31.46	4.27

	Measured D						Eq. #	Predicted D					
		se		se		se			se		se		se
Rb	0.01	0.00	0.01	0.00	0.02	0.00	4	**0.65**	**0.28**	**0.75**	**0.32**	**0.71**	**0.30**
Sr	0.56	0.07	0.62	0.07	0.56	0.05	7	**0.39**	**0.11**	**0.38**	**0.10**	**0.40**	**0.11**
Ba	0.14	0.01	0.17	0.02	0.17	0.01							
Pb	0.05	0.01	0.09	0.01	0.08	0.01	8	0.05	0.01	**0.05**	**0.01**	**0.05**	**0.01**
Th	0.01	0.00	0.02	0.00	0.02	0.00							
U	0.01	0.00	0.01	0.00	0.02	0.01							
Ti	12.65	1.12	12.89	0.49	13.43	1.60	17	10.99	3.87	12.90	4.54	12.85	4.52
Zr	0.59	0.08	0.58	0.05	0.63	0.08	18	0.71	0.31	0.82	0.36	0.81	0.36
Hf	1.02	0.21	0.97	0.10	1.05	0.16	19	**2.08**	**0.88**	**2.54**	**1.07**	**2.37**	**1.00**
Nb	3.39	0.20	3.27	0.17	3.25	0.29	15	2.95	0.99	4.02	1.35	3.69	1.24
Ta	0.89	0.19	0.96	0.07	1.00	0.19	21	**1.82**	**0.81**	**2.24**	**1.00**	**2.08**	**0.93**
La	1.20	0.16	1.28	0.09	1.36	0.12	32	1.08	0.39	1.31	0.46	1.21	0.43
Ce	2.48	0.18	2.73	0.17	2.88	0.20	23	2.79	1.09	3.70	1.45	3.38	1.32
Pr	4.67	0.54	4.76	0.29	5.45	0.57							
Nd	6.94	1.06	6.67	0.36	7.73	0.60	24	6.55	2.73	8.85	3.69	8.05	3.36
Sm	10.39	1.91	12.86	0.89	12.68	2.45	25	9.49	3.67	12.55	4.85	11.64	4.50
Eu	7.04	1.57	7.97	0.54	8.39	1.77							
Gd	15.62	3.15	17.19	1.29	16.25	3.96	36	**6.07**	**2.08**	**7.51**	**2.57**	**7.10**	**2.43**
Tb	14.66	2.95	17.04	1.21	16.98	3.11							
Dy	15.42	3.23	15.99	1.05	13.72	4.34	27	11.86	4.85	16.56	6.77	14.99	6.12
Ho	12.26	2.95	15.11	1.00	15.63	3.97							
Er	10.80	2.40	11.69	0.61	12.12	3.15	38	8.06	3.08	10.34	3.95	9.50	3.63
Tm	9.89	1.24	10.67	0.76	9.75	3.09							
Yb	7.62	0.85	8.06	0.41	7.73	1.86	39	**4.33**	**1.30**	**5.33**	**1.60**	**4.96**	**1.49**
Lu	6.99	1.41	6.68	0.48	6.94	1.78	30	**3.68**	**0.84**	**4.75**	**1.08**	**4.50**	**1.03**
Y	11.68	2.09	11.96	0.57	12.85	1.88	41	**8.09**	**2.75**	10.15	3.45	**9.33**	**3.18**

n indicates the number of analysis; predicted D in bold font indicate offset from measured D.

Table 4.6

CHAPTER 5

Amphibole sub-crystal scale compositional bimodality reflects arc magma hybridization

J. ZHANG*, M. C. S. HUMPHREYS, G. F. COOPER, J. P. DAVIDSON, C. G. MACPHERSON

DEPARTMENT OF EARTH SCIENCES, UNIVERSITY OF DURHAM, DURHAM, DH1 3LE, UK

*Corresponding author. E-mail: jing.zhang5@durham.ac.uk

ABSTRACT

Amphiboles in the 1951 andesite and diktytaxitic and plutonic magmatic enclaves from Mt. Lamington display compositional bimodality (magnesiohornblende-tschermakite/MgHbl-Tsch vs. magnesiohastingsite/MgHst). We applied amphibole-related thermometric and chemometric equations to amphibole crystal chemistry and calculated both crystallization temperature and melt compositions. We interpret that MgHst crystallize from a hotter, less silica-rich melt and MgHbl-Tsch from a cooler, more silica-rich melt. Chemometric equations from a previous study (Ridolfi *et al*., 2010) indicate that the two types of amphiboles crystallised at widely different pressures. However, bulk-rock and amphibole crystal textures indicate quenching-driven crystallisation of MgHst in diktytaxitic enclaves following the recharge of the enclave-forming magma against the cooler host andesite, and therefore a large difference in crystallisation pressure is highly unlikely. Instead, magma hybridization brings the two different types of amphiboles together. We also observe the amphibole compositional bimodality in sub-crystal scale. Two different types of oscillatory zoned amphibole phenocrysts in the 1951 andesite are identified: spiky and diffuse. Crystal chemistry variations across spiky oscillatory zoning (MgHbl-Tsch & low-Mg# MgHst) are interpreted to reflect magma temperature or pressure fluctuations, without the effect of magma replenishment. It probably results from magma convection within a zone which is only thermally affected by the recharge of the enclave-forming magma. In contrast, diffuse oscillatory zoning (MgHbl-Tsch & high-Mg# MgHst) is thought to be driven by fluctuations in temperatures and/or pressures and mafic magma input, and is inferred to be caused by magma convection in a zone both thermally and geochemically affected by magma recharge. This study provides strong quantitative evidence of magma mixing in producing volcanic products at Mt Lamington, similar to other centres at convergent margins, and demonstrates the wider potential of amphibole for inferring the melt compositions and thermal regimes associated with magmatic processes at a range of volcanic environments.

KEY WORDS: Amphibole, Compositional bimodality, Mt. Lamington, Magma mixing, Oscillatory zoning.

This chapter is prepared as a paper manuscript to be submitted to *Lithos*.

5.1. INTRODUCTION

Open magmatic processes such as partial melting, fractional crystallization, magma mixing and crustal assimilation have been revealed as globally important in producing magmas of intermediate compositions beneath subduction-related volcanoes (Davidson, 1996; Macpherson, 2008; McCulloch & Bennett, 1994; O'Hara, 1977). Amphibole is a common mineral phase present in water-bearing arc magmas, the crystallization of which is a complex function of magmatic intensive parameters, such as temperature (T), pressure (P), oxygen fugacity (fO_2), as well as melt (in this chapter 'melt' refers to the melts from which amphiboles are crystallized, rather than magmas which include crystals) compositions (Ridolfi *et al.*, 2008; Ridolfi & Renzulli, 2012; Ridolfi *et al.*, 2010). Any changes in the magmatic temperature and melt compositions caused by open magmatic processes, can thus in principle be recorded in amphibole geochemical and/or textural variations. Therefore, careful examination of amphibole crystal texture, combined with in-situ geochemical analyses of crystal zones provides the key to fingerprinting the pre-eruptive magma evolution history in the magma plumbing system (Chambefort *et al.*, 2013; De Angelis *et al.*, 2013; Erdmann *et al.*, 2014; Kiss *et al.*, 2014; Ruprecht *et al.*, 2012; Shane & Smith, 2013; Turner *et al.*, 2013; Ubide *et al.*, 2014).

Through the contribution from earlier studies (Erdmann *et al.*, 2014; Putirka, 2016; Ridolfi *et al.*, 2008; Ridolfi & Renzulli, 2012; Ridolfi *et al.*, 2010), and progress made during this Ph.D. research, amphibole crystallization temperature, and melt major and trace element compositions can be well constrained, with reasonable uncertainties, from amphibole major and trace element compositions. The reconstruction of melt chemistry and temperature can be used to explore open magmatic processes which contribute to amphibole compositional and textural diversity, complementary to other petrological and geochemical approaches, e.g. crystal size distribution studies (Cashman & Marsh, 1988; Marsh, 1988) and crystal isotopic stratigraphy (Davidson *et al.*, 2007). We have demonstrated the applicability of this approach for studying magma mixing or petrological cannibalism processes in case studies of Mt. Pinatubo (Philippines) and the Ongatiti ignimbrite of the Mangakino Volcano, New Zealand (see Chapter 4).

In this chapter, we will revisit Mt. Lamington volcano, Papua New Guinea, to explore open magmatic processes occurred in the magma plumbing system which has shaped the geochemistry of the 1951 eruption products dramatically, from the perspective of amphibole crystal textural and compositional stratigraphy. We present new amphibole textural and geochemical data, in addition to Chapter 2 (Zhang *et al.*, 2015). We first apply amphibole-only thermometer models to Mt. Lamington amphiboles, to calculate the crystallization temperature. Then we apply our melt major and trace element calibration models (Chapter 3 and 4) to provide estimations of the melt compositions. Finally, we discuss the magmatic processes that contribute to the compositional and textural complexity of the Mt. Lamington amphiboles, and summarize the implications of amphibole crystal complexity in understanding the formation of intermediate arc magma compositions globally.

5.2. BACKGROUND

This section summarizes the geological setting, the 1951 eruption and the petrology of its products of Mt. Lamington, which have been introduced in Chapter 2. The reason why this section is presented here is to keep this chapter as a complete paper manuscript.

5.2.1. Geological setting

Mt. Lamington (8º57'S, 148º09'E) is a Quaternary composite volcano located on the northern face of the Papuan Peninsula, Papua New Guinea. The Papuan Peninsula is semi-confined by the northward-subducting Solomon Sea Basin, the fast-spreading Woodlark Sea Basin, and the Coral Sea Basin (Baldwin *et al.*, 2012). The middle section of the Papuan Peninsula (8ºS to 9º50'S), from southwest to northeast, is composed of the following main geological units (**Fig. 5.1**; Davies, 2012; Smith, 2013a): (1) Aure Fold Belt (AFB), a Late Oligocene-Pliocene westward-facing thrust and fold belt dominated by thick clastic-dominated sediments; (2) Owen Stanley Metamorphic Complex (OSMC); (3) Papuan

Ultramafic Belt (PUB), an ophiolite belt; (4) Quaternary composite volcanoes as well as volcanic and sedimentary deposits, including Mt. Lamington. It is suggested that AFB and OSMC represent the deformation region and mountain roots of paleo-orogen belt, formed by the collision between the paleo-margin of the Australian continent and paleo-arcs (Davies, 2012; Smith, 2013a); and PUB represent an obducted Late Cretaceous oceanic crust emplaced in the Eocene followed the continent-arc collision (Davies & Jaques, 1984; Davies & Smith, 1971; Lus *et al.*, 2004). In the context of no active subduction beneath the Papuan Peninsula currently, Quaternary volcanic activities with subduction trace element signatures are related to the partial melting of subduction-modified mantle (Arculus *et al.*, 1983; Johnson *et al.*, 1978; Zhang *et al.*, 2015), which is probably triggered by the westward propagation of the Woodlark spreading-rifting system (Baldwin *et al.*, 2008; Smith, 2013b; Taylor *et al.*, 1995).

5.2.2. Overview of the 1951 eruption of Mt. Lamington

The 1951 eruption of Mt. Lamington, which lasted until 1956, represents the most recent volcanic activity on the Papuan Peninsula. Prior to this eruption, Mt. Lamington has never been regarded as a volcano, due to the absence of observations and records of volcanic eruptions. The beginning of the volcanic unrest was marked by seismic activities about one week prior to the first climax eruption, coupled with observations of ash-bearing gas emissions from the crater and landslides outside of the crater walls. The climax eruption occurred on 21st January, 1951 and produced ash clouds of up to 12 km in height and pyroclastic density currents which devastated an area of 174 km^2 and took 3,000 lives. Subsequent major explosive eruptions reassumed several times and gradually died out by early March, 1951, coupled with intermittent dome construction-and-collapse within the crater. Then this eruption transitioned to episodes of dome growth of variable growth rate which lasted to 1956 (Taylor, 1958). The dome sits within craters of older volcanic products of shoshonitic composition (pre-1951 shoshonite, unknown age) and is nearly 600 m higher than the base of the crater. It comprises of andesitic lavas (1951 andesite) and contains abundant mafic-intermediate magmatic enclaves, as well as ultramafic PUB xenoliths (Arculus *et al.*, 1983; Taylor, 1958; Zhang *et al.*, 2015).

5.2.3. Petrology of the 1951 andesite and magmatic enclaves

The petrology, whole-rock geochemistry and mineral compositions of the 1951 andesite and enclaves are fully described by Zhang *et al.* (2015), and summarized here. The dome lavas are vesicular, porphyritic medium/high-K andesite (59.2-61.2 wt % SiO_2, 2.1-2.2 wt % K_2O) with 56-64% phenocrysts, dominated by plagioclase, amphibole, and minor biotite and Fe-Ti oxides. Magmatic enclaves have bulk compositions of medium-K basalt to basaltic andesite (49.0-54.2 wt % SiO_2, 1.1-1.7 wt % K_2O). The mineralogy of the enclaves are similar to the andesite host, except that the enclaves are more amphibole-rich and some of them contain a greater proportion of amphibole- and orthopyroxene-rimmed olivine crystals. The olivine-bearing enclaves have a characteristic diktytaxitic texture, represented by acicular framework-forming amphiboles, glassy matrix and abundant bubbles; while other enclaves are characterized by the replacement of olivines with amphibole-dominated crystal aggregates, and they are called plutonic-textured enclaves. The textural variation from diktytaxitic texture to plutonic texture is gradational, observed by increasing crystal grain size, decreasing melt content, thickening of the olivine reaction rims (orthopyroxene-oxides-amphibole) and a corresponding decrease in the size of olivine. The presence of olivine with reaction rims is interpreted as a result of recycling earlier-fractionated crystals through mafic recharge during magma *en route*; amphibole-dominated crystal clusters in plutonic enclaves form from complete olivine reaction with melt; and thus the textural variation of enclaves is believed to be due to the quenching of the recharged enclave-forming magma against the andesitic magma body with different undercooling rates (Zhang *et al.*, 2015).

Morphology and major element crystal chemistry of amphiboles from the 1951 andesite and magmatic enclaves hosted therein are also described and discussed by Zhang *et al.* (2015). Back Scattered Electron (BSE) imaging reveal the majority of amphibole phenocrysts in 1951 andesite,

previously described as 'optically unzoned' in Zhang *et al.* (2015), are strongly oscillatory zoned. Therefore, we have targeted amphibole major element compositional data across crystal zonings using electron probe microanalysis (EPMA). Here, we discuss the implications of the oscillatory zoning in amphibole.

5.3. ANALYTICAL METHODS

5.3.1. Electron probe microanalysis (EPMA)

The samples of 1951 andesite and magmatic enclaves hosted therein were prepared as standard probe sections, polished and carbon-coated to a thickness of ca. 25 nm. Backscattered electron (BSE) images were collected with the Hitachi SU-70 FEG scanning electron microscope at Durham University, prior to elemental analyses. Major and minor elements of amphibole were analysed at Edinburgh University, using the Cameca SX100 electron microprobe equipped with 5 wavelength-dispersive spectrometers. A 15 kV accelerating voltage, 20-60 s counting time on peak position, and PAP correction procedure are used for all analyses. Amphibole are analysed using a 10 µm defocused beam, with 4 nA beam current for major elements (Si, Al, Fe, Mg, Ca, Na, K) and 100 nA for minor elements (Ti, Mn, Cl, F, Cr). Calibration was proceeded on the following standards: wollastonite (Si, Ca), spinel (Al, Mg), fayalite (Fe), jadeite (Na), orthoclase (K), rutile (Ti), pure metal (Mn, Cr), NaCl (Cl) and synthetic $RbMnF_3$ (F). Analytical reproducibility is monitored through repeated analyses of St. John's Island Olivine (SJIO). Representative amphibole major element compositions are given in **Table 5.1**, and the full EPMA dataset of amphibole and plagioclase, as well as internal standards, are given in the **Appendix Table**.

5.3.2. Laser ablation-inductively coupled plasma-mass spectrometer (LA-ICP-MS)

Trace elements of amphiboles are analysed using the Laser ablation-inductively coupled plasma-mass spectrometer (LA-ICP-MS) at Durham Geochemistry Centre, Durham University. A NewWave UP193 laser ablation system is connected with a Thermo Scientific X Series 2 quadruple ICP-MS. The analyses are carried out on probe sections (30 µm thickness) after electron probe microanalysis (EPMA) is finished and surface carbon-coating is removed. Spots where EPMA data has acquired are prioritized for LA-ICP-MS analyses. Amphiboles are mainly analysed using 75 or 35 µm laser beam (for point analysis and chemical profiling, respectively), pulsed at 5 Hz, 80% power conditions with output energy of c.a. 6.0 mJ. Each spot is ablated for 60 s (dwell time) after 60 s of washout between ablations. The ablated particles are transported into ICP-MS through the carrier gas of helium and argon. NIST612 is applied as the calibration standard and analysed at the beginning, in the middle and at the end of each run, coupled with secondary standards of NIST610, BHVO-2G and BCR-2G: together those standards provide monitoring and correction on the instrumental drift during and between individual runs. The BHVO-2G and BCR-2G measured alongside the amphibole analyses report < 20 % precision (except Sr, Nb and Y) and ≤ 16 % accuracy (**Table 5.1**; **Appendix Fig. 5.1**). MnO and TiO_2 derived from both EPMA and LA-ICP-MS show good internal consistency ($R^2 > 0.6$; see **Appendix Fig. 5.2**). Representative amphibole EPMA - LA-ICP-MS data with typical analytical errors are given in **Table 1-2**, and the full processed EPMA and LA-ICP-MS dataset with standards analyses and analytical uncertainties are presented in the **Appendix Table**.

5.4. RESULTS

5.4.1. Mt. Lamington amphibole texture and crystal chemistry

Representative textures of Mt. Lamington amphiboles are illustrated in BSE images of **Fig. 5.2** and **5.3**; their major element oxides components (in wt %) and stoichiometric calculations (in apfu) are shown in **Fig. 5.4** and **5.5**, Cl and F contents are illustrated in **Fig. 5.6**. **Fig. 5.7** presents profiles of chemical analyses across zonings of amphibole crystals from 1951 andesite, as well as greyscale patterns which are obtained from greyscale analyses of BSE images using the software ImageJ.

Greyscale variations in BSE image-recorded amphibole crystals are positively correlated with amphibole Fe content and negatively correlated with Mg content and Mg#. Representative amphibole trace element data are plotted in **Fig. 5.8**. The amphibole textural types, features and crystal chemistry is also summarized in **Table 3**.

All amphibole crystals from Mt. Lamington magmas are calcic with high Mg# values of 0.68-0.99 (**Fig. 5.5b**). They fall into the fields of MgHbl ($0.5 < Al_T < 1.5$, $(Na+K)_A < 0.5$), Tsch ($1.5 < Al_T < 2.5$, $(Na+K)_A < 0.5$) and MgHst ($1.5 < Al_T < 2.5$, $(Na+K)_A \geq 0.5$, $Al_{VI} < Fe^{3+}$; **Fig. 5.5a**). For simplicity we categorize them into two compositional populations, and refer to those amphiboles sitting in the fields of magnesiohornblende and tschermakite as '*MgHbl-Tsch*', and the rest as '*MgHst*'. Their chemistry is generally comparable to other names used in some previous studies, such as 'hornblende' and 'pargasite', respectively (e.g. Kiss *et al.*, 2014). Amphiboles from both 1951 andesite and diktytaxitic enclaves display bimodal compositions; while in the plutonic enclave, amphibole has only MgHbl-Tsch compositions. We will discuss their crystal chemistry in further details below.

5.4.1.1. Amphibole in the 1951 andesite

In the 1951 andesite, zoned amphibole crystals display three main textures: oscillatory zoning, simple zoning and patchy zoning (**Fig. 5.2**).

Oscillatory zoning either occurs as discrete phenocryst rims surrounding cores that may be unzoned, simple zoned or patchy zoned; or as individual oscillatory zoned crystals (**Fig. 5.2a-c**). The oscillatory zoning is categorized into two subtypes: *spiky* and *diffuse*. The spiky oscillatory zoning (**Fig. 5.2a**) is characterized by abrupt variations in composition, visible as sharp changes in greyscale in BSE images (**Fig. 5.7a-b**). Such zoning is often rhythmic, starting with a bright (Fe-rich) band which darkens gradually towards the rim and ends with a resorption surface which marks the beginning of another zone. In contrast, the diffuse oscillatory zoning (**Fig. 5.2b**) is typified by broad, diffuse zones, characterized by smooth greyscale patterns (**Fig. 5.7c-d**). Geochemically, both types of oscillatory zoning have MgHst and MgHbl-Tsch compositions, however, the spiky oscillatory zoning shows a negative correlation between Al_T and Mg# (**Fig. 5.5b**); whereas the diffuse oscillatory zonings lack such negative correlation, they are characterized by the co-presence of MgHbl-Tsch and MgHst with concomitant elevated Al_T and Mg# (**Fig. 5.5b**). Mg# of MgHst in spiky oscillatory zoned phenocrysts are always less than 0.78, while in diffuse oscillatory zoned phenocrysts they are always higher than 0.78. Therefore, we term MgHst with Mg#<0.78 as 'low-Mg# MgHst' and those with Mg#>0.78 as 'high-Mg# MgHst'. Low-Mg# MgHst of the spiky oscillatory zones can be present in single crystals multiply, with zoning width less than c.a. 50 μm (e.g. **Fig. 5.7a-b**); while the high-Mg# MgHst of the diffuse oscillatory zoning are always present continuously with zoning width up to c.a. 110 μm (e.g. **Fig. 5.7c-d**)

Simple zoning (**Fig. 5.2c**) refers to those amphiboles with sharp optical core-rim colour contrast, which is characterized by MgHbl-Tsch cores and overgrowth of high-Mg# MgHst rims. MgHbl-Tsch cores are frequently rounded, patchy zoned and contain abundant melt and mineral inclusions, such as plagioclase, apatite, biotite and Fe-Ti oxides (e.g. **Fig. 5.2d**). Separated from the core with a resorption surface, the rims are sometimes oscillatory zoned, and sometimes normally zoned (defined as increasing Si and decreasing Mg# rimward). Unlike the cores, the rims are commonly free from melt and mineral inclusions.

Patchy zoning (**Fig. 5.2d**) often occurs in the cores of amphibole phenocrysts, comprising irregular-shaped relatively dark and bright patches as revealed in BSE images; they are similar to examples described in Shiveluch Volcano (Humphreys *et al.*, 2006) and Ciomadul Volcano (Kiss *et al.*, 2014). Both brighter and darker patches have MgHbl-Tsch composition, however, brighter patches have slightly higher Al_T, Ti, $(Na+K)_A$, and lower Mg# than darker patches (see Table 3 in Chapter 2).

Breakdown textures are a common feature of amphiboles from arc volcanoes, such as Soufrière Hills Volcano (Plail *et al.*, 2014), Mt. St. Helens (Rutherford & Hill, 1993) and Merapi Volcano (Chadwick *et al.*, 2013; van der Zwan *et al.*, 2013) and have also been experimentally reproduced (De Angelis *et al.*, 2015). Rare breakdown rims composed of Fe-Ti oxides, orthopyroxene and plagioclase with thickness of 4-10 μm are occasionally observed in amphibole phenocrysts with red/deep reddish brown pleochroism from the 1951 andesite (**Fig. 3**).

5.4.1.2. Amphibole in the magmatic enclaves

Within the diktytaxitic enclaves, there are three main types of amphiboles: simple-zoned, framework-forming (acicular) and olivine-rimming amphiboles (**Fig. 5.2e-g**; Zhang *et al.*, 2015). Acicular amphiboles (**Fig. 5.2e**) are interpreted to crystallize as a result of quenching during the intrusion of the enclave-forming magma at the base of the andesite magma body (Zhang *et al.*, 2015). Amphiboles rimming olivines (**Fig. 5.2g**) are products of reaction between olivine and more silicic melt (Zhang *et al.*, 2015). Both framework-forming (acicular) and olivine-rimming amphiboles are MgHst, typically with Mg# higher than 0.78. Simple-zoned ('phenocryst-like'; Zhang *et al.*, 2015) amphiboles (**Fig. 5.2f**) have MgHbl-Tsch cores and MgHst rims, and are compositionally similar to simple-zoned amphibole phenocrysts from 1951 andesite. The cores are interpreted to have crystallised in the andesite magma and then been transferred into the enclave-forming magma during magma mixing, where MgHst rims are crystallized (Zhang *et al.*, 2015).

In the plutonic enclave, MgHbl-Tsch amphiboles form crystal aggregates (**Fig. 5.2h**), with glass present along crystal boundaries (Zhang *et al.*, 2015). The majority of those amphiboles are unzoned, although some display weak patchy zoning. MgHbl-Tsch from the plutonic enclave are compositionally more homogeneous than MgHbl-Tsch in 1951 andesite and the diktytaxitic enclaves, with a smaller variation range of Al_T, and distinguishable from the latter by slightly lower FeO_{tot} and MnO and higher MgO (**Fig. 5.4c, d, e**). None of the amphibole crystals from magmatic enclaves shows any breakdown textures.

5.4.1.3. Amphibole Cl, F and trace element chemistry

Cl contents in Mt. Lamington amphiboles display a strong negative correlation with amphibole Mg#, with an obvious kink at Mg# of 0.80 and Cl of 0.02-0.03 wt %, consistent with the observations of Humphreys *et al.* (2009b) and Sato *et al.* (2005). Cl in MgHbl-Tsch and low-Mg# MgHst (Mg# < 0.78) from 1951 andesite and enclaves are higher than high-Mg# MgHst in 1951 andesite and diktytaxitic enclaves (**Fig. 5.6a**). F content remains relatively constant in Mt. Lamington amphiboles compared to Cl (0.10-0.25 wt % for the majority, except some high-Mg# MgHst in 1951 andesites have higher F up to 0.35 wt %) (**Fig. 5.6b**).

Rb is strongly incompatible in amphibole (Chapter 4) and displays a weak positive correlation with Al_T; Sr and Ba are moderately positively correlated with Al_T, Ti, Ca and $[Na+K]_A$ (e.g. **Fig. 5.8a**). Sr and Ba are higher in MgHst than MgHbl-Tsch from both 1951 andesite and magmatic enclaves. Pb, U and Th are strongly incompatible in amphibole (Chapter 4). Pb shows weak negative correlations against Al_T and Mg#, i.e. MgHbl-Tsch are slightly more enriched in Pb than MgHst (e.g., **Fig. 5.8b**). U and Th do not show any correlations with amphibole major element components.

HFSE display different geochemical behaviours in amphibole: Zr and Hf display no obvious correlations with either Mg# or Al_T (e.g., **Fig. 5.8c**); Nb and Ta are moderately negatively correlated with Mg# and Al_T (e.g. **Fig. 5.8d**). MgHbl-Tsch from 1951 andesite and both types of magmatic enclaves are slightly more enriched in Nb and Ta compared to high-Mg# MgHst. No correlation is found for Zr, Hf, Nb, and Ta against Ti.

Concentrations of REE and Y in MgHbl-Tsch and low-Mg# MgHst in andesites are higher than MgHbl-Tsch in the plutonic enclave and high-Mg# MgHst in diktytaxitic enclaves and 1951 andesite (e.g. **Fig. 5.8e-f**), and they display moderate negative correlations against increasing Al_T in

general. Chondrite-normalized REE patterns (data of C1-chondrite are from Sun and McDonough, (1989) generally show a "hump" shape skewed towards LREE, peaking at Pr, Nd and Sm (**Fig. 5.9**). Eu anomaly (Eu/Eu*), although the accuracy of which is compromised by large analytical uncertainties of Sm, Gd and Eu, displays a poor-moderate negative correlation with Sm (**Fig. 5.8g**), i.e. the higher the REE concentration, the larger the negative Eu anomaly (**Fig. 5.9**). Eu/Eu* also display a poor-moderate positive correlation with Sr in general (**Fig. 5.8h**).

In summary, amphiboles from both 1951 andesite and diktytaxitic enclaves comprise both MgHbl-Tsch and MgHst; while in plutonic enclaves, amphiboles have only MgHbl-Tsch compositions. MgHst are relatively enriched in Al_2O_3, TiO_2 and Na_2O and depleted in SiO_2 compared to MgHbl-Tsch (**Fig. 5.4**). Low-Mg# MgHst display a negative Al_T and Mg# correlation together with MgHbl-Tsch in spiky oscillatory zoned phenocrysts, while high-Mg# MgHst have elevated Al_T and Mg# (**Fig. 5.5b**), and depleted Mn, Fe and Cl (**Fig. 5.4c, e, 6**). The MgHst group have higher Rb, Sr, Ba and Eu/Eu*, and lower Nb, Ta, Pb, REE and Y, compared to the MgHbl-Tsch group.

5.4.2. Mt. Lamington amphibole crystallization temperature and melt compositions

5.4.2.1. Amphibole thermometry

Amphibole-only thermometer models are provided by Ridolfi *et al.* (2010) and Ridolfi & Renzulli (2012). However, their models include calibration by pressure yielded from barometer models of Ridolfi *et al.* (2010) and Ridolfi & Renzulli (2012), the accuracy of which have been questioned in more recent studies (Erdmann *et al.*, 2014, Putirka, 2016). A recent study of Putirka (2016) provides amphibole-only thermometer model without pressure calibration (amphibole-only pressure-independent model, Eq. 5 therein), which is derived by regressional analyses carried out on a larger experimental database compared to Ridolfi *et al.* (2010) and Ridolfi & Renzulli (2012). The accuracy of this thermometer model is ± 30 ºC (standard error of estimate; Putirka, 2016). Application of this thermometer model to Mt Lamington amphiboles indicates crystallisation temperatures in the range 800-1,000 ºC (**Table 5.4**; **Fig. 5.10**). The majority of MgHbl-Tsch from both andesites and diktytaxitic and plutonic enclaves crystallize under temperatures of 800-900 ºC, with an average of 840±30 ºC (796-931 ºC; n=188), 857±30 ºC (799-924 ºC; n=27) and 850±30 ºC (788-881 ºC; n=39), respectively. MgHst from diktytaxitic enclaves, in contrast, crystallize under a higher range of temperature, encompassing 866-997 ºC with an average of 957±30 ºC (n=48). This temperature is consistent with temperature at which olivine is becoming unstable in Krawczynski *et al.* (2012)'s experiments at 500 MPa (975 ºC). The agreement reemphasizes our earlier conclusion derived from Chapter 2 that the amphibole rim growth on olivine crystals in diktytaxitic enclaves is caused by temperature drop below the thermal stability field of olivine during quenching and melt evolution with extensive amphibole and plagioclase crystallization (Zhang *et al.*, 2015). The range of variation is also similar to high-Mg# MgHst from diffuse oscillatory zoned amphibole phenocrysts (880-990 ºC; average 960±30 ºC; n=44), and slightly higher than low-Mg# MgHst from spiky oscillatory zoned amphibole phenocrysts (856-926 ºC; average 892±30 ºC; n=24). They are in good agreement with the temperature calculated according to the thermometers of Ridolfi *et al.* (2010) and Ridolfi & Renzulli (2012) (R^2 = 0.978, 0.935, respectively).

5.4.2.2. Estimating melt major element compositions

We applied the chemometric equations derived in Chapter 3 to Mt. Lamington amphiboles to calculate the major element compositions of the melts from which they are crystallized (*Eq. 2* for SiO_2, *Eq. 6* for TiO_2, *Eq. 19* for Al_2O_3, *Eq. 10* for FeO, *Eq. 12* for MgO, *Eq. 14* for CaO and *Eq. 18* for K_2O; they are all temperature-independent equations). Representative results are given in **Table 5.4** and illustrated in **Fig. 5.10**, **5.11**. The majority of MgHbl-Tsch are crystallized in silicic melt with c.a. 70-80 wt % SiO_2 and 14-16 wt % Al_2O_3, most high-Mg# MgHst are crystallized in a melt with <63 wt % SiO_2 and 17-19 wt % Al_2O_3, while low-Mg# MgHst are crystallized in intermediate melt compositions relative to high-Mg# MgHst and MgHbl (e.g. **Fig. 5.14b**). The melt from which MgHbl-Tsch crystallized, generally referring to the melt of 1951 andesite magma and plutonic enclaves, have

lower TiO_2, FeO, MgO and CaO and higher K_2O than the melt from which MgHst are crystallized (**Fig. 5.11**). Low-Mg# MgHst in spiky oscillatory zoned phenocrysts in 1951 andesite are crystallized from more evolved melt compositions (62-71 wt % SiO_2, 2.6-3.4 wt % K_2O) compared to high-Mg# MgHst from diffuse oscillatory zoned phenocrysts, which are derived from a melt with similar geochemical contents (55-64 wt % SiO_2, 1.3-2.3 wt % K_2O) to the melt of MgHst-bearing diktytaxitic enclave-forming magma.

5.4.2.3. Estimating melt trace element compositions

The empirical $^{Amph/L}D$-predicting equations derived in Chapter 4 are applied to Mt. Lamington amphibole major and trace element analyses in order to calculate $^{Amph/L}D$ and infer corresponding melt trace element compositions for Sr, Pb, Zr, Nb, Sm and Y (*Eq. 7* for D Sr, *Eq. 8* for D Pb, *Eq. 18* for D Zr, *Eq. 15* for D Nb, *Eq. 25* for D Sm and *Eq. 41* for D Y; they are all temperature-independent equations). Representative results are listed in **Table 5.3**, illustrated in **Fig. 5.12** and described here. The calculated melt trace element compositions are plotted against the estimated melt SiO_2 content in **Fig. 5.13**.

For Sr, the predicted $^{Amph/L}D$ for all Mt. Lamington amphiboles are in the range of 0.2-0.5, invariable against the large span of amphibole Sr concentrations (**Fig. 5.12a**), in contrast, the amphibole Sr contents are strongly positively correlated with the inferred melt Sr contents (**Fig. 5.12b**). High-Mg# MgHst from both diktytaxitic enclaves and andesite are crystallized from melts with higher Sr content than low-Mg# MgHst and MgHbl-Tsch from andesite and both types of enclaves (**Fig. 5.12b**). With increasing melt silica content, Sr is gradually decreasing amongst all Mt. Lamington amphiboles (**Fig. 5.13**).

For Pb, the predicted $^{Amph/L}D$ for all Mt. Lamington amphiboles show insignificant variations (**Fig. 5.12c**), while the variation in amphibole Pb content is strongly related to the variation of the melt Pb contents (**Fig. 5.12d**). There is a moderate positive correlation between the calculated melt Pb content and the calculated melt SiO_2 content (**Fig. 5.13b**). Pb content is increasing with increasing melt SiO_2 content (**Fig. 5.13b**), except several outliers caused by higher amphibole Pb contents.

For Zr, the predicted $^{Amph/L}D$ for MgHbl-Tsch from 1951 andesites and both types of enclaves and low-Mg# MgHst from 1951 andesites are higher than high-Mg# MgHst from 1951 andesites and diktytaxitic enclaves. However, the predicted $^{Amph/L}D_{Zr}$ does not correlate with amphibole Zr concentrations within individual compositional groups (**Fig. 5.12e**). The inferred melt Zr concentrations for high-Mg# MgHst from 1951 andesites and diktytaxitic enclaves are higher than for MgHbl-Tsch from 1951 andesites and both types of enclaves and low-Mg# MgHst from 1951 andesites, and they display positive correlations with amphibole Zr contents within individual group (**Fig. 5.12f**). The predicted melt Zr contents are decreasing against increasing predicted melt SiO_2 content among all Mt. Lamington amphiboles, while correlations within individual groups are not robust (**Fig. 5.13c**).

For Nb, the higher Nb contents in MgHbl-Tsch and low-Mg# MgHst are corresponding to higher predicted $^{Amph/L}D_{Nb}$ compared to high-Mg# MgHst (**Fig. 5.12g**). The predicted $^{Amph/L}D_{Nb}$ and amphibole Nb contents display a positive correlation trend in general, while the correlations are weak in individual groups (**Fig. 5.12g**). In contrast, the inferred Nb contents in the melts from which high-Mg# MgHst are crystallized largely overlaps with those from which low-Mg# MgHst and MgHbl-Tsch are crystallized (**Fig. 5.12h**). The predicted melt Nb contents display negative correlation with predicted melt SiO_2 contents (**Fig. 5.13d**), and the negative correlation is also seen in MgHbl-Tsch from 1951 andesites and plutonic enclave, and MgHst from diktytaxitic enclaves (**Fig. 5.13d**).

For REE (taking Sm as an example) and Y, distinctively higher concentrations in MgHbl-Tsch relative to MgHst are correlated with higher predicted $^{Amph/L}D$ (**Fig. 5.12i, k**). The estimated REE and Y contents in melts crystallizing MgHst and MgHbl-Tsch display overlapping range of

variation (**Fig. 5.12j, l**), however, they are strongly negatively correlated with melt SiO_2 content (**Fig. 5.13e-f**).

The correlations between amphibole trace element contents and predicted $^{Amph/L}D$ and calculated melt trace element compositions are consistent with earlier results displayed by amphiboles from Mt. Pinatubo and Ongatiti in Chapter 4.

5.5. DISCUSSION

5.5.1. Magmatic processes revealed from amphibole and inferred melt compositions

5.5.1.1. Magma hybridization evidenced by amphibole bimodal major element compositions

Mt. Lamington amphiboles in both 1951 andesites and diktytaxitic enclaves show compositional bimodality of MgHst (low SiO_2 and high Al_2O_3) and MgHbl-Tsch (high SiO_2 and low Al_2O_3). More specifically, amphibole compositional bimodality is also revealed in the sub-crystal scale in Mt. Lamington. For example, in the simple zoned amphiboles in both 1951 andesites (simple zoned phenocrysts; **Fig. 5.2c**) and diktytaxitic enclaves (phenocryst-like amphiboles; **Fig. 5.2f**), distinct core-rim compositions (MgHbl-Tsch core overgrown by high-Mg# MgHst rim) are suggested to be crystallized in the andesitic host magma and the enclave-forming magma, respectively (see Chapter 2) (Zhang *et al.*, 2015). Textural variations and major element chemistry were used to infer that crystal transfer from the andesite to the intruding enclave-forming magma and further crystallization produce simple zoned phenocryst-like amphibole (antecryst) in diktytaxitic enclaves; those crystals can then be recycled to the andesite host through enclave disaggregation (Humphreys *et al.*, 2009a) and preserved as simple zoned phenocryst (Zhang *et al.*, 2015). This crystal transfer and recycling process reflects mingling between the andesite host magma and the enclave-forming magma.

The compositional bimodality described above is also present in the two types of oscillatory zoned phenocrysts in 1951 andesites (**Fig. 5.2a, 5.2b, 5.7**). As mentioned earlier, MgHst in spiky oscillatory zonings are characterized by low-Mg# (<0.78), while MgHst in diffuse oscillatory zonings are high-Mg# (>0.78). The low-Mg# MgHst and MgHbl-Tsch in spiky oscillatory zonings display negative correlation between Mg# and Al_T, while high-Mg# MgHst has higher Al_T and Mg# compared to MgHbl-Tsch in the same diffuse oscillatory zoned crystals (**Fig. 5.5b**). The importance of using Mg# - Al_T systematics to infer variations in amphibole crystallization conditions is highlighted by previous studies, e.g. Kiss *et al.* (2014); Thornber *et al.* (2008). The continuous negative Mg# - Al_T trend across spiky oscillatory zonings is ascribed to T/P-sensitive substitutions, such as edenite exchange ($Si_T + []_A = Al_T + [Na, K]_A$; **Fig. 5.5a**), Ti-Tschermak exchange ($2\ Si_T + [Mg, Fe^{2+}, Mn]_{M1-3} = 2\ Al_T + Ti_{M1-3}$; **Fig. 5.5d**), Al-Tschermak exchange ($Si_T + [Mg, Fe^{2+}, Mn]_{M1-3} = Al_T + Al_{M1-3}$; **Fig. 5.5e**), and plagioclase exchange ($Si_T + Na_{M4} = Al_T + Ca_{M4}$; **Fig. 5.5f**), which are demonstrated by robust positive correlations between amphibole $(Na+K)_A$, Ti, Ca and Al_T and moderate positive correlation between Al_{M1-3} and Al_T (Anderson & Smith, 1995, Bachmann & Dungan, 2002, Hammarstrom & Zen, 1986, Ruprecht *et al.*, 2012, Shane & Smith, 2013, Thornber *et al.*, 2008). Therefore, the spiky oscillatory zoning appears to reflect temperature/pressure fluctuations in the magmatic environment, e.g. the thermometer model of (Putirka, 2016) gives average MgHbl-Tsch and low-Mg# MgHst crystallization temperatures of 840±30 ºC and 892±30 ºC, respectively (**Fig. 5.10**). In contrast, melt chemical and thermal response to mafic magma replenishment events, e.g. increasing temperature and Mg# and decreasing melt SiO_2 content, can lead to the crystallization of MgHst with concomitantly increasing Al_T and Mg# contents, e.g. Kiss *et al.* (2014). It is illustrated as the deviation of the MgHst in diktytaxitic enclaves and high-Mg# MgHst in andesites from other amphiboles in **Fig. 5.5b**. Therefore, we conclude that the presence of diffuse oscillatory zoned amphibole phenocrysts with MgHbl-Tsch and high-Mg# compositions represents magma mixing processes that occurred in the magma plumbing system of Mt. Lamington. We will discuss the formation mechanism of the two types of oscillatory zonings in Section 5.5.2.

5.5.1.2. Does the plutonic enclave represent mushy margin related to the andesites or the enclave magma?

The plutonic enclave (LAM-10I) is characterized by high vesicle-free crystallinity and crystal clusters dominated by coarse-grained, interlocking amphiboles (up to 69.1 vol %) with the presence of melt films between crystal boundaries (**Fig. 5.2h**; Zhang *et al.*, 2015). This texture indicates that the formation of the plutonic enclave is probably through slow crystallization of the mushy margins of a magma body (Holness *et al.*, 2007, Zhang *et al.*, 2015). However, it is unclear whether the mushy margin is linked with the andesite magma body or the enclave-forming magma body. We can use our inferred melt major and trace element compositions to test this issue.

The amphiboles in the plutonic enclave have MgHbl-Tsch compositions, in contrast to the diktytaxitic enclaves which are MgHst-dominated. The plutonic amphiboles are similar to amphibole phenocrysts of MgHbl-Tsch compositions in 1951 andesites. Thus it is easy to jump to the conclusion that the plutonic enclave represent crystal mushy margin formed at the thermal boundary layers of the andesite magma body. However, fractional crystallization-driven melt compositional evolution and heat loss in the enclave-forming magma may also generate amphiboles of MgHbl-Tsch compositions in theory (Chapter 3), and the melt compositions predicted from the plutonic amphiboles have lower Fe, Mn, Cl, REE and Y contents than those of the andesite. The andesite bulk-rock compositions are relatively homogeneous compared to the magmatic enclaves (Chapter 2). The limited range of variations of the major element contents in 1951 andesites are more related to fractionation crystallization of amphibole and plagioclase, rather than mixing with the enclaves (see **Fig. 2.7** in Chapter 2), although chemical contributions from the enclave-forming magma (e.g. the presence of high-Mg# MgHst in diffuse oscillatory zonings) are clearly seen. If the bulk-rock and amphibole compositional variations in 1951 andesites are related to the fractionation of the plutonic enclave (in this case, it should be called 'cumulate'), we should observe a coherent trend in the predicted melt compositions between the plutonic enclave and 1951 andesites. However, the predicted melt REE and Y contents from MgHbl-Tsch in the plutonic enclave and in the 1951 andesites display near-parallel variation trends against increasing melt SiO_2 contents (**Fig. 5.13e, f**). This suggests that the plutonic enclave is not a cumulate fragment fractionated from the melt parental to 1951 andesites. Instead, the melt REE, Y variations against melt SiO_2 content in the plutonic enclave display a coherent trend with the variations in the MgHst from diktytaxitic enclaves (**Fig. 5.13e, f**). This indicates that the relatively evolved (high Si content) amphibole compositions in the plutonic enclave compared to MgHst in diktytaxitic enclaves are attributed to evolved melt compositions which may be driven by extensive amphibole and plagioclase crystallization as observed in diktytaxitic enclaves (see **Fig. 2.3** in Chapter 2).

5.5.1.3. The formation of 1951 andesites are related to fractionation of MgHst rather than MgHbl-Tsch

In Chapter 2 we demonstrate that the formation of 1951 andesites are related to deep fractional crystallization of ol + sp + cpx and shallow fractionation of amph + plag. The inferred melt REE and Y contents from MgHbl-Tsch in 1951 andesites define a decreasing trend against increasing melt SiO_2 contents (**Fig. 5.13e, f**), and this evolution trend must be derived from fractionation from a magma source with lower SiO_2 and higher REE and Y contents. Since fractional crystallization of MgHbl-Tsch will only push the residual melt to even higher SiO_2 content, we think that the fractionation of MgHbl-Tsch from the parental melt to 1951 andesites is not important. In contrast, the fractionation of MgHst, together with plagioclase (Zhang *et al.*, 2015), should be responsible for the production of andesitic magma in the magma plumbing system of Mt. Lamington.

5.5.1.4. Other processes implied by amphibole trace element compositions

Data from (Loewen, 2013) shows large variations in Zr/Nb and Ba/La ratios in amphiboles from Mt. Pinatubo, Mt. St. Helens and Mt. Hood (Zhang *et al.*, 2015). The MgHbl have lowest Zr/Nb and Ba/La ratio, while MgHst have the highest and Tsch are intermediate (see Fig. 17 in Chapter 2). This observation was used to help explain the bulk-rock Zr/Nb and Ba/La variations in the magmatic

enclaves, and their differences with the 1951 andesites (Zhang *et al.*, 2015). Zr/Nb and Ba/La ratios are typically used to investigate variations in source composition for more mafic rocks as these ratios are invariant to fractionation of olivine, pyroxene and plagioclase. However, for more evolved magmas it is unlikely that these ratios reflect variations in source composition. Instead, it was proposed that amphibole fractional crystallization and/or assimilation can change the bulk-rock Zr/Nb and Ba/La ratios (Zhang *et al.*, 2015). With our newly collected Mt. Lamington amphibole trace element data, we observe that the Zr/Nb and Ba/La ratios of Mt. Lamington amphiboles define a coherent trend in the plot in logarithmic scale (**Fig. 5.14a**). The MgHbl-Tsch from 1951 andesites, diktytaxitic and plutonic enclaves have the lowest Zr/Nb and Ba/La, while these ratios are higher in MgHst from 1951 andesites and diktytaxitic enclaves, which also overlap the bulk-rocks of 1951 andesites and magmatic enclaves (**Fig. 5.14a**).

The mechanisms required to explain the spread of bulk-rock Zr/Nb and Ba/La ratios in 1951 andesites and magmatic enclaves depend on the Zr/Nb and Ba/La ratios in the host melts. For example, if the melt has low Zr/Nb and Ba/La ratios similar to MgHbl-Tsch amphiboles (source melt 1 in **Fig. 5.14b**), then fractionation or assimilation of MgHbl-Tsch would be ineffective at changing bulk Zr/Nb and Ba/La and the observed variations would be better explained by MgHst assimilation. If the host melts have intermediate Zr/Nb and Ba/La ratios similar to source melt 2 in **Fig. 5.14b**, the variation range can be explained by either MgHbl-Tsch and MgHst assimilation or fractional crystallization. Conversely, if the host melts have high Zr/Nb and Ba/La ratios similar to those of high-Mg# MgHst (source melt 3 in **Fig. 5.14b**), then the observed variation can only be explained by MgHbl-Tsch assimilation or fractionation. In the previous section (section 5.5.1.3), we demonstrated that the production of 1951 andesite should be more related to the fractionation of MgHst rather than MgHbl-Tsch from its precursor. Because the 1951 andesites have Zr/Nb and Ba/La ratios similar to MgHst, therefore MgHst fractionation and assimilation cannot effectively modify those ratios of 1951 andesites, and hence the Zr/Nb and Ba/La ratios of 1951 andesites should represent the source rocks of Mt. Lamington magmas (similar to source melt 3 in **Fig. 5.14b**). The variation and deviation of those ratios in the magmatic enclaves from 1951 andesites can then be explained by MgHbl-Tsch assimilation. This is consistent with the presence of phenocryst-like amphiboles with MgHbl-Tsch compositions in the diktytaxitic enclaves.

The analysed and inferred trace element contents of amphiboles and corresponding melts provide additional insights into the mineral phases that had crystallized and/or were co-crystallizing with amphibole. For example, the amphibole Sr content is strongly related to melt Sr content (**Fig. 5.12b**), and therefore amphibole Sr content variation reflects melt Sr content variation as opposed to amphibole major element chemistry effects on the partition coefficient (see Chapter 4). The MgHbl-Tsch in 1951 andesites have lower Sr content and more apparent europium anomaly (Eu/Eu*) compared to MgHst in diktytaxitic enclaves, suggesting that a higher degree of plagioclase co-crystallization with amphibole occurred in 1951 andesites (**Fig. 5.8h**). Furthermore, the melt Nb contents are decreasing with increasing melt SiO_2 contents as predicted from MgHst in diktytaxitic enclaves and MgHbl-Tsch in the plutonic enclave and 1951 andesites (**Fig. 5.13d**). This suggests the co-crystallization of ilmenite and/or rutile with amphibole, since Nb is most compatible in rutile and ilmenite (Foley *et al.*, 2000, Green & Pearson, 1987, Jenner *et al.*, 1993, Xiong *et al.*, 2005). This interpretation is consistent with the petrological observations of ilmenite in 1951 andesites and both types of enclaves (Zhang *et al.*, 2015). Apatite is a major host for magmatic REE and Y (Fujimaki, 1986, Luhr *et al.*, 1984, Nagasawa & Schnetzler, 1971). Therefore, apatite co-crystallization is probably responsible for decreasing melt REE and Y with increasing SiO_2 content (**Fig. 5.13e-f**), and this is in agreement with the presence of abundant apatite inclusions in amphibole crystals (**Fig. 5.2a, h**).

5.5.2. Origin of the spiky and diffuse oscillatory zonings in amphibole phenocrysts

The preservation of spiky and diffuse oscillatory zoned amphibole phenocrysts in 1951 andesite offers additional insights into the magma movement and evolution in response to the invasion of enclave-

forming magma. The spiky oscillatory zoning is inferred to reflect mainly fluctuations in temperature and/or pressure, while the diffuse oscillatory zoning is inferred to reflect changes in melt composition (see section 5.5.1.1). We propose a scenario (**Fig. 5.15**) to explain the co-presence of spiky and diffuse oscillatory zoned crystals in the 1951 andesite.

The andesite magma body responds both chemically and thermally during the intrusion of the enclave-forming magma. Directly above the interface between the andesite and the enclave-forming magma, there is a chemical diffusion zone where chemical exchange (magma mixing) and heat transfer from the enclave magma to andesites can occur and diffuse oscillatory zoned amphiboles can be produced, and above the chemical diffusion zone there is a thermal diffusion zone where spiky oscillatory zoned amphiboles can be produced (**Fig. 5.15**). Magma mixing may be difficult to be triggered in this zone due to the decreasing temperature and increasing viscosity away from the intrusion interface; therefore, the andesite magma body is probably largely thermally affected in the thermal diffusion zone with less chemical input from the enclave magma. Thermally driven magma convection can be triggered within both the chemical and thermal diffusion zones in the andesite magma body. Oscillatory zoning could result from the amphibole crystals passing through T/P/melt chemistry contours, or from multiple recharge events. Those crystals convecting within the thermal diffusion zone experience T/P fluctuation and crystallize spiky oscillatory zoning, while those convecting within the chemical diffusion zone are affected by changing T/P as well as magma geochemistry and thus crystallize MgHbl-Tsch as well as MgHst with concurrent raised Al_T and Mg# (high-Mg# MgHst). This also explains the similarity of the amphibole crystal chemistry and the calculated melt compositions between the high-Mg# MgHst in diffuse oscillatory zoned phenocrysts and the MgHst in diktytaxitic enclaves.

As soon as crystals grows at magmatic temperature, if adjacent crysta zones are out of equilibrium with each other, diffusion of elements (e.g. Fe-Mg exchange) is likely at magmatic temperatures. Even if there is a chemical gradient within a magma chamber which chanes the composition during the growth of a crystal zone, the actural boundary between two zones is still likely to be sharp immediately after growth. Therefore, the difuse appearance of the crystals shoule be more related to the diffusion post crystal growth. There are extremely limited data for the diffusion of elements in amphibole due to its complex chemical compositon. However, it is possible that the texturally diffused crystals have been residen within the magma body for a longer time than the spiky oscillatory zoned crystals. Moreover, hotter melt in the chemical diffusion zone may facilitate more rapid Fe-Mg exchange in the amphibole crystals and produce diffuse oscillatory zoning as well.

5.5.3. Implications of magma mixing from amphibole compositional bimodality

Mt. Lamington MgHbl-Tsch and MgHst from andesite and enclaves are crystallized under two different temperature regimes as well as from contrasting melt compositions (**Fig. 5.10, 5.11**). The crystallization of MgHst in diktytaxitic enclaves is driven by quenching of the enclave magma against the andesite magma (see **Fig. 2.16** and discussions in Chapter 2; Zhang *et al.*, 2015), therefore it should occur at a depth/pressure range similar to the crystallization of MgHbl-Tsch in andesites, in contrast to the predictions of previous amphibole-only thermobarometers (Ridolfi *et al.*, 2010). The presence of MgHbl-Tsch and MgHst in both andesite and enclaves indicates mass transfer between andesite and the enclave-forming magma.

Amphibole compositional bimodality is common in Mt. Lamington and has also been demonstrated in recent case studies such as Mt. Pelée (Pichavant *et al.*, 2002), Unzen Volcano (Sato *et al.*, 2005), Shiveluch Volcano (Humphreys *et al.*, 2006), Mt. St. Helens (Thornber *et al.*, 2008), Soufrière Hills (Humphreys *et al.*, 2009a), Mt. Hood (Koleszar, 2011), Augustine Volcano (De Angelis *et al.*, 2013), Ciomadul Volcano (Kiss *et al.*, 2014), Mt. Merapi (Erdmann *et al.*, 2014) and the Ongatiti eruption of the Mangakino volcanic centre (Cooper & Wilson, 2014). Kent (2014) suggests that the amphibole compositional bimodality is a ubiquitous phenomenon in global subduction zones; felsic amphiboles (MgHbl-Tsch) are crystallized in a cool, silicic source stalled in

shallow crust, while mafic amphiboles crystallize in a hot, mafic magma source at depth. We propose that the crystallization of bimodal amphibole populations may not occur over a large depth range, according to the results of experimental studies (bimodal amphibole populations are produced in 200 MPa experiments, see **Fig. 3.1b** in Chapter 3) and the case study of Mt. Lamington (Zhang *et al.*, 2015). Their co-presence in hand-specimen scale or even in sub-crystal scale cannot be explained by models arguing for fractional crystallization of mantle-derived melts in producing intermediate magma compositions at convergent margins (Kent, 2014). Instead, hybridization of the two magmas stalled under different thermal and geochemical conditions can bring the two contrasting types of amphiboles in an overall intermediate melt. Therefore, amphibole compositional bimodality from Mt. Lamington and widely occurring in arc magmatism indicates that magma mixing is the dominant way of producing intermediate magmas beneath arc volcanoes, consistent with conclusions driven by earlier studies, e.g. Anderson, 1976; Eichelberger, 1978; Kent *et al.*, 2010; Reubi & Blundy, 2009.

5.6. CONCLUSION

Mt. Lamington amphiboles from the 1951 andesites and magmatic enclaves display compositional bimodality (MgHst vs. MgHbl-Tsch). We interpret that the bimodal amphibole populations are crystallized in different melt under contrasting thermal conditions, i.e. MgHst from hotter, less silica-rich melt and MgHbl-Tsch from cooler, more silica-rich melt, rather than at large range of depths. The recharge of enclave-forming magma into overlying andesite magma, followed by magma mixing, brings the two different types of amphiboles together shortly before the Mt. Lamington 1951 eruption took place.

The amphibole compositional bimodality is also revealed in sub-crystal scale across oscillatory zonings in amphibole phenocrysts in 1951 andesites. Two types of oscillatory zonings are identified: spiky and diffuse. The spiky oscillatory zonings are characterized by the co-presence of MgHbl-Tsch and low-Mg# MgHst, reflecting temperature/pressure fluctuations during crystallization, and the effect of magma replenishment is not significant; whilst diffuse oscillatory zonings are composed by MgHbl-Tsch and high-Mg# MgHst, which we believe the variation is driven by both T/P fluctuation and mafic magma input. We believe the oscillatory zonings are caused by crystal movement along magma convection and thus we propose the below scenario to explain the formation of the two different types of oscillatory zonings: spiky oscillatory zoned amphiboles are formed during convection within thermal diffusion zone where the andesite magma body is heated by the recharge of the enclave magmag; in contrast, diffuse oscillatory zoned amphiboles are ascribed to magma convection within chemical diffusion zone where the andesite magma is heated and mixed with the enclave magma (**Fig. 5.15**).

We also use the reconstructed melt chemistry to demonstrate that the plutonic enclave represents a slowly crystallized mushy margin of the enclave magma, rather than a cumulate fragment fractionated from the andesite magma. The amphibole compositions in cumulates generated during the formation of andesites should be dominantly MgHst, rather than MgHbl-Tsch. Assimilation of MgHbl-Tsch in the enclave magma, petrologically observed as incorporating penocryst-like amphiboles from andesites, is able to explain the variations of Zr/Nb and Ba/La ratios in the magmatic enclaves. The inferred melt compositions from amphibole crystal chemistry also records the co-crystallization of ilmenite (and maybe rutile) and apatite together with Mt. Lamington amphiboles.

5.7. ACKNOWLEDGEMENT

This research forms a part of J. Zhang's PhD project, which is funded by Durham Doctoral Studentship, Durham University and China Scholarship Council (201206170178). M.C.S. Humphreys is supported by a Royal Society University Research Fellowship. G.F. Cooper is supported by a NERC Postdoctoral Research Fellowship. The authors want to thank Richard Arculus for providing Mt. Lamington samples and Ian Chaplin for preparing the probe sections. Chris Hayward and Chris Ottley are thanked for providing tremendous help in collecting and evaluating EPMA and LA-ICP-MS data, respectively.

5.8. REFERENCES

Anderson, A. T. (1976). Magma Mixing - Petrological Process and Volcanological Tool. *Journal of Volcanology and Geothermal Research* **1**, 3-33.

Anderson, J. L. & Smith, D. R. (1995). The Effects of Temperature and F(O2) on the Al-in-Hornblende Barometer. *American Mineralogist* **80**, 549-559.

Arculus, R. J., Johnson, R. W., Chappell, B. W., Mc Kee, C. O. & Sakai, H. (1983). Ophiolite-contaminated andesites, trachybasalts, and cognate inclusions of Mount Lamington, Papua New Guinea: anhydrite-amphibole-bearing lavas and the 1951 cumulodome. *Journal of Volcanology and Geothermal Research* **18**, 215-247.

Bachmann, O. & Dungan, M. A. (2002). Temperature-induced Al-zoning in hornblendes of the Fish Canyon magma, Colorado. *American Mineralogist* **87**, 1062-1076.

Baldwin, S. L., Fitzgerald, P. G. & Webb, L. E. (2012). Tectonics of the New Guinea Region. *Annual Review of Earth and Planetary Sciences* **40**, 495-520.

Baldwin, S. L., Webb, L. E. & Monteleone, B. D. (2008). Late Miocene coesite-eclogite exhumed in the Woodlark Rift. *Geology* **36**, 735-738.

Cashman, K. V. & Marsh, B. D. (1988). Crystal Size Distribution (Csd) in Rocks and the Kinetics and Dynamics of Crystallization .2. Makaopuhi Lava Lake. *Contributions to Mineralogy and Petrology* **99**, 292-305.

Chadwick, J. P., Troll, V. R., Waight, T. E., Zwan, F. M. & Schwarzkopf, L. M. (2013). Petrology and geochemistry of igneous inclusions in recent Merapi deposits: a window into the sub-volcanic plumbing system. *Contributions to Mineralogy and Petrology* **165**, 259-282.

Chambefort, I., Dilles, J. H. & Longo, A. A. (2013). Amphibole Geochemistry of the Yanacocha Volcanics, Peru: Evidence for Diverse Sources of Magmatic Volatiles Related to Gold Ores. *Journal of Petrology* **54**, 1017-1046.

Cooper, G. F. & Wilson, C. J. N. (2014). Development, mobilisation and eruption of a large crystal-rich rhyolite: The Ongatiti ignimbrite, New Zealand. *Lithos* **198**, 38-57.

Davidson, J. P. (1996). Deciphering mantle and crustal signatures in subduction zone magmatism. In: Bebout, G. E., Scholl, D. W., Kirby, S. H. & Platt, J. P. (eds.) *Subduction Top to Bottom*. Washington, D. C.: American Geophysical Union, 251-262.

Davidson, J. P., Morgan, D. J., Charlier, B. L. A., Harlou, R. & Hora, J. M. (2007). Microsampling and Isotopic Analysis of Igneous Rocks: Implications for the Study of Magmatic Systems. *Annual Review of Earth and Planetary Sciences* **35**, 273-311.

Davies, H. L. (2012). The geology of New Guinea - the cordilleran margin of the Australian continent. *Episodes* **35**, 87-102.

Davies, H. L. & Jaques, A. L. (1984). Emplacement of ophiolite in Papua New Guinea. *Geological Society, London, Special Publications* **13**, 341-349.

Davies, H. L. & Smith, I. E. (1971). Geology of Eastern Papua. *Geological Society of America Bulletin* **82**, 3299-3312.

De Angelis, S. H., Larsen, J. & Coombs, M. (2013). Pre-eruptive Magmatic Conditions at Augustine Volcano, Alaska, 2006: Evidence from Amphibole Geochemistry and Textures. *Journal of Petrology* **54**, 1939-1961.

De Angelis, S. H., Larsen, J., Coombs, M., Dunn, A. & Hayden, L. (2015). Amphibole reaction rims as a record of pre-eruptive magmatic heating: An experimental approach. *Earth and Planetary Science Letters* **426**, 235-245.

Eichelberger, J. C. (1978). Andesitic Volcanism and Crustal Evolution. *Nature* **275**, 21-27.

Erdmann, S., Martel, C., Pichavant, M. & Kushnir, A. (2014). Amphibole as an archivist of magmatic crystallization conditions: problems, potential, and implications for inferring magma storage prior to the paroxysmal 2010 eruption of Mount Merapi, Indonesia. *Contributions to Mineralogy and Petrology* **167**.

Foley, S. F., Barth, M. G. & Jenner, G. A. (2000). Rutile/melt partition coefficients for trace elements and an assessment of the influence of rutile on the trace element characteristics of subduction zone magmas. *Geochimica et Cosmochimica Acta* **64**, 933-938.

Fujimaki, H. (1986). Partition-Coefficients of Hf, Zr, and Ree between Zircon, Apatite, and Liquid. *Contributions to Mineralogy and Petrology* **94**, 42-45.

Green, T. H. & Pearson, N. J. (1987). An Experimental-Study of Nb and Ta Partitioning between Ti-Rich Minerals and Silicate Liquids at High-Pressure and Temperature. *Geochimica et Cosmochimica Acta* **51**, 55-62.

Hammarstrom, J. M. & Zen, E. A. (1986). Aluminum in Hornblende: an Empirical Igneous Geobarometer. *American Mineralogist* **71**, 1297-1313.

Holness, M. B., Anderson, A. T., Martin, V. M., Maclennan, J., Passmore, E. & Schwindinger, K. (2007). Textures in Partially Solidified Crystalline Nodules: a Window into the Pore Structure of Slowly Cooled Mafic Intrusions. *Journal of Petrology* **48**, 1243-1264.

Humphreys, M. C. S., Blundy, J. D. & Sparks, R. S. J. (2006). Magma Evolution and Open-System Processes at Shiveluch Volcano: Insights from Phenocryst Zoning. *Journal of Petrology* **47**, 2303-2334.

Humphreys, M. C. S., Christopher, T. & Hards, V. (2009a). Microlite transfer by disaggregation of mafic inclusions following magma mixing at SoufriSre Hills volcano, Montserrat. *Contributions to Mineralogy and Petrology* **157**, 609-624.

Humphreys, M. C. S., Edmonds, M., Christopher, T. & Hards, V. (2009b). Chlorine variations in the magma of Soufriere Hills Volcano, Montserrat: Insights from Cl in hornblende and melt inclusions. *Geochimica et Cosmochimica Acta* **73**, 5693-5708.

Jenner, G. A., Foley, S. F., Jackson, S. E., Green, T. H., Fryer, B. J. & Longerich, H. P. (1993). Determination of Partition-Coefficients for Trace-Elements in High-Pressure Temperature Experimental Run Products by Laser-Ablation Microprobe Inductively-Coupled Plasma-Mass Spectrometry (Lam-Icp-Ms). *Geochimica et Cosmochimica Acta* **57**, 5099-5103.

Johnson, R. W., Mackenzie, D. E. & Smith, I. E. (1978). Delayed partial melting of subduction-modified mantle in Papua New Guinea. *Tectonophysics* **46**, 197-216.

Kent, A. J. (2014). Bimodal amphibole populations in arc magmas. *Goldschmidt*, 1232.

Kent, A. J. R., Darr, C., Koleszar, A. M., Salisbury, M. J. & Cooper, K. M. (2010). Preferential eruption of andesitic magmas through recharge filtering. *Nature Geoscience* **3**, 631-636.

Kiss, B., Harangi, S., Ntaflos, T., Mason, P. R. D. & Pál-Molnár, E. (2014). Amphibole perspective to unravel pre-eruptive processes and conditions in volcanic plumbing systems beneath intermediate arc volcanoes: a case study from Ciomadul volcano (SE Carpathians). *Contributions to Mineralogy and Petrology* **167**.

Koleszar, A. (2011). Controls on Eruption Style and Magma Compositions at Mount Hood, Oregon. Ph.D. thesis, Oregon State University, 1-199.

Krawczynski, M. J., Grove, T. L. & Behrens, H. (2012). Amphibole stability in primitive arc magmas: effects of temperature, H2O content, and oxygen fugacity. *Contributions to Mineralogy and Petrology* **164**, 317-339.

Loewen, M. W. (2013). Volatile mobility of trace metals in volcanic systems. Ph,D. thesis, Oregon State University.

Luhr, J. F., Carmichael, I. S. E. & Varekamp, J. C. (1984). The 1982 Eruptions of El-Chichon Volcano, Chiapas, Mexico: Mineralogy and Petrology of the Anhydrite-Bearing Pumices. *Journal of Volcanology and Geothermal Research* **23**, 69-108.

Lus, W. Y., McDougall, I. & Davies, H. L. (2004). Age of the metamorphic sole of the Papuan Ultramafic Belt ophiolite, Papua New Guinea. *Tectonophysics* **392**, 85-101.

Macpherson, C. G. (2008). Lithosphere erosion and crustal growth in subduction zones: Insights from initiation of the nascent East Philippine Arc. *Geology* **36**, 311-314.

Marsh, B. D. (1988). Crystal Size Distribution (Csd) in Rocks and the Kinetics and Dynamics of Crystallization .1. Theory. *Contributions to Mineralogy and Petrology* **99**, 277-291.

McCulloch, M. T. & Bennett, V. C. (1994). Progressive growth of the Earth's continental crust and depleted mantle: Geochemical constraints. *Geochimica et Cosmochimica Acta* **58**, 4717-4738.

Nagasawa, H. & Schnetzler, C. C. (1971). Partitioning of rare earth, alkali and alkaline earth elements between phenocrysts and acidic igneous magma. *Geochimica et Cosmochimica Acta* **35**, 953-968.

O'Hara, M. J. (1977). Geochemical evolution during fractional crystallization of a periodically refilled magma chamber. *Nature* **266**, 503-507.

Pichavant, M., Martel, C., Bourdier, J. L. & Scaillet, B. (2002). Physical conditions, structure, and dynamics of a zoned magma chamber: Mount Pelee (Martinique, Lesser Antilles Arc). *Journal of Geophysical Research-Solid Earth* **107**.

Plail, M., Barclay, J., Humphreys, M. C. S., Edmonds, M., Herd, R. A. & Christopher, T. E. (2014). Chapter 18 Characterization of mafic enclaves in the erupted products of Soufriere Hills Volcano, Montserrat, 2009 to 2010. *Geological Society, London, Memoirs* **39**, 343-360.

Putirka, K. A. (2016). Amphibole thermometers and barometers for igneous systems, and some implications for eruption mechanism of felsic magmas at arc volcanoes. *American Mineralogist* **in press**.

Reubi, O. & Blundy, J. (2009). A dearth of intermediate melts at subduction zone volcanoes and the petrogenesis of arc andesites. *Nature* **461**, 1269-1273.

Ridolfi, F., Puerini, M., Renzulli, A., Menna, M. & Toulkeridis, T. (2008). The magmatic feeding system of El Reventador volcano (Sub-Andean zone, Ecuador) constrained by texture, mineralogy and thermobarometry of the 2002 erupted products. *Journal of Volcanology and Geothermal Research* **176**, 94-106.

Ridolfi, F. & Renzulli, A. (2012). Calcic amphiboles in calc-alkaline and alkaline magmas: thermobarometric and chemometric empirical equations valid up to 1,130°C and 2.2 GPa. *Contributions to Mineralogy and Petrology* **163**, 877-895.

Ridolfi, F., Renzulli, A. & Puerini, M. (2010). Stability and chemical equilibrium of amphibole in calc-alkaline magmas: an overview, new thermobarometric formulations and application to subduction-related volcanoes. *Contributions to Mineralogy and Petrology* **160**, 45-66.

Ruprecht, P., Bergantz, G. W., Cooper, K. M. & Hildreth, W. (2012). The Crustal Magma Storage System of Volcan Quizapu, Chile, and the Effects of Magma Mixing on Magma Diversity. *Journal of Petrology* **53**, 801-840.

Rutherford, M. J. & Hill, P. M. (1993). Magma ascent rates from amphibole breakdown: An experimental study applied to the 1980–1986 Mount St. Helens eruptions. *Journal of Geophysical Research* **98**, 19667-19685.

Sato, H., Holtz, F., Behrens, H., Botcharnikov, R. & Nakada, S. (2005). Experimental petrology of the 1991-1995 Unzen dacite, Japan. Part II: Cl/OH partitioning between hornblende and melt and its implications for the origin of oscillatory zoning of hornblende phenocrysts. *Journal of Petrology* **46**, 339-354.

Shane, P. & Smith, V. C. (2013). Using amphibole crystals to reconstruct magma storage temperatures and pressures for the post-caldera collapse volcanism at Okataina volcano. *Lithos* **156-159**, 159-170.

Smith, I. E. M. (2013a). The chemical characterization and tectonic significance of ophiolite terrains in southeastern Papua New Guinea. *Tectonics* **32**, 159-170.

Smith, I. E. M. (2013b). High-magnesium andesites: the example of the Papuan Volcanic Arc. *Geological Society, London, Special Publications* **385**, 117-135.

Sun, S. S. & McDonough, W. F. (1989). Chemical and isotopic systematics of oceanic basalts: implications for mantle composition and processes. *Geological Society, London, Special Publications* **42**, 313-345.

Taylor, B., Goodliffe, A., Martinez, F. & Hey, R. (1995). Continental Rifting and Initial Sea-Floor Spreading in the Woodlark Basin. *Nature* **374**, 534-537.

Taylor, G. A. (1958). The 1951 eruption of Mount Lamington, Papua. *Bureau of Mineral Resources, Geology and Geophysics* **38**.

Thornber, C., Pallister, J. S., Lowers, H. A., Rowe, M. C., Mandeville, C. & Meeker, G. P. (2008). Chemistry, mineralogy and petrology of amphibole in Mount St. Helens 2004-2006 Dacite. In: Sherrod, D. R., Scott, W. E. & Stauffer, P. H. (eds.) *A volcano rekindled: the renewed eruption of Mount St Helens, 2004-2006*. Washington: U.S. Geological Survey Professional Paper.

Turner, S. J., Izbekov, P. & Langmuir, C. (2013). The magma plumbing system of Bezymianny Volcano: Insights from a 54 year time series of trace element whole-rock geochemistry and amphibole compositions. *Journal of Volcanology and Geothermal Research* **263**, 108-121.

Ubide, T., Gale, C., Arranz, E., Lago, M. & Larrea, P. (2014). Clinopyroxene and amphibole crystal populations in a lamprophyre sill from the Catalonian Coastal Ranges (NE Spain): A record of magma history and a window to mineral-melt partitioning. *Lithos* **184**, 225-242.

van der Zwan, F. M., Chadwick, J. P. & Troll, V. R. (2013). Textural history of recent basaltic-andesites and plutonic inclusions from Merapi volcano. *Contributions to Mineralogy and Petrology* **166**, 43-63.

Xiong, X. L., Adam, J. & Green, T. H. (2005). Rutile stability and rutile/melt HFSE partitioning during partial melting of hydrous basalt: Implications for TTG genesis. *Chemical Geology* **218**, 339-359.

Zhang, J., Davidson, J. P., Humphreys, M. C. S., Macpherson, C. G. & Neill, I. (2015). Magmatic Enclaves and Andesitic Lavas from Mt. Lamington, Papua New Guinea: Implications for Recycling of Earlier-fractionated Minerals through Magma Recharge. *Journal of Petrology* **56**, 2223-2256.

5.9. FIGURES

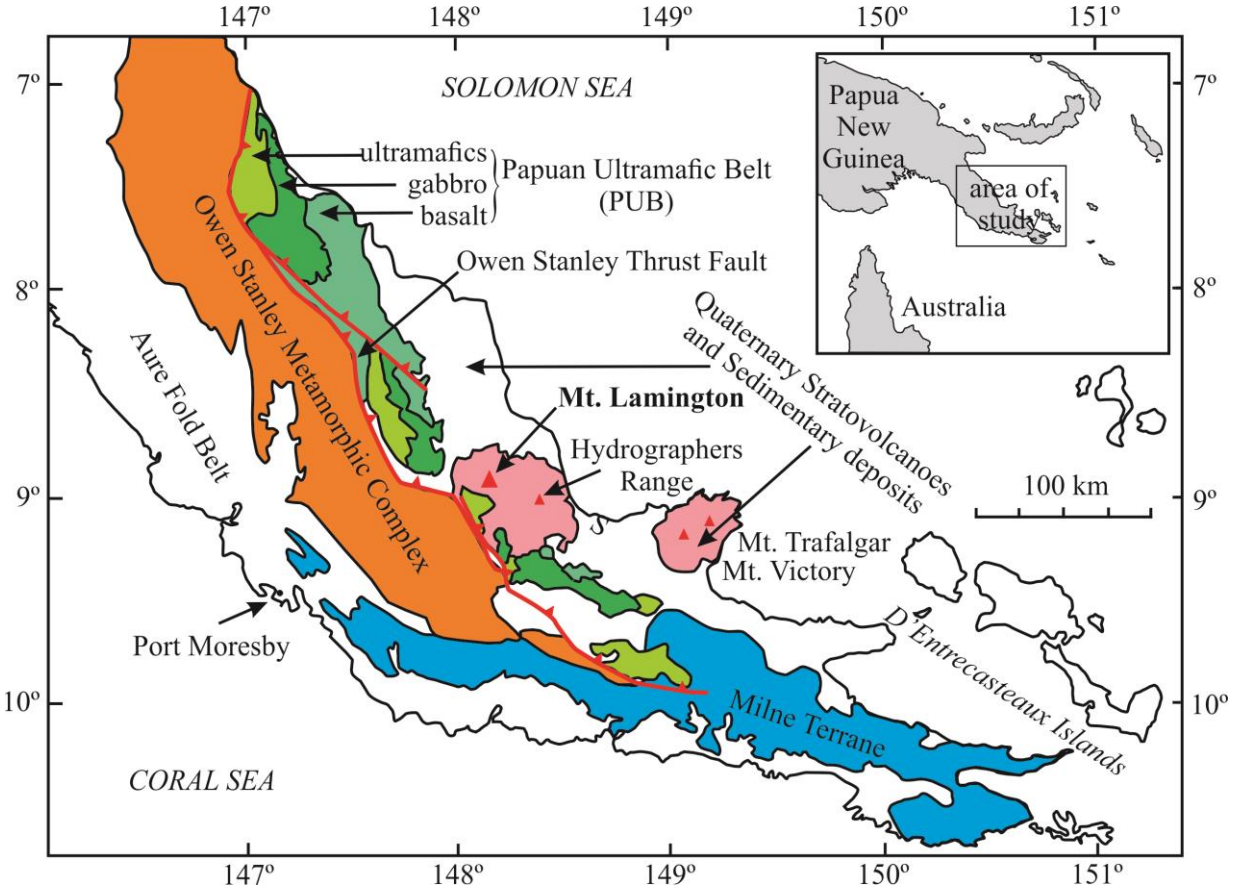

Fig. 5.1 Geology map of the Papuan Peninsula.

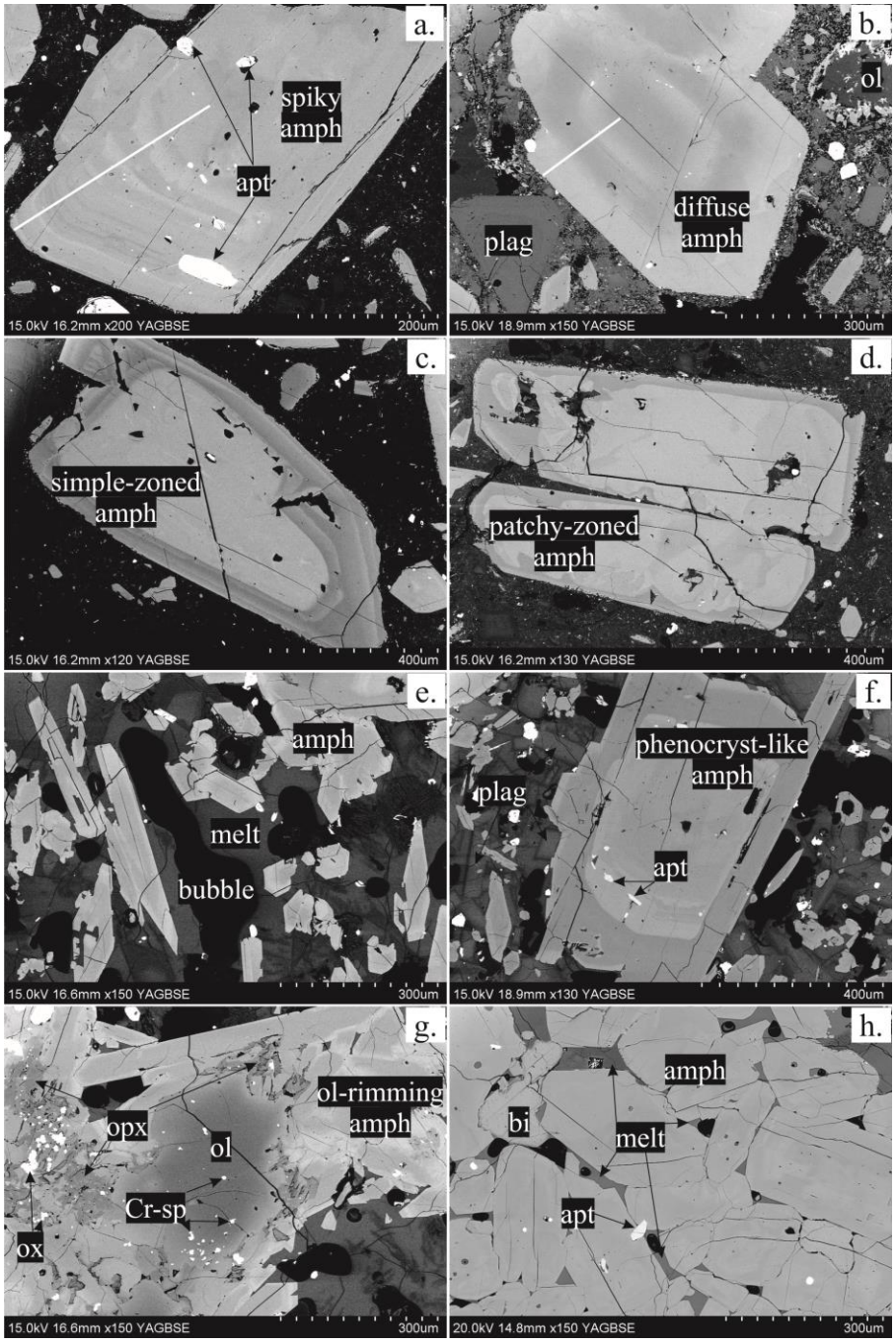

Fig. 5.2 Back-scattered electron (BSE) images of amphiboles with different crystal textures from the 1951 andesite (a, b, c) and diktytaxitic (e, f, g) and plutonic (h) enclaves of Mt. Lamington: (a) amphibole phenocryst with spiky oscillatory zoning; (b) amphibole phenocryst with diffuse oscillatory zoning; (c) amphibole phenocryst with simple zoning, the rim of the crystal also show spiky oscillatory zoning; (d) the core of this phenocryst shows patchy zoning; (e) acicular (framework-forming) amphibole in glassy matrix of diktytaxitic enclave; (f) an apatite-bearing phenocryst-like amphibole in one of the diktytaxitic enclaves, coexisting with plagioclase in the glassy matrix; (g) amphiboles grow on the surface of spinel-bearing olivine (olivine-rimming amphibole) as a reaction product between olivine and melt; (h) irregular-shaped amphibole forming crystal aggregates in plutonic enclave, with the presence of melt in between the crystals. The two white lines in (a, b) represent the traverse of EPMA and the result are shown in Fig. 6 a, c. Symbols: amph – amphibole; plag – plagioclase; apt – apatite; ol – olivine; opx – orthopyroxene; ox – Fe-Ti oxides; Cr-sp – chromian spinel; bi – biotite.

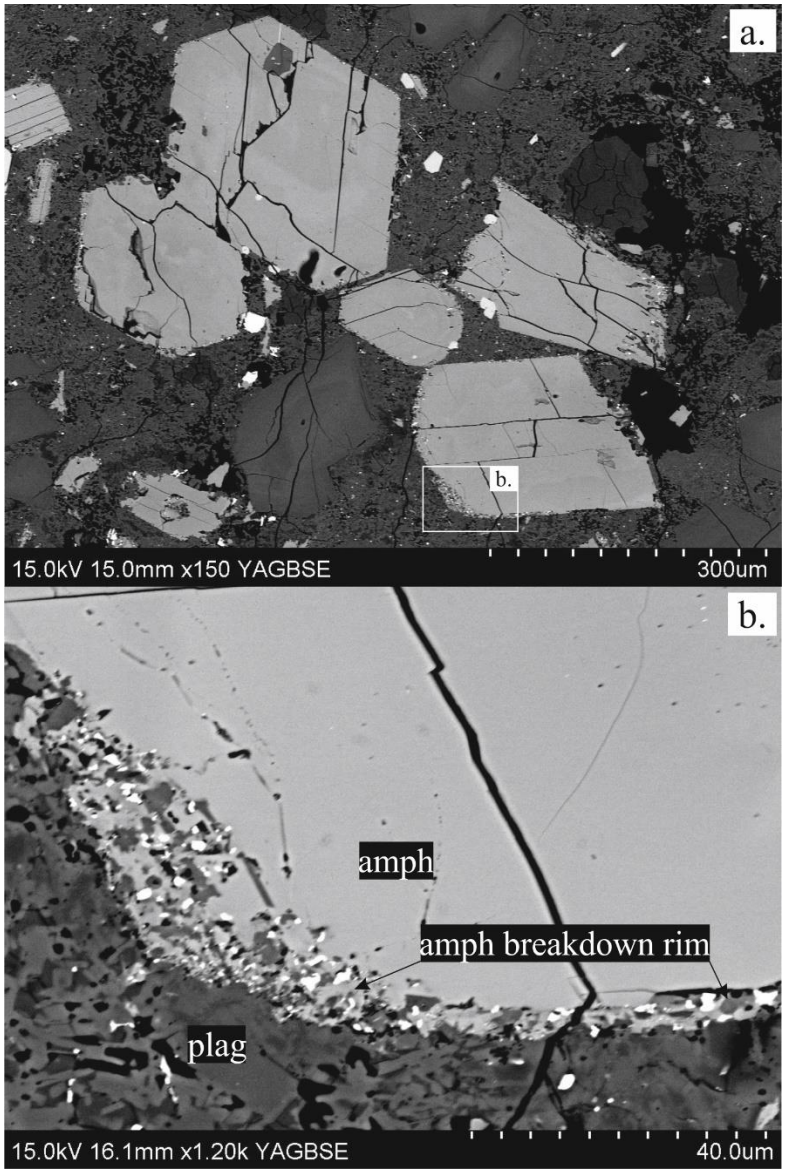

Fig. 5.3 Breakdown texture occurred to amphibole phenocrysts in 1951 andesite of Mt. Lamington. Reaction rims of Fe-Ti oxides, orthopyroxene and plagioclase with thicknesses of 4 – 10 μm develop in response to decompression during magma ascent out of amphibole stability field. See text for discussions.

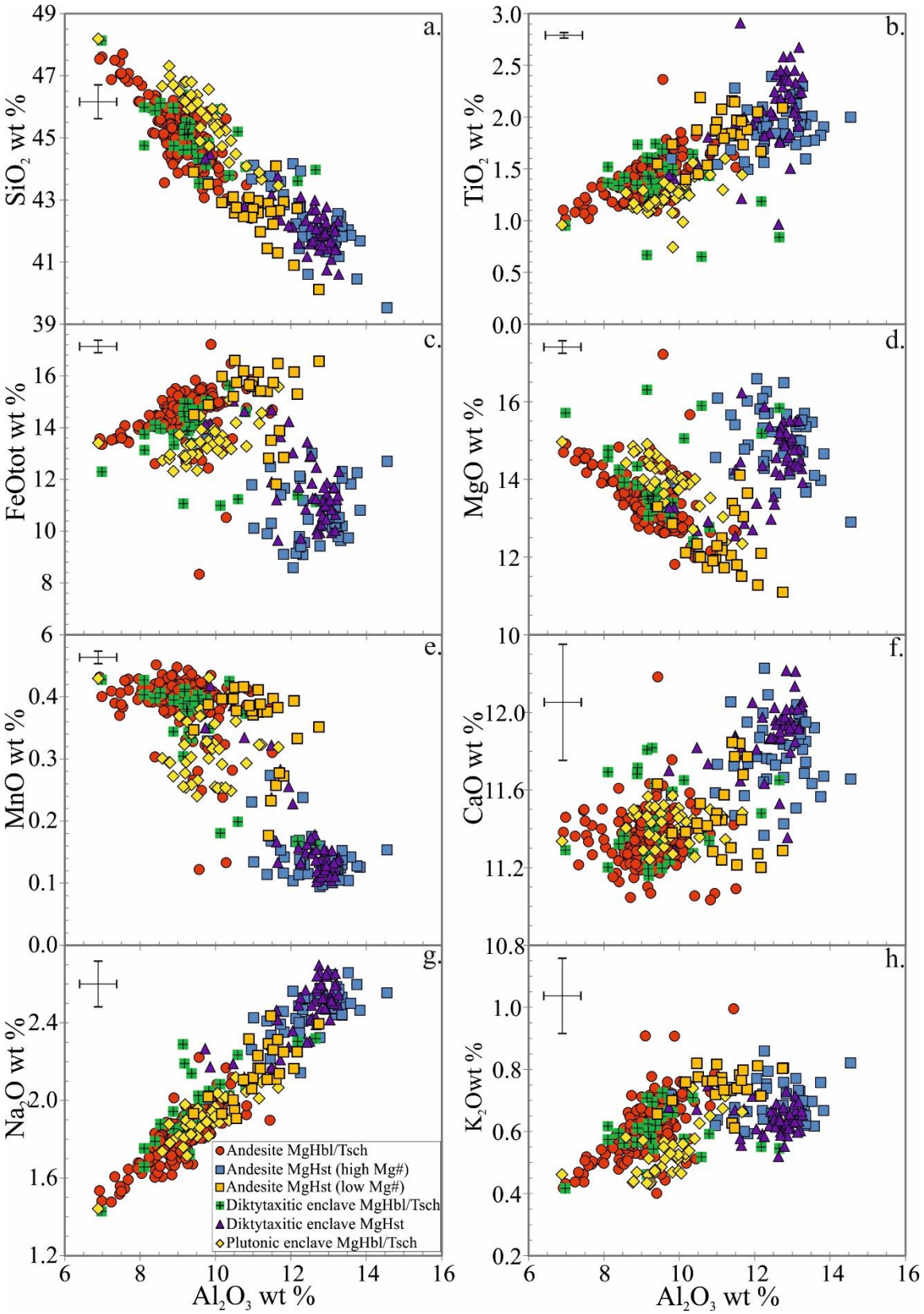

Fig. 5.4 Mt. Lamington amphibole major element compositions. Error bars indicate the 1σ statistical counting errors during the electron probe microanalysis.

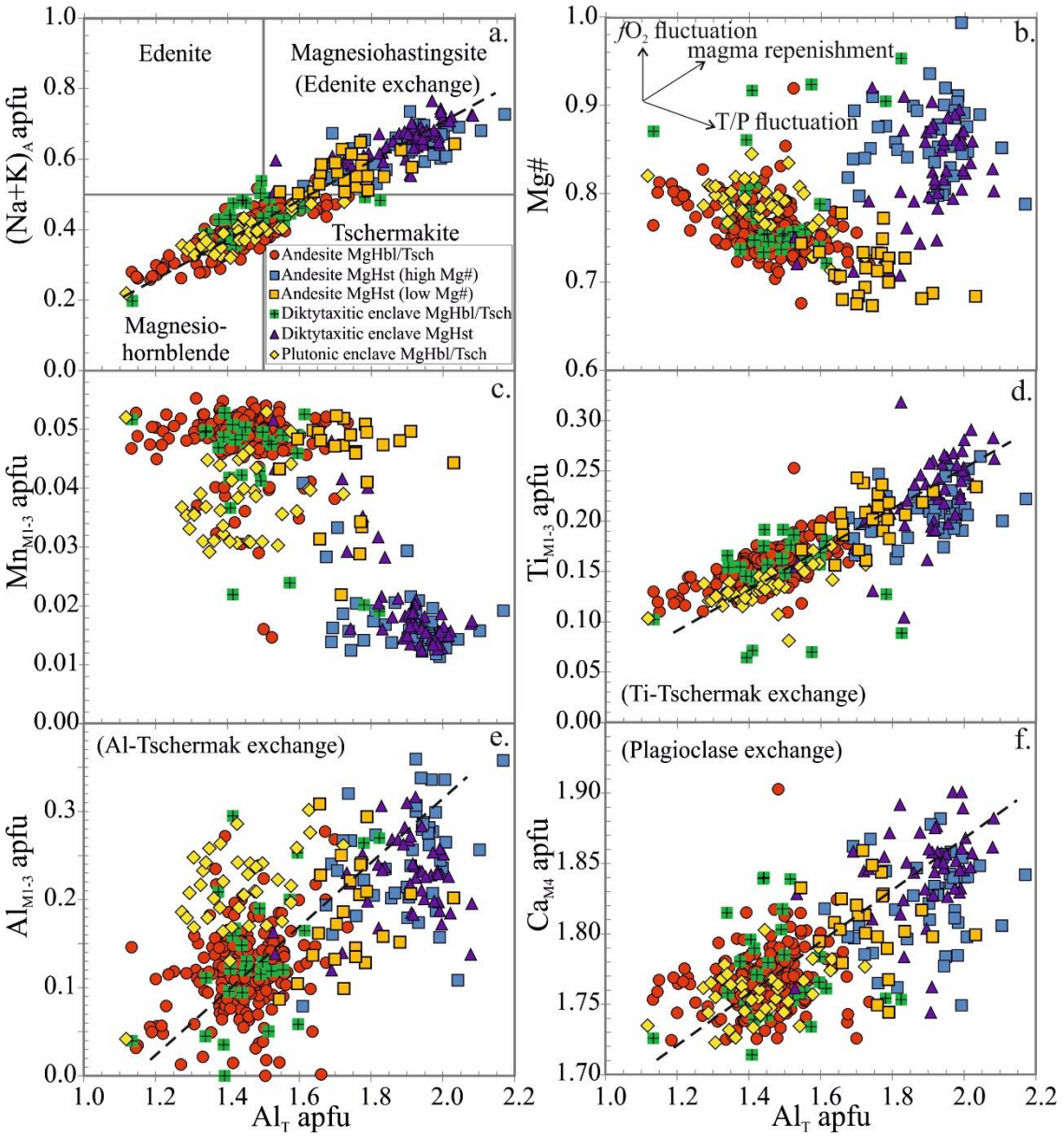

Fig. 5.5 Mt. Lamington amphibole stoichiometric calculation results: (a) classification under the scheme of IMA 2012 recommendation; the dashed line implies temperature-sensitive edenite exchange (vacancy$_A$ + Si$_T$ = (Na, K)$_A$ + Al$_T$); (b) in MgHbl-Tsch – low-Mg# MgHst group, Al$_T$ correlates with Mg# negatively, following the trend of variation caused by temperature/pressure fluctuation; whereas in high-Mg# MgHst group, Al$_T$ shows no obvious correlation with Mg#, concomitant elevated Al$_T$ and Mg# indicate contribution from magma replenishment; (c) Mn and Al$_T$ show a generally negative correlation, (d) Ti-Tschermak exchange (Mn$_{M1-3}$ + 2 Si$_T$ = Ti$_{M1-3}$ + 2 Al$_T$); (e) less obvious positive correlation between Al$_T$ and Al$_{M1-3}$, which indicates the Al-Tschermak exchange (Si$_T$ + (Mg, Fe)$_{M1-3}$ = Al$_T$ + Al$_{M1-3}$) is not as important as the edenite and Ti-tschermak exchanges; (f) positive correlation between Ca$_{M4}$ and Al$_T$ indicates plagioclase exchange (Si$_T$ + Na$_{M4}$ = Al$_T$ + Ca$_{M4}$).

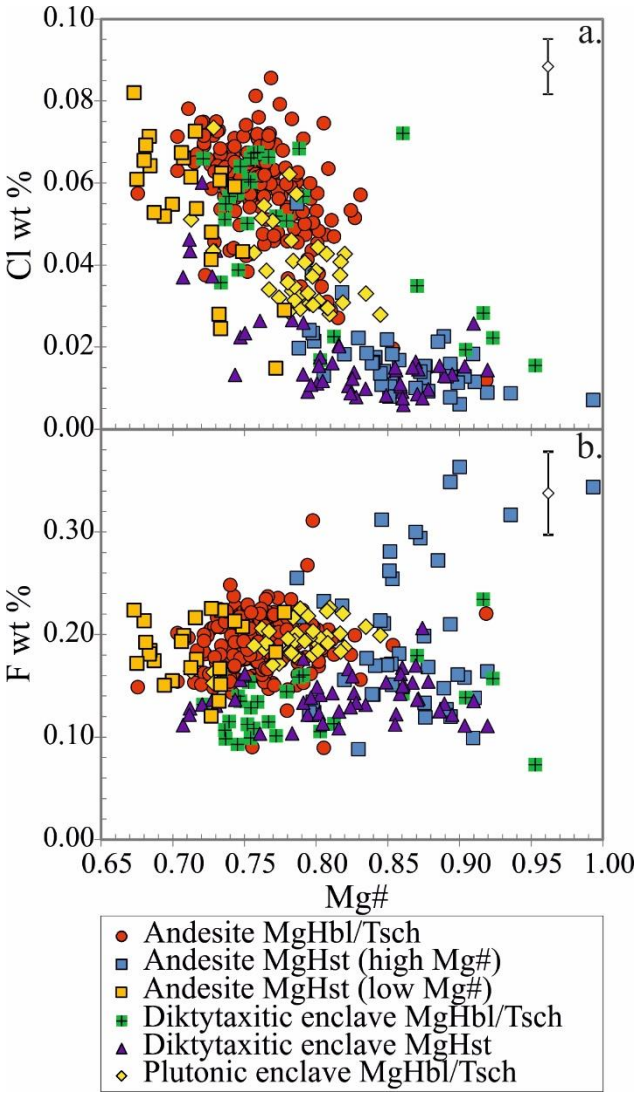

Fig. 5.6 Mt. Lamington amphibole Cl and F contents against Mg#. (a) Cl contents of Mt. Lamington amphiboles display a negative correlation with amphibole Mg#; (b) F contents in Mt. Lamington amphiboles are generally not distinguishable except that some of the high-Mg# MgHst in amphibole phenocrysts in the 1951 andesite can have a higher F content. Error bars indicate the 1σ statistical counting errors during the electron probe microanalysis.

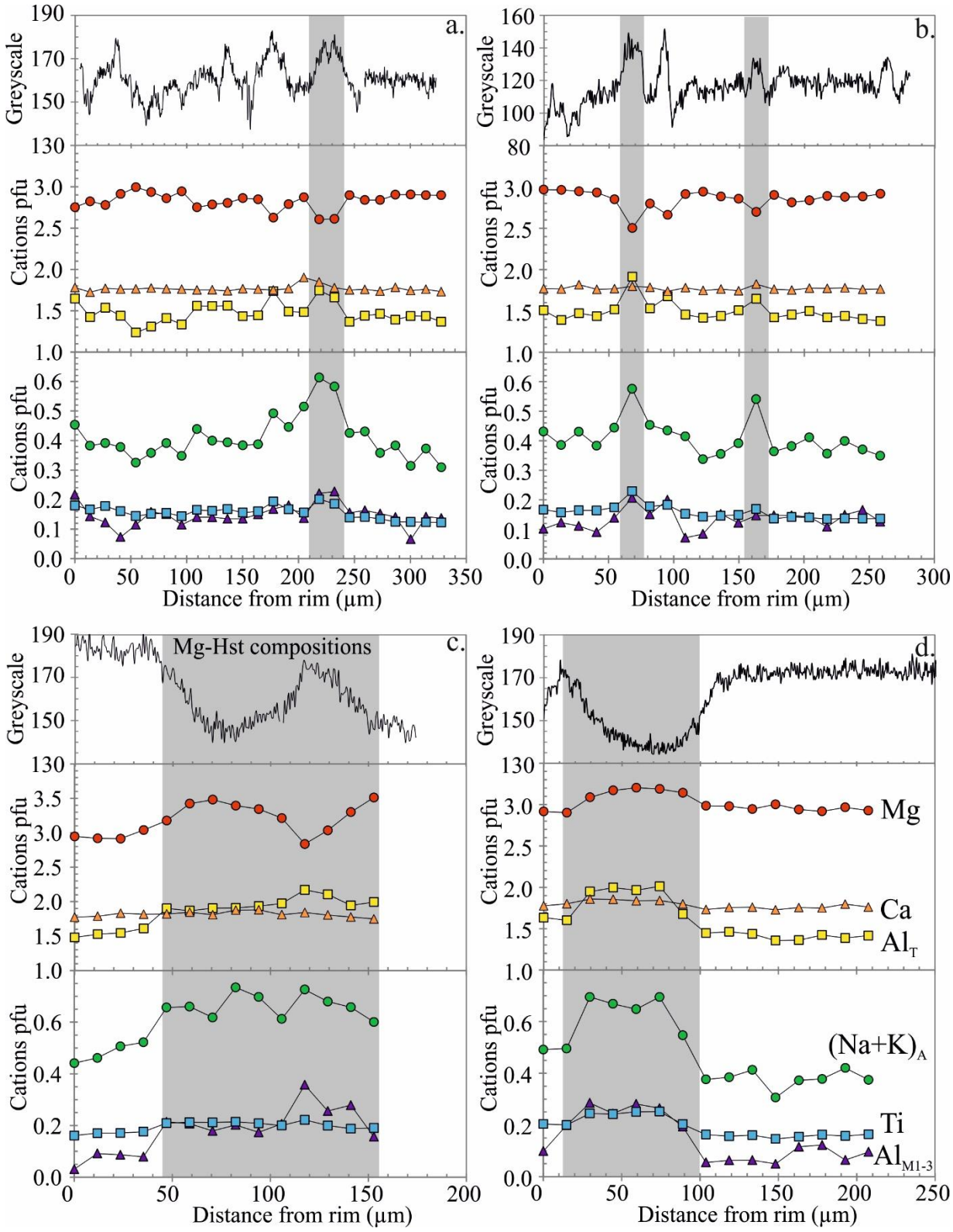

Fig. 5.7 Greyscale variations on amphibole phenocrysts in BSE images and corresponding compositional variations of spiky oscillatory zonings (a, b) and. diffuse oscillatory zonings (c, d) in amphibole phenocrysts from 1951 andesite. The greyscale profile is derived from image profiling analysis using the software ImageJ, the strong oscillations of smaller amplitude represent the analytical uncertainty of the greyscale, while the larger oscillations correspond to the oscillatory zonings of the crystals.

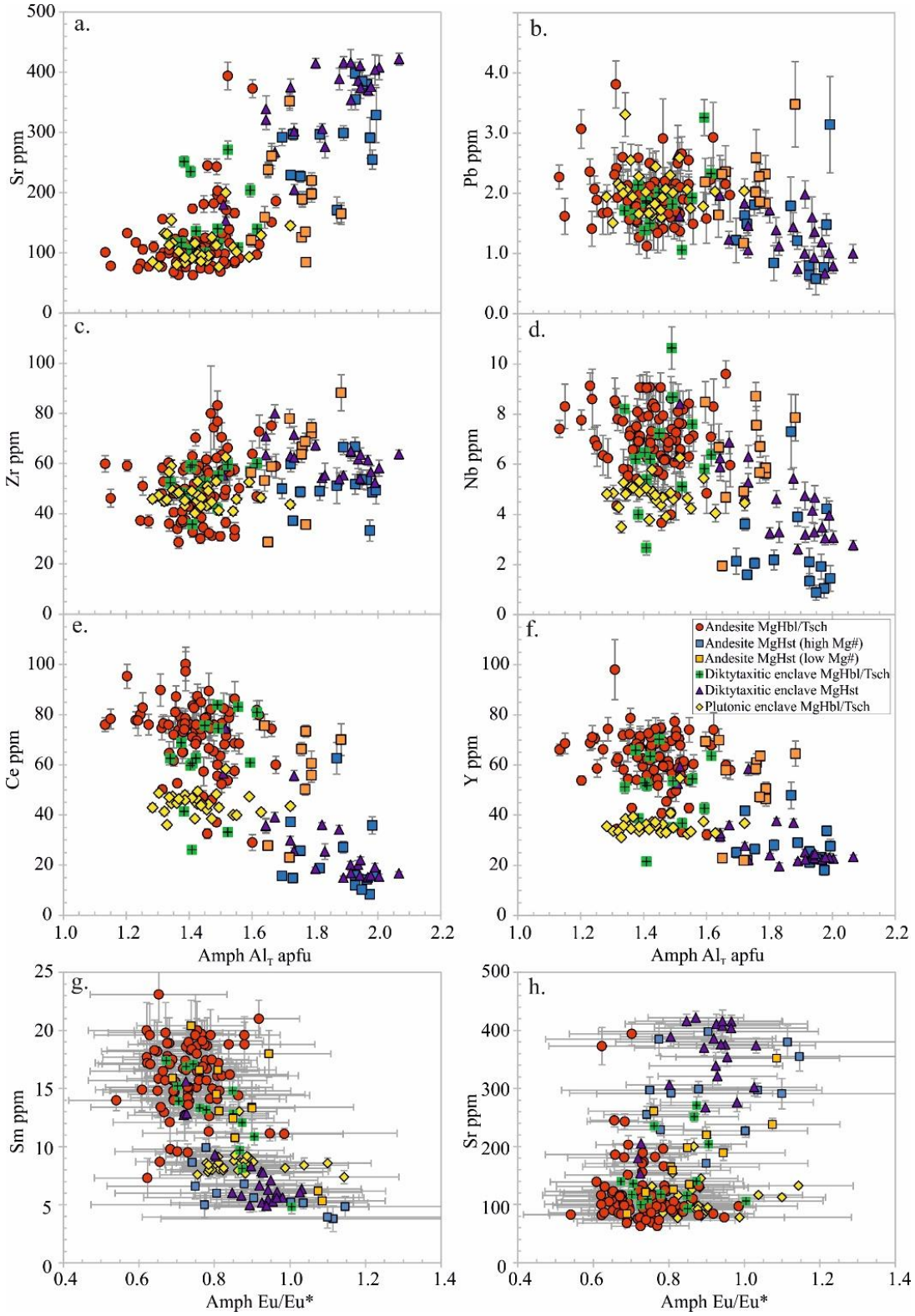

Fig. 5.8 Amphibole trace element compositions plotted against amphibole tetrahedral Al (a-f) and Eu/Eu* (g-h). Error bars on the amphibole trace element concentrations represent the 2σ internal standard errors generated during the LA-ICP-MS analysis and raw data conversion; error bars on the Eu/Eu* are calculated with 2σ internal standard errors of Sm, Eu and Gd according to error propagation.

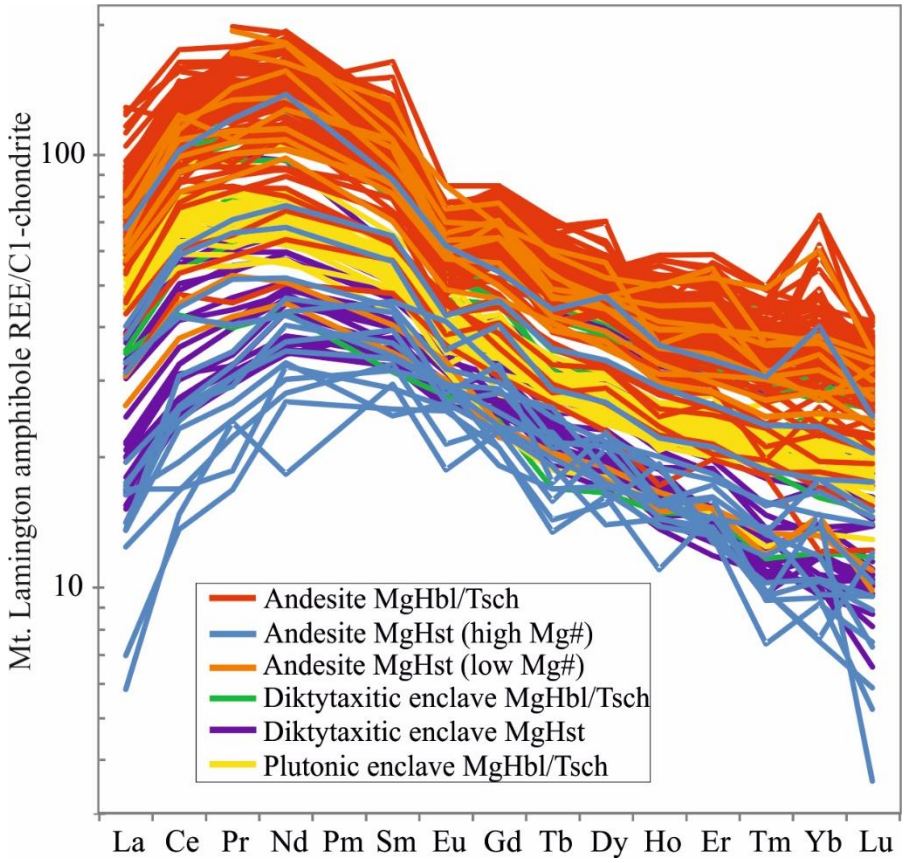

Fig. 5.9 Chondrite-normalized Mt. Lamington amphibole REE patterns.

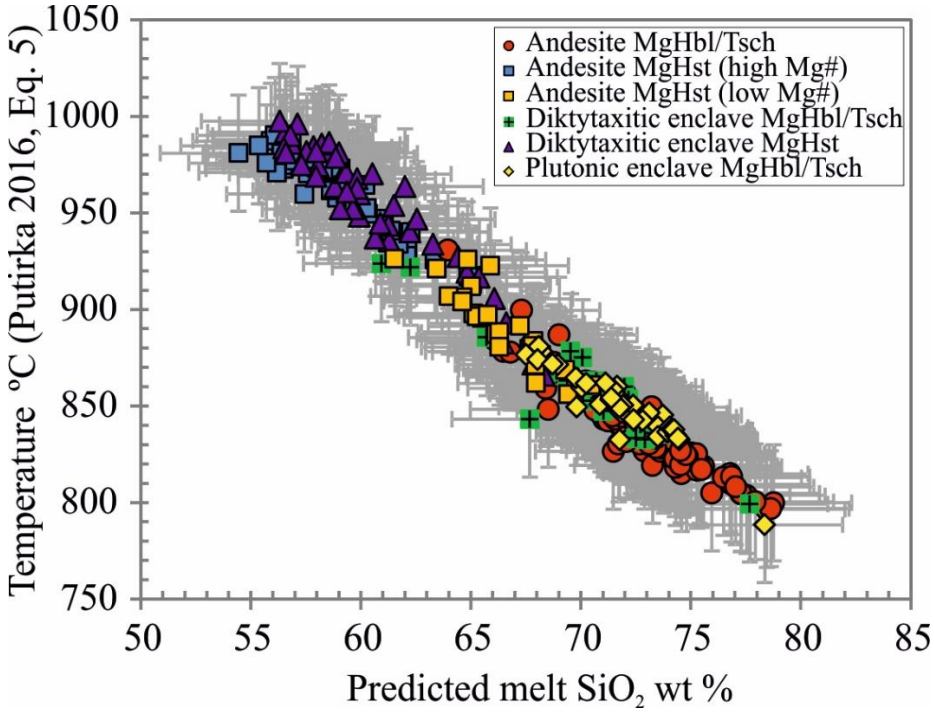

Fig. 5.10 Predicted crystallizing temperature and melt SiO_2 content of amphiboles from Mt. Lamington. MgHst are crystallized from hotter and less silicic melt compared to MgHbl-Tsch. The errors of predicted melt SiO_2 content are given as the standard error of the multiple regression analysis (± 3.55 wt %, Chapter 3), the error of Putirka (2016)'s amphibole-only pressure-independent thermometer is ± 30 ºC.

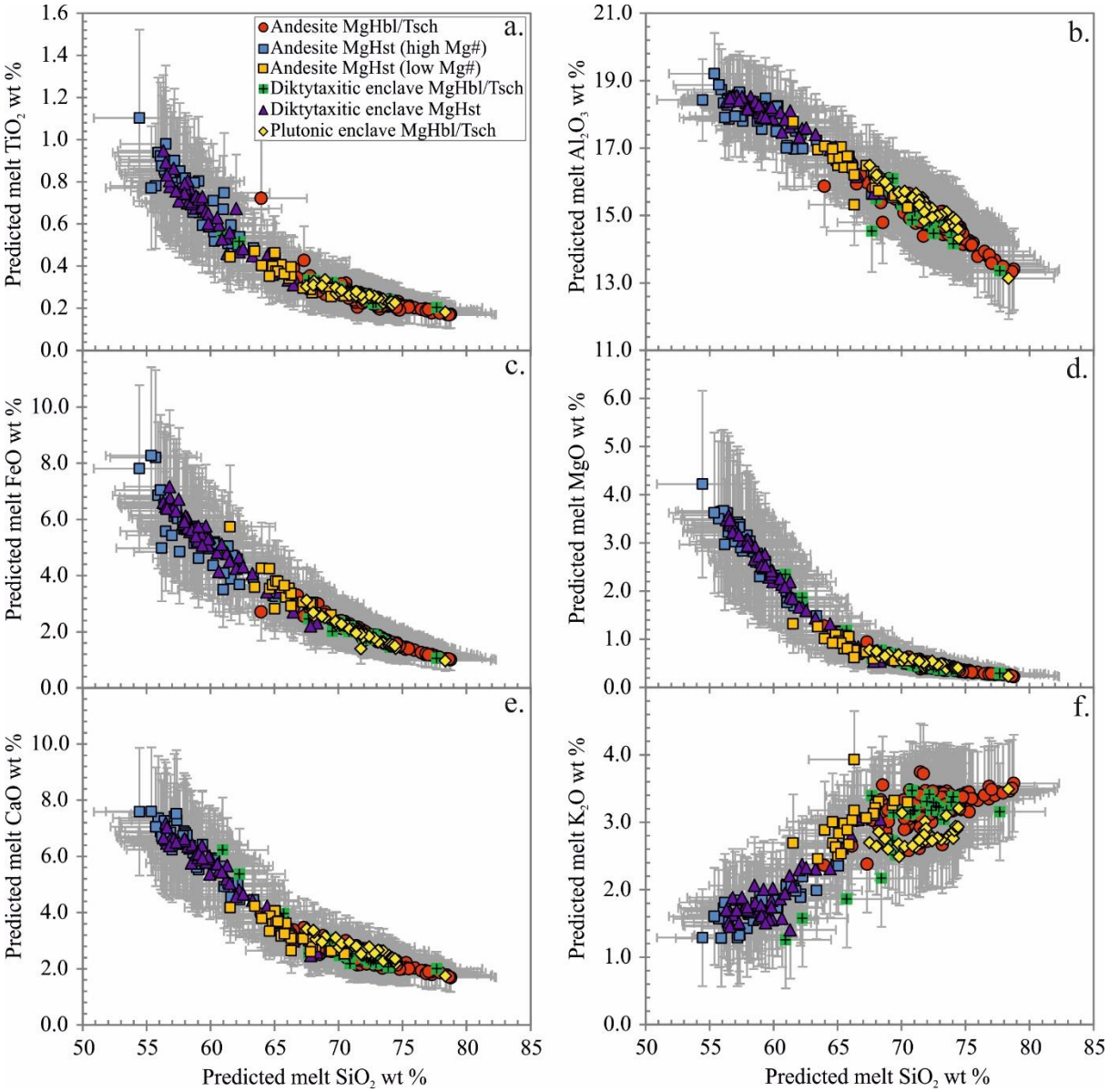

Fig. 5.11 Predicted major element compositions of the melt from which Mt. Lamington amphiboles are crystallized. The equations used are reported in Chapter 3 (*Eq. 2* for SiO_2, *Eq. 6* for TiO_2, *Eq. 19* for Al_2O_3, *Eq. 10* for FeO, *Eq. 12* for MgO, *Eq. 14* for CaO and *Eq. 18* for K_2O). The errors of SiO_2, Al_2O_3, and K_2O are given as the standard error of the multiple regression analysis (Chapter 3). The errors of TiO_2, MgO, CaO and FeO are calculated according to error propagation (e.g. $\sigma FeO = FeO \cdot \sigma lnFeO$).

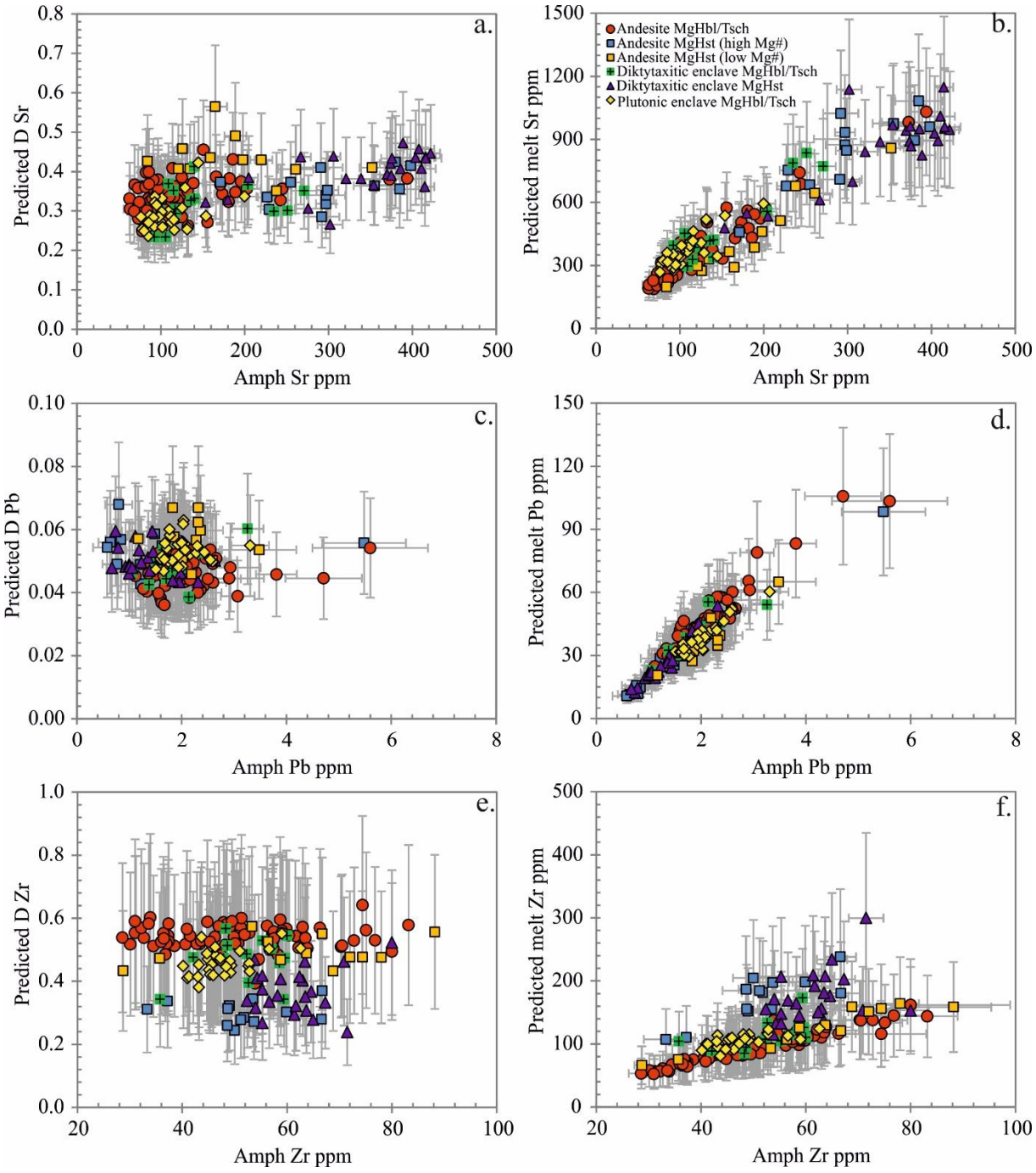

Fig. 5.12 Predicted trace element partition coefficients and melt trace element contents, plotted against amphibole trace element contents. The predicted $^{Amph/L}D$ are calculated using equations from Chapter 4 (*Eq. 7* for D Sr, *Eq. 8* for D Pb, *Eq. 18* for D Zr, *Eq. 15* for D Nb, *Eq. 25* for D Sm and *Eq. 41* for D Y; they are all temperature-independent equations). See text for details.

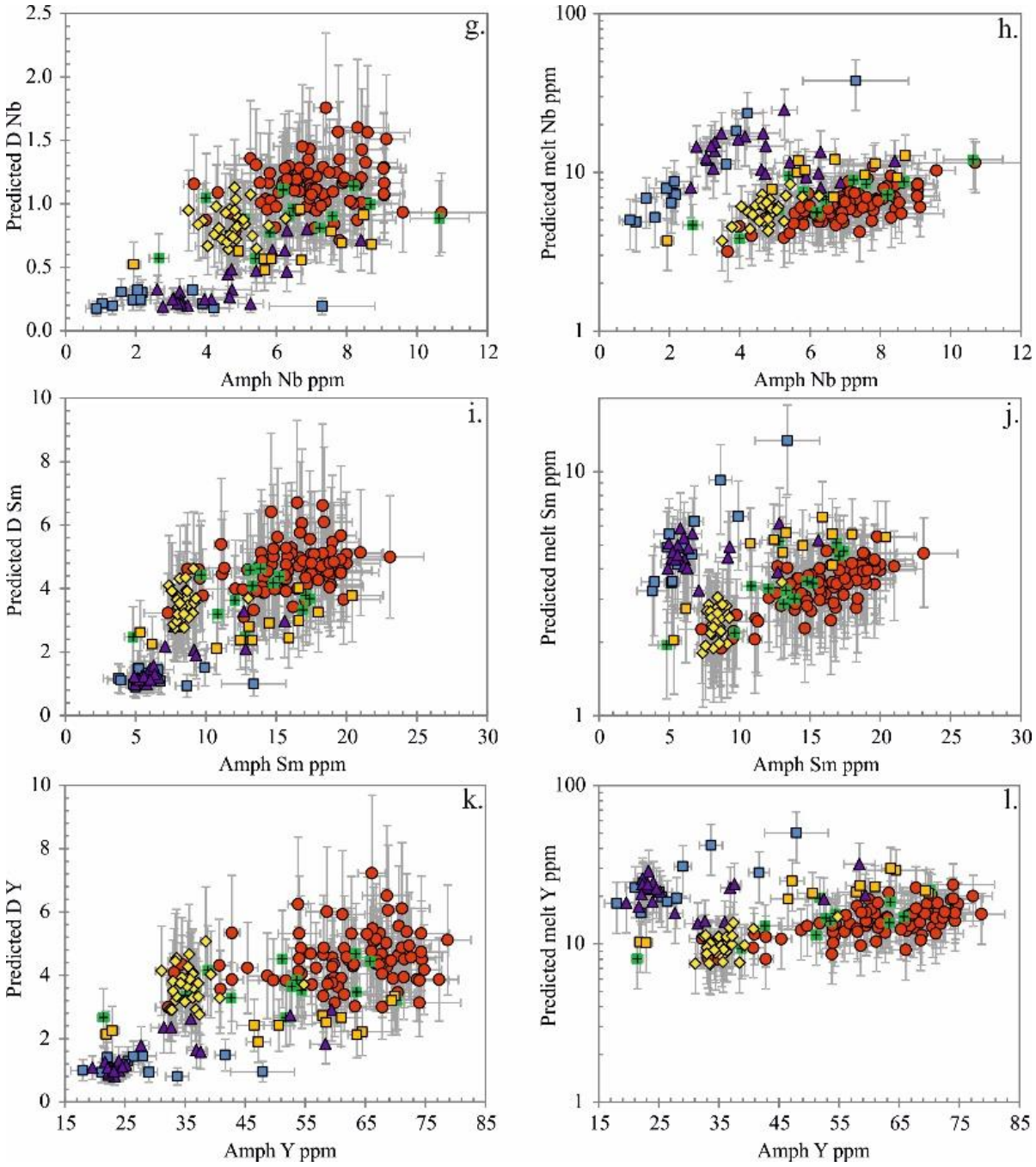

Fig. 5.12 continued.

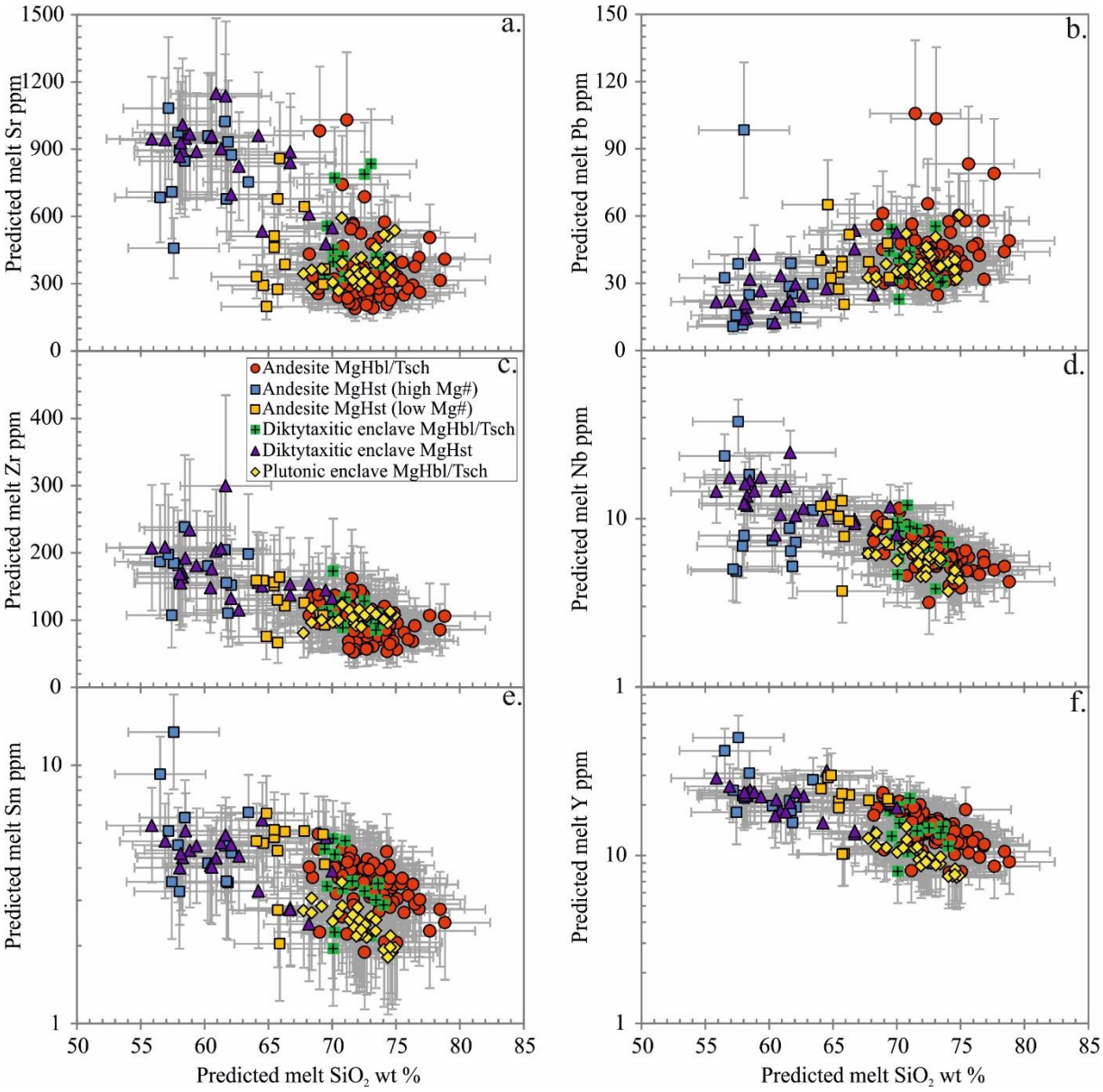

Fig. 5.13 Inferred major and trace element compositions of melts from which Mt. Lamington amphiboles are crystallized. See text for discussions.

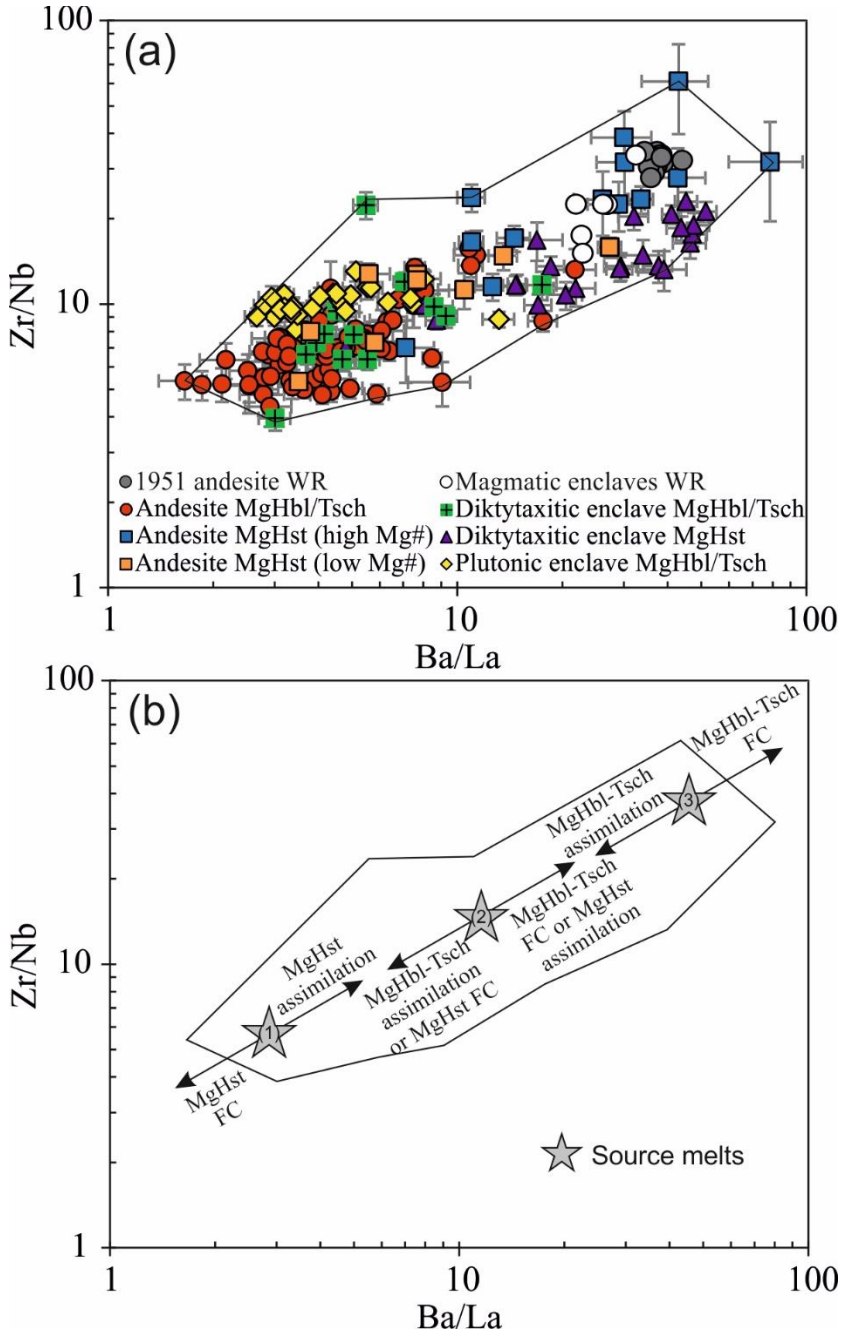

Fig. 5.14 (a) Zr/Nb and Ba/La ratios of Mt. Lamington bulk rocks and amphiboles therein. (b) Schematic illustrations of how fractional crystallization (FC) and/or assimilation of MgHst and MgHbl-Tsch will modify the Zr/Nb and Ba/La ratios of the source melts (grey stars). If the source melts have low Zr/Nb and Ba/La ratios similar to MgHbl-Tsch (source melt 1), the variation range of Zr/Nb and Ba/La ratios can be explained by MgHst assimilation; if the source melts have Zr/Nb and Ba/La ratios similar to source melt 2, the variation range can be explained by both MgHbl-Tsch and MgHst assimilation and fractional crystallization; if the source melts have high Zr/Nb and Ba/La ratios similar to high-Mg# MgHst, the variation range can only be explained by MgHbl-Tsch assimilation. We interpret that the source melts of Mt. Lamington andesites and enclave magma have Zr/Nb and Ba/La ratios similar to MgHst (source melt 3). See further discussions in the text.

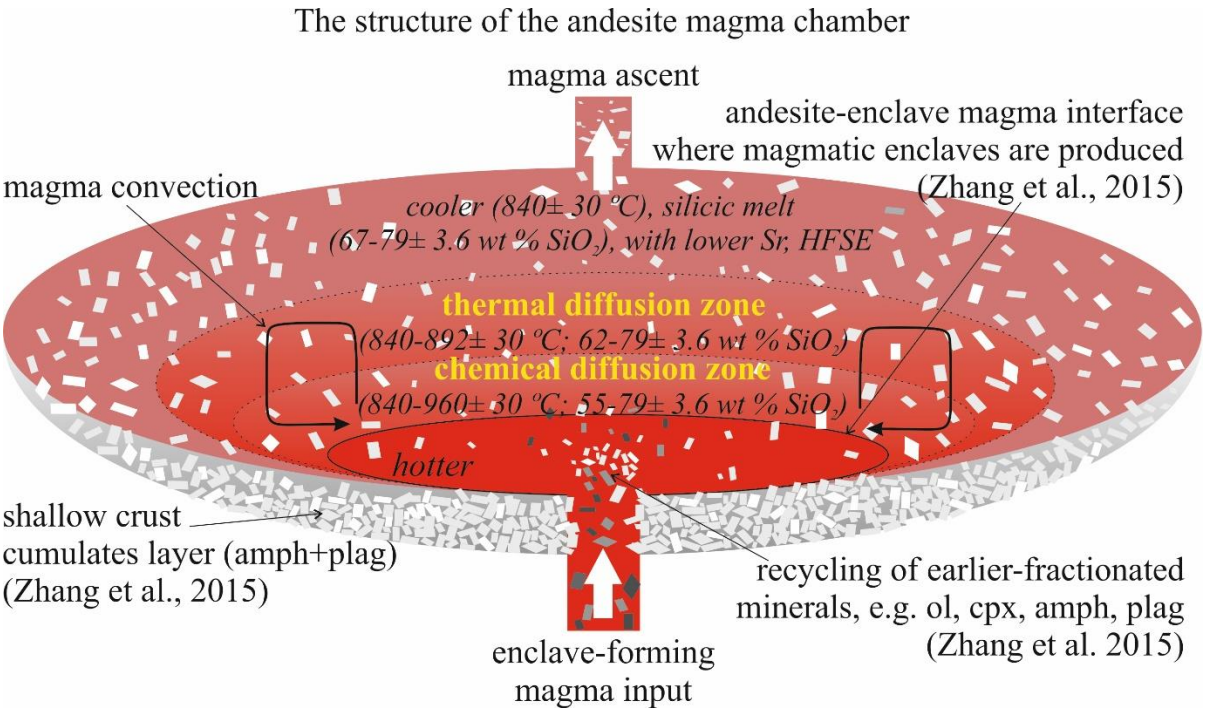

Fig. 5.15 The schematic cartoon of the structure of the andesite magma chamber of Mt. Lamington prior to the 1951 eruption. Intrusion of the hotter, enclave-forming magma into the base of the andesite magma body yields to magma mixing in the chemical diffusion zone in the andesite directly above the interface of the andesite-enclave forming magma, and magma heating in thermal diffusion zone, which is further away from the chemical diffusion zone. Magma mixing cannot occur within the thermal diffusion zone. Thermal gradients across the thermal and chemical diffusion zone will drive magma convection within andesite. Amphibole phenocrysts moving within the thermal diffusion zone crystalize spiky oscillatory zoning (MgHbl-Tsch and low-Mg# MgHst), and those moving within chemical diffusion zone form diffuse oscillatory zoning (MgHbl-Tsch and high-Mg# MgHst) instead.

5.10. TABLES

Table 1: Representative Mt. Lamington amphibole major element compositions

	Diktytaxitic enclaves			Plutonic enclave		Spiky zoned pheno.			Diffuse zoned pheno.			1σ error	Secondary standards			
	8-0014-30	8-0015-03	8-0015-09	10-0008-7	10-0004-17	14-01-AM2	14-01-AM2	14-01-AM2	14-17-AM	14-17-AM	14-17-AM		SJI ol		SEC cpx	
Analysis	#1	#2	#3	#4	#5	#6	#7	#8	#9	#10			Aver.	2S.D.	Aver.	2S.D.
Species	Mg-Hst	Tsch	Mg-Hbl	Tsch	Mg-Hbl	Mg-Hbl	Tsch	Mg-Hst	Mg-Hbl	Mg-Hst			n=6		n=9	
SiO_2	42.90	43.79	45.09	43.46	46.17	44.47	43.95	41.29	45.14	41.71	0.57	40.46	0.34	50.76	0.48	
TiO_2	2.53	1.64	1.43	1.44	1.15	1.51	1.47	1.96	1.43	2.30	0.03					
Al_2O_3	12.06	10.37	9.18	11.67	9.20	8.99	9.23	11.65	8.40	13.17	0.49			0.67	0.07	
FeOt	9.56	15.63	14.41	15.58	12.88	14.74	14.54	16.48	14.35	10.30	0.28	9.92	0.15	16.40	0.51	
MgO	15.33	12.40	13.49	12.34	14.67	13.12	13.15	11.51	13.58	14.85	0.16	49.51	0.35	8.28	0.10	
CaO	11.74	11.27	11.19	11.48	11.37	11.42	11.34	11.45	11.44	11.84	0.28			22.72	0.81	
MnO	0.12	0.43	0.41	0.32	0.28	0.39	0.39	0.38	0.42	0.13	0.01	0.12	0.01	0.51	0.02	
Na_2O	2.46	2.03	2.19	2.07	1.98	1.78	1.85	2.31	1.83	2.44	0.13			0.75	0.02	
K_2O	0.60	0.71	0.62	0.66	0.51	0.67	0.66	0.76	0.56	0.69	0.23					
F	0.13	0.13	0.13	0.15	0.20	0.25	0.23	0.19	0.18	0.25	0.05					
Cl	0.01	0.07	0.07	0.04	0.04	0.06	0.07	0.07	0.06	0.01	0.01					
Total	97.44	98.47	98.21	99.21	98.45	97.40	96.87	98.06	97.38	97.70		100.01		100.09		
T Si	6.198	6.384	6.550	6.278	6.613	6.538	6.490	6.117	6.614	6.035						
T Al(IV)	1.802	1.616	1.450	1.722	1.387	1.462	1.510	1.883	1.386	1.965						
Total	8.000	8.000	8.000	8.000	8.000	8.000	8.000	8.000	8.000	8.000						
M1-3 Al(VI)	0.252	0.166	0.121	0.265	0.167	0.096	0.097	0.151	0.064	0.281						
M1-3 Ti	0.275	0.180	0.156	0.156	0.124	0.166	0.163	0.218	0.157	0.251						
M1-3 Fe^{3+}	0.565	0.863	0.801	0.889	0.839	0.802	0.843	0.853	0.791	0.696						
M1-3 Mg	3.303	2.695	2.921	2.657	3.133	2.876	2.895	2.541	2.967	3.203						
M1-3 Fe^{2+}	0.591	1.043	0.949	0.993	0.704	1.010	0.953	1.189	0.968	0.551						
M1-3 Mn	0.015	0.053	0.050	0.039	0.034	0.049	0.049	0.048	0.052	0.016						
Total	5.000	5.000	5.000	5.000	5.000	5.000	5.000	5.000	5.000	5.000						
M4 Ca	1.818	1.761	1.742	1.777	1.745	1.798	1.794	1.817	1.795	1.836						
M4 Na	0.182	0.239	0.258	0.223	0.255	0.202	0.206	0.183	0.205	0.164						
Total	2.000	2.000	2.000	2.000	2.000	2.000	2.000	2.000	2.000	2.000						
A Na	0.507	0.334	0.358	0.357	0.295	0.306	0.324	0.481	0.315	0.521						
A K	0.111	0.132	0.115	0.122	0.093	0.127	0.125	0.144	0.105	0.127						
Total	0.617	0.466	0.473	0.478	0.388	0.432	0.449	0.625	0.420	0.648						
Mg#	0.848	0.721	0.755	0.728	0.817	0.740	0.752	0.681	0.754	0.853						

1σ error is the average of the X-ray counting statistical errors; the two secondary standards are St. John's Island olivine and SEC clinopyroxene;

Table 5.1

Table 5.2

Table 2: Representative Mt. Lamington amphibole trace element compositions (in ppm)

	Diktytaxitic enclaves						Plutonic enclave				Spiky zoned pheno.						Diffuse zoned pheno.				BHVO-2G (n=14)			BCR-2G (n=8)		
Analysis	#1	2σ er.	#2	2σ er.	#3	2σ er.	#4	2σ er.	#5	2σ er.	#6	2σ er.	#7	2σ er.	#8	2σ er.	#9	2σ er.	#10	2σ er.	Aver.	2SD (%)	% diff	Aver.	2SD (%)	% diff
Rb	5.34	0.60	1.55	0.21	1.20	0.23	1.59	0.18	1.20	0.17	1.05	0.59	2.17	0.54	2.00	0.62	1.33	0.51	3.30	0.89	9.7	14.9	-6.1	51.0	14.4	8.7
Sr	415	11	140	6	100	4	145	7	83	4	97	12	86	11	165	14	115	13	380	28	410.2	22.2	-3.6	373.2	25.8	9.7
Ba	209	7	95	6	74	4	59	3	43	3	96	13	100	11	156	17	60	7	137	15	126.5	15.3	3.5	677.4	7.5	0.1
Pb	1.72	0.21	2.33	0.26	2.01	0.24	2.04	0.20	1.66	0.13	2.91	0.66	2.50	0.63	3.48	0.71	1.27	0.28	5.48	0.80	1.8	12.2	-9.6	10.6	4.7	-3.3
Zr	67.3	2.1	60.0	2.3	52.7	1.6	43.7	1.4	43.2	1.6	56.2	6.4	57.5	5.3	88.2	7.2	49.9	3.9	53.5	3.9	161.0	9.2	6.4	172.3	7.5	-6.4
Hf	2.62	0.26	3.11	0.34	2.35	0.28	2.17	0.27	2.59	0.41	2.68	0.68	2.37	0.63	3.68	0.65	1.97	0.61	2.83	0.66	4.0	12.8	8.1	4.5	6.3	-9.1
Nb	3.25	0.22	6.37	0.44	7.24	0.52	4.45	0.30	5.32	0.37	7.94	0.99	8.10	1.10	7.86	0.93	6.91	0.89	1.92	0.50	19.7	40.0	-8.7	14.6	45.9	16.0
Ta	0.18	0.04	0.26	0.04	0.27	0.04	0.17	0.04	0.21	0.04	0.27	0.12	0.18	0.09	0.17	0.08	0.15	0.06	0.11	0.06	1.1	12.7	2.0	0.7	10.1	-3.3
La	5.09	0.27	21.01	0.92	18.77	0.97	12.45	0.56	12.35	0.40	24.80	2.60	19.50	2.10	14.90	1.70	18.50	1.40	3.20	0.53	14.9	8.2	2.1	24.6	3.9	-1.1
Ce	18.5	0.7	80.9	2.3	75.7	2.7	43.5	1.3	48.0	1.5	89.4	7.1	82.5	6.1	70.0	6.3	76.4	5.0	14.2	1.4	36.2	4.2	4.3	51.1	5.6	-3.4
Nd	21.2	1.5	70.5	3.0	69.1	2.4	32.4	2.2	34.7	1.8	86.8	9.9	76.5	7.4	73.1	6.9	64.0	5.9	15.4	2.2	23.8	5.5	2.6	27.1	7.5	-5.4
Sm	6.10	0.38	17.40	1.40	16.90	1.20	8.33	0.61	9.08	0.62	19.60	3.50	18.00	3.00	14.50	2.10	20.00	2.50	3.80	1.10	6.0	8.4	1.1	6.4	6.4	-3.1
Eu	1.82	0.18	3.61	0.17	3.78	0.21	2.35	0.13	2.22	0.16	3.78	0.73	3.41	0.64	3.82	0.82	3.76	0.56	1.54	0.26	1.9	8.7	5.9	1.8	8.6	-6.1
Gd	5.44	0.42	15.45	0.71	15.00	0.97	7.91	0.48	6.39	0.47	15.20	2.30	13.70	2.00	14.50	1.90	16.70	2.20	4.70	1.10	5.8	10.8	7.7	6.0	11.2	-10.6
Dy	5.14	0.36	13.13	0.69	12.94	0.66	7.11	0.56	6.03	0.43	12.50	1.80	11.70	1.50	11.90	1.40	13.60	1.80	5.30	1.00	5.0	10.0	5.6	6.0	7.2	-6.9
Er	2.39	0.23	6.93	0.41	7.53	0.48	4.37	0.30	3.41	0.26	7.40	1.10	7.54	0.92	8.60	1.20	7.49	0.80	2.64	0.62	2.3	16.9	8.1	3.4	12.1	-13.5
Yb	2.32	0.30	6.25	0.60	6.90	0.55	4.18	0.34	3.35	0.47	12.30	2.60	9.90	2.00	10.20	2.60	5.60	1.00	1.60	0.57	1.8	10.8	7.5	3.2	11.2	-5.6
Lu	0.27	0.04	0.85	0.09	1.00	0.10	0.53	0.04	0.49	0.08	0.80	0.22	0.96	0.19	0.89	0.20	0.83	0.18	0.13	0.07	0.2	19.0	11.9	0.5	14.1	-8.3
Y	24.0	0.8	63.6	1.7	70.2	2.9	36.8	1.1	33.6	1.0	59.5	6.0	58.7	4.2	64.5	5.0	67.0	4.1	23.2	1.7	24.6	21.7	5.5	34.7	21.0	-6.3

2σ error is the 2 standard error generated during transferring particle counting data into concentration data with the the Iolite v. 2.5 software; % diff indicates the deviation of the average of standard analyses from the published values in percentage.

Table 3: Summary of Mt. Lamington amphibole textural types, features and crystal chemistry

Sample type	Amphibole textural types	Features	Crystal chemistry
1951 andesite	Spiky oscillatory zoned	Abrupt compositional variations, sharp and rhythmic greyscale variation pattern, presence of resorption surface, zoning width < 50 µm	Low-Mg# MgHst, MgHbl-Tsch
	Diffuse oscillatory zoned	Broad, diffuse zoning, smooth greyscale variation pattern, zoning width up to 110 µm	High-Mg# MgHst, MgHbl-Tsch
	Simple zoned	MgHbl-Tsch cores overgrown by high-Mg# MgHst rims, clear core-rim boundary	High-Mg# MgHst, MgHbl-Tsch
	Patchy zoned	Irregular, partially resored Al-rich brighter patches and Al-poor darker patches	MgHbl-Tsch
Diktytaxitic enclaves	Acicular	Framework-forming crystals of the diktytaxitic texture,	High-Mg# MgHst
	Simple zoned / Phenocryst-like	MgHbl-Tsch cores overgrown by high-Mg# MgHst rims, clear core-rim boundary, similar to simple zoned amphibole in 1951 andesite	High-Mg# MgHst, MgHbl-Tsch
	Olivine-rimming	Primary phase of the outer rim of resorbed olvine crystals	High-Mg# MgHst
Plutonic enclave	Cluster-forming	irregular and interlocking, melt present along crystal boundaries, unzoned or weakly patchy zoned	MgHbl-Tsch

Table 5.3

Table 5.4

Table 4: Representative predicted amphibole crystallizing temperature and melt major and trace element compositions

	Diktytaxitic enclaves						Plutonic enclave				Spiky zoned pheno.						Diffuse zoned pheno.			
	#1	1σ	#2	1σ	#3	1σ	#4	1σ	#5	1σ	#6	1σ	#7	1σ	#8	1σ	#9	1σ	#10	1σ
T °C	970	30	863	30	855	30	877	30	849	30	842	30	851	30	904	30	836	30	980	30
SiO_2	60.9	3.6	69.4	3.6	71.0	3.6	67.8	3.6	72.0	3.6	72.4	3.6	71.2	3.6	64.6	3.6	73.8	3.6	58.0	3.6
TiO_2	0.7	0.3	0.3	0.1	0.3	0.1	0.3	0.1	0.3	0.1	0.2	0.1	0.3	0.1	0.4	0.1	0.2	0.1	0.8	0.3
Al_2O_3	17.6	1.2	15.7	1.2	15.3	1.2	16.5	1.2	15.1	1.2	14.7	1.2	15.0	1.2	17.0	1.2	14.5	1.2	18.3	1.2
FeOt	4.3	1.6	2.6	1.0	2.2	0.8	3.1	1.2	1.9	0.7	1.9	0.7	2.1	0.8	4.2	1.6	1.6	0.6	5.7	2.2
MgO	2.1	1.0	0.5	0.3	0.4	0.2	0.8	0.4	0.5	0.2	0.4	0.2	0.5	0.2	0.9	0.4	0.4	0.2	3.0	1.4
CaO	5.4	1.6	2.7	0.8	2.2	0.7	3.4	1.0	2.5	0.8	2.3	0.7	2.5	0.7	3.3	1.0	2.1	0.6	6.8	2.0
K_2O	1.9	0.7	3.1	0.7	3.2	0.7	2.7	0.7	2.8	0.7	3.5	0.7	3.3	0.7	3.0	0.7	3.4	0.7	1.6	0.7
D Sr	0.36	0.10	0.41	0.11	0.30	0.08	0.42	0.12	0.25	0.07	0.37	0.10	0.37	0.10	0.56	0.16	0.33	0.09	0.42	0.12
D Pb	0.05	0.02	0.05	0.02	0.05	0.01	0.06	0.02	0.05	0.01	0.04	0.01	0.04	0.01	0.05	0.02	0.04	0.01	0.06	0.02
D Zr	0.33	0.15	0.54	0.24	0.40	0.17	0.54	0.24	0.38	0.17	0.58	0.25	0.54	0.24	0.56	0.24	0.54	0.24	0.34	0.15
D Nb	0.31	0.10	0.91	0.30	0.81	0.27	0.72	0.24	0.75	0.25	1.20	0.40	1.02	0.34	0.69	0.23	1.24	0.42	0.24	0.08
D La	0.21	0.08	0.45	0.16	0.45	0.16	0.38	0.14	0.42	0.15	0.57	0.20	0.50	0.18	0.35	0.13	0.60	0.21	0.17	0.06
D Sm	1.40	0.54	3.68	1.42	3.32	1.28	3.05	1.18	3.22	1.25	4.91	1.90	4.27	1.65	2.91	1.12	1.96	3.67	1.17	0.45
D Y	1.30	0.44	3.47	1.18	3.21	1.09	2.92	0.99	3.33	1.13	4.28	1.46	3.72	1.27	2.22	0.75	4.47	1.52	1.06	0.36
Sr	1148	336	339	99	331	97	344	101	330	97	265	78	234	68	292	86	346	101	895	262
Pb	33	10	44	14	44	13	32	10	35	11	65	20	56	17	65	20	31	10	98	30
Zr	203	91	110	50	133	60	81	36	113	51	98	44	107	48	159	71	92	42	155	70
Nb	10.6	3.7	7.0	2.5	9.0	3.1	6.2	2.2	7.1	2.5	6.6	2.3	7.9	2.8	11.4	4.0	5.6	2.0	7.9	2.8
La	24	9	46	17	42	16	33	12	30	11	43	16	39	14	42	16	31	11	19	7
Sm	4.4	1.7	4.7	1.9	5.1	2.0	2.7	1.1	2.8	1.1	4.0	1.6	4.2	1.7	5.0	2.0	3.9	1.6	3.2	1.3
Y	18	7	18	7	22	8	13	4	10	4	14	5	16	6	29	10	15	5	22	8

Temperature is calculated with the pressure-independent amphibole-only model of Putirka (2016); melt major element compositions are calculated with the temperature-independent chemometric equations in Chapter 3; D are calculated with the temperature-independent equations in Chapter 4.

CHAPTER 6

Conclusions and future work

6.1. KEY FINDINGS

6.1.1. The petrogenesis of Mt. Lamington 1951 andesite and magmatic enclaves

6.1.1.1. What is the interrelationship between the 1951 andesite and its magmatic enclaves?

Two major types of mafic-intermediate magmatic enclaves are identified within the andesitic dome lavas produced during the 1951eruption of Mt. Lamington: diktytaxitic and plutonic-textured. We demonstrate that diktytaxitic enclaves are formed when the enclave magma is quenched against the overlying andesite magma and generates a foam layer, which floats upward into the andesite magma. In contrast, the plutonic-textured enclaves represent slow-cooling crystallization products of the enclave-forming magma away from the direct contact zone with the andesite magma (Chapter 2). We demonstrate with amphibole and inferred melt compositional data that the plutonic enclave with up to 69 vol. % amphibole does not represent a fragment of cumulates related to the formation of the 1951 andesite, instead, it represents a slowly crystallized mushy margin of the enclave magma (Chapter 5). Therefore, the presence of magmatic enclaves in the 1951 andesite indicates mingling of the enclave magma with the andesite magma. The bulk-rock geochemistry of the 1951 andesites and magmatic enclaves cannot be related by fractional crystallization models, suggesting that the enclave magma is not a parent to the 1951 andesite (Chapter 2).

6.1.1.2. What is the origin of olivine crystals with disequilibrium textures in the 1951 andesite and diktytaxitic enclaves?

Both andesite and enclaves contain abundant olivine crystals with amphibole reaction rims, which appear to be responsible for the high Cr and Ni concentrations in the Mt. Lamington magmas. Contamination of the magmas by the PUB suggested by an earlier study (Arculus *et al.*, 1983) is not necessary and would seem to require an unreasonable thermal budget. The olivines are euhedral and do not show deformation textures, as observed in the PUB olivines; additionally their geochemical signatures are inconsistent with the PUB harzburgite and dunite xenoliths. Therefore the olivines cannot have an ophiolite origin, and instead are suggested to be products of earlier fractional crystallization from magmas that may have been precursor(s) to the 1951 andesite and/or pre-1951 shoshonite. Their presence, as well as that of xenocrysts of clinopyroxene and amphibole, is probably a result of remobilization and recycling of these products of earlier fractional crystallization by the enclave-forming magma (Chapter 2).

6.1.1.3. What is the petrogenesis of the 1951 andesite and magmatic enclaves?

Evidence for crystal exchange between the enclaves and the andesite host is seen in the petrology and further confirmed with mineral data. Isotopic data indicate that the 1951 andesite and enclave-forming magma sources have the same isotopic composition; trace element signatures indicate a subduction-related component. We interpret variable trace element ratios Zr/Nb and Ba/La to be a result of significant fractionation or assimilation of amphibole. The dominant processes that led to the formation of the 1951 andesite and enclave-bearing magma are likely to be deep fractional crystallization of mafic phases followed by shallow fractionation of amphibole ± plagioclase (Chapter 2). Particularly, we infer that the amphibole compositions in cumulates generated during the formation of andesites should be dominantly MgHst, rather than MgHbl-Tsch (Chapter 5). Assimilation of MgHbl-Tsch in the enclave magma, petrologically observed as incorporation of phenocryst-like amphiboles from andesites, is able to explain the variations of Zr/Nb and Ba/La ratios in the magmatic enclaves (Chapter 2 and 5).

6.1.2. Open-system processes revealed by melt chemistry inversion from calcic amphiboles

6.1.2.1. What are the P-T-X conditions of crystallization of calcic amphiboles according to experimental studies?

Calcic amphiboles selected from the experimental studies (Parg, MgHst, Kaer, Tsch and MgHbl), display large compositional variability over the wide range of P-T-melt chemistry (X) conditions (200-2,500 MPa; 750-1,100 °C; basanitic-rhyolitic melt compositions). The crystallization of calcic amphiboles occurs over a large temperature range (750-1,050 °C) at low pressure conditions (200-400 MPa), while under high pressure conditions (2,000-2,500 MPa), the crystallization of calcic amphiboles are linked to the highest temperatures (1,050-1,100 °C). Parg crystallization occurs from the hottest (1,100 ºC) and most mafic (basanitic) melt with c.a. 40 wt % SiO_2, and continues to intermediate melt at 900-950 ºC. MgHst crystallizes in basaltic to dacitic melts at ~900-1,050 ºC, as well as (rarely) at lower temperature (800-850 ºC) in more evolved melts with >65 wt% SiO_2. Kaer crystallizes from melts with similar SiO_2 and Al_2O_3 contents to those MgHst-bearing melts, but with higher TiO_2 and lower CaO and MgO contents. Tsch crystallizes primarily at lower temperatures (800-950 ºC) in dacitic-rhyolitic melts with >60 wt % SiO_2 and decreasing Al_2O_3, TiO_2, CaO and MgO. MgHbl only crystallizes from the most silicic melt with c.a. > 70 wt % SiO_2, over a range of temperatures. MgHst, MgHbl and Tsch can all crystallize at the same pressure (e.g. 200 MPa). The poor correlations between pressure and amphibole tetrahedral Al content (Al_T) demonstrate a weak control by pressure on calcic amphibole crystal chemistry. In contrast, amphibole Al_T are strongly correlated with melt SiO_2 and TiO_2 contents and intermediately correlated with temperature, suggesting that melt compositions and temperature are more important controlling factors to amphibole compositions than pressure (Chapter 3).

6.1.2.2. Can we improve our ability to infer accurately the major element compositions of melts from which calcic amphiboles are crystallized, using the crystal chemistry and/or the crystallization temperature of calcic amphibole?

We have used multiple-regression methods to recalibrate empirical chemometric equations to calculate the major element composition of melts in equilibrium with calcic amphibole. The equations are based on amphibole formula proportions ± temperature from published experimental P-T-X data, and are independent of pressure. Compared with the pressure-dependent equations provided by (Ridolfi & Renzulli, 2012), the new equations yield improved precision and accuracy. The results of multiple regression analyses demonstrate that temperature has a minor impact on improving the precision of calibrating melt compositions with amphibole crystal chemistry, which suggests that temperature is less important than melt compositions in controlling amphibole crystal chemistry. This is convenient for application of the equations to natural amphiboles where temperature is typically unknown (Chapter 3).

6.1.2.3. What are the implications of using the chemometric equations in reconstructing major element compositions of melts in equilibrium with volcanic and plutonic amphiboles?

Using the chemometric equations, reconstructed melt compositions in equilibrium with the rims of amphiboles in pumice clasts of the Ongatiti ignimbrite are in good agreement with the matrix glass compositions published by (Cooper & Wilson, 2014). This suggests that equilibrium between the amphibole rims and melts of matrix glass compositions is achieved. The cores of amphiboles from the Ongatiti ignimbrite show large compositional variation as well as disequilibrium textures (e.g. patchy zoning, resorption/dissolution texture), and the predicted melt compositions also display large compositional variations. We interpret that the variation in the predicted melt compositions from amphibole cores may be due to different degrees of equilibration of the amphiboles derived from crystal mushes with evolved melts over a range of timescales. This interpretation is an alternative to the model provided by (Cooper & Wilson, 2014) which instead suggests that source heterogeneity is a major contribution to the crystal chemical diversity in the Ongatiti ignimbrite (Chapter 3).

Our multiple regression model is also able to predict the compositions of melts from amphiboles in clinopyroxenite, hornblendite and hornblende gabbro xenoliths in Grenada lavas, which are consistent with melt inclusions hosted in those cumulates, as reported by (Stamper *et al.*, 2014). The predicted melts cover a wide range of compositional variations, which may a result of *in situ* melt evolution due to extensive crystallization of the cumulate mineral phases, or equilibration of the cumulate fragments with later evolved melts (Chapter 3)

In order to give unequivocal interpretations of these predicted melt compositions we would require detailed knowledge of the textural setting of the crystals from which the amphibole major element data are collected (Cooper & Wilson, 2014, Stamper *et al.*, 2014). Without this information, uncertainty remains as to the primary cause of the compositional variations in the predicted melts. Therefore, we propose that the melt compositions inferred from amphiboles displaying disequilibrium textures, such as patchy zoning as a result of resorption/dissolution, should be interpreted carefully for revealing open magmatic processes which may be responsible for the diversity in amphibole crystal chemistry and textures (Chapter 3).

6.1.2.4. Can we infer trace element partition coefficients of calcic amphiboles ($^{Amph/L}D$) from the crystal chemistry and/or crystallization temperatures of calcic amphiboles?

Multiple regression (MR) analyses can be used to parameterize published $^{Amph/L}D$ of Rb, Sr, Pb, HFSE, REE and Y for calcic amphiboles of Parg, MgHst, Kaer, Tsch and MgHbl compositions. It is demonstrated that temperature and amphibole major element components assigned to different crystallographic sites show different significance in controlling $^{Amph/L}D$ of those elements. Application of the multiple regression-derived $^{Amph/L}D$-estimating models to tests, including experimentally derived $^{Amph/L}D$ which are independent from those employed in the MR analyses, and those calculated from Ongatiti MgHbl-glass pairs, yields good agreement with measurements for predicting $^{Amph/L}D$ of Sr, Pb, Ti, Zr, Nb, LREE and MREE. This suggests that reasonable accuracy is achieved for predicting $^{Amph/L}D$ of those elements with MR analyses (Chapter 4).

6.1.2.5. What is the dominant control over trace element concentrations in calcic amphiboles, melt compositions or $^{Amph/L}D$?

Published amphibole major and trace element compositional data from Mt. Pinatubo, Mt. Hood, Shiveluch Volcano, Mt. St. Helens and the Ongatiti ignimbrite of Mangakino Volcano are applied as case studies. $^{Amph/L}D$ and major and trace element contents in the melt are inferred based on amphibole crystal chemistry. This enables us to constrain whether the differences of trace element concentrations in amphiboles with contrasting major element compositions are due to the differences of $^{Amph/L}D$ or melt trace element concentrations. We demonstrate that melt trace element contents are the dominant factor governing Sr, Pb, Ti and Zr concentrations in amphibole, but for Nb, REE and Y, partition coefficients instead are the primary control (Chapter 4).

6.1.2.6. What magmatic processes can we infer from the reconstructed melt major and trace element compositions?

We use case studies of Mt. Pinatubo (Chapter 4), the Ongatiti ignimbrite of Mangakino Volcano (Chapter 4) and Mt. Lamington (Chapter 5) to demonstrate that the inferred melt trace compositions have significant implications in decoding magmatic processes that contribute to amphibole compositional diversity in arc magma plumbing systems. Bimodal amphibole populations and hence inferred melt compositions in Mt. Pinatubo indicate magma mingling process, which is consistent with conclusions driven by earlier studies, e.g. (Pallister *et al.*, 1996). The inferred melt trace element compositions from bimodal groups also record co-crystallization of plagioclase, ilmenite, zircon and apatite together with amphiboles to varying degrees, and the interpretation can be generally supported by petrographic evidence (e.g. Pallister *et al.*, 1996). For Ongatiti amphiboles, the melt Pb and La variations predicted from patchy zoned cores indicate recycling crystal mush components derived from a mafic melt followed by equilibration with a felsic rim-crystallizing melt. The rims of the Ongatiti amphiboles record co-crystallization of zircon, apatite and minor ilmenite, which are also

confirmed by petrographic evidence (Cooper & Wilson, 2014). The inferred melt compositions from the crystal chemistry of Mt. Lamington amphibole also record the co-crystallization of ilmenite and apatite, consistent with petrographic observations (Zhang *et al.*, 2015).

6.1.3. Amphibole compositional bimodality reflects arc magma hybridization

6.1.3.1. How does amphibole compositional bimodality form in arc magmas and what are the implications?

Mt. Lamington amphiboles from the 1951 andesites and magmatic enclaves display compositional bimodality (MgHst vs. MgHbl-Tsch). We interpret that the bimodal amphibole populations are crystallized in different melt under contrasting thermal conditions, i.e. MgHst from hotter, less silica-rich melt and MgHbl-Tsch from cooler, more silica-rich melt, rather than at large range of depths. The recharge of enclave-forming magma into overlying andesite magma, followed by magma mixing, brings the two different types of amphiboles together shortly before the Mt. Lamington 1951 eruption took place (Chapter 5).

Amphibole compositional bimodality is common in Mt. Lamington and has also been demonstrated in recent case studies such as Mt. Pelée, Unzen Volcano, Shiveluch Volcano, Mt. St. Helens, Soufrière Hills Volcano, Mt. Hood, Augustine Volcano, Ciomadul Volcano, Mt. Merapi and the Ongatiti eruption of the Mangakino volcanic centre. (Kent, 2014) suggests that the amphibole compositional bimodality is a ubiquitous phenomenon in global subduction zones; felsic amphiboles (MgHbl-Tsch) are crystallized in a cool, silicic source stalled in shallow crust, while mafic amphiboles crystallize in a hot, mafic magma source at depth. We propose that the crystallization of bimodal amphibole populations may not occur over a large depth range, according to the results of experimental studies (bimodal amphibole populations are produced in 200 MPa experiments) and the case study of Mt. Lamington (Zhang *et al.*, 2015). Their co-presence in hand-specimen scale or even in sub-crystal scale cannot be explained by models arguing for fractional crystallization of mantle-derived melts in producing intermediate magma compositions at convergent margins (Kent, 2014). Instead, hybridization of the two magmas stalled under different thermal and geochemical conditions can bring the two contrasting types of amphiboles in an overall intermediate melt. Therefore, amphibole compositional bimodality from Mt. Lamington and widely occurring in arc magmatism indicates that magma mixing is the dominant way of producing intermediate magmas beneath arc volcanoes, consistent with conclusions of earlier studies (Chapter 5).

6.1.3.2. What can we infer from the sub-crystal scale compositional bimodality revealed in the two types of oscillatory zoned amphibole phenocrysts in Mt. Lamington 1951 andesites?

The amphibole compositional bimodality is also revealed in sub-crystal scale across oscillatory zonings in amphibole phenocrysts in 1951 andesites. Two types of oscillatory zonings are identified: spiky and diffuse. The spiky oscillatory zonings are characterized by the co-presence of MgHbl-Tsch and low-Mg# MgHst, reflecting temperature/pressure fluctuations during crystallization, and the effect of magma replenishment is not significant; whilst diffuse oscillatory zonings are composed by MgHbl-Tsch and high-Mg# MgHst, which we believe the variation is driven by both T/P fluctuation and mafic magma input. We believe the oscillatory zonings are caused by crystal movement along magma convection and thus we propose the below scenario to explain the formation of the two different types of oscillatory zonings: spiky oscillatory zoned amphiboles are formed during convection within thermal diffusion zone where the andesite magma body is heated by the recharge of the enclave magma; in contrast, diffuse oscillatory zoned amphiboles are ascribed to magma convection within chemical diffusion zone where the andesite magma is heated and mixed with the enclave magma (Chapter 5).

6.2. FUTURE PERSPECTIVES

6.2.1. Amphibole perspective to unravel open-system processes in other volcanic systems

Amphibole phenocrysts from Mt. Hood andesitic dome lavas and mafic enclaves display a continuous compositional variation from Tsch to MgHbl (Koleszar, 2011). (Koleszar, 2011) suggests that the andesite at Mt. Hood is a product of extensive hybridization between a cool, shallow-stored, MgHbl-bearing silicic magma and a hot, MgHst-bearing mafic magma. The continuum in amphibole compositions suggest that magma chemical mixing occurs, and this is distinguishable from mechanical magma mingling occurred in the magma plumbing system of Mt. Pinatubo.

Furthermore, amphiboles from Shiveluch Volcano also display a continuous variation from Tsch to MgHbl in major element compositions, corresponding to complex textural variations including patchy zoning and oscillatory zoning formed in response to magma mixing processes (Humphreys *et al.*, 2006). However, the trace element compositions of amphiboles from Shiveluch Volcano do not display obvious variation trends against amphibole major element compositions (e.g. **Fig. 5.5f1** in Chapter 5). Even the predicted $^{Amph/L}D$ and trace element contents in melts show scattered variation against amphibole trace element contents (e.g. **Fig. 5.5f2, f3** in Chapter 5). However, we observe linear correlations between inferred melt trace element compositions and melt major element compositions (e.g. **Fig. 5.5f4** in Chapter 5). With further textural information these data could be used to test the hypothesis that patchy zoned crystals in the Shiveluch andesites grew during the formation of earlier cumulates (Humphreys *et al.*, 2006).

Similarly, amphiboles from the dome-forming dacites and dacitic white pumices of the May 18, 1980 eruption of Mt. St. Helens also have a compositional variation range of Tsch and MgHbl. However, trace element contents in amphiboles and inferred melts do not display any obvious variation trends (e.g. Zr, Nb, REE and Y) against major elements in amphiboles and inferred melts (e.g. **Fig. 5.5d4, d5, e4, e5, f4, f5** in Chapter 5). (Thornber *et al.*, 2008) suggested that in the magma plumbing system of Mt. St. Helens, thorough mixing of multiple magmas sourced from different depths may have occurred, probably accounting for the diverse compositional and textural variations in amphibole crystals. Therefore, amphiboles from Mt. St. Helens may provide an insight into mixing of more than two magma components in the arc magma plumbing system, which may also be the driving force in generating the largely variant, but non-systematic amphibole compositions. This insight is in complementary to the bimodal recharge-driven magma mingling/mixing as the dominant mechanism at Mt. Pinatubo, Mt. Hood and Shiveluch Volcano, and recycling crystal mush components prior to equilibration with a felsic melt occurred prior to the Ongatiti eruption at Mangakino Volcano.

We propose that in the future work, further indications of magma mixing processes through melt chemistry inversion from Mt. Hood, Shiveluch Volcano and Mt. St. Helens amphiboles require detailed investigation of the crystal chemistry data associated with textural information, chemical analyses of matrix glasses and/or melt inclusions, and whole-rock petrological observations.

6.2.2. Timescales of enclave-andesite interaction

We demonstrated that the formation of diktytaxitic and plutonic enclaves are under different cooling rates when the enclave magma intruded at the base of andesite magma chamber (Chapter 2). Recycled olivine crystals with reaction rim textures in diktytaxitic enclaves and 1951 andesites can potentially preserve the information on timescales over which the enclave-andesite interaction has occurred, and thus shed light on the timing between enclave-andesite magma mixing and eruption. There are two methods of determining the timescales. First, results of earlier experimental studies show that the width of disequilibrium-induced reaction rims growing on olivines is linearly correlated with the duration of experiments (Coombs & Gardner, 2004, Grant *et al.*, 2014). Therefore, we are able to infer the timescales over which the amphibole-dominated reaction rims are developed on the olivine

crystals, following careful measurements of the width of reaction rims, and further calculations to rule out of the bias effect caused by crystal orientation. Second, we can carry out chemical analyses of major and trace elements traversing olivine crystals, and then apply diffusion chronometry (Costa *et al.*, 2008, Saunders *et al.*, 2012) to work out the diffusion timescales of various elements in the olivine as a result of olivine reaction with melt (Coogan *et al.*, 2005, Qian *et al.*, 2010, Tollan *et al.*, 2015). We can test the results yielded from the two methods by checking their consistency. Knowledge of the timescales between magma interactions and eruption might in future help to inform interpretation of monitoring datasets.

6.3. REFERENCES

Arculus, R. J., Johnson, R. W., Chappell, B. W., Mc Kee, C. O. & Sakai, H. (1983). Ophiolite-contaminated andesites, trachybasalts, and cognate inclusions of Mount Lamington, Papua New Guinea: anhydrite-amphibole-bearing lavas and the 1951 cumulodome. *Journal of Volcanology and Geothermal Research* **18**, 215-247.

Coogan, L. A., Hain, A., Stahl, S. & Chakraborty, S. (2005). Experimental determination of the diffusion coefficient for calcium in olivine between 900 degrees C and 1500 degrees C. *Geochimica et Cosmochimica Acta* **69**, 3683-3694.

Coombs, M. L. & Gardner, J. E. (2004). Reaction rim growth on olivine in silicic melts: Implications for magma mixing. *American Mineralogist* **89**, 748-758.

Cooper, G. F. & Wilson, C. J. N. (2014). Development, mobilisation and eruption of a large crystal-rich rhyolite: The Ongatiti ignimbrite, New Zealand. *Lithos* **198**, 38-57.

Costa, F., Dohmen, R. & Chakraborty, S. (2008). Time Scales of Magmatic Processes from Modeling the Zoning Patterns of Crystals. *Reviews in Mineralogy and Geochemistry* **69**, 545-594.

Grant, T. B., Milke, R., Wunder, B., Wirth, R. & Rhede, D. (2014). Experimental study of phlogopite reaction rim formation on olivine in phonolite melts: Kinetics, reaction rates, and residence times. *American Mineralogist* **99**, 2211-2226.

Humphreys, M. C. S., Blundy, J. D. & Sparks, R. S. J. (2006). Magma Evolution and Open-System Processes at Shiveluch Volcano: Insights from Phenocryst Zoning. *Journal of Petrology* **47**, 2303-2334.

Kent, A. J. (2014). Bimodal amphibole populations in arc magmas. *Goldschmidt*, 1232.

Koleszar, A. (2011). Controls on Eruption Style and Magma Compositions at Mount Hood, Oregon. Oregon State University, 199.

Pallister, J., Hoblitt, R., Meeker, G. P., Knight, R. J. & Siems, D. F. (1996). Magma Mixing at Mount Pinatubo: Petrographic and Chemical Evidence from the 1991 Deposits. In: Newhall, C. & Punongbayan, R. S. (eds.) *Fire and Mud: Eruptions and Lahars of Mount Pinatubo, Philippines*. Seattle: University of Washington Press, 687-731.

Qian, Q., O'Neill, H. S. C. & Hermann, J. (2010). Comparative diffusion coefficients of major and trace elements in olivine at similar to 950 degrees C from a xenocryst included in dioritic magma. *Geology* **38**, 331-334.

Ridolfi, F. & Renzulli, A. (2012). Calcic amphiboles in calc-alkaline and alkaline magmas: thermobarometric and chemometric empirical equations valid up to 1,130°C and 2.2 GPa. *Contributions to Mineralogy and Petrology* **163**, 877-895.

Saunders, K., Blundy, J., Dohmen, R. & Cashman, K. (2012). Linking Petrology and Seismology at an Active Volcano. *Science* **336**, 1023-1027.

Stamper, C. C., Blundy, J. D., Arculus, R. J. & Melekhova, E. (2014). Petrology of Plutonic Xenoliths and Volcanic Rocks from Grenada, Lesser Antilles. *Journal of Petrology* **55**, 1353-1387.

Thornber, C., Pallister, J. S., Lowers, H. A., Rowe, M. C., Mandeville, C. & Meeker, G. P. (2008). Chemistry, mineralogy and petrology of amphibole in Mount St. Helens 2004-2006 Dacite. In: Sherrod, D. R., Scott, W. E. & Stauffer, P. H. (eds.) *A volcano rekindled: the renewed eruption of Mount St Helens, 2004-2006*. Washington: U.S. Geological Survey Professional Paper.

Tollan, P. M. E., O'Neill, H. S. C., Hermann, J., Benedictus, A. & Arculus, R. J. (2015). Frozen melt–rock reaction in a peridotite xenolith from sub-arc mantle recorded by diffusion of trace elements and water in olivine. *Earth and Planetary Science Letters* **422**, 169-181.

Zhang, J., Davidson, J. P., Humphreys, M. C. S., Macpherson, C. G. & Neill, I. (2015). Magmatic Enclaves and Andesitic Lavas from Mt. Lamington, Papua New Guinea: Implications for Recycling of Earlier-fractionated Minerals through Magma Recharge. *Journal of Petrology* **56**, 2223-2256.